

Polarimetric weather radar: from signal processing to microphysical retrievals

THÈSE N° 6639 (2015)

PRÉSENTÉE LE 31 JUILLET 2015

À LA FACULTÉ DE L'ENVIRONNEMENT NATUREL, ARCHITECTURAL ET CONSTRUIT
LABORATOIRE DE TÉLÉDÉTECTION ENVIRONNEMENTALE
PROGRAMME DOCTORAL EN GÉNIE CIVIL ET ENVIRONNEMENT

ÉCOLE POLYTECHNIQUE FÉDÉRALE DE LAUSANNE

POUR L'OBTENTION DU GRADE DE DOCTEUR ÈS SCIENCES

PAR

Jacopo GRAZIOLI

acceptée sur proposition du jury:

Prof. A. Rinaldo, président du jury
Prof. A. Berne, directeur de thèse
Prof. H. Ruschenberg, rapporteur
Prof. S. Nesbitt, rapporteur
Prof. M. Lehning, rapporteur



ÉCOLE POLYTECHNIQUE
FÉDÉRALE DE LAUSANNE

Suisse
2015

Acknowledgements

This thesis gave me the opportunity to work side by side with many great people, that i would like mention here. I thank my supervisor, Alexis Berne, for all the excellent guidance of these last four years, for the many useful suggestions and advices and for giving me the opportunity to work not only in my office but in many fantastic (outdoor) places. Thanks to all my brilliant colleagues, the past and the present ones, at the LTE laboratory: it is much easier to work in such a nice environment. Thanks to Alina, our secretary, Andre and Denis, our technicians, and to all the technical and scientific staff of EPFL (and in particular of the ENAC faculty): scientific research would just not be possible without you. A big thank also goes to our French colleagues of the LTHE of Grenoble for the incredible support during our measurement campaigns in Ardèche. I feel like naming one of you for all: Brice Boudevillain who even drove for more than 12 hours in a row between France and Switzerland to help us when we really needed it. I do not want to forget our Swiss colleagues of the SLF of Davos and of the PSI institute: the measurement campaigns that we conducted in the Alps required a lot of their support. Thanks to all the people who collaborated with us in different and exciting projects. Especially, thanks to Devis Tuia, who brought many interesting ideas and suggestions coming from different fields of research and was always available for any kind of discussion. If i think about my four years here, i immediately remember about all my colleagues, PhD students and postdocs of our department: thanks, all of you, for any big or small moment that we shared. A very special thought goes, with love, to my girlfriend Gosia. Thanks for your support, for the many beautiful moments and for pushing me to look at the world with a bit more of curiosity.

J. G.

Abstract

Accurate modelling of liquid, solid and mixed-phase precipitation requires a thorough understanding of phenomena occurring at various spatial and temporal scales. At the smallest scales, precipitation microphysics defines all the processes occurring at the level where precipitation is a discrete process. The knowledge of these microphysical processes originates from the interpretation of snowfall and rainfall measurements collected with various sensors. Direct sampling, performed with in-situ instruments, provides data of superior quality. However, the development of remote sensing (and dual-polarization radar in particular) offers a noteworthy alternative: large domains can in fact be sampled in real time and with a single instrument. The drawback is obviously the fact that radars measure precipitation indirectly. Only through appropriate interpretation radar data can be translated into physical mechanisms of precipitation.

This thesis contributes to the effort to decode polarimetric radar measurements into microphysical processes or microphysical quantities that characterize precipitation. The first part of the work is devoted to radar data processing. In particular, it focuses on how to obtain high resolution estimates of the specific differential phase shift, a very important polarimetric variable with significant meteorological importance. Then, hydrometeor classification, i.e. the first qualitative microphysical aspect that may come to mind, is tackled and two hydrometeor classification methods are proposed. One is designed for polarimetric radars and one for an in-situ instrument: the two-dimensional video disdrometer. These methods illustrate the potential that supervised and unsupervised techniques can have for the interpretation of meteorological measurements.

The combination of in-situ measurements and polarimetric data (including hydrometeor classification) is exploited in the last part of the thesis, devoted to the microphysics of snowfall and in particular of rimed precipitation. Riming is shown to be an important factor leading to significant accumulation of snowfall in the alpine environment. Additionally, the vertical structure of rimed precipitation is examined and interpreted.

Keywords: precipitation microphysics, polarimetric radar, snowfall, rainfall, remote sensing

Sommario

La modellazione e previsione della precipitazioni in fase solida, liquida o mista richiede un'approfondita conoscenza di molteplici interazioni che si verificano a varie scale spaziali e temporali. La microfisica della precipitazione tratta in particolare di tutti i processi che si verificano ad una scala alla quale la precipitazione é un fenomeno discreto. La conoscenza di questa microfisica trae origine dall'interpretazione di misure di pioggia e neve raccolte per mezzo di specifici strumenti. Le classiche misure dirette (in-situ) sono in grado di fornire dati e osservazioni di ottima qualità, ma in rapporto a piccole scale spaziali. In questo contesto il telerilevamento (e la tecnologia radar polarimetrica) offre un'alternativa interessante: aree molto vaste possono essere osservate in tempi molto brevi. Le misure di telerilevamento sono purtroppo indirette e richiedono un'accurata interpretazione prima di assumere un qualsivoglia significato meteorologico. Questo lavoro di tesi contribuisce agli sforzi atti a decodificare le misure radar e tradurle in osservazioni microfisiche della precipitazione. La prima parte della tesi é dedicata puramente al trattamento di dati e in particolare alla stima della differenza specifica di fase (una variabile molto importante per varie applicazioni meteorologiche). In seguito, i dati radar e i dati di un videodisdrometro bi-dimensionale sono utilizzati al fine di classificare le idrometeore della precipitazione, grazie ad un algoritmo di classificazione supervisionato (nel caso del video-disdrometro) e di un metodo non supervisionato (nel caso dei dati radar). Nell'ultima parte della tesi, dati raccolti "in-situ" e dati di telerilevamento (raccolti da un radar polarimetrico) vengono utilizzati in maniera complementare per descrivere e comprendere la microfisica della neve in una valle delle alpi centrali svizzere, con un'attenzione particolare per la struttura verticale di questo tipo di precipitazione.

Parole chiave: microfisica delle precipitazioni, radar polarimetrici, neve, pioggia, telerilevamento

Contents

Acknowledgements	i
Abstract (English/Italiano)	iii
Most important symbols	xi
Most important acronyms	xiii
1 Introduction	1
Introduction	1
1.1 Motivation	1
1.2 Polarimetric radar measurements	3
1.2.1 Radar equation in meteorology	3
1.2.2 Polarimetric variables	4
1.3 Microphysics and microstructure of precipitation	7
1.3.1 Microstructure: the particle size distribution (PSD)	7
1.3.2 Basic definitions of precipitation microphysics	9
1.4 Thesis outline	10
2 Estimation of the specific differential phase shift upon propagation (K_{dp})	13
K_{dp} estimation	13
2.1 Summary	14
2.2 Introduction	15
2.3 Data sets	17
2.3.1 X-band polarimetric radar data from Brazil	17
2.3.2 X-band polarimetric radar data from Switzerland	17
2.3.3 Simulated rainfall fields	17
2.4 Algorithm description	19
2.4.1 K_{dp} estimation	19
2.4.2 Kalman Filtering	20
2.4.3 Treatment of the δ_{hv} effect	23
2.4.4 Covariance matrices and ensemble estimation	25
2.4.5 Estimation in the backward direction	26

Contents

2.4.6	Practical implementation issues	27
2.4.7	Compilation of a final K_{dp} estimate	28
2.5	Evaluation on simulated radar measurements in rain	31
2.5.1	Description of two other standard algorithms	31
2.5.2	Strategy to evaluate K_{dp}	33
2.5.3	Results of the comparison	33
2.6	Evaluation with X-band radar data in rain and in snow	35
2.7	Summary and Conclusion	39
3	Hydrometeor classification from two-dimensional video disdrometer data	41
	Hydrometeor classification from 2DVD data	41
3.1	Summary	42
3.2	Introduction	42
3.3	Dataset description	44
3.3.1	Experiment locations	44
3.3.2	2DVD instrument and data pre-processing	44
3.3.3	From single particles to global features	46
3.4	Hydrometeor classification	48
3.4.1	Hydrometeor classes and training set	48
3.4.2	Classification method	50
3.5	Results and discussion	53
3.5.1	Performance assessment metrics	53
3.5.2	Evaluation of the quality of the training set	54
3.5.3	Evaluation of the classification performances	55
3.5.4	Ranking of descriptors	56
3.6	Application on unlabeled data	57
3.6.1	17 March 2011	57
3.6.2	12 January 2011	57
3.6.3	5 August 2010	59
3.7	Summary and conclusions	61
4	A clustering approach to polarimetric hydrometeor classification	63
	Hydrometeor classification from polarimetric radar measurements: a clustering approach	63
4.1	Summary	64
4.2	Introduction	64
4.3	Background on clustering techniques	66
4.3.1	Hierarchical data clustering	66
4.3.2	Distance metric	66
4.3.3	Merging rule	67
4.4	Data and processing	68

4.4.1	Data source	68
4.4.2	Polarimetric data	70
4.5	Clustering of polarimetric radar data	71
4.5.1	Data preparation	71
4.5.2	Subset undergoing clustering analysis	72
4.5.3	Clustering algorithm: data similarity and spatial smoothness	73
4.6	Selection of the optimal cluster partition	76
4.6.1	Cluster quality metrics	76
4.6.2	Selection of n_{opt} : Fig. 4.2b	77
4.7	From unlabelled clusters to hydrometeor classes: Fig. 4.2c	78
4.7.1	Global characteristics of the clusters	78
4.7.2	Clusters at positive temperatures	79
4.7.3	Cluster around 0 °C	83
4.7.4	Clusters at negative temperatures	83
4.8	Summary and conclusions	89
5	Riming in winter alpine snowfall during CLACE 2014	93
	Riming in winter alpine snowfall during CLACE 2014: polarimetric radar and in-situ observations	93
5.1	Summary	94
5.2	Introduction	94
5.3	Measurement campaign and instruments	96
5.3.1	Instruments	96
5.3.2	Precipitation events	98
5.4	Analysis of rimed precipitation	99
5.4.1	Riming and snowfall accumulation	99
5.4.2	Evolution of rimed precipitation events	100
5.4.3	Vertical structure	105
5.5	Case study (EV3): turbulence, wind shear, and snowfall enhancement	109
5.5.1	Detailed description of EV3	109
5.5.2	The role of turbulence and wind shear	113
5.6	Summary and Conclusions	114
6	Conclusions and outlook	117
	Conclusions and outlook	117
6.1	Summary	117
6.2	Contribution of this thesis	118
6.3	Perspectives	118

Contents

A Appendix of Chapter 2	121
A.1 Adaptations for S- and C-band frequencies of the KFE algorithm	121
A.2 Parametrization of covariance matrices	121
A.3 Simulated rainfall events	122
A.4 Realistic profiles of phase related variables	123
A.5 Statistical Descriptors	124
A.6 Accuracy evaluation at C-band and S-band using simulated fields	125
B Appendix of Chapter 3	129
B.1 Minimum number of particles for a reliable classification	129
C Appendix of Chapter 4	131
C.1 Polarimetric characteristics of the seven clusters	131
C.2 DR2009 algorithm	131
Bibliography	150

Most important symbols

Symbol	Units	Description
C_r or C_r^*	[-]	Radar calibration factor or radar constant
$C(\epsilon_z)$	[-]	Covariance matrix of the measurement errors
$C(\epsilon_s)$	[-]	Covariance matrix of the errors of the forward projection
D	[mm]	Particle diameter (or reference size)
D_e	[mm]	Equivolume diameter
d_m	[-]	Kernel weight in Multiple Kernel Learning
f_{hh}	[m] or [cm]	Complex forward scattering amplitude, horizontal polarization
F_t	[-]	Observation model matrix
K	[-]	Kernel function matrix
K	[-]	Refractivity of an hydrometeor type
K_t	[-]	Kalman gain matrix
K_{dp}	[° km ⁻¹]	Specific differential phase shift upon propagation
K_i	[-]	Refractivity of ice
K_w	[-]	Refractivity of liquid water
n_c	[-]	Number of clusters in a dataset
N_D	[-]	Number of objects in a dataset
$N(D)$	[mm ⁻¹ m ⁻³]	Drop size distribution or particle size distribution
$N_A(D)$	[mm ⁻¹ m ⁻² s ⁻¹]	Areal particle size distribution
N_t^*	[m ⁻³]	Generic concentration parameter of a PSD
$N_V(D)$	[mm ⁻¹ m ⁻³]	Volumic particle size distribution
P	[W] or [mW]	Power
P_t	[W] or [mW]	Power transmitted by a radar
P_r	[W] or [mW]	Power received by a radar
r	[m] or [km]	Range distance
\mathbf{s}		State vector
s_{hh}	[m] or [cm]	Complex backscattering amplitude, horizontal polarization
T_t	[-]	Observation model matrix
\mathbf{v}	[-]	Vector of parameters (for Support Vector Machine)
v	[m s ⁻¹]	Hydrometeor fall velocity

Most important symbols

V_r	[m ³]	Radar resolution volume
\mathbf{x}		Vector of observations
\mathbf{z}		Measurements vector
Z	[dBZ] or [mm ⁶ m ⁻³]	Radar reflectivity factor
Z_{DR}	[dB] or	Differential reflectivity
Z_e	[dB] or	Differential reflectivity
Z_h	[mm ⁶ m ⁻³]	Radar horizontal reflectivity factor
Z_H	[dBZ]	Radar horizontal reflectivity factor
α	[-]	Normalization prefactor of a gamma PSD
δ_{hv}	[°]	Differential phase shift upon backscattering
δ_z	[m] or [km]	Altitude difference with respect to the 0°C level
ϵ		Noise level
η	[m ⁻¹]	Radar reflectivity
\mathcal{K}	[-]	Cohen's Kappa
λ	[m] or [mm] or [cm]	Radar wavelength
Λ	[-]	Rate parameter of a gamma PSD
μ	[-]	Shape parameter of a gamma PSD
ρ	[-]	Pearson correlation coefficient
ρ_{hv}	[-]	Copolar correlation coefficient
σ		Standard deviation
σ_b	[m ²] or [cm ²]	Backscattering cross section
$\sigma_{b,H}$	[m ²] or [cm ²]	Backscattering cross section, horizontal polarization
Φ_{dp}	[°]	Differential phase shift upon propagation
Ψ_{dp}	[°]	Total differential phase shift

Most important acronyms

Acronym	Description
2DVD	2-Dimensional Video Disdrometer
AHC	Agglomerative Hierarchical Clustering
AS	Accuracy Spread
ALI	Adaptive Length linear interpolation
CLACE	Cloud and Aerosol Characterization Experiment
CH	Confoederation Helvetica i.e., Switzerland
DFA	Detrended Fluctuation Analysis
DSD	Drop Size Distribution
FD	Fractal Dimension
GCPEX	GPM Cold-season Precipitation Experiment
GPM	Global Precipitation Measurement
HC	Hydrometeor Classification
HyMEX	Hydrological cycle in the Meditteranean Experiment
IMC	Ice Mass Content
JFJ	JunFrauJoch (place in Switzerland)
KF	Kalman Filter
KFE	Kalman Filter Ensembles
KS	Kleine Scheidegg (place in Switzerland)
LWC	Liquid water Content
MAE	Maennlichen (place in Switzerland)
MKL	Multiple Kernel Learning
MNAE	Mean Normalized Absolute Error
MNB	Mean Normalized Bias
MWD	Moving Window Derivative
NSE	Nash Sutcliffe Efficiency
NWP	Numerical Weather Prediction
OA	Overall Accuracy
MXPol	Mobile X-band Polarimetric
PF	Pixel Fraction
POD	Probability Of Detection
POFD	Probability Of False Detection

Most important acronyms

PPI	Plan Position Indicator
PRP	Percentage of Rimed Precipitation
PSD	Particle size distribution
RHI	Range Height Indicator
RMSE	Root Mean Squared Error
SLW	Supercooled liquid Water
SVM	Support Vector Machine
STAR	Simultaneous transmission and reception
WPA	Weighted Pairwise Average

1 Introduction

1.1 Motivation

Many natural conditions that allow the generation, conservation, and replication of life on our planet are related to a unique chemical specie: water. Water interacts with the Earth both at the surface, in the sub-surface, and in the atmosphere of the planet. It changes phase, composition, purity and yet it comes back with the same characteristics at each step of the water cycle.

Even though a cycle does not have a well defined start or end point, from a human perspective the water cycle starts with precipitation. Precipitation is in fact the first and more immediate interaction between water and our environment. Both the absence and the excess of precipitation (e.g., *Trenberth et al.*, 2003; *Ciais et al.*, 2005) have a direct social and economical impact on the modified environment of our societies, but also on natural ecosystems. In the recent times, these impacts occurs into a context where the climate evolves faster than during the last centuries (i.e. climate change), adding additional unknowns to their predictability and magnitude (*Hurrell*, 1995; *Frei et al.*, 2006). It is consequently important, now more than in the past, to better understand the processes that govern precipitation at various spatial and temporal scales. Observation, interpretation, and insight into precipitation are indispensable steps in order to achieve an accurate parametrization of numerical weather models (e.g., *Gregory et al.*, 2000) and in the end to be able to produce robust forecasts.

Precipitation has been observed and experienced for millennia, has been scientifically studied for centuries and yet today a lot remains to be observed, discovered and understood because of its complexity. Being the flux of (liquid or solid) hydrometeors from the atmosphere to the Earth's surface, precipitation is the result of complex interactions between turbulent atmospheric dynamics and cloud microphysics that span from a few microns and seconds to thousands of kilometres and days (e.g., *Lovejoy et al.*, 2008). Moreover, it varies according to the spatial and temporal scales of interest (*Fabry*, 1996). The first and most immediate question concerning precipitation is its quantification. This exercise dates back to antiquity, when the ancestors of the modern rain gauges were developed in Greece and India. The first

Chapter 1. Introduction

systematic measurements of rain started to be collected in the Seventeenth century, and in the same time snowfall started to be monitored in an organized manner too.

The 20th century, and in particular its second half, was a prolific period for the development of precipitation measurement devices: rain gauges, snow gauges, snow height measurements have been designed and invented in this period of time. At the same time the researchers started to investigate precipitation over smaller scales: not only the quantification but also the small-scale features of precipitation were recognized to be important to be able to describe, model, and forecast precipitation. This interest in the microphysics and microstructure of precipitation led to the development of particle counters, particle imagers, optical disdrometers and video-disdrometers (*Drufuca and Zawadzki, 1975; Loffler-Mang and Joss, 2000; Kruger and Krajewski, 2002; Garrett et al., 2012*). Such sensors provide very detailed information but only over relatively small sampling volumes. Also, they can be used for continuous monitoring, but at the level of the ground only while precipitation is formed and evolves up to many kilometres above ground. Aircraft-based instruments are a noteworthy exception to this spatial issue, but in turns they are not well suited to provide continuous monitoring (time-wise). The combination of a good spatial and temporal coverage can be potentially achieved by means of remote sensing.

The modern concept of remote sensing of precipitation by means of active and passive sensors is nothing but the legacy brought to us by the otherwise destructive World Wars of the 20th century. Weather radars in particular, that constitute the main focus of this thesis, are the direct descendants of military radars operating at microwave frequencies. Briefly after the end of World War II the potential of radars as means to observe and describe weather (*Maynard, 1946*) and, more specifically, precipitation (*Marshall et al., 1947*) was recognized. Like what happened for ground measurements, weather radars have also been initially employed to retrieve rainfall intensity only. Then, the technological development led (among many other improvements) to dual-polarization systems (*Seliga and Bringi, 1976*) and to better spatial and temporal resolution. Weather radars have been thus used to study processes of increasing complexity. Nowadays, even though accurate quantifications remain crucial research lines (*Berne and Krajewski, 2013*), radars can observe fine-scale microphysical processes of precipitation like the formation of hail, the aggregation and riming of ice crystals, or hydrometeor sorting by size (e.g. *Ulbrich and Atlas, 2007; Schneebeli et al., 2013; Chandrasekar et al., 2013*).

Weather radars, according to their operating frequency and deployment platform, sample precipitation from the meteorological microscale (*Marzano et al., 2010a; Luke et al., 2010; Schneebeli et al., 2013*) to the meso and synoptic scales (*Houze and Medina, 2005; Nesbitt and Anders, 2009; Bluestein and Snyder, 2015*) in nearly real-time. The inherent issue with such measurements is that they are unavoidably indirect. They need to be carefully interpreted before to exhibit any meteorological meaning. At the point scale direct in-situ measurements are in fact still more insightful than indirect radar retrievals and more scientific efforts are required to fill this gap. This thesis is dealing with the interpretation of weather radar data. Together with many other recent research works, it aims to contribute to the efforts to link

radar observations and microphysics of precipitation.

1.2 Polarimetric radar measurements

This thesis is devoted to the estimation and interpretation of polarimetric radar measurements. For the sake of clarity it is important to specify that the term "polarimetric radar" in the majority of cases is used here to define dual-polarization (HH, VV) pulsed Doppler radars operating in simultaneous transmission and reception (STAR hereafter) mode (e.g. *Ryzhkov et al.*, 2005a). The present section provides the definition of the polarimetric variables of major interest for meteorological purposes. The meteorological meaning of the quantities is prioritized with respect to the aspects purely related with the radar technology

1.2.1 Radar equation in meteorology

Weather radars transmit in the atmosphere an electromagnetic wave at microwave frequencies. This signal, while crossing some regions of the atmosphere where clouds or precipitation are present, is partially re-directed (backscattered) towards the radar. The amount of the incident signal that gets backscattered depends on the properties of the targets encountered as well as on the radar characteristics, first of all the wavelength. The basic relation linking the power received by a radar, the power transmitted, the characteristics of the radar and the targets encountered in the volume of reference is called the radar equation. For radars transmitting signal in pulses, as most weather radars do (*Doviak and Zrnić*, 1993, chap. 4), and targeting precipitation, a simplified expression of the radar equation is the following:

$$P(r) = \overset{\text{Radar specs}}{\boxed{C_r}} \times \underset{\text{Targets}}{\boxed{\eta(r)}} \times \overset{\text{Incident power}}{\boxed{\frac{P_t}{r^2}}} \quad (1.1)$$

where $P(r)$ [W] is the average power reflected towards the radar by the targets encountered at a radial distance r [km], P_t [W] is the power transmitted by the radar, $\eta(r)$ is the reflectivity [m^2m^{-3}] and C_r is a constant that depends only the characteristics of the radar system. In this case, C_r takes the units of [m^3]. The reflectivity η is the term describing the interaction between the incident wave and the targets (precipitation particles, i.e. hydrometeors) that populate the radar resolution volume centred at a distance r . It is expressed as:

$$\eta(r) = \frac{1}{V_r} \sum_{i=1}^N \sigma_b^i \quad (1.2)$$

where V_r [m^3] is the radar resolution volume associated with the radial distance r , N is the number of hydrometeors within V_r , and σ_b [m^2] denotes the backscattering cross section of

individual hydrometeors. σ_b is a measure of the detectability of the target from the radar perspective. Equation 1.2 is in general valid if V_r is uniformly populated by hydrometeors. It is worth noting that η in equation 1.1 contains meteorological information, but its unit components σ_b^i depends also on the frequency (wavelength) of the radar (*Doviak and Zrnić, 2006*). To separate these two aspects, since the early stage of development of radar meteorology (*Marshall et al., 1947*), η has been redefined in the following manner:

$$\eta = \frac{\pi^5 |K|^2}{\lambda^4 10^{18}} Z \quad (1.3)$$

where λ [mm] is the incident wavelength, K is the refractive factor of the hydrometeors with respect to the incident wave (K is related to the complex refractive index of water, *Liebe et al., 1991*) and Z is called radar reflectivity factor. This term, if the wavelength is much larger than the size of single hydrometeors (i.e. we are in the Rayleigh regime, *Doviak and Zrnić, 2006*), depends on the characteristics of the population of hydrometeors and not anymore on the wavelength. Therefore, under these conditions, it is a purely meteorological variable. The radar equation (Eq.1.1) can now be inverted and written in terms of reflectivity factor Z :

$$Z_e = C_r^* \frac{P_r r^2}{P_t 0.93} \quad (1.4)$$

where C_r^* is a newly defined calibration constant including the characteristics of the radar and the 0.93 is the squared modulus of the refractive factor of liquid water (K_w) that is relatively constant in the Rayleigh regime. Because it is assumed that the Rayleigh regime approximation holds and because K_w is used here despite the fact that the radar might be sampling ice-phase hydrometeors, the reflectivity factor in the equation is called "equivalent" reflectivity factor Z_e (*Smith, 1984*). Given this clarification, in the following we will use the term reflectivity factor and/or simply reflectivity as synonyms of Z_e . It is worth noting that the equivalent reflectivity factor was originally defined when most of the weather radars were mainly collecting measurements in Rayleigh regime conditions. This assumption is on average reasonable for centimetre wavelengths (X-,C-,S- band in ascending wavelength) radars, although non-Rayleigh effects can be easily observed even within this range of radar frequencies (e.g., *Thurai et al., 2008*), while it is definitely unreasonable for recent mm-wavelength systems.

1.2.2 Polarimetric variables

The principle of dual polarization in weather radars involves the transmission and reception of waves with a different polarization, in most of the cases an orthogonal couple of horizontal and vertical (H-V) linearly polarized signals (*Bringi and Chandrasekar, 2001*). Because raindrops are not spherical, but become more oblate as their size increases (*Beard and Chuang, 1987; Beard et al., 2010*), and also ice-phase hydrometeors exhibit geometrical anisotropy (e.g. *Vivekanandan et al., 1994; Bechini et al., 2013; Schneebeli et al., 2013*), dual polarization, combined with the capability of measuring the phase (in addition to the magnitude) of the waves, allows to retrieve more information about the characteristics of the hydrometeors

in a given sampling volume. This allows to compute other variables (with meteorological meaningfulness) than the reflectivity factor presented in Eq. 1.4.

This thesis is dealing with STAR radars and in this section it is provided the definition of the four classical polarimetric variables (Z_H , Z_{DR} , K_{dp} and ρ_{hv}) that are obtained from STAR measurements. The description is more oriented to underline the microphysical significance of each variable rather than explaining the (technical) processing steps that are necessary for its estimation.

Horizontal (Vertical) reflectivity factor

The reflectivity factor at horizontal (vertical) polarization Z_H (Z_V) is the dual-polarization counterpart of Z (see Eqs. 1.4 and 1.2). Taking Z_H as example (Z_V is analogous), it is defined (in dB¹) as:

$$Z_H = 10 \log_{10} \left(\frac{10^6 \lambda^4}{\pi^5 |K_w|^2} \int_{D_{min}}^{D_{max}} \sigma_{b,h}(D) N(D) dD \right) \quad (1.5)$$

where λ [cm] is the incident wavelength, $N(D)$ is the particle size distribution (PSD hereafter) in [$\text{mm}^{-1}\text{m}^{-3}$], $\sigma_{b,h}(D)$ [cm^2] is the size-dependent backscattering cross section and D [mm] is a reference dimension for the particles in the radar resolution volume. For rainfall, D is the equivolume spherical diameter of the drops (e.g., *Ulbrich, 1983*), mainly because the available raindrop shape-size models are very accurate (e.g., *Thurai et al., 2009*). For ice-phase hydrometeors D is not defined in a straightforward manner and both the major dimension of the ice crystals/snowflakes (*Liu, 2008*) or the equivolume diameter of the melted crystals (e.g., *Dolan and Rutledge, 2009*) have been used.

The microphysical expression of Z_H is simplified in rainfall in the Rayleigh regime ($\lambda \gg D$, *Doviak and Zrnić, 2006*) by means of the famous relation that relates Z_H to the 6th moment of the drop size distribution:

$$Z = 10 \log_{10} \left(\int_{D_{min}}^{D_{max}} D^6 N(D) dD \right). \quad (1.6)$$

The merit of this expression is to highlight the size-dependence of Z_H . Generally speaking Z_H depends on the particle size and size distribution, on the incident wavelength, as well as on temperature and on dielectric properties of the hydrometeors (this dependence is carried by $\sigma_{b,h}$).

¹In this thesis we adopt the convention to use capital subscripts for Z_H (Z_{DR}) if it is expressed in dBZ (dB)

Differential reflectivity

The fact that hydrometeors are often not spherical and that they fall with preferred orientation led, since the very early development of meteorological radar polarimetry (*Seliga and Bringi, 1976*), to realize that Z_H and Z_V could be simply combined to define a new variable. This idea is at the foundation of the differential reflectivity (Z_{DR} [dB]):

$$Z_{DR} = Z_H - Z_V. \tag{1.7}$$

Z_{DR} is positive (negative) for oblate (prolate) targets, respectively. Z_{DR} is a priori independent of particle concentration (number density) and for a population of hydrometeors of same dielectric properties it is largely influenced by the shape of the biggest particles, i.e. the ones which carry larger Z_H .

Copolar cross correlation coefficient

Z_H and Z_V for a pulsed radar are usually calculated as average values of several pulses (*Bringi and Chandrasekar, 2001*) transmitted over small time intervals. This is done in order to reduce the noise of the measurements and to collect more samples within each radar resolution volume (assuming that ergodicity is a reasonable assumption). However, the correlation coefficient between Z_H and Z_V calculated over all the individual pulses carries physical information as well and it defines the copolar cross correlation coefficient ρ_{hv} (e.g., *Bringi and Chandrasekar, 2001*). ρ_{hv} can be defined in microphysical terms as follows:

$$\rho_{hv} = \frac{\int_{D_{min}}^{D_{max}} s_{hh}^*(D)s_{vv}(D)N(D) dD}{\sqrt{Z_h * Z_v}} \tag{1.8}$$

where $Z_{h,v}$ is the horizontal (vertical) reflectivity expressed in linear units while $s_{hh,vv}$ [cm] is the complex backscattering amplitude of individual hydrometeors at horizontal (vertical) polarization (e.g. *Mishchenko et al., 1996*). For a more direct interpretation, it is worth noting that these quantities, $s_{hh,vv}$, are closely related to the backscattering cross sections ($\sigma_{b,h} = 4\pi|s_{hh}|^2$). ρ_{hv} is very sensitive to inhomogeneities within the radar resolution volumes, that cause pulse-to-pulse variations in Z_h - Z_v couples and therefore lower the correlation. The two most known (but not unique) applications of ρ_{hv} are the identification of the melting layer of precipitation (transition from snow to rain, e.g. *Matrosov et al., 2007*) and the discrimination of non-meteorological targets (e.g., *Rico-Ramirez and Cluckie, 2008*).

Specific differential phase shift upon propagation

The variables presented until now are based on the power that the hydrometeors encountered along the propagation path of a radar beam reflect back towards the location of the radar itself. The specific differential phase shift upon propagation (K_{dp}) is instead based on the phase of the waves transmitted and received by the radar. These waves are in fact slowed down along their propagation path by the interaction with the hydrometeors. The principle of K_{dp} is that non-spherical targets will slow down the waves polarized along their major dimension much more than the ones polarized along their minor dimension. K_{dp} is defined as

$$K_{dp} = \frac{180}{\pi} 10^3 \lambda \int_{D_{min}}^{D_{max}} \Re[f_{hh}(D) - f_{vv}(D)] N(D) dD \quad (1.9)$$

where λ [m] is the wavelength, $f_{hh(vv)}$ [m] are the forward complex scattering amplitudes, at horizontal (vertical) polarization, and \Re indicates the real part operator. K_{dp} takes the units of $^{\circ}\text{km}^{-1}$ and represents the rate at which the difference in phase (H-V) changes. It depends on the number of non-spherical hydrometeors in a radar resolution volume, their geometry and their dielectric properties. Unfortunately K_{dp} is not a direct observable of polarimetric radars (as Z_H for instance) but it needs to be estimated from the radar measurement of total differential phase shift Ψ_{dp} [$^{\circ}$]. This estimation step is of crucial importance to ensure that K_{dp} has significant microphysical meaning and the full Chapter 2 of this thesis is dedicated to this task.

1.3 Microphysics and microstructure of precipitation

The final intention of the present thesis is to link polarimetric radar measurements with microphysical processes occurring during precipitation. The terms “microphysics” and “microstructure” have already appeared several times until now. The present section is therefore devoted to clarify the definition of these two concepts.

1.3.1 Microstructure: the particle size distribution (PSD)

The term microstructure defines all the statistics that describe measurable quantities of a population of hydrometeors at a spatial scale at which precipitation is a discrete process (*Jameson and Kostinski, 1997*). The targets of those statistics are usually the velocities, sizes or shapes of the population of hydrometeors under investigation.

In the field of radar meteorology it is common practice to focus on the distribution of sizes by means of the concept of particle size distribution (PSD), and then to express the other quantities as a function of the size. In fact, many established relations exist to link fall velocities of raindrops (e.g., *Beard, 1976*), or other hydrometeors (e.g., *Heymsfield, 1972; Hanesch,*

Chapter 1. Introduction

1999; Yuter *et al.*, 2006) to the respective sizes. Shape-size relations are also well defined for rain (e.g., *Andsager et al.*, 1999; *Thurai and Bringi*, 2005), while for other hydrometeors the parametrization is more complex and usually a single relation cannot describe all the variability.

The PSD or DSD (drop size distribution, in case of rainfall), is a function $N(D)$ that represents the number of hydrometeors per unit size and volume (volumic DSD) and therefore takes the units of $[\text{mm}^{-1} \text{m}^{-3}]$. It is worth noting that actual ground measurements of PSD, collected with disdrometers (e.g. *Löffler-Mang and Joss*, 2000; *Kruger and Krajewski*, 2002) are usually based on reference surfaces, and not directly on volumes. The disdrometers characterize the PSD as the number of objects per unit size, crossing a unit area per unit time (areal PSD) $[\text{mm}^{-1} \text{m}^{-2} \text{s}^{-1}]$. The link between areal and volumic PSD is done through the hydrometeor fall velocities:

$$N_A(D) = v(D)N_V(D) \quad (1.10)$$

where $N_A(D)$ is the areal PSD, $N_V(D)$ is the volumic PSD and $v(D)$ is the terminal fall velocity of the particle $[\text{m s}^{-1}]$. In the previous section and in the following ones we always refer to volumic $N_V(D)$ as $N(D)$. D $[\text{mm}]$ is a generic reference dimension, as already discussed for Eq. 1.5.

The optimal mathematical expression of a PSDs and DSDs through parametric functions is still under debate in the scientific community. This aspect was discussed from the times of (*Joss and Gori*, 1978), until very recently, by (*Ignaccolo and De Michele*, 2014). The topic is evergreen also because it is strictly linked with the evaluation of the accuracy of disdrometric measurements, that is an open scientific question as well (e.g. *Battaglia et al.*, 2010; *Jaffrain and Berne*, 2011; *Raupach and Berne*, 2015). For rainfall, a gamma distribution in the form of:

$$N(D) = \alpha N_t^* D^\mu \exp -\Lambda D \quad (1.11)$$

has been widely employed since *Ulbrich* (1983). $N_t^* [\text{m}^{-3}]$ is a concentration, μ a shape and Λ a rate parameter respectively. α is a normalization factor that makes N_t the actual volumic number concentration and it is defined as:

$$\alpha = \frac{1}{\int_{D_{min}}^{D_{max}} D^\mu \exp(-\Lambda D) dD}$$

It is worth noting that this family of functions includes also exponential and power-law relations. Those have been used for example to parametrize the PSD of ice-phase hydrometeors (*Heymsfield*, 1977; *Platt*, 1997; *Ryan*, 2000) or of cloud droplets (*Whiteman and Melfi*, 1999). Ultimately, all the quantities defined in Sec.1.2.2 are linked to the PSD and therefore the knowledge of the PSD, or at least of some of its properties, is crucial for the field of radar meteorology.

1.3.2 Basic definitions of precipitation microphysics

The term “microphysics” indicates all the qualitative and quantitative aspects that describe precipitation, as well as all the dominant processes that contribute to generate and modify them. The concept of “microphysics” is closely related but slightly different from “microstructure” because the former does not rely only on statistical properties over a reference volume and it can include purely qualitative aspects too. For the purpose of this thesis the two microphysical aspects of interest are: (i) the hydrometeor content of precipitation, and (ii) the habits and processes characterizing ice-phase precipitation.

Hydrometeor type

A microphysical description of precipitation starts by the definition of “precipitation type”. In other words it starts by answering to the question: “what is precipitating?”. Many hydrometeor types exist and their classical definition involves a certain subjectivity as well as the choice of a level of classification complexity. A first and simplistic distinction can be made between liquid-phase (rainfall) and ice-phase (snowfall) precipitation. More complex and complete catalogues exist (i.e., the METAR format <http://meteocentre.com/doc/metar.html>) that classify precipitation into: rain, snow, snow pellets, snow grains, ice crystals, ice pellets, hail, graupel, drizzle, freezing rain, mixed phase precipitation and freezing fog.

The level of detail of the classification depends on the field of application, but the definition of hydrometeor types is more important than it would appear at a first glance. The presence of specific hydrometeors can represent a hazard, like hailstones (*Brooks et al.*, 2003), while other can be the indicators of specific environmental conditions. For instance, melting snowflakes (*Oraltay and Hallett*, 1989) indicates temperatures around 0°C, while dendritic ice crystals may indicate temperatures around -15°C and significant supersaturation with respect to ice (*Magono and Lee*, 1966).

The development of automatic techniques to classify hydrometeors from in-situ or remote sensing instruments is relatively recent. Remote sensing instruments, like polarimetric radars, have the potential to provide information on very large domains in nearly real-time and the introduction of radar polarimetry led to the fast development of hydrometeor classification schemes (*Straka et al.*, 2000; *Dolan and Rutledge*, 2009; *Thompson et al.*, 2014; *Bechini and Chandrasekar*, 2015). All these algorithms are based on the complementarity of the radar polarimetric variables and a significant part of the present thesis is as well devoted to the development of hydrometeor classification schemes (Chapter 3 and 4).

Ice-phase precipitation: notes on habits and processes

The study of ice-phase precipitation is complicated by the great variability of sizes, fall velocities, shapes, crystalline structures and densities of hydrometeors when compared with rainfall.

Chapter 1. Introduction

These peculiarities define the “habits” of ice crystals or of generic ice-phase hydrometeors²

The characteristics of a snowflake at the ground level depend on its “falling history”: for instance the temperature and humidity profiles, the wind field and the presence of supercooled liquid water (SLW) are aspects that drive the evolution of the ensemble of snowflakes/ice crystals forming snowfall. The simultaneous observation of all these aspects to get the full picture is challenging. It is usually not properly captured by single remote sensors (*Bechini et al.*, 2013, e.g.) and requires a combination of multiple instruments to be properly characterized (e.g., *Hogan et al.*, 2003; *Westbrook and Illingworth*, 2013).

Precipitation of ice-phase hydrometeors is in fact the result of the interactions between cloud ice crystals, supercooled liquid water (SLW) droplets and water vapour. After nucleation, the processes of aggregation, riming, and vapour deposition contribute to the growth of the crystals up to the point where their sizes and densities are large enough to let them fall towards the earth surface and further interact with the lower layers of the atmosphere (e.g., *Pruppacher and Klett*, 1997; *Straka et al.*, 2000; *Cantrell and Heymsfield*, 2005).

The shape, density, and growth rate of individual crystals depend largely on the temperature and relative humidity of formation (*Magono and Lee*, 1966; *Chen and Lamb*, 1994; *Fukuta and Takahashi*, 1999; *Takahashi*, 2014). Individual crystals can branch together (aggregation) and/or collect supercooled liquid water droplets that freeze upon impact on the surface of the crystals (riming). In contrast to aggregation, riming generates a net increase of the mass of precipitation because the rimed crystals or snowflakes have much larger fall velocities than individual water droplets in supercooled liquid water clouds that would otherwise not be able to reach the ground. Aggregation contributes indirectly to the mass transfer by generating larger and faster targets for riming (*Houze and Medina*, 2005).

1.4 Thesis outline

The objective of this thesis is to link polarimetric radar observations and precipitation microphysics. Two broad topics will be covered. At first the automatic classification of hydrometeors from polarimetric measurements and in-situ sensors will be tackled. In a second step the microphysics and vertical structure of ice-phase precipitation will be examined in the alpine environment, with a particular focus on rimed snowfall. In order to investigate these two aspects a prerequisite is necessary. All polarimetric observables should be collected at the highest available resolution, and therefore the estimation of high resolution specific differential phase shift will be part of this thesis as well.

The thesis is structured as follows: Chapter 2 is devoted to the estimation of the specific differential phase shift upon propagation (K_{dp}). This variable is not directly available from polarimetric radar measurements and its estimation involves some sort of data smoothing. It

²In this sense the habit is a subset of the concept of hydrometeor type

is shown that this leads to significant errors and biases when K_{dp} is employed at the spatial scale of the radar range gate. To mitigate this issue, a novel algorithm is proposed, based on Kalman filtering, that better follows the fine scale variations of K_{dp} and that is a-priori applicable in all meteorological conditions (i.e. it is not parametrized for rainfall only). An accurate K_{dp} estimate is the prerequisite for any further analysis or interpretation.

Chapter 3 presents a hydrometeor classification algorithm applied to two-dimensional video disdrometer (2DVD) data. It is shown that supervised classification (machine learning) can be an interesting tool to mimic human interpretation for automatic detection of hydrometeor types, when the data of the instrument allow to perform direct supervision. This operation cannot be performed on radar data and the 2DVD-based classification has the potential to provide time series of in-situ references for polarimetric radar measurements, in addition to its valuable point information. The 2DVD-based classification is performed over populations of hydrometeors (with a temporal resolution of 60 seconds), classified by means of multiple, mainly geometrical, particle descriptors.

Chapter 4 is devoted to hydrometeor classification from polarimetric weather radars. In this section a novel approach to hydrometeor classification is proposed, based on measured data rather than on scattering simulations. Hydrometeor classes obey the hypothesis of showing similarities in terms of polarimetric data as well as spatial consistency in the physical space. A simple method is built on these two assumptions and 7 hydrometeor categories that describe well the data collected by an X-band polarimetric radar in different locations of central Europe are identified. It will be shown that the hydrometeor classes identified in this way are similar to the ones obtained with a method based on scattering simulations, but they are better tailored on the specificities of the instrument used to collect the data.

Chapter 5 is devoted to snowfall microphysics, and in particular to the riming process. The data collected during a highly-instrumented field campaign in the central Alps of Switzerland are used to show that riming is an important process that largely affects the accumulation of snowfall. Additionally, the vertical structure of rimed precipitation events is described and interpreted. A special focus of this chapter will be on the description of the possible role that wind shear driven turbulence may have both in terms of snowfall microphysics and, more in general, on the enhancement of snow accumulation. Chapter 6, finally, summarizes the main contributions of this thesis and underlines possible future developments.

Note that the thesis is a compilation of published (or to be submitted) articles and therefore might contain small repetitions in particular in the introduction in each chapter. The author apologizes in advance for any inconvenience caused by this particular format.

2 Estimation of the specific differential phase shift upon propagation (K_{dp})

This chapter is adapted from two manuscripts:

- Schneebeli, M., J. Grazioli, and A. Berne (2014), Improved estimation of the specific differential phase shift using a compilation of kalman filter ensembles, *IEEE T. Geosci. Remote Sens.*, 52(8), 5137–5149, doi: 10.1109/TGRS.2013.2287017
- Grazioli, J., M. Schneebeli, and A. Berne (2014a), Accuracy of phase-based algorithms for the estimation of the specific differential phase shift using simulated polarimetric weather radar data, *IEEE Geosci. Remote Sens. Lett.*, 11(4), 763–767, doi: 10.1109/LGRS.2013.2278620

It presents a novel method for the retrieval of K_{dp} and an evaluation of the accuracy of K_{dp} estimates at the radar range gate scale.

2.1 Summary

A new algorithm for the accurate estimation of the specific differential phase shift on propagation (K_{dp}) from noisy total differential phase shift (Ψ_{dp}) measurements is presented. The new approach, which is based on the compilation of ensembles of Kalman Filter estimates, does not rely on additional data like the reflectivity or the differential reflectivity in order to constrain the solution and it is based on Ψ_{dp} only. The dependence of the solution on Ψ_{dp} only allows one to apply the algorithm in various environmental conditions without reducing its performance. Drawbacks that are usually inherent in algorithms of this kind (like the loss of the small-scale structure and the smoothing of high peak values) are partially overcome by a two-step algorithm design, which first determines an ensemble of possible solutions and then selects and averages the ensemble members such that the estimated K_{dp} profile has a better agreement with the truth. The algorithm is thoroughly evaluated and compared with commonly used algorithms, chosen among the ones which use as main input the measured and noisy total differential phase shift Ψ_{dp} . The comparison is conducted by means of simulated two dimensional fields of drop size distribution, over 6 simulated rain event. The new algorithm outperforms the classical ones in terms of Efficiency, Correlation and RMSE. The mean normalized absolute error in the estimation of K_{dp} at the radar resolution volume scale ranges however from 27% to 30% for all the algorithms evaluated, and significant negative biases up to -50% emerge at the highest values of K_{dp} for the most biased algorithms. The novel algorithm is also experimentally evaluated by applying it on X-band radar data that were acquired in northern Brazil during the CHUVA campaign and at a high alpine site in Switzerland during snowfall. Results show the spatial fine structure and the high values of precipitation are better represented with the new method.

2.2 Introduction

The specific differential phase shift on propagation (K_{dp}) is defined as the spatial derivative of the phase difference between the horizontal (H) and vertical (V) polarization state of a propagating radar signal that is induced by forward scattering. Thanks to the high correlation between K_{dp} and the rain rate R at all weather radar frequencies (*Sachidananda and Zrnica*, 1986, 1987; *Matrosov et al.*, 1999, 2002) and to the fact that K_{dp} is less affected by partial beam blockage, radar miscalibration, attenuation along the propagation path and hail (*Illingworth*, 2004), it has been proposed to use K_{dp} instead of the radar reflectivity Z for inferring rain rates from dual-polarization radar measurements (*Ryzhkov and Zrnica*, 1996; *Zrnica and Ryzhkov*, 1996). In addition, K_{dp} is not only useful for rain measurements, it also serves as input for hydrometeor classification schemes and has been proven to be useful for the detection of graupel particles (*Dolan and Rutledge*, 2009; *Schneebeli et al.*, 2013) and dendritic snow crystals (*Bechini et al.*, 2011; *Kennedy and Rutledge*, 2011; *Schneebeli et al.*, 2013).

Despite these advantages, there are issues associated with the use of K_{dp} , the most notable being its derivation from noisy total differential phase (Ψ_{dp}) measurements. The noise that is inherent in the phase measurements requires some sort of smoothing of the input Ψ_{dp} range vector such that its spatial derivative can be calculated. Smoothing of Ψ_{dp} however directly leads to smoothed K_{dp} values that neither follow small-scale fluctuations nor high peak values, hence the exact spatial structure of precipitation is not well captured. At higher frequencies (e.g., C- and mostly X-band), the differential phase shift on backscatter (δ_{hv}), i.e., the phase shift that is induced upon the backscattering process), is an additional source of error in the calculation of K_{dp} : Φ_{dp} and δ_{hv} add up to Ψ_{dp} but it is not straightforward to separate the two contributions. Therefore, accurate K_{dp} estimates can only be obtained if (1) δ_{hv} is constant along the range gate interval that defines the spatial resolution of K_{dp} (and is used for the numerical calculation of the spatial derivative) or (2) δ_{hv} can be estimated separately.

Numerous algorithms have been proposed in the last two decades that aimed at tackling some or all of these problems. These algorithms need to be separated into two groups: the first group containing algorithms whose K_{dp} estimates are purely based on Ψ_{dp} measurements (*Hubbert et al.*, 1993; *Hubbert and Bringi*, 1995; *Wang and Chandrasekar*, 2009; *Vulpiani et al.*, 2012) and the second group using auxiliary data like the reflectivity Z and(or) the differential reflectivity Z_{DR} together with consistency relations between polarimetric observables in order to obtain an improved fine-scale structure of K_{dp} or a more accurate estimate of δ_{hv} (*Otto and Russchenberg*, 2011; *Schneebeli and Berne*, 2012). As shown in *Schneebeli and Berne* (2012) and *Schneebeli et al.* (2012), K_{dp} can be estimated very accurately with an algorithm from the second group, but only in rain conditions and if the radar is well calibrated. As soon as the consistency relations between the polarimetric variables are violated (by beam blockage, partial beam filling, non-liquid precipitation or radar miscalibration) the applicability of such algorithms is usually hampered. The group of algorithms that only uses the range profile of Ψ_{dp} as input variable is more generally applicable but the accuracy of the K_{dp} estimates

might be low, especially at the single range gate scale (i.e., pixel scale). For many quantitative precipitation estimation (QPE) applications, the pixel scale might not be very relevant, since rain intensities that are inferred from radar measurements are usually integrated over time, which evens out the errors in the representation of the small-scale precipitation structures. Due to this, very good agreements between rain accumulations determined with K_{dp} based rain intensity estimators and ground based in-situ sensors could be achieved (*Matrosov, 2010; Wang and Chandrasekar, 2010*). For certain disaster prevention applications like urban hydrology, flash-flood and landslide forecasting, the rain rate must however be known at a high spatial and temporal resolution. Therefore it is important to carefully choose the rain rate estimator and keep in mind that high intensity rain rates are poorly captured with usual K_{dp} estimates. Moreover, polarimetric radars are also used as a tool for microphysical research and hydrometeor identification (HID) became a popular tool for such applications (*Straka et al., 2000; Vivekanandan et al., 1999; Schneebeli et al., 2013*). Most of the commonly used HID schemes are using K_{dp} as an input variable and try to classify every individual radar range gate into a certain hydrometeor category. This might also lead to inconsistencies because of the already mentioned representativeness error of usual K_{dp} estimates at the pixel scale. Other radar inversions, like DSD retrieval techniques, employ as well K_{dp} at the range gate scale (*Zhang et al., 2001; Gorgucci et al., 2009*).

In this Chapter, a novel algorithm for the accurate determination of K_{dp} from Ψ_{dp} measurements is presented, which does not employ any additional measurements to constrain the solution. In contrast to traditional K_{dp} estimators, simple smoothing of the noisy Ψ_{dp} is replaced by a more sophisticated Kalman Filter (KF), which is operated in the forward and backward directions of the range profile. KF allows to include easily in the estimation process the geometry of the problem under investigation, as well as the available parametrization. In addition, an ensemble of K_{dp} estimates is obtained by a variable weighting of the covariance matrix that represents the spatial precipitation structure. With this approach, the final K_{dp} product is compiled from a selection and combination of an ensemble of initial K_{dp} estimates. The algorithm will be referred to as Kalman Filter Ensemble (KFE). In order to avoid misunderstandings, it is important to underline that the proposed algorithm is different from Ensemble Kalman Filtering (EnKF, e.g., *Evensen, 1994*) and Extended Kalman Filtering (EKF, e.g., *Gelb, 1988*).

In the end of this Chapter it will be presented also an evaluation of the quality of K_{dp} estimates using simulated DSD fields, that allow a quantitative assessment at the scale of the radar range gate. The quality of K_{dp} is assessed by analysing the performance of two different commonly employed algorithms¹, and KFE. The performance of the proposed algorithm is compared also on real data of rainfall and snowfall to the algorithm proposed by *Hubbert and Bringi (1995)* (which is based on the work done in *Hubbert et al. (1993)*) and modified to adaptive interpolation gate lengths as it is described in the first part of *Wang and Chandrasekar (2009)*.

The Chapter is organized as follows: Section 2.3 shortly describes the radar and simulated data

¹Algorithms that, like KFE, base their estimation on the measured differential phase shift Ψ_{dp} .

set used in this study. The algorithm is detailed in Section 2.4. Evaluations of the performance of the proposed algorithm and of other common approaches are presented in Section 2.5 and the conclusions are provided in Section 2.6.

2.3 Data sets

2.3.1 X-band polarimetric radar data from Brazil

In April 2011, a mobile X-band polarimetric radar was deployed outside of the city of Fortaleza, northern Brazil. The radar was installed on a five-meter high tower, but elevations below 2° were nevertheless almost completely blocked. The field campaign was part of the CHUVA project (<http://chuvaproject.cptec.inpe.br/portal/noticia.ultimas.logic>) that contributes to the ground validation efforts for the Global Precipitation Measurement (GPM) satellite mission. Around 13 intense convective precipitation events were recorded during the one-month period. The radar reflectivities were corrected for rain and radome attenuation by using a self-consistency scheme (*Schneebeli and Berne, 2012*). Details on the radar measurements, the applied data correction algorithms as well as on the meteorological conditions can be found in *Schneebeli et al. (2012)*. One event that took place on April 13, 2011 will be discussed in this Chapter. It was characterized by a melting layer height of around 4.5 km above sea level and peak rain rate intensities that exceeded 100 mm h^{-1} , as indicated by the rain gauges and Parsivel disdrometers that were deployed at a distance of about 20 km from the radar.

2.3.2 X-band polarimetric radar data from Switzerland

Radar data collected during snowfall are taken from an X-band polarimetric radar that was deployed in Davos, Switzerland, from September 2009 to July 2011. The radar was installed on the slope of a ski resort at an altitude of 2133 m above sea level and overlooked the Landwasser valley. Due to the surrounding mountains that exceed heights of 3000 m, the first clutter free elevation was found at 9° . Details on the campaign and on the radar can be found in *Schneebeli et al. (2013)*; *Scipion et al. (2013)*. The K_{dp} algorithms are applied on data that were collected on March 26, 2010. This particular day was characterized by an incoming cold front that led to high snowfall intensities (around 40 cm of snow accumulation in 3 hours). Ψ_{dp} measurements in the first 4 km were corrupted by phase jitter (*Hubbert et al., 1993*) and are therefore excluded from the analysis. The radar was far above the freezing level, and the attenuation is assumed to be negligible in dry snow (*Matrosov, 1992*; *Doviak and Zrnić, 2006*).

2.3.3 Simulated rainfall fields

Simulated measurements have been used in order to test and evaluate (quantitatively) the proposed retrieval algorithm and other methods. In fact, it is not possible for this purpose to employ observations physically collected by a weather radar because the intrinsic value

Chapter 2. Estimation of the specific differential phase shift upon propagation (K_{dp})

of K_{dp} would not be available. This kind of comparisons are based on a set of simulated two-dimensional rain fields, described in this Section.

Two dimensional DSD fields

The simulation of liquid precipitation events is conducted with the procedure extensively described in *Schleiss et al.* (2012). This method allows to generate rain events with a temporal resolution of 5 min and a spatial resolution of 0.1 km, on a squared domain of 40×40 km². At each grid point and timestep, the parameters of a Gamma DSD are provided:

$$N(D) = \alpha N_t D^\mu \exp(-\Lambda D) \quad (2.1)$$

where N_t [m⁻³], Λ [mm⁻¹] and μ [-] are the concentration, rate and shape parameters, and D [mm] is the equivolumetric diameter of a particle. α is a normalization factor such that the integration of the DSD on the range of diameters [D_{min} , D_{max}] leads to the total drop concentration N_t .

Parameters corresponding to the climatology of Switzerland (supposed to be representative of temperate mid-latitude rain) obtained from radar and disdrometer data, are used to generate DSD fields that have the same statistical and structural properties of actually occurred events. Ground observations of DSD spectra together with the spatial structure of the storms, including the intermittency of the rainfall fields, are taken into account with a geostatistical approach. From the simulated DSD fields, the polarimetric radar variables can be computed. In the present work, six different simulated events are employed, each of them described by 10 subsequent timesteps (at 5 min resolution). The events are different in terms of type, intensity and intermittency. Intermittency is defined as the percentage of the pixels over the domain that are associated with zero rainfall rate. A summary of the basic characteristics of the events in terms of rainfall intensity is provided in Appendix A.3.

Simulation of phase-related radar observables

A set of realistic profiles of phase-related radar observables are obtained from the 2-D DSD fields available. Radar profiles are extracted both in the South to North and East to West directions in each DSD field. Profiles with less than 50 gates corresponding to actual rain are discarded from the following analysis and a total of 15670 profiles are kept. Radar frequencies of S (2.8 GHz), C (5.6 GHz) and X (9.4 GHz) bands have been considered, as well as a radar range resolution of 0.1 km, an antenna half power beam width of 1.5° and a Gaussian noise in the measured differential phase. The knowledge of the DSD at each grid point allows to compute polarimetric radar variables. In the present study, the ones of major interest are K_{dp}

$[\text{° km}^{-1}]$ and δ_{hv} $[\text{°}]$ (Otto and Russchenberg, 2011):

$$K_{dp} = \frac{180}{\pi} 10^3 \lambda \int_{D_{min}}^{D_{max}} \Re[f_{hh}(D) - f_{vv}(D)] N(D) dD \quad (2.2)$$

$$\delta_{hv} = \text{arg} \left[\int_{D_{min}}^{D_{max}} s_{hh}^*(D) s_{vv}(D) N(D) dD \right] \quad (2.3)$$

where λ [m] is the wavelength, $f_{hh,vv}$, $s_{hh,vv}$ [m] are the forward and backward complex scattering amplitudes, at horizontal and vertical polarization, respectively and \Re indicates the real part operator. These last quantities are obtained with the T-matrix scattering simulation code by Mishchenko *et al.* (2002) with the following parameters. The temperature was assumed to be 15 °C, and the refractive index of water has been calculated according to Liebe *et al.* (1991). The raindrop axis ratio is considered to be 1 for $D \leq 0.7$ mm; for $0.7 \text{ mm} < D \leq 1.5$ mm is given by interpolation of tabulated values of Beard and Kubesh (1991); while for $D > 1.5$ mm Thurai and Bringi (2005) is used. The canting angle of falling particle is randomly chosen from a normal distribution of values with mean of 0° and standard deviation of 10° (Park *et al.*, 2005). The axis ratio and the canting angle models together constitute the set of relations linking the size of drops with their geometry, and are necessary to calculate the scattering amplitudes. The equivolumetric diameter D is discretized from D_{min} of 0.1 mm to D_{max} of 6 mm (consistent with DSD observations of Jaffrain and Berne (2011)) with a step ΔD of 0.01 mm. The half-power beamwidth of 1.5° is taken into account by means of a Gaussian weighting function (Doviak and Zrnić, 1993) on the DSDs, such that the weighted DSD is used in the scattering simulation when more than one grid point is present in the resolution volume. Profiles of Φ_{dp} $[\text{°}]$ and Ψ_{dp} $[\text{°}]$ are obtained as:

$$\Phi_{dp}(k) = 2 \sum_{i=1}^k K_{dp}(i) \Delta r \quad (2.4)$$

$$\Psi_{dp}(k) = \Phi_{dp}(k) + \delta(k) + \epsilon \quad (2.5)$$

where k is the k -th range gate, Δr [km] is the range resolution and ϵ $[\text{°}]$ is a white noise. The standard deviation of ϵ is varied from 0° to 3° (e.g. Schneebeli and Berne, 2012).

2.4 Algorithm description

2.4.1 K_{dp} estimation

The estimation of K_{dp} deals with the retrieval of the local (half) slope of Φ_{dp} at each radar range gate, when the actual available information is Ψ_{dp} . In the following it is described

how the problem is tackled with a Kalman Filtering approach when $\delta_{hv} = 0$ and in the more realistic case of $\delta_{hv} \neq 0$.

2.4.2 Kalman Filtering

Let us start from the standard discrete KF formulation *Kalman* (1960) which is based on the following two basic linear equations:

$$\mathbf{z}(i) = F_i \mathbf{s}(i) + \epsilon_{\mathbf{z}(i)} \quad (2.6)$$

$$\mathbf{s}(i+1) = T_i \mathbf{s}(i) + \epsilon_{\mathbf{s}(i)} \quad (2.7)$$

Eq.(2.6) describes how a set of measurements $\mathbf{z}(i)$ that are taken at the location i can be estimated from the state $\mathbf{s}(i)$. The matrix F_i is called the observation model and establishes a linear relation between the state and the measurements. Observation model errors and measurement noise contribute thereby to the error $\epsilon_{\mathbf{z}(i)}$. Eq.(2.7) describes the forward propagation of a state at location i to the neighboring location $i+1$ by employing the transition matrix T_i . Errors that are due to uncertainties in the forward projection are contained in $\epsilon_{\mathbf{s}(i)}$. The above equations allow to introduce a priori information into the filtering process. Such information is provided by establishing relations between measurements and the state estimate as well as with the underlying model that describes the transition from one state to the next. The error terms $\epsilon_{\mathbf{z}}$ and $\epsilon_{\mathbf{s}}$ are assumed to be normally distributed, with zero mean and they are fully defined by the respective error covariance matrices ($C(\epsilon_{\mathbf{z}})$ and $C(\epsilon_{\mathbf{s}})$). It will be shown in Section 2.4.4 that $\epsilon_{\mathbf{z}}$ is modeled as white noise, therefore leading to a diagonal covariance matrix $C(\epsilon_{\mathbf{z}})$.

A formulation for $\mathbf{z}(i)$ and $\mathbf{s}(i+1)$ has now to be found that allows us to use the KF technique to filter the measured Ψ_{dp} profile in order to obtain a smoothed Φ_{dp} profile (which ideally does not contain any δ_{hv} contribution anymore). By simplifying the technique described in Schneebeli and Berne (*Schneebeli and Berne, 2012*) who proposed a method for filtering Ψ_{dp} by means of KF that not only included Ψ_{dp} as input variable but also the reflectivities $Z_{H,V}$ as well as additional constants, the following definitions are obtained:

$$\mathbf{z}(i) = \begin{pmatrix} \Psi_{dp}(i) \\ \tilde{\Psi}_{dp}(i) \end{pmatrix} \quad (2.8)$$

$$\mathbf{s}(i) = \begin{pmatrix} K_{dp}(i) \\ \Phi_{dp}(i) \\ \tilde{\Phi}_{dp}(i) \end{pmatrix} \quad (2.9)$$

The radar range gates along the propagation path are denoted with the location index i and the notation $\tilde{X}(i) = X(i+1)$ (where X stands for Φ_{dp} or Ψ_{dp}) is used to indicate that \tilde{X} belongs

to the KF estimation process at location i . This might give the impression of an unnecessary complication, but it helps avoid ambiguities in the formulation of the algorithm. Recalling the

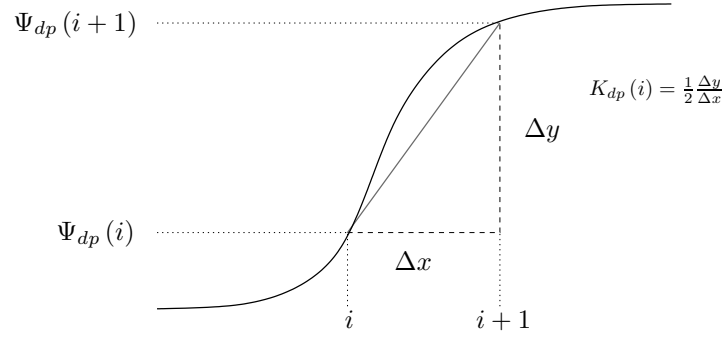


Figure 2.1: Schematic of the K_{dp} estimation process. The solid black line indicates Ψ_{dp} and the slope of the grey line is proportional to K_{dp} at the i -th range gate.

original definitions embedded in Eqs. (2.5, 2.4), the observation $\mathbf{z}(i)$ can be expressed as:

$$\Psi_{dp}(i) = \tilde{\Phi}_{dp}(i) - 2\Delta r K_{dp}(i) \quad (2.10)$$

$$\tilde{\Psi}_{dp}(i) = \Phi_{dp}(i) + 2\Delta r K_{dp}(i) \quad (2.11)$$

The factor 2 comes from the fact that Ψ_{dp} is the 2-way total differential phase shift. With the definition of the state and measurement vector in Eqs.(2.8, 2.9) and the relations of Eqs. (2.10, 2.11) it is readily shown that an observation model matrix is defined as:

$$\mathbf{F} = \begin{pmatrix} -2\Delta r & 0 & 1 \\ 2\Delta r & 1 & 0 \end{pmatrix} \quad (2.12)$$

where the index i was dropped since this matrix is not subject to any changes along the range path.

The above equations are only true under the assumption that (1) $\delta_{nv} = 0$ and (2) $K_{dp}(i) = K_{dp}(i+1)$. Especially assumption (1) is rather strong and does not hold in reality. This issue will however be treated separately in the further development. Assumption (2) obviously also introduces an error, since it is unlikely that the K_{dp} values at two neighboring range gates are exactly equal. On the other hand, one can expect a certain similarity between neighboring K_{dp} values. The information about the error that is inherent in assumption (2) is going to be contained in the covariance matrix which is associated with the state transition from one gate i to the next $i+1$. The calculation of this covariance matrix is detailed in the upcoming section 2.4.4.

With the definition of the state vector in Eq.(2.9) and Eq.(2.7) a model for the propagation of

the state from range gate i to range gate $i + 1$ can be formulated like

$$\mathbb{T} = \begin{pmatrix} 1 & 0 & 0 \\ 0 & 0 & 1 \\ 2\Delta r & 0 & 1 \end{pmatrix} \quad (2.13)$$

where again the index i was dropped and also Eq.(2.13) implies the assumption that $K_{dp}(i) = K_{dp}(i + 1)$.

In the following, the complete formulation of the KF is presented. It must be kept in mind that a thorough introduction to KF theory is beyond the scope of this Chapter, and the reader is referred to classical text books (e.g., *Gelb* (1988)). The estimation procedure for a KF is the following: A given filtered (a posteriori) state, denoted with the superscript (+), which exists at a certain location $i - 1$ (written as $\mathbf{s}^{(+)}(i - 1)$) is propagated forward in space, which leads to an a priori estimate, denoted with the superscript (-), at the location i (written as $\mathbf{s}^{(-)}(i)$). The a priori estimate is then combined with the measurements made at location i , leading to an a posteriori state $\mathbf{s}^{(+)}(i)$, which is the final filtered state at location i . From there, the a posteriori state is propagated further in space and the described procedure is repeated.

Classical KF theory allows now the calculation of a filtered a posteriori state $\mathbf{s}^{(+)}$ from the a priori state $\mathbf{s}^{(-)}$ like

$$\mathbf{s}^{(+)}(i) = \mathbf{s}^{(-)}(i) + K_i [\mathbf{z}(i) - F\mathbf{s}^{(-)}(i)] \quad (2.14)$$

The a priori state $\mathbf{s}^{(-)}(i)$ in the above equation needs to be calculated with Eq.(2.7) from the a posteriori state $\mathbf{s}^{(+)}(i - 1)$. For every a posteriori state, an associated error covariance matrix is calculated with

$$P_{\mathbf{s}_i}^{(+)} = (I - K_i F) P_{\mathbf{s}_i}^{(-)} \quad (2.15)$$

where I denotes the identity matrix and $P_{\mathbf{s}_i}^{(-)}$ is the error covariance matrix associated with the a priori state and calculated as

$$P_{\mathbf{s}_i}^{(-)} = \mathbb{T} P_{\mathbf{s}_{i-1}}^{(+)} \mathbb{T}^T + C(\epsilon_{\mathbf{s}(i)}) \quad (2.16)$$

where T denotes the matrix transpose. In Eqs.(2.14,2.15), K_i denotes the so-called Kalman gain, which is defined as *Gelb* (1988)

$$K_i = P_{\mathbf{s}_i}^{(-)} F^T [F P_{\mathbf{s}_i}^{(-)} F^T + C(\epsilon_{\mathbf{z}(i)})]^{-1} \quad (2.17)$$

In Eqs.(2.16,2.17), $C(\epsilon_{\mathbf{s}(i)})$ and $C(\epsilon_{\mathbf{z}(i)})$ denote the covariance matrices that are associated with the errors $\epsilon_{\mathbf{s}(i)}$ that arise from the state transition and from errors $\epsilon_{\mathbf{z}(i)}$ that stem from a combination of measurement noise and observation model inaccuracies, respectively.

2.4.3 Treatment of the δ_{hv} effect

As mentioned in the introduction, δ_{hv} that varies from one gate to the next can introduce errors in the estimation of K_{dp} . In classical K_{dp} estimation methods, it is assumed that K_{dp} cannot be negative and that therefore Φ_{dp} cannot decrease along the range profile. With the technique described in *Hubbert and Bringi (1995)* it is then possible to remove δ_{hv} from the Ψ_{dp} profile. In our approach δ_{hv} is considered as a function of K_{dp} , according to T-matrix calculations that are shown in Figure 2.2 for a frequency of 9.41 GHz.

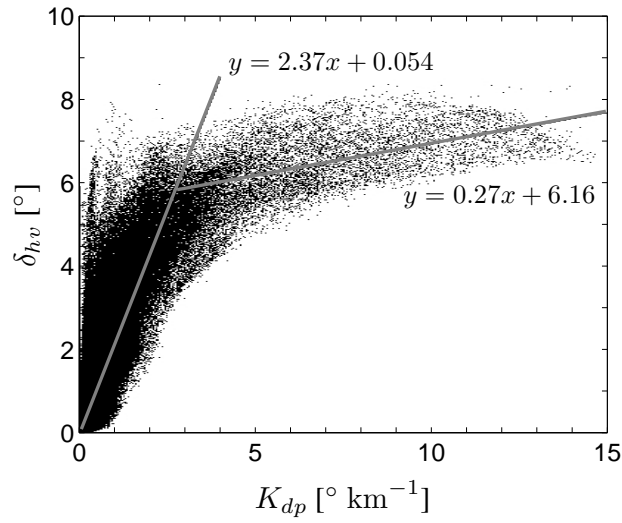


Figure 2.2: Relation between K_{dp} and δ_{hv} for a frequency of 9.41 GHz based on T-matrix calculations of simulated drop size distributions. The grey lines indicate segmental linear fits.

The scatter plot can be approximated with the indicated two linear fits that have the following equations:

$$\delta_{hv}^{\text{fit}} = \begin{cases} 2.37K_{dp} + 0.054 & ; K_{dp} \leq 2.5^\circ \text{ km}^{-1} \\ 0.27K_{dp} + 6.16 & ; K_{dp} > 2.5^\circ \text{ km}^{-1} \end{cases} \quad (2.18)$$

In order to remove δ_{hv} contamination from the estimated K_{dp} values, a separate δ_{hv} state variable needs to be introduced such that the state vector formerly given in Eq.(2.9) now reads

$$\mathbf{s}(i) = \begin{pmatrix} K_{dp}(i) \\ \delta_{hv}(i) \\ \Phi_{dp}(i) \\ \tilde{\Phi}_{dp}(i) \end{pmatrix} \quad (2.19)$$

The system of equations that were given in Eqs.(2.10,2.11) is then extended to three equations

Chapter 2. Estimation of the specific differential phase shift upon propagation (K_{dp})

that contain δ_{hv} as well as the relation given in Eq.(2.18) such that

$$\Psi_{dp}(i) = \tilde{\Phi}_{dp}(i) - 2\Delta r K_{dp}(i) + \delta_{hv}(i) \quad (2.20)$$

$$\tilde{\Psi}_{dp}(i) = \Phi_{dp}(i) + 2\Delta r K_{dp}(i) + \delta_{hv}(i) \quad (2.21)$$

$$c = \delta_{hv}(i) - b K_{dp}(i) \quad (2.22)$$

The parameters b of Eq.(2.22) is thereby chosen according to the linear fits given in Eq.(2.18), while c plays the role of an additional and artificial measurement describing the residual between δ_{hv} and $b K_{dp}$. Since the value $K_{dp}(i)$ is not known a priori, b and c must be based on the $K_{dp}^{(-)}(i)$ estimate.

If the left side of the above system is considered as the measurements, a new measurement vector can be defined as

$$\mathbf{z}(i) = \begin{pmatrix} \Psi_{dp}(i) \\ \tilde{\Psi}_{dp}(i) \\ c \end{pmatrix} \quad (2.23)$$

In order to properly relate the newly defined vectors \mathbf{z} and \mathbf{s} with each other, also the matrix F needs to be adapted like

$$F = \begin{pmatrix} -2\Delta r & 1 & 0 & 1 \\ 2\Delta r & 1 & 1 & 0 \\ -b & 1 & 0 & 0 \end{pmatrix} \quad (2.24)$$

The matrix T also is extended to take into account the new state vector. The forward projection of $\delta_{hv}(i)$ to the next range gate $i + 1$ is modeled as:

$$\delta_{hv}^{(-)}(i+1) = \delta_{hv}^{(+)}(i) \quad (2.25)$$

which leads to the following state transition matrix:

$$T = \begin{pmatrix} 1 & 0 & 0 & 0 \\ 0 & 1 & 0 & 0 \\ 0 & 0 & 0 & 1 \\ 2\Delta r & 0 & 0 & 1 \end{pmatrix} \quad (2.26)$$

Although the $K_{dp} - \delta_{hv}$ relation was calculated for rain only, the algorithm can also be applied for snow conditions, as it will be shown in Section 2.6. The $K_{dp} - \delta_{hv}$ relation exhibits in fact a lot of scatter, hence the constraint that is induced by this relation is weak. The scatter stems from the large ensemble of different rainfall types that were included in the modeling approach. Thanks to this, the given $K_{dp} - \delta_{hv}$ relation is only frequency dependent and otherwise generally applicable. $K_{dp} - \delta_{hv}$ relations for commonly used S- and C-band radar

frequencies are given in Appendix A.1. If a more suitable $K_{dp} - \delta_{hv}$ relation becomes available for snowfall, it can easily be implemented.

2.4.4 Covariance matrices and ensemble estimation

The determination of the error covariance matrices is the key difficulty in any Bayesian optimization scheme. The fact that a large ensemble of simulated DSD profiles (that can be used as a representation of the true state \mathbf{s}^t) is available makes possible the relatively straightforward calculation of $C(\epsilon_{\mathbf{s}(i)})$ and $C(\epsilon_{\mathbf{z}(i)})$. These resulting covariance matrices are going to be calculated for simulated data. The data set has been parametrized according to measured DSD spectra and storm structures, and hereafter it is assumed that the simulation represents collected observations with sufficient accuracy.

The error $\epsilon_{\mathbf{s}(i)}$ can be written as the difference between the true state at range gate i and the state that was projected from to range gate $i - 1$ to i :

$$\epsilon_{\mathbf{s}(i)} = \mathbf{s}^t(i) - \mathbf{T}\mathbf{s}^t(i - 1) \quad (2.27)$$

The DSD fields and subsequent T-matrix simulations with the Fortran implementation of *Mishchenko and Travis* (1998) enables the calculation of the true states $\mathbf{s}^t(i - 1)$ and $\mathbf{s}^t(i)$. The covariance matrix $C(\epsilon_{\mathbf{s}(i)})$ is then readily inferred from a large ensemble of the difference vectors given in Eq.(2.27).

Similarly, the error $\epsilon_{\mathbf{z}(i)}$ can be regarded as the difference between the actual (noisy) measurement \mathbf{z}^n (the superscript n indicating the inherent noise of the measurement) and the measurement prediction from the associated state, i.e.,

$$\epsilon_{\mathbf{z}(i)} = \mathbf{z}^n(i) - \mathbf{F}\mathbf{s}^t(i) \quad (2.28)$$

and $C(\epsilon_{\mathbf{z}(i)})$ is again calculated from a large ensemble of these differences. Since real measurements are not available at this stage, \mathbf{z}^n needs to be obtained by first calculating $\Psi_{dp}(i)$ and $\Psi_{dp}(i + 1)$ from the T-matrix simulated K_{dp} and δ_{hv} profile according to Eq. 2.5.

The matrix $C(\epsilon_{\mathbf{s}(i)})$ controls how much the state can vary from one range gate to the next. The larger the elements of this matrix are, the more variance is allowed, hence the less noise in Ψ_{dp} is suppressed. On the contrary, a state estimate with low gate-to-gate fluctuations is obtained when $C(\epsilon_{\mathbf{s}(i)})$ is small. A large ensemble of measurements is supposed to include the whole variety of state variations, hence the resulting matrix $C(\epsilon_{\mathbf{s}(i)})$ is representative for the whole ensemble of profiles, but it over- or underestimates the gate-to-gate variation for individual profile sections. In order to obtain an ensemble of filtered state estimates that allow different gate variability, the covariance matrix $C(\epsilon_{\mathbf{s}(i)})$ is scaled with a set of factors $a = 10^b$ with $b = -1, -0.8, -0.6, \dots, 0.8, 1$. The range of values a was chosen like this since it was found that a division or multiplication of $C(\epsilon_{\mathbf{s}(i)})$ with a value higher than 10 does not

change the KF results any further compared to what is obtained with a value of 10.

Although the covariance matrices were calculated based on simulated DSDs whose statistical properties correspond to the storm structures that are found in Switzerland, it was shown in *Schneebeli et al.* (2012) that such covariance matrices can also be applied to data that was acquired in very different meteorological conditions (like severe convective situations in northern Brazil). This is not a proof for the general applicability to any data set, but it shows that the training data set contains enough variability to cover a broad range of storm situations. As an additional test of the sensitivity of the final K_{dp} estimate to the covariance matrix the diagonal matrix elements have been scaled by a factor of 2 and the off diagonal elements by +50% and by -50%. Although these alterations obviously lead to a slightly worse final K_{dp} product, the overall performance remains very similar to the one obtained with the originally estimated covariance matrices.

2.4.5 Estimation in the backward direction

The state transition covariance matrix introduces a certain inertia in the estimation due to the assumption that the a priori state of $K_{dp}(i + 1)$ is equal to the a posteriori state of $K_{dp}(i)$. This inertness leads to a shifting of the K_{dp} peak values towards the propagation direction of the estimation. In order to get rid of this effect, the same estimation process that was described in the previous section can also be executed in the backward direction, i.e., from the end of the range gate profile towards low Ψ_{dp} values close to the radar. This estimation in the backward direction will shift the K_{dp} maxima in the opposite direction and hence compensates the shift that was introduced with the estimation in the forward direction. To do so, the measured Ψ_{dp} profile only needs to be inverted according to

$$\Psi_{dp}^{inv}(i) = \Psi_{dp}^{end} - \Psi_{dp}(\text{nrg} + 1 - i) \quad (2.29)$$

where Ψ_{dp}^{end} denotes the last valuable differential phase measurement along the profile and nrg denotes the number of range gates, hence $i = \text{nrg}$ is the index of the last element at the end of the range gate profile. The same KF that was developed for the forward direction can be applied to Ψ_{dp}^{inv} , and the resulting K_{dp}^{inv} is easily back-transformed:

$$K_{dp}(i) = K_{dp}^{inv}(\text{nrg} + 1 - i) \quad (2.30)$$

The effect of the forward and backward estimation as well as the effect of the different scaling factors on K_{dp} is illustrated in Figure 2.3. It can be seen that the forward and backward estimation smears out the peaks in opposite directions, whereas the different scaling of the covariance matrices leads to an ensemble of estimates whose members represent the true K_{dp} differently.

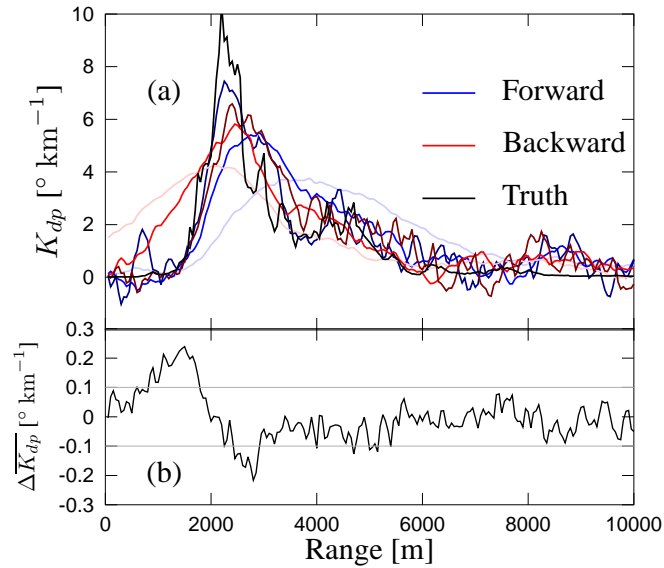


Figure 2.3: (a) Simulated K_{dp} measurements (black line) together with an ensemble of KF estimates that were obtained for a set of example covariance scaling factors with values of 0.1, 1, and 10 estimated in the forward (from light blue to dark blue for increasing scaling) and backward (from light red to dark red) direction. (b) The spatial derivative of the K_{dp} ensemble mean (i.e., the mean over all the ensemble members of the backward and forward estimation process). This quantity is used to decide which KF estimation direction should be used for the final K_{dp} product.

2.4.6 Practical implementation issues

With the state and measurement vectors as well as the state transition and observation model matrices that were defined in the previous sections, K_{dp} and Φ_{dp} can be estimated from a profile of noise-affected Ψ_{dp} measurements. There are however a couple of practical issues that need to be taken into account for the successful implementation of this filter for general radar profiles.

Initialization of the algorithm

At the beginning of each profile, there are no available data to initialize the algorithm, since no KF state estimate with its corresponding error covariance matrix has yet been calculated. Due to the propagation of one state to the next there must be an estimate of a state vector available already at the beginning (for the forward direction) or at the end (for the backward direction) of the range gate profile. An incorrect estimate of the first state might lead to a long conditioning phase where the a posteriori state vector estimates exhibit large deviations from

the truth and just slowly approach a correct range of values. In order to overcome this effect, satisfactory results were obtained by artificially enhancing the measured Ψ_{dp} profile with around 20 (or more) $\Psi_{dp} = 0^\circ + \eta$ values at the beginning of the profile and the same number of $\Psi_{dp} = \Psi_{dp}^{\text{end}} + \epsilon$ values, where ϵ denotes a Gaussian noise component that corresponds to the true measurement noise. With this procedure it is ensured that data that agrees with the assumptions of the KF is already available at the first range gates. After this enhancement, all the elements of the a priori estimate of the state vector at the first range gate can be set for the forward direction to

$$\mathbf{s}^{(-)}(1) = [0, 0, 0, 0]^T \quad (2.31)$$

and to

$$\mathbf{s}^{(-)}(1) = [0, 0, \Psi_{dp}^{\text{end}}, \Psi_{dp}^{\text{end}}]^T \quad (2.32)$$

for the backward direction. The a priori state covariance matrix at the first range gate can be approximated with $P_{\mathbf{s}(1)}^{(-)} = C(\epsilon_{\mathbf{s}(1)})$. The algorithm can be also adversely affected by folding of the differential phase, ground clutter and low SNR. These issues have to be adequately solved before applying KFE.

Intermittency

Differential phase measurements are not defined in non-rainy sections of a range profile. For the purpose of the estimation, missing values Ψ_{dp} values are linearly interpolated and, similarly to the previous section, a Gaussian noise component, whose standard deviation is in agreement with the true measurement noise, is added to the interpolated values. After the filtering process, K_{dp} and Φ_{dp} estimates that stem from range gates that were filled with interpolated values are tagged as ‘not defined’ and consequently removed from the profile.

2.4.7 Compilation of a final K_{dp} estimate

There are different ways how a final K_{dp} product can be compiled from the ensemble of K_{dp} estimates (hereafter K_{dp}^{ens1}) that are generated in the forward and backward direction and with different scaling of the transition covariance matrix. Some guidelines will be provided here to describe how our product was compiled, but there might exist more and even better possibilities and the reader is invited to try out and improve our suggestion. First, from Figure 2.3 it is seen that the forward estimates better represent the increasing K_{dp} values, while the ensemble of backward estimates better represent decreasing K_{dp} values. This effect can be used to select either forward or backward estimates in order to reduce the spatial spreading of K_{dp} . The backward or forward estimates are selected depending on the general behavior of the ensemble mean of K_{dp} , denoted as $\bar{K}_{dp}^{\text{ens1}}$. The following criteria were applied

and found to provide stable results for selecting the appropriate estimation direction:

$$\begin{cases} \text{forward} & \text{if } \bar{K}_{dp}^{\text{ens1}}(i) - \bar{K}_{dp}^{\text{ens1}}(i+1) \leq -0.1^\circ \text{ km}^{-1} \\ \text{backward} & \text{if } \bar{K}_{dp}^{\text{ens1}}(i) - \bar{K}_{dp}^{\text{ens1}}(i+1) \geq +0.1^\circ \text{ km}^{-1} \end{cases} \quad (2.33)$$

The threshold of $\pm 0.1^\circ \text{ km}^{-1}$ was selected based on the results that are given in Figure 2.3-b), showing the behavior of the spatial derivative of the mean of the K_{dp} estimates as a function of the radar range. Values that are within the two thresholds, i.e., if $-0.1^\circ \text{ km}^{-1} \leq \bar{K}_{dp}^{\text{ens1}}(i) - \bar{K}_{dp}^{\text{ens1}}(i+1) \leq 0.1^\circ \text{ km}^{-1}$, the new K_{dp} ensemble is calculated as the mean of the forward and the backward estimates. The result of this selection process is shown in Figure 2.4-a), where the forward and backward estimates are compiled to one ensemble, named K_{dp}^{ens2} , according to the mentioned selection rules. It is seen that the spatial extent of the high K_{dp} values is well represented with the newly compiled ensemble values and the spatial spread is reduced.

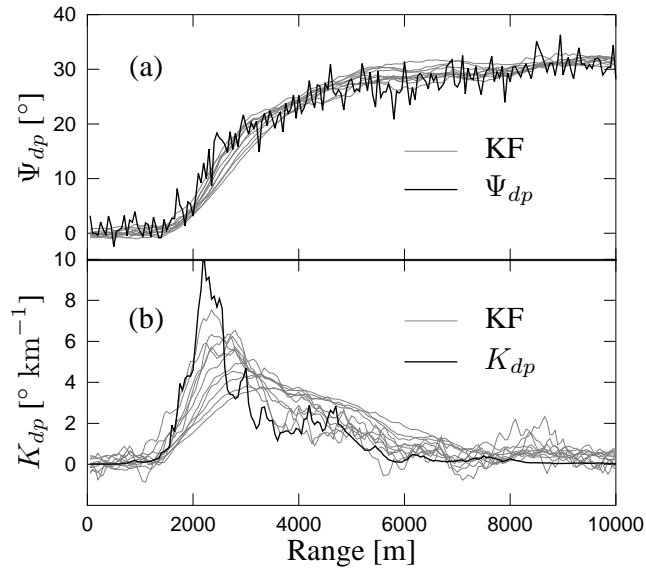


Figure 2.4: (a) Simulated Ψ_{dp} measurements (black line) together with an ensemble of KF estimates that were obtained for a set of covariance scaling factors with values of $0.1 \leq a \leq 10$. (b) The same as in (a) but for K_{dp} . Large scaling factors a lead to higher and noisier K_{dp} estimates.

The mean over this ensemble of values at every range gate, i.e., $\bar{K}_{dp}^{\text{ens2}}(i+1)$, provides a final K_{dp}^{final} estimate that is generally accurate. One can however make further use of the ensemble values in order to obtain an ever better approximation of the true K_{dp} value. One possibility to do so is to consider the mean and standard deviation (std) of K_{dp}^{ens2} . The idea behind this is the

following: when $\text{std} [K_{dp}^{\text{ens}2}(i)]$ is small, only few ensemble members need to be considered for K_{dp}^{final} , while a high standard deviation indicates that the mean over a larger ensemble needs to be taken. Similarly, when the mean over the ensemble $\overline{K_{dp}^{\text{ens}2}}$ is low, ensemble members that were calculated with a largely scaled covariance matrix $aC(\epsilon_{s(i)})$ (i.e., where the factor a is large) should not be considered for the calculation of K_{dp}^{final} , because it is unlikely to have large variations around $K_{dp}(i)$ when going to $K_{dp}(i+1)$. Consequently, ensemble members that were calculated with a low a should not be considered where $\overline{K_{dp}^{\text{ens}2}}$ assumes high values. These qualitative considerations can be translated into an algorithm in many different ways since it is difficult to give a recipe that works optimally under all conditions. In the following just one possible implementation is shown which was found to give good results after a lot of testing and tuning.

The N ensemble members are denoted with e_j , where $j = 1, 2, \dots, N$, and each e_j corresponds to a different covariance scaling factor a_j . For the calculation of the final estimate K_{dp}^{final} , the following approach is used:

$$K_{dp}^{\text{final}}(i) = \frac{1}{2l+1} \sum_{j=k-l}^{k+l} e_j \quad (2.34)$$

where the variables that define the summation limits k and l depend on the mean and the standard deviation of the ensemble members n_b . This dependence is expressed as

$$\begin{aligned} k &= \text{round} \left\{ \overline{K_{dp}^{\text{ens}2}}(i) \beta_1 + \beta_2 \right\} \\ l &= \text{round} \left\{ \text{std} [K_{dp}^{\text{ens}2}(i)] \gamma_1 + \gamma_2 \right\} \end{aligned} \quad (2.35)$$

where the operator $\text{round}\{\}$ indicates that the values in the brackets are rounded. In addition, the conditions

$$\begin{cases} k-l = 1 & \text{if } k-l < 1 \\ k+l = N & \text{if } k+l > N \end{cases} \quad (2.36)$$

apply for Eq.(2.34).

The parameters α_1, α_2 and β_1, β_2 need to be experimentally determined. In our case, good results were obtained with the values $\beta_1 = 2, \beta_2 = 0$ and $\gamma_1 = 2, \gamma_2 = 0$. It is seen from Eq.(2.35) that the ensemble standard deviation is used to determine how many ensemble members should be selected (few ensemble members are selected for low standard deviations) while the ensemble mean determines from which part of the ensemble these members are taken (i.e., ensemble members with high scaling factors a are selected if the ensemble mean is high). The K_{dp}^{final} profile that was compiled with this method, from the ensemble in Figure 2.3, is shown in Figure 2.5. An overall agreement with the true K_{dp} profile can be observed, albeit it is still obvious that the extreme small-scale fluctuations of the true K_{dp} cannot be resolved with the KFE technique.

2.5. Evaluation on simulated radar measurements in rain

It is interesting to investigate if the improvement in K_{dp} estimation using KFE is coming from the Kalman Filter or from the ensemble approach. An ensemble approach applied to other algorithms (not shown here) showed significant improvement but they were still outperformed by KFE. This suggests that both the ensemble combination and the Kalman Filter are contributing to an improved estimation of K_{dp} .

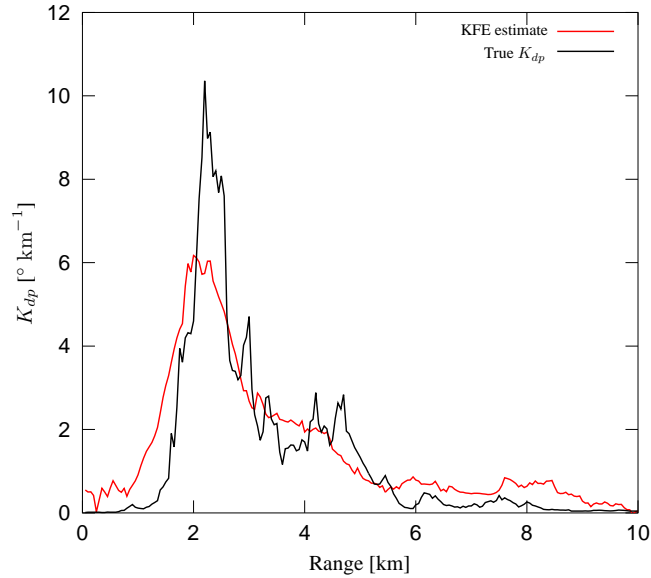


Figure 2.5: Example of a simulated K_{dp} profile and its reconstruction with the proposed KFE algorithm.

2.5 Evaluation on simulated radar measurements in rain

2.5.1 Description of two other standard algorithms

Two different algorithms for the estimation of the specific differential phase shift K_{dp} are compared with KFE. They fulfill the requirement of independence between phase-related and power-related radar variables and they are briefly described here below:

Adaptive length linear interpolation (ALI)

A common way to estimate K_{dp} is through first order polynomial interpolation of Φ_{dp} along radar paths. The first step is therefore to obtain Φ_{dp} profiles from the measured Ψ_{dp} (e.g., by means of the recursive filter described in *Hubbert and Bringi (1995)*; *Wang and Chandrasekar (2009)*). Once Φ_{dp} profiles are obtained, K_{dp} is calculated through a linear least-square fit on a path-length L [km] using n samples of Φ_{dp} . n is easily obtained as $n = L/\Delta r$, where Δr [km] is the range resolution. The K_{dp} value is then assigned to the mid-point of the estimation path

Chapter 2. Estimation of the specific differential phase shift upon propagation (K_{dp})

(e.g., *Gorgucci et al.* (1999)).

The choice of the estimation length L is delicate and different lengths ranging from 1 to 10 km have been used in weather radar studies *Gorgucci et al.* (1999); *Brandes et al.* (2001). The adaptive length linear interpolation (hereafter ALI) method, is based on a length L which is varied as a function of the horizontal reflectivity Z_H , used as an indicator of the local variability of the precipitation field. In the formulation described in *Wang and Chandrasekar* (2009) and for a range gate resolution of 0.1 km, L [km] is 4.5 for $Z_H \leq 35$, 3 for $35 < Z_H \leq 45$ and 1.5 for $Z_H > 45$. It must be noted that a precise and accurate value of reflectivity is not necessary to select the length L , and the selection is given by reasonably wide ranges of variation. Therefore the K_{dp} estimate can be considered independent from Z_H .

The advantages of the ALI method are its simplicity and stability. On the other hand its estimates of K_{dp} profiles tend to look excessively smooth, when compared with other methods. Furthermore, when the estimation of K_{dp} is carried by means of linear interpolation along a path of length L , the inner assumption is that the variation of K_{dp} along L are negligible.

Moving window range derivative (MWD)

K_{dp} can be estimated through a multistep moving window range derivative (hereafter MWD) of raw Ψ_{dp} profiles, a technique described in detail in *Vulpiani et al.* (2012). The process is iterative and it proceeds as follows. A preliminary estimation of K_{dp} (K_{dp}^*), is obtained as:

$$K_{dp}^*(i) = \frac{\Psi_{dp}(i + n/2) - \Psi_{dp}(i - n/2)}{2L}; \quad (2.37)$$

where L [km] is the estimation path and i is its center range gate, to which the value of K_{dp}^* is assigned.

After this first step, K_{dp}^* is quality controlled and non-physic values are identified and corrected as follows: we selected (at X-band) the thresholds for a minimum (maximum) acceptable K_{dp} to -1 (20) $^{\circ} \text{ km}^{-1}$. Estimates lower than the minimum threshold or higher than the maximum one are set to the respective limits. These outliers seldom occurred in the present study. From K_{dp}^* , a profile of estimated differential phase shift $\hat{\Phi}_{dp}$ is obtained using Eq. (2.4). The final estimate of K_{dp}^* is then obtained by iterating the previous steps. The convergence is quick and 10 iterations have been conducted, which allows to achieve a standard deviation $\sigma(K_{dp}^*)$ of the estimates always below $0.01^{\circ} \text{ km}^{-1}$ *Vulpiani et al.* (2012). The choice of the estimation length L is the free parameter of the algorithm and in the present work it has been tested for lengths of 1, 2, 3, 4 and 5 km.

The possibility to provide estimates with a low standard deviation is an advantage of the MWD method. On the other hand, this does not guarantee the accuracy of the estimates themselves, meaning their closeness to the inherent and unknown true K_{dp} values. Furthermore, as for the ALI method, the results tend to be smooth. The smoothing is increasing with increasing L ,

2.5. Evaluation on simulated radar measurements in rain

such that the peaks of K_{dp} are more pronounced when short estimation lengths are employed. This increase in sensitivity with respect to small scale variations of K_{dp} is however balanced by a reduced stability of the estimation itself. An optimal trade-off between stability and sensitivity has been found with $L = 2$ km (not shown here) and therefore in the following we will refer to MWD as MWD2.

2.5.2 Strategy to evaluate K_{dp}

The goal of the present section is to evaluate the performance of the algorithms presented for the estimation of K_{dp} at the radar resolution volume scale, in a set of different rainfall events and with a special focus on the correct estimation of the highest K_{dp} values, physically associated with intense and relatively small rain cells and therefore particularly difficult to capture. The results are discussed here in more details for X-band, while for S and C bands the reader is addressed to the Appendix of this Chapter (Appendix A.3). The choice of X-band is motivated by the wider range of variation of K_{dp} and the presence of more marked δ_{hv} effects at this frequency, making the estimation more challenging. For the evaluation, the set of simulated radar profiles described in Section 2.3.3 is employed.

Evaluation criteria

The accuracy of the estimation of K_{dp} is quantified on the dataset of the simulated events described in Sec. 2.3.3 by the Mean Normalized Absolute Error MNAE [%], Mean Normalized Bias (MNB) [%], Nash-Sutcliffe Efficiency (NSE) [-], Root Mean Squared Error (RMSE) [$^{\circ}$ km $^{-1}$] and Pearson correlation coefficient (ρ) [-]. MNAE and MNB quantify the average percentage magnitude and direction (underestimation or overestimation) of the deviations between estimated and true values while NSE indicates the ability of the algorithms to follow the overall trends of the true K_{dp} values. Eventually, RMSE quantifies the average deviation from the true values, in K_{dp} units of [$^{\circ}$ km $^{-1}$]. These criteria give a global view of the performance obtained, but they are influenced by the distribution of the true K_{dp} values, that it is usually very (positively) skewed. A second step in the evaluation is then to analyze the quality of K_{dp} estimates as a function of the K_{dp} value itself.

2.5.3 Results of the comparison

The comparison among ALI, MWD2 and KFE is shown in Table 2.1. In terms of MNAE, the results are similar for the three algorithms, with values ranging from 27% to 30.3%. The overall bias is positive for ALI and MWD2 (3.5% and 5.5%), while KFE is practically unbiased. From all criteria (except MNAE), ALI is consistently outperformed by MWD2 and KF. Although KFE performs slightly better than MWD2 for all criteria except MNAE, it is difficult to state which of these two is the most accurate. A similar hierarchy can be observed at the other frequencies considered. The range of variation of K_{dp} values decreases almost linearly with

Chapter 2. Estimation of the specific differential phase shift upon propagation (K_{dp})

Table 2.1: Summary of MNB and MNAE [%], Nash-Sutcliffe Efficiency (NSE), correlation coefficient (ρ) and RMSE [$^{\circ}$ km $^{-1}$] for the three K_{dp} estimation methods at X, C and S band.

Band	Method	MNB	MNAE	NSE	ρ	RMSE
X	KFE	0.1	28.8	0.82	0.9	0.55
X	ALI	5.4	30.3	0.65	0.81	0.7
X	MWD2	3.5	27	0.78	0.88	0.59
C	KFE	3.4	25.7	0.83	0.91	0.33
C	ALI	6.4	27	0.66	0.82	0.44
C	MWD2	4.4	22.8	0.78	0.88	0.37
S	KFE	4.5	26	0.82	0.91	0.15
S	ALI	7.4	29.5	0.72	0.85	0.18
S	MWD2	5.5	24	0.78	0.89	0.17

decreasing frequencies leading to lower RMSE values at C- and S-Band, for all the algorithms. It is interesting to note that also MNAE decreases, while MNB increases. This suggests that high K_{dp} values, which are larger at X-Band than at C- and S-Band, carry the majority of the negative biases, as it is shown in the following.

It is therefore necessary to observe how the errors in the estimation, quantified by the Normalized Relative Error (NRE [%]) vary as a function of the true K_{dp} itself. Focussing on X-band and referring to Figure 2.6, it can be observed that when K_{dp} increases, it tends to be strongly underestimated, with a NRE that becomes more and more negative. For K_{dp} values greater than 6° km $^{-1}$, the ALI method leads to median underestimations in the order of -50%, MWD2 around -30% and lower, while KFE, even though biased, is able to limit the median deviations to values higher than -15% (with the exception of $K_{dp} > 13^{\circ}$ km $^{-1}$ where the performance deteriorates for all the algorithms). Furthermore, for these high K_{dp} values, KFE keeps the 25% and 75% quantiles of errors around -25% and 0% respectively and MWD2 around -50% and -25%. The quantiles of the errors for ALI decrease more sharply, ranging from -50% (Q25) and 0% (Q75), for $K_{dp} \approx 6^{\circ}$ km $^{-1}$ to -60% (Q25) and -40% (Q75), for $K_{dp} \approx 12^{\circ}$ km $^{-1}$. For K_{dp} values greater than 5° km $^{-1}$ KFE performs better, while for lower values all the algorithms have comparable performances. The systematic bias observed for high values of K_{dp} is associated with the structure of the storms. In fact, these high values are present in the cores of convective rain cells, which have a sharp transition between areas of low and high rainfall intensity. All the estimation methods employed make use of an estimation length (ALI and MWD2) or consistency between contiguous range gates (KFE) that unavoidably smooths the K_{dp} peaks, when the rainfall gradients are sharp.

It clearly appears overall that K_{dp} estimates can be affected by large biases especially for $K_{dp} > 5^{\circ}$ km $^{-1}$, and that these biases are significantly reduced by KFE, in comparison with other algorithms. Similar conclusions hold at C- and S-band.

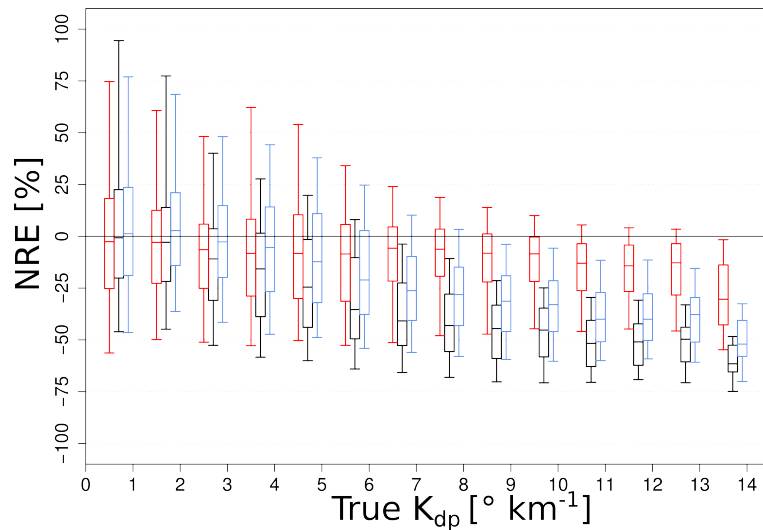


Figure 2.6: Evolution of the NRE [%] as a function of the true K_{dp} value for the ALI, MWD2 and KFE methods at X-band. The widths over which the statistics are calculated are constantly equal to $1 \text{ }^\circ \text{ km}^{-1}$, and centered from 0.5 to $13.5 \text{ }^\circ \text{ km}^{-1}$; a displacement is added to ease the readability. The 5 lines of each box represent 5% quantile, lower-quartile, median, upper quartile, and 95% quantile values respectively.

2.6 Evaluation with X-band radar data in rain and in snow

It is important to test the proposed algorithm not only on simulated but also on real radar data even though in this case a “true” reference is not available. This is done by applying the algorithm, together with ALI, on X-band radar data that were collected in tropical rainfall during the CHUVA campaign *Schneebeli et al. (2012)* and in alpine snowfall in Switzerland *Schneebeli et al. (2013)*. ALI is shown here as a standard reference because MWD is designed for rainfall only.

In order to overcome the lack of true measurements, the behaviour of the $K_{dp}(Z_H)$ relation is examined. An example of this relation, for simulated data, is shown in Fig. 2.7, where the relation between K_{dp} and Z_H in rain is shown for K_{dp} values determined with ALI and KFE. For Z_H values below 30 dBZ, ALI exhibits less scatter than KFE, but for Z_H values above 30 dBZ, the KFE algorithm estimates much better the high values of K_{dp} and the true K_{dp} - Z_H relation is also more closely followed.

The same $K_{dp} - Z_H$ relation that was used for the evaluation of the algorithm on the simulated measurements (Figure 2.7) was also compiled for the X-band radar data collected in Brazil. The reflectivity measurements were thereby corrected for rain and radome attenuation *Schneebeli et al. (2012)* and the results are shown in Figure 2.8, where also the PPI scans of the K_{dp} fields (determined with the two different algorithms) and the PPI scan of the reflectivity field are shown. From the $K_{dp} - Z_H$ scatter plot (Figure 2.8-d), who was compiled from range profiles that were limited to a distance of 20 km in order to ensure that the measurements are not affected by the melting layer, it is seen that the KFE algorithm exhibits a narrower scatter and also reaches higher values (approximately $11.5 \text{ }^\circ \text{ km}^{-1}$, compared to ALI, whose

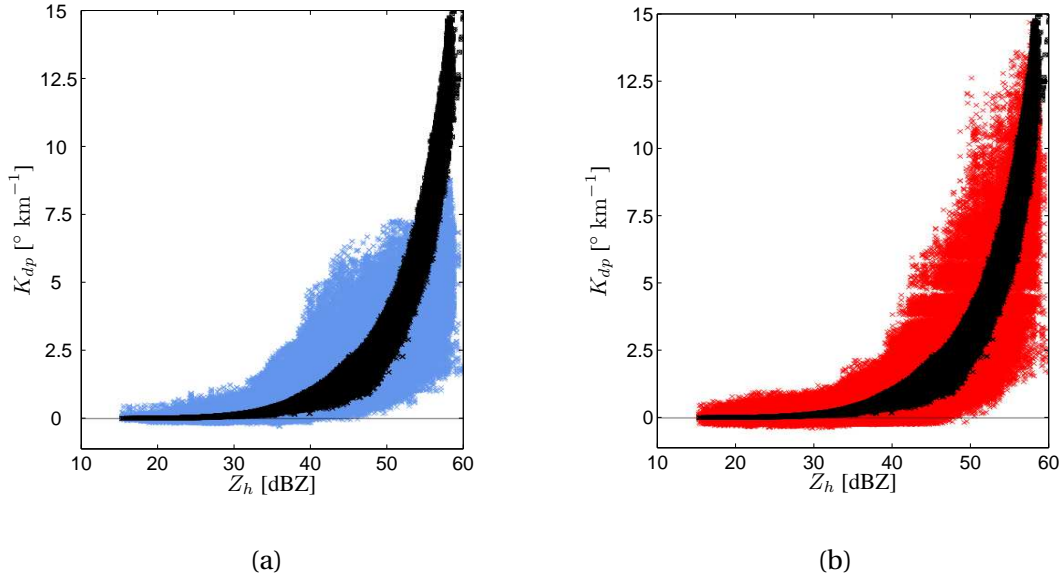


Figure 2.7: (a) The true K_{dp} (black) as well as the K_{dp} estimated from the ALI algorithm (blue) as a function of the radar reflectivity at horizontal polarization Z_H for simulated radar data. (b) The same as in (a) but for the K_{dp} estimated from the KFE algorithm (red).

maximal K_{dp} estimates are limited to values around 8° km $^{-1}$). Therefore KFE better follows the trends of the $K_{dp}(Z_H)$ theoretical relation for high Z_H values. It is also noteworthy that the KFE algorithm, in contrast to the evaluation on the simulated measurements, exhibits less unreasonable negative values than ALI in these real conditions. It must however be noted that for subsequent quantitative precipitation estimation, negative K_{dp} values will be set to zero in any case.

The K_{dp} PPI scans are a bit more difficult to compare since the differences between the two algorithms are not obvious at first sight. It is however clearly visible that the ALI algorithm spatially spreads the K_{dp} values more, hence the PPI scan shown in Figure 2.8-a appears to be smoother and the level of details is smaller. The chosen PPI scan consists of several intermittent rain systems, which shows that intermittency does not pose any problem to the KFE algorithm, if it is applied according to the guidelines given in Section 2.4.6.

A generally applicable algorithm that is supposed to be used for hydrometeor classification should not only be tested in rain conditions but also for data collected during snowfall. The data collected with an X-band polarimetric radar in the Swiss Alps hereby provide an excellent possibility for such an evaluation. For solid precipitation, a well-defined $K_{dp} - Z_H$ relation like for rain does not exist, hence a different method for the evaluation of the K_{dp} estimates is required. It was therefore decided to evaluate the algorithms with the so-called detrended fluctuation analysis (DFA) Peng *et al.* (1994), which is a method for determining the statistical self-affinity of a signal. The method has been widely used for the analysis of remotely-sensed signals of geophysical targets Ivanova *et al.* (2002); Schneebeli and Mätzler (2009); Brocard *et al.* (2011). Although this analysis will not allow us to decide which algorithm performs

2.6. Evaluation with X-band radar data in rain and in snow

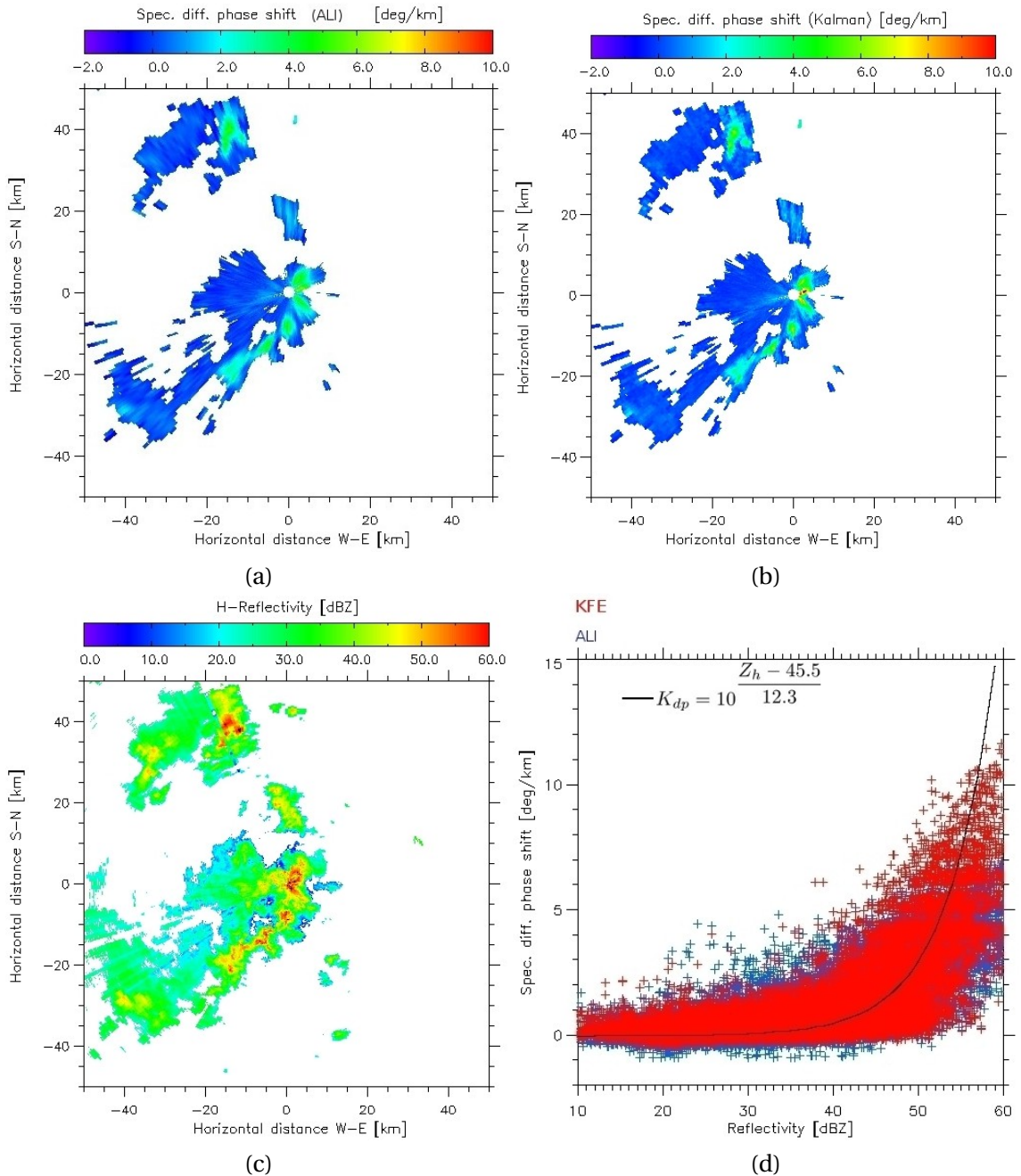


Figure 2.8: X-band polarimetric radar data obtained in Fortaleza, Brazil, showing (a) a PPI scan at 4° elevation of K_{dp} inferred with the ALI algorithm. (b) Same as in (a) but showing K_{dp} inferred with the KFE algorithm. (c) The same PPI scan that was shown in (a) and (b) showing the radar reflectivity Z_H . (d) The two K_{dp} estimates of the PPI scans given in (a) and (b) plotted as a function of the corresponding Z_H . The blue line shows the averaged theoretical relation obtained from DSD measurement, which is given in *Schneebeli et al.* (2012).

better in snowfall, it will be helpful to point out the differences between the K_{dp} estimates of the two algorithms. In order to apply the DFA technique, a range gate profile $y(r)$ of length N is divided into N/τ non-overlapping segments, each containing τ values. Furthermore,

Chapter 2. Estimation of the specific differential phase shift upon propagation (K_{dp})

the mean-square difference between $y(r)$ and the local linear trend $z(r) = ur + v$ within a segment of length τ can be written as

$$F^2(\tau) = \frac{1}{\tau} \sum_{r=k\tau+1}^{(k+1)\tau} [y(r) - z(r)]^2, \quad k = 0, 1, \dots, \frac{N}{\tau} - 1. \quad (2.38)$$

The DFA function $\overline{F^2}(\tau)$ is then defined as the average of $F^2(\tau)$ over the N/τ periods. This function was reported to follow a power law of the form $[\overline{F^2}(\tau)]^{\frac{1}{2}} \sim \tau^\alpha$, with an exponent α , being equal to the Hurst exponent *Mandelbrot and Wallis* (1968), representing the correlation properties of the signal. If $\alpha = 0$, there is no correlation in the signal (white noise). If $\alpha < 0.5$, the signal is antipersistent, and $\alpha > 0.5$ indicates persistence, while a value of $\alpha = 0.5$ is characteristic of Brownian motion *Ivanova et al.* (2002). The absolute value of the DFA function characterizes the noise amplitude. The DFA function of the two differently determined K_{dp} estimates is plotted in Figure 2.9-d as a function of the radar range.

From the K_{dp} and Z_H PPI scans shown in Figure 2.9, it is seen that for solid precipitation, high Z_H values do not necessarily indicate high K_{dp} values. The overall visual impression of the two K_{dp} PPI scans is again similar, but the values obtained with ALI seem to exhibit a certain radial structure, which is not visible in the K_{dp} estimates obtained with KFE. This radial structure is revealed in the DFA function: while the slope of the function (i.e., the α coefficient) is larger for the KFE estimate until a range interval of about 800 m (indicating signal persistence for the KFE estimate and K_{dp} values dominated by white noise for the ALI estimate), the opposite behavior is observed for range lengths between 800 and 4000 m. Towards longer intervals, the slope of the DFA function approaches $\alpha = 0.5$, which is the expected value at infinitely long range lengths. Although it cannot be decided on which algorithm performs better based on these DFA results, the analysis enables one to observe noise properties that are due to the different methods used for inferring the K_{dp} estimates. The interval lengths that are used to calculate the K_{dp} values from the smoothed differential phase are reflected in the fact that the DFA function associated with the ALI algorithm exhibits persistence for range intervals between 800 and 4000 m. In contrast to this, the forward projection of one state at a certain range gate to the adjacent one in the KFE algorithm formulation leads to persistence already at small range intervals. From these observations it can be concluded that small-scale fluctuations in K_{dp} can be better detected with the KFE algorithm, while the ALI algorithm spreads the K_{dp} signal over a wider range than the KFE algorithm. It is also seen that the noise amplitude at the smallest range interval (i.e., at the length of one range gate) is similar for both algorithms.

In snow, the better localization of K_{dp} that is obtained with the KFE algorithm is visually less obvious than for rain, since the spatial variability is generally smaller in snow than in rain *Germann and Joss* (2001). The KFE algorithm might however also be advantageous in non-liquid precipitation if some small-scale features, like precipitation-generating cells for instance, are present.

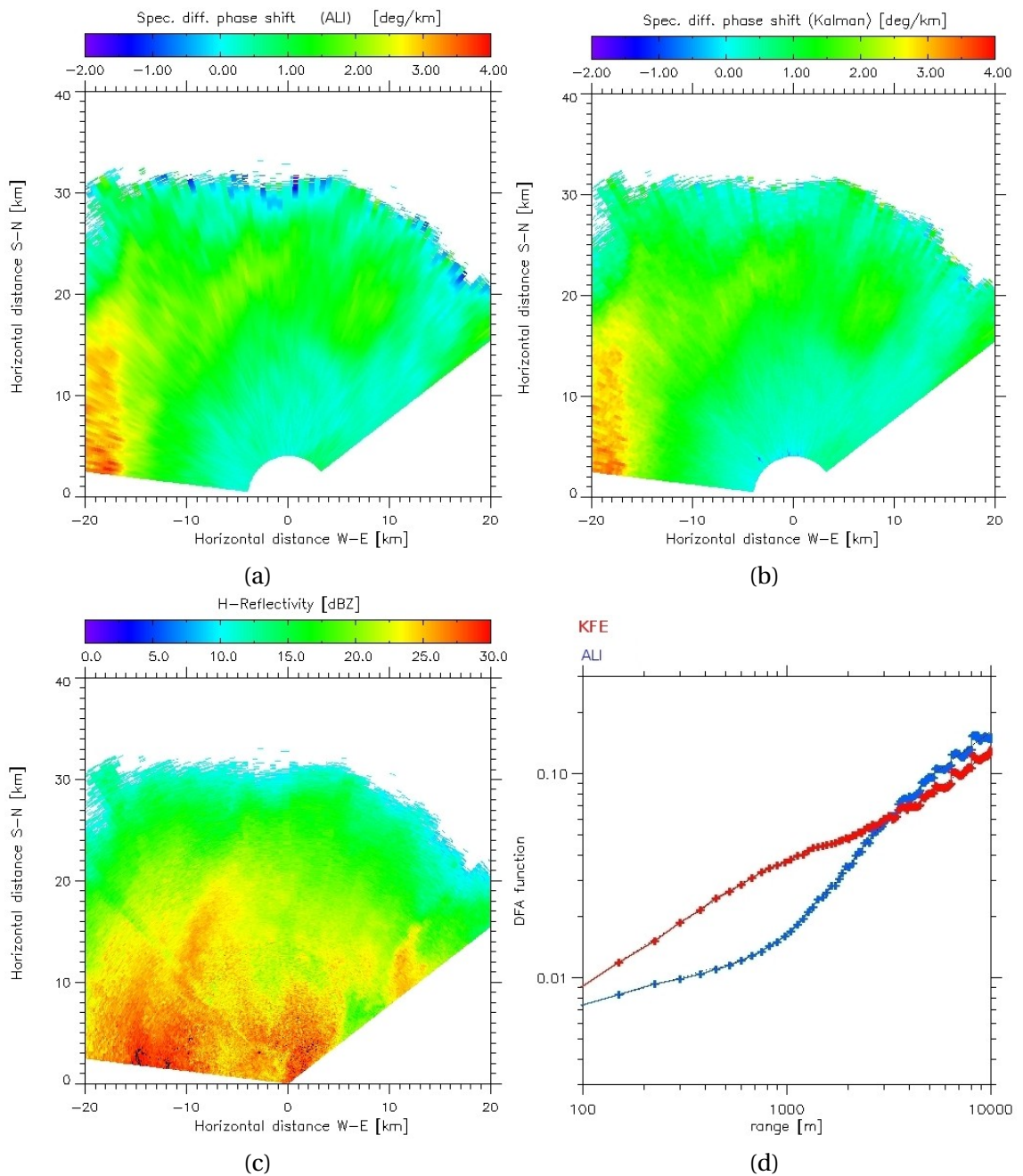


Figure 2.9: (a,b,c) Same as in Figure 2.8 but for snow data obtained in Davos at an elevation angle of 9° . (d) Detrended fluctuation analysis of the two different K_{dp} estimates shown in (a) and (b).

2.7 Summary and Conclusion

An algorithm based on ensemble of Kalman Filter estimates for an improved estimation of the specific differential phase shift on propagation K_{dp} is proposed. The algorithm runs a Kalman filter along a radar range gate profile in the forward (away from the radar) and backward direction (towards the radar) for different error covariance matrix parametrizations,

Chapter 2. Estimation of the specific differential phase shift upon propagation (K_{dp})

which leads to an ensemble of K_{dp} estimates. In a second step, an improved K_{dp} estimate is compiled from a selection of the K_{dp} ensemble members. The selection procedure is based on the behavior of the ensemble average, of its range derivative and of the ensemble standard deviation at every individual range gate.

The algorithm was tested and evaluated on X-band simulated radar measurements at the scale of the radar resolution volume, against two different methods, namely adaptive length linear interpolation (ALI) and moving window range derivative (MWD2). It is shown that significant biases can be hidden in the general statistics, and they emerge clearly only for less frequent high K_{dp} values. For $K_{dp} > 5^\circ \text{ km}^{-1}$, all the methods are negatively biased. This underestimation is in the order of -50% and -30% for the ALI and MWD2 methods, while KFE is able to keep it to values higher than -15% (in median). This aspect is particularly important when instantaneous K_{dp} values at the radar resolution volume scale are needed. Taking into account the different analyses, it can be stated that KFE obtains the best performances. The outcome of the present work should anyway warn the reader that the estimation of K_{dp} at the scale of the radar resolution volume is affected by significant errors ($\approx 25\text{-}30\%$), and special care should be devoted to the selection of the appropriate estimation scheme in order to minimize them, and to avoid excessive biases in the highest K_{dp} values.

The novel algorithm was tested also on real data coming from two contrasting radar data sets, one being collected during tropical convective rain and the other one during intense snowfall in the Alps. For the data obtained in rain, it was shown that the KFE algorithm exhibits less scatter in the $K_{dp} - Z_H$ relation, which is an indirect indication that K_{dp} can be retrieved with higher accuracy. For the snow case, it was shown that signal persistence is already reached for small range gate intervals, while the standard algorithm requires much longer intervals in order to obtain persistence.

The application of the proposed algorithm is not limited to X-band frequencies. For other frequencies, the $K_{dp} - \delta_{hv}$ relation shown in Figure 2.2 needs to be recalculated. Results for typical weather radar frequencies are given in Appendix A.1. The algorithm also depends on the radial radar resolution (i.e., the length of an individual range gate), since this influences the covariance matrix associated with the forward projection of the state vector. In Appendix A.2, a parametrization of this covariance matrix is provided as a function of the range gate length. Although the algorithm is versatile as it works in a wide range of conditions, it should only be applied to already cleaned Ψ_{dp} data, that is, data that are acquired with a sufficiently high signal-to-noise ratio (≥ 3 dB) and that already underwent basic clutter treatment (like clutter removal with a Doppler filter for instance). In this way it is ensured that noise or clutter effects do not hamper the applicability of the algorithm. The final K_{dp} product can be compiled from the ensemble of K_{dp} estimates in many ways. One possibility is suggested, which has been proven to be meaningful. There might be many more (and better) possibilities, which could possibly be tailored to specific applications, radar types and meteorological conditions for instance. The reader is strongly encouraged to adapt the suggested algorithm framework to his/her own needs.

3 Hydrometeor classification from two-dimensional video disdrometer data

This chapter is adapted from the manuscript:

- Grazioli, J., D. Tuia, S. Monhart, M. Schneebeli, T. Raupach, and A. Berne (2014b), Hydrometeor classification from two-dimensional video disdrometer data, *Atmos. Meas. Tech.*, 7(9), 2869–2882, doi: 10.5194/amt-7-2869-2014

It presents a supervised hydrometeor classification scheme developed for the two-dimensional video disdrometer (2DVD) instrument. The method is both a novel approach to sample in-situ microphysics and it will be useful in Chapter 4, as a comparison tool with the retrievals of a polarimetric radar.

3.1 Summary

The first hydrometeor classification technique based on two-dimensional video disdrometer (2DVD) data is presented. The method provides an estimate of the dominant hydrometeor type falling over time intervals of 60 s during precipitation, using as input the statistical behavior of a set of particle descriptors, calculated for each particle image. The employed supervised algorithm is a support vector machine (SVM), trained over 60 second precipitation time steps labeled by visual inspection. In this way, eight dominant hydrometeor classes can be discriminated. The algorithm achieved high classification performances, with median overall accuracies (Cohen's \mathcal{K}) of 90 % (0.88), and with accuracies higher than 84 % for each hydrometeor class.

3.2 Introduction

The two-dimensional video disdrometer (*Kruger and Krajewski, 2002*), 2DVD hereafter, significantly improves the capability of ground observations to describe the microphysics and microstructure of precipitation both in the solid and the liquid phase. The system, based on simultaneous observations of falling objects with two orthogonally-oriented cameras, has been used to characterize the relationships linking raindrop shape, size and terminal velocity (e.g. *Thurai and Bringi, 2005; Thurai et al., 2009*). It has also been employed to validate weather radar rainfall estimates (*Schuur et al., 2001; Thurai et al., 2008; Cao et al., 2008; Zhang et al., 2008*). Regarding snowfall, the 2DVD has been used to derive the statistical properties of particle size distributions of winter storms (*Brandes et al., 2007*), to improve the radar retrieval of equivalent liquid precipitation (*Huang et al., 2010*), and to simulate radar observations from measured snowfall microstructure (*Zhang et al., 2011*).

In the present Chapter 2DVD measurements are employed for the classification of hydrometeors, with a special focus on ice-phase precipitation. The expression “hydrometeor classification” refers to techniques that aim to retrieve qualitative information about the dominant hydrometeor type that characterizes the precipitation. Such information can then be used for risk assessment (hazardous hydrometeor identification, like hail), for parametrization and validation of numerical weather prediction (NWP) models (e.g., *Xue et al., 2000*), or to support microphysical investigations (e.g., *Houze, 1993; Schneebeli et al., 2013*). Hydrometeor classification techniques are nowadays implemented for different types of measurements. Typical examples in remote sensing are algorithms designed for ground-based polarimetric weather radars (*Straka et al., 2000; Dolan and Rutledge, 2009; Chandrasekar et al., 2013*), or for airborne radars and lidars observing ice phase clouds (e.g., *Shupe, 2007; Delanoë et al., 2013*). These sensors enable the sampling of large domains at high resolution on a short time scale, but their classification retrievals are indirect, constrained by numerical simulations, and difficult to validate extensively. On the contrary, airborne particle probe imagers (e.g., *Feind, 2008*), allow direct classification along aircraft flight paths but only (given the high cost of these platforms) during intensive measurement campaigns. Ground-based instruments

sample precipitation directly on site (although on small sampling volumes), and could be used to classify hydrometeors, thus becoming a point reference for remote sensing retrievals. Only few research works have been devoted to the implementation of classification schemes for such instruments, and their focus was mostly on mixed-phase precipitation (Yuter *et al.*, 2006), or in the exploration of the potential synergy between multiple sensors (Marzano *et al.*, 2010a). Some commercial disdrometers (e.g. PARSIVEL, Löffler-Mang and Joss, 2000), originally designed for rainfall studies, provide a basic estimation of the precipitation type associated with each measurement by making assumptions on fall velocity and equivalent rainfall intensity.

In this context the information provided by the 2DVD is of particular interest because a pair of two dimensional views, together with fall velocity, is provided for each particle. Such features alone allow expert users to interpret the images and visually recognize in them specific hydrometeor types (e.g., Zhang *et al.*, 2011). This suggests that automatic classification methods, based on training over visually interpreted (labeled) episodes, may be well suited to perform hydrometeor classification. Supervised classification algorithms, such as the support vector machine, (SVM, Boser *et al.*, 1992) are nowadays used to perform similar kinds of tasks. For example, such techniques have been used in land cover classification (Camps-Valls and Bruzzone, 2005), wind power forecasts (Foresti *et al.*, 2011; Zeng and Qiao, 2011), and weather prediction (Sullivan, 2009). The SVM is a linear and binary supervised classifier, that finds the optimal separations between observations belonging to different classes. These observations are defined by a set of numerical features and the optimal separation is learned from a training set in which the association between input observation and output class is known. The SVM is able to handle high dimensional inputs, is less prone to over-fitting issues than other supervised methods (Camps-Valls and Bruzzone, 2009), and has been shown to perform relatively well on the prediction of weather types (e.g., Elmore, 2010). Furthermore the SVM allows the retrieval of the most relevant input features driving the classification, and can rank them in order of importance, with the implementation of multiple kernel learning (SVM-MKL) techniques (Rakotomamonjy *et al.*, 2008; Tuia *et al.*, 2010).

In this Chapter a SVM model is trained on 2DVD data in order to classify eight hydrometeor classes of the dominant type of precipitation during time intervals of length Δt . Aggregation over time intervals is conducted to reduce the computational cost that may be excessive if each particle is individually considered. A relatively short Δt of 60 s is chosen to minimize the effect of mixing of separate hydrometeor types. Individual 2DVD images are summarized over Δt with a high-dimensional set of numerical features, constituting the necessary input for the SVM classifier. Data collected in the Swiss Alps, in the French Jura and in the southern part of Ontario, Canada, are used to train and validate the model.

The Chapter is structured as follows. Section 3.3 describes the experimental set-up and the basic 2DVD data. Section 3.4 presents the hydrometeor classification model. Section 3.5 presents the main results and their quality assessment, while Section 3.6 provides examples of the outputs of the hydrometeor classification. Section 3.7 concludes the Chapter and lists some future perspectives.

3.3 Dataset description

3.3.1 Experiment locations

The 2DVD data employed in the experiments were collected during three distinct field campaigns, between September 2009 and March 2013. The first campaign took place from September 2009, until June 2011 in Davos (CH): the 2DVD was deployed in the Swiss Alps, at an altitude of about 2500 m a.s.l. Data for a total of 1700 h of precipitation in liquid, mixed, and solid phase were collected during this time frame. The second campaign took place in Remoray (FR), from December 2012 until March 2013, at an altitude of about 920 m, in the context of an experiment focused on melting hydrometeors. 270 h of precipitation in solid, liquid and mixed phase were collected in this experiment. The third complementary campaign includes about 200 h of data (mainly solid precipitation) collected by three 2DVD instruments between December 2011 and March 2012 in the framework of the Global Precipitation Measurement mission (GPM, <http://pmm.nasa.gov/precipitation-measurement-missions>), in the Cold-season Precipitation Experiment (GCPEX) that took place in Ontario (CA).

3.3.2 2DVD instrument and data pre-processing

The 2DVD working principle is extensively described in *Kruger and Krajewski (2002)*. Here the most relevant features of the instrument are briefly summarized. Figure 3.1 illustrates the 2DVD measurement principle (see Fig. 3 of *Kruger and Krajewski, 2002*, for more details).

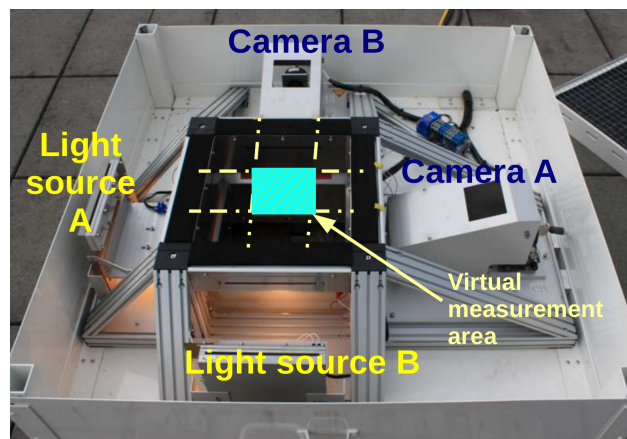


Figure 3.1: 2DVD measurement principle.

Two orthogonal light sources coupled with two (A and B) line scanning cameras, generate two stacked measurement planes of about $11\text{ cm} \times 11\text{ cm}$. The planes are vertically separated by a distance of around 6.2–7 mm (the exact value is determined by mechanical calibration). The cameras capture the falling particles at a resolution of 512 pixels (0.2 mm) at 34 kHz, and the vertical distance between the measurement areas of cameras A and B enables the measurement of fall velocity.

The raw images need to be processed before being employed. This involves the filtering of unreasonable measurements, and the rematching of the measurements taken from camera A and B, in order to ensure that both images actually refer to the same particle. Filtering and rematching of 2DVD images is based on the work of *Hanesch* (1999) and *Huang et al.* (2010). Their methods were followed with a noteworthy modification. Those studies, which were interested in snowfall only, restricted the maximum fall velocity to 4 ms^{-1} and 6 ms^{-1} , respectively. This upper boundary is increased to 14 ms^{-1} , large enough to include with sufficient margins the range of variation found in rain (e.g., *Beard*, 1976) as well as large graupel (*List and Schemena*, 1971).

Despite this filtering, some non-realistic particles can still be observed in the output. These particles appear as large objects, vertically oriented and elongated, as shown in Fig. 3.2. Because of these peculiarities, they are easily identified and excluded from the analysis presented in this Chapter. The exact nature of these artifacts is unknown, but their vertical orientation and dimension suggest that they may be associated with small-scale wind effects, melting, or dripping, causing some particles to reside for an anomalous amount of time in the measurement areas of the two cameras. The proportion of rejected particles is on average 3%, and it ranges between 0.5% and 13% per day. A few precipitation events required higher rejection rates. They were excluded from the analysis presented in this work.

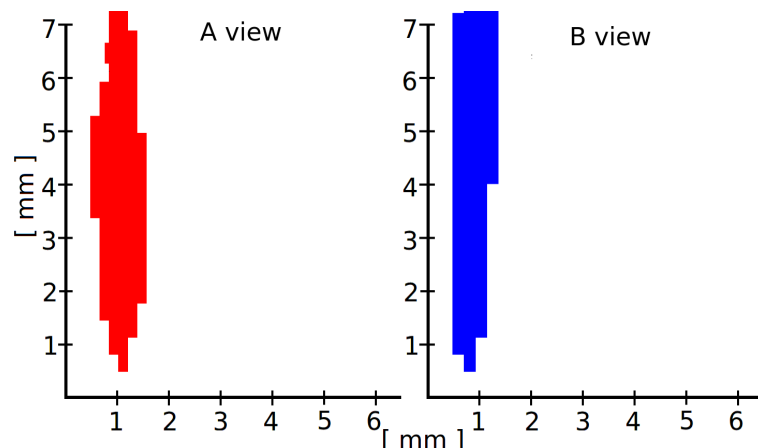


Figure 3.2: Example of A-B views of a non-realistic particle, that needs to be filtered.

Two additional potential sources of uncertainty (whose magnitude is currently not known in snowfall) are the image distortion that can occur when the horizontal component of the falling velocity of the particles is significant, and the local winds generated by the geometry of the instrument. To date, image distortion can be corrected only in rain, and in particular only for raindrops that possess an axis of rotational symmetry (*Schönhuber et al.*, 2008). On the contrary, the winds induced by the instrument itself can lead to an under-estimation of particles having lower density and dimension¹. Further research, which is beyond the scope of this Chapter, is needed to develop correction schemes for snowfall measurements in order

¹ This issue is more severe for the first generation of the 2DVD instrument (*Nespor et al.*, 2000). All the data employed in the present study were collected with second and third generation 2DVDs.

Chapter 3. Hydrometeor classification from two-dimensional video disdrometer data

Table 3.1: List of descriptors chosen to describe the particles recorded. Descriptors 1 and 2 come from combination of camera A and B; 3 to 6 describe particle size; 7 to 13 particle shape.

	Symbol	Full name	Units
1	v	fall velocity	[ms ⁻¹]
2	D_e	equivolumetric diameter	[mm]
3	$A_{A,B}$	shaded area	[mm ²]
4	$P_{A,B}$	shaded perimeter	[mm]
5	$T_{A,B}$	particle thickness	[mm]
6	$W_{A,B}$	particle width	[mm]
7	$PF_{A,B}$	pixel fraction	[-]
8	$FORM_{A,B}$	form index	[-]
9	$SqP_{A,B}$	square pixel metric	[-]
10	$FD_{A,B}$	fractal dimension	[-]
11	$SI_{A,B}$	shape index	[-]
12	$ELONG_{A,B}$	elongation	[-]
13	$ROUND_{A,B}$	roundness	[-]

to compensate for these two potential issues.

3.3.3 From single particles to global features

Pairs of 2DVD A-B images are available for each particle falling in the measurement area. For the purpose of the present work, it is useful to summarize this large amount of information by choosing a set of relevant descriptors². Then, the statistical distributions of these descriptors in a time step Δt are used as input information for the hydrometeor classification. The descriptors chosen in this work are listed in Table 3.1, and can be divided into 3 groups.

Joint descriptors

Two descriptors are obtained by combining the views of cameras A and B. They are: particle falling velocity v [ms⁻¹], and equivolumetric diameter D_e [mm]. D_e denotes the diameter of a sphere having the same volume as the falling particle. This descriptor was originally developed for raindrops, for which volumes could be calculated accurately from the 2-D views. It can be extended to particles of any shape as a reference measure of particle size. In the present work D_e is calculated according to the formulation of *Huang et al.* (2010).

²The particle descriptors are calculated in the present work from “.SNO”-format 2DVD data.

Particle size

Other descriptors can be computed separately for camera A and camera B. Fig. 3.3 illustrates some of them. The apparent shaded areas $A_{A,B}$ and perimeters $P_{A,B}$ are readily available from the 2DVD measurements, while thicknesses $T_{A,B}$ and widths $W_{A,B}$ of each particle are defined with respect to a bounding box around the particle (Fig. 3.3). v , D_e , A , P , T and W together describe the particle bulk dimension and velocity.

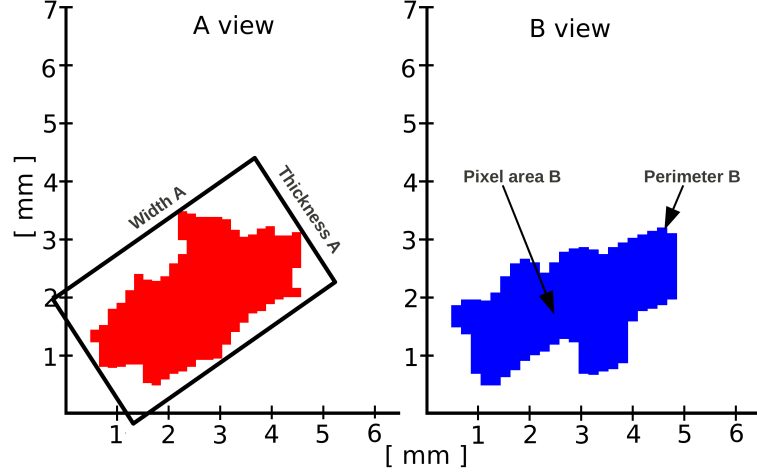


Figure 3.3: Examples of particles descriptors of 2DVD images (camera A and B). On camera A: width (W_A [mm]) and thickness (T_A [mm]) of the bounding box enclosing the particle. On camera B: particle apparent perimeter (P_A [mm]) and shaded area (A_A [mm²]).

Particle shape

Additional descriptors are computed to better characterize particle shape. They are dimensionless shape metrics commonly used in the analysis of land-cover images for remote sensing (Jiao and Liu, 2012), adapted for use on 2DVD images:

$$PF_{A,B} = \frac{A_{A,B}}{A_{A,B}^r} \quad (0, 1) \quad (3.1)$$

$$FORM_{A,B} = \frac{4\pi A_{A,B}}{P_{A,B}^2} \quad (0, 1) \quad (3.2)$$

$$SqP_{A,B} = 1 - 4 \frac{\sqrt{A_{A,B}}}{P_{A,B}} \quad [1 - 2/\sqrt{\pi}, 1) \quad (3.3)$$

$$FD_{A,B} = 2 \frac{\ln(P_{A,B}/4)}{\ln(A_{A,B})} \quad [1, 2] \quad (3.4)$$

$$SI_{A,B} = \frac{P_{A,B}}{4\sqrt{A_{A,B}}} \quad [\sqrt{\pi}/2, +\infty) \quad (3.5)$$

$$ELONG_{A,B} = \frac{W_{A,B}}{T_{A,B}} \quad [1, +\infty) \quad (3.6)$$

$$ROUND_{A,B} = 4 \frac{A_{A,B}}{\pi W_{A,B}^2} \quad (0, 1) \quad (3.7)$$

Chapter 3. Hydrometeor classification from two-dimensional video disdrometer data

where $A_{A,B}^r$ [mm²] is the area of the bounding box calculated for image A (or B). $PF_{A,B}$ is called pixel fraction and compares the shaded area with the area of the bounding box. $PF_{A,B}$ is an index of compactness, as is the roundness index, ($ROUND_{A,B}$) that compares the shaded area with a circular approximation. $FORM_{A,B}$ and square pixel metric $SqP_{A,B}$ are shape complexity indices based on the area-to-perimeter ratio, (they increase with decreasing complexity), while fractal dimension $FD_{A,B}$ and shape index $SI_{a,b}$ are indexes based on the perimeter-to-area ratio (they increase with increasing complexity). $ELONG_{A,B}$ evaluates the degree of elongation of the particles.

As introduced above, the feature vector used in the SVM model refers to the distribution of descriptors in a time step Δt . Let us consider a time step Δt , during which N particles are recorded. The mean, median, some quantiles (10 %, 25 %, 75 %, 90 %) and interquantiles (Q75–25, Q90–10) of each descriptor over the N particles available are computed. Additionally, for the descriptors 3 to 13 of Table 3.1, the correlation coefficient between the measurements of camera A and B is computed. This leads to a set of 203 features calculated per time step: 16 derived from camera combinations, 88 calculated separately for A and B (so 176 in total), and 11 correlation coefficients. Δt is selected to be 60 s, as a trade-off between representativeness and temporal resolution. Additionally, no statistics are computed if N is lower than 20 particles for a specific time step (Appendix B.1). The 88 features calculated separately for A and B have been verified to be consistent between each other, with biases generally lower than 10 %. This suggests that for these 88 features, the information carried by a single camera is sufficient. Therefore one can define, for each valid time step, a final feature vector \mathbf{x} containing 115 useful features, by using only the 88 single features from one of the two cameras.

3.4 Hydrometeor classification

This section details the proposed supervised classification approach. First the hydrometeor classes are defined, then it is detailed how a training set is obtained, and finally the classifier employed and its implementation are presented.

3.4.1 Hydrometeor classes and training set

The principle of supervised classification methods is to use a set of N_{train} labeled observations (or a training set) to train a classifier that will learn how to interpret new unlabeled observations. In this case, the appropriate dominant hydrometeor type needs to be assigned to a population of time steps of length Δt . The 2DVD offers the possibility to visualize the actual hydrometeor images, and the supervision was therefore conducted manually, according to the judgement of trained operators. Two operators independently interpreted the images by visualizing particle shapes, velocities, and taking into account the on-site environmental conditions (time of the year, temperature). Additionally, for the data collected in Davos (CH), X-band radar observations over the region were available (e.g. *Schneebeli et al.*, 2013), thus

3.4. Hydrometeor classification

providing contextual information about the structure of the precipitation, and in stratiform cases, about the altitude of the melting layer.

The visualization and pre-interpretation of a wide range of time steps led to the selection of 8 hydrometeor classes, to describe the possible precipitation types in the available dataset. Figure 3.4 shows an example of a typical particle belonging to each class. The classes are: Small particle-like (SP), Dendrite-like (D), Column-like (C), Graupel-like (G), Rimed particle-like (RIM), Aggregate-like (AG), Melting snow-like (MS), and Rain (R). The “-like” is added to emphasize that this approach identifies the dominant type of hydrometeor, which does not necessarily imply that: (i) there is only one type of hydrometeor in the considered time step, and (ii) that all hydrometeors exhibit pristine shape and geometry.

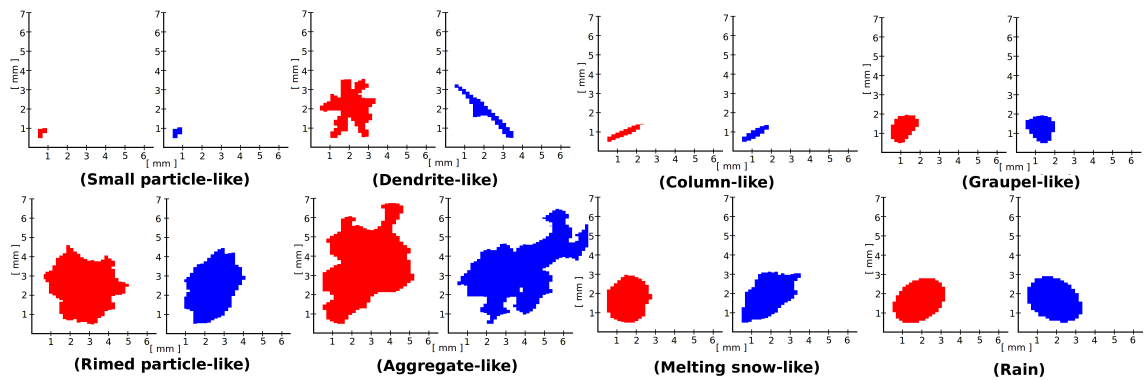


Figure 3.4: Examples of particle images (two camera views: A left, B right), belonging to time steps dominated by a particular hydrometeor class.

The definitions for some hydrometeor classes require clarification. SP time steps refer to particles falling during ice-phase precipitation that, given their size and the resolution of the instrument (0.2 mm), do not allow proper visual shape recognition. Small aggregates, as well as single ice crystals, can be assumed to belong to this class. RIM is observed when riming processes smooth the shapes of the hydrometeors and increase their fall speed, while G time steps refer to fully developed graupel, in which the original shape of the rimed crystal is no longer recognizable. MS is observed when the instrument records precipitation within the melting layer, and in these time steps raindrops, snowflakes, and smoother snowflakes with larger fall speed co-exist in a mixed phase.

The creation of the training set involved the inspection of all the particles within each time step, in order to retrieve the dominant particle type and to provide the appropriate label. Particular attention was paid to select time steps that were as pure as possible, for the subsequent training of the classifier. The training set employed in the present work includes $N_{\text{train}} = 400$ time steps, each of them numerically characterized by the 115 components of the associated feature vector \mathbf{x} defined in Sect. 3.3.3.

3.4.2 Classification method

This section presents the classifier used, the SVM. Then, it is detailed an extension of the SVM that allows the retrieval of the importance of each input feature (or group of features) in the model: SVM-MKL.

SVM

The Support Vector Machine (*Boser et al., 1992; Scholkopf and Smola, 2001*), also known as the large margin classifier, is a linear classifier, which finds the best linear separation between samples belonging to two classes. In our case, samples are time steps i of length Δt , represented by a vector \mathbf{x}_i of $d = 115$ features, and the classes are the dominant types of hydrometeors, y_i . The model is trained on known couples $X_{\text{train}} = \{\mathbf{x}_i, y_i\}_{i=1}^{N_{\text{train}}}$, with $\mathbf{x}_i \in \mathbb{R}^d$ and $y_i \in [-1, 1]$. It must generalize well on a set of unknown samples, for which the dominant hydrometeor type $X_{\text{val}} = \{\mathbf{x}_\nu\}_{\nu=1}^{N_{\text{val}}}$ is unknown.

The SVM finds the best linear separation, of type $f(\mathbf{x}) = \langle \mathbf{w}, \mathbf{x} \rangle + b$, for which all training samples are at least at a distance of 1 from the separating plane. In other words, for all training samples $f(\mathbf{x})$ must be greater or equal to one. To differentiate between positive and negative examples, we also multiply this expression by 1 if the sample is of the positive class and by -1 if it is of the negative class (the two types of hydrometeors). Summing up, the constraint is $y_i(\langle \mathbf{w}, \mathbf{x}_i \rangle + b) \geq 1, \forall i \in N_{\text{train}}$. The strategy pursued by the SVM (more details in *Boser et al., 1992*) is to find the separation which maximizes the distance between the closest points of each class, which are also called support vectors. This distance is called the margin and is inversely proportional to the norm of the parameters vector, i.e. $\|\mathbf{w}\|^2$. In order to allow some classification errors, we also introduce a term $\mathbf{x}i_i$, which is non-zero for samples classified wrongly. The margin maximization problem is the following one:

$$\min_{\mathbf{w}, b, \mathbf{x}i} \left\{ \underbrace{\frac{1}{2} \|\mathbf{w}\|^2}_{\text{Complexity of the function}} + C \underbrace{\sum_{i=1}^{N_{\text{train}}} \mathbf{x}i_i}_{\text{Training errors}} \right\} \quad (3.8)$$

$$\text{s.t.} \left\{ \begin{array}{l} y_i [\langle \mathbf{x}, \mathbf{w} \rangle + b] \geq 1 - \mathbf{x}i_i \\ \mathbf{x}i_i \geq 0 \text{ and } i = 1, \dots, N_{\text{train}} \end{array} \right.$$

C is a parameter that controls the constraint of perfect classification: if we allow some errors (by keeping C low), the margin becomes larger, thus reducing the dependence of the final model on training samples, that may be noisy or issued from errors in the measurements. A too high value of C increases drastically the value of the cost function, as soon as errors are made. In this case, the resulting model will achieve perfect classification of the training samples, but the risk of over-fitting the training data and achieving poor generalization in the

validation phase is higher.

This optimization model is solved using Lagrangian multipliers α , which allow us to rewrite the problem as:

$$\begin{aligned} \max_{\alpha} \left\{ \sum_{i=1}^{N_{\text{train}}} \alpha_i - \frac{1}{2} \sum_{i,j=1}^{N_{\text{train}}} \alpha_i \alpha_j y_i y_j \langle \mathbf{x}_i, \mathbf{x}_j \rangle \right\} \\ \text{s.t. } 0 \leq \alpha_i \leq C \text{ and } \sum_{i=1}^{N_{\text{train}}} \alpha_i y_i = 0 \end{aligned} \quad (3.9)$$

When the optimal solution of Eq. (3.9) is found (i.e., the vector of coefficients α), the label of an unknown sample \mathbf{x}_v is assigned on the basis of the sign of the decision function, i.e., its position with respect to the hyperplane ($f(\mathbf{x}) = 0$):

$$y_v = \text{sign} \left(\sum_{i=1}^{N_{\text{train}}} \alpha_i y_i \langle \mathbf{x}_i, \mathbf{x}_v \rangle + b \right). \quad (3.10)$$

It can be observed that in the present formulation, the SVM is only a binary classifier. A number of strategies exist to reduce multiclass problems to binary problems, and in the present work the one-against-one rule was employed (*Hastie and Tibshirani, 1998*). One-against-one builds as many binary classifiers as there are pairs of classes. Each classifier is therefore used to assign the time step to one of two possible classes. The time step is eventually classified into the class that received the most assignments.

Nonlinear SVM

The SVM, as it has been presented above, can solve only linear problems (it defines a linear hyperplane). However, there is an elegant solution to solve nonlinear problems. Let us go back to Eqs. (3.9) and (3.10): the solution of the optimization does not depend on the training samples themselves, but only on the dot products between samples (see $\langle \mathbf{x}_i, \mathbf{x}_j \rangle$ in Eq. 3.9). In the same way, the prediction for a new sample only depends on its dot products with the training samples (see $\langle \mathbf{x}_i, \mathbf{x}_v \rangle$ in Eq. 3.10). Dot products are measures of similarity between the samples. To perform nonlinear classification one needs to find an estimate of their similarity in a projected space of higher dimension \mathcal{H} , where linear separation becomes possible³. To avoid defining explicitly the coordinates of the samples in the projected space, i.e., $\phi(\mathbf{x}_i)$, we can use functions that, even if expressed with points in the original space, correspond to dot products in the projected space \mathcal{H} : these functions are called kernels. Without entering mathematical details, that the interested reader can find in *Scholkopf and Smola (2001)*, a kernel corresponds to a similarity function such that $K(\mathbf{x}_i, \mathbf{x}_j) = \langle \phi(\mathbf{x}_i), \phi(\mathbf{x}_j) \rangle$. This means

³The Cover theorem states that the probability of linear separability increases with the dimensionality of the space (*Cover, 1965*).

that, for a given projection $\phi(\cdot)$, the kernel computed from \mathbf{x}_i and \mathbf{x}_j will correspond to their similarity in the space \mathcal{H} defined by $\phi(\cdot)$. A classification, which is linear in the projected space, is nonlinear in the original space, as illustrated in Fig. 3.5.

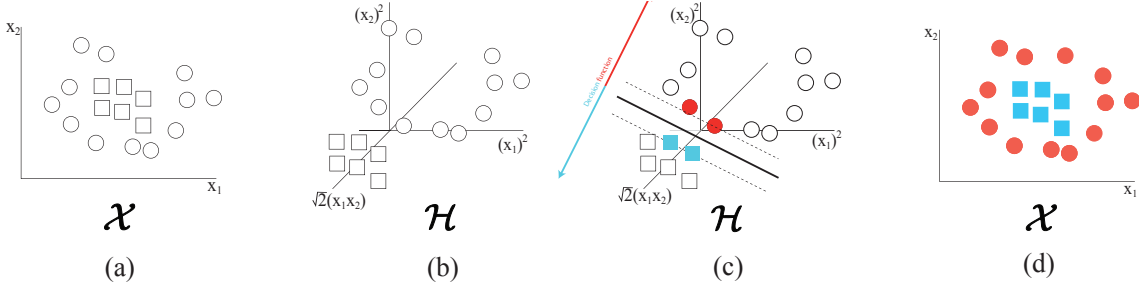


Figure 3.5: Illustration of the nonlinear SVM. (a) A nonlinearly separable dataset in the input space \mathcal{X} , involving two classes (squares and circles). (b) Projection on a 3D space \mathcal{H} by the kernel $K(\mathbf{x}_i, \mathbf{x}_j) = \langle \mathbf{x}_i, \mathbf{x}_j \rangle^2$. (c) Linear classification in the projected space \mathcal{H} (filled dots are support vectors). (d) Corresponding nonlinear decision function in the original space \mathcal{X} . Adapted from *Volpi et al.* (2013).

In practice, in order to obtain a nonlinear classification with the SVM, we replace the dot products in Eqs. (3.9) and (3.10) by kernel functions $K(\mathbf{x}_i, \mathbf{x}_j)$ and $K(\mathbf{x}_i, \mathbf{x}_\nu)$, respectively. A classical kernel to obtain such a behavior is the Radial Basis Function (RBF), which is computed as follows:

$$K(\mathbf{x}_i, \mathbf{x}_j) = \exp\left(-\frac{\|\mathbf{x}_i - \mathbf{x}_j\|^2}{2\sigma^2}\right). \quad (3.11)$$

The RBF kernel acts as a Gaussian similarity, which is maximal when considering the same samples ($K(\mathbf{x}_i, \mathbf{x}_i) = 1$), and decreases jointly with the decrease of similarity between the samples. The bandwidth σ controls the steepness of the Gaussian bell.

SVM-MKL

Even if very successful, SVM remains a black-box model, in the sense that no information about the importance of the initial variables can be retrieved from its results. All operations are optimized in the projected space \mathcal{H} : this means that, while it avoids computation of projection of the samples explicitly, it also prevents the assessment of the importance of the different variables involved. Recent research has offered a solution to this problem by introducing the concept of Multiple Kernel Learning (MKL, *Rakotomamonjy et al.*, 2008).

SVM-MKL builds on the so-called Mercer conditions stating that a weighted sum of any positive definite function (a requirement for all kernel functions) is again definite positive (*Mercer*, 1905). This means that we can design a valid kernel by a linear combination of M base kernels $K_m(\mathbf{x}_i, \mathbf{x}_j)$, each one considering single time step features (in this case $M = 115$) or sets of time

step features (in this case $M < 115$ and equals the number of groups of descriptors):

$$K(\mathbf{x}_i, \mathbf{x}_j) = \sum_{m=1}^M d_m K_m(\mathbf{x}_i, \mathbf{x}_j). \quad (3.12)$$

d_m is the weight attributed to each kernel K_m and is a measure of the importance of this kernel in the combination, i.e., of the variables composing it. It usually sums up to 1. The SimpleMKL algorithm proposed in *Rakotomamonjy et al. (2008)* optimizes alternatively the weights and the SVM and retrieves at the same time the relative importance of each group (d_m), and the SVM model associated with the final weighted combination.

In the experiment of this Chapter SimpleMKL is used to find the best combination of a series of RBF kernels K_m , each one assigned to a set of features referring to the same particle descriptor ($M = 13$, see Table 3.1). As an example, K_1 takes into account the eight statistical features (Q10, Q25, Q50, Q75, Q90, IQ75–25, IQ90–10, mean) associated with the hydrometeor fall velocity v descriptor, while K_2 the eight features associated with the equivolumetric diameter D_e , and so on.

3.5 Results and discussion

3.5.1 Performance assessment metrics

The evaluation of the accuracy of classification is conducted via different metrics. The available N_{train} training observations are divided in two parts (N_{train}^* and N_{val}^*). N_{train}^* observations are used as training set to optimize the SVM parameters C and σ and to train the SVM, while the remaining N_{val}^* observations are kept for validation. A comparison is made between the SVM classification output $\{y_i^*\}_{i=1}^{N_{\text{val}}^*}$, and the true labels $\{y_i\}_{i=1}^{N_{\text{val}}^*}$ by evaluating an 8×8 confusion matrix \mathbf{C} , as shown in Table 3.2. The elements $C(i, j)$ contain the number of observations classified in the i -th class, which in reality belong to the j -th class. The diagonal contains the correct classifications.

Given the confusion matrix, the global performance of the classifier is quantified by the overall accuracy (OA), and Cohen's Kappa (\mathcal{K}):

$$OA = \frac{\sum_{i=1}^S C(i, i)}{N} \times 100 \quad (3.13)$$

$$\mathcal{K} = \frac{OA - P_{\text{est}}}{1 - P_{\text{est}}} \quad (3.14)$$

$$P_{\text{est}} = \frac{\sum_{i=1}^S \left(\sum_{j=1}^S C_{j,i} \sum_{j=1}^S C_{i,j} \right)}{N^2}$$

Chapter 3. Hydrometeor classification from two-dimensional video disdrometer data

Table 3.2: Example of a confusion matrix obtained during validation of the SVM classification for a validation set N_{val}^* of 100 observations. Correct classifications are situated on the diagonal, and misclassification are in the off-diagonal entries.

		True							
		SP	D	C	G	RIM	AG	MS	R
Predicted	SP	14	0	1	3	0	0	0	0
	D	0	9	0	0	0	3	0	0
	C	0	0	9	0	0	0	0	0
	G	1	0	0	9	0	0	0	0
	RIM	0	0	0	0	8	0	0	0
	AG	0	0	0	0	0	11	1	0
	MS	0	0	0	2	0	1	13	0
	R	0	0	0	0	0	0	0	15

where S is the total number of classes, and N the total number of observations (in our case $S = 8$ and $N = N_{val}^*$). \mathcal{K} takes into account the correct prediction that might occur by chance, namely P_{est} , and is a robust metric in the case of unbalanced classes.

Then, let us look at the performances obtained within each class. For this purpose, we use:

$$OA_k = \frac{C(k, k)}{\sum_{i=1}^S C(k, i)} \times 100 \quad (3.15)$$

$$POD_k = \frac{C(k, k)}{\sum_{i=1}^S C(i, k)} \quad (3.16)$$

$$POFD_k = \frac{\left[\sum_{i=1}^S C(k, i) \right] - C(k, k)}{\sum_{i=1}^S C(k, i)} \quad (3.17)$$

where OA_k is the accuracy of the k -th class, and POD_k and $POFD_k$ are respectively the associated probabilities of detection and false detection.

3.5.2 Evaluation of the quality of the training set

N_{train} observations are available in total as a training set, and it must be verified that this amount is sufficient for the present task. In other words we want to assess here if a larger N_{train} would improve significantly the hydrometeor classification. To do so we proceeded as follows: (1): $N_{train} = 400$ was initially randomly split into $N_{train}^* = 300$ and $N_{val}^* = 100$; (2): N_{train}^* was iteratively reduced in size, while the original N_{val}^* was kept for validation; (3): Evaluation of the performance was conducted at each step; (4): steps (1)–(3) were repeated with 200 realizations of the original split.

3.5. Results and discussion

Table 3.3: Mean values and relevant quantiles of \mathcal{K} [-] and OA [%], calculated over 200 iterations of the SVM validation procedure.

Parameter	Q10	Q25	Q50	Q75	Q90	mean
\mathcal{K}	0.84	0.86	0.88	0.91	0.93	0.88
OA	86	88	90	92	94	89

Figure 3.6 shows the evolution of \mathcal{K} as a function of the number of training samples in the training set (N_{train}^*). It can be observed that N_{train}^* larger than 200 did not lead to significant improvements in terms of \mathcal{K} , while when N_{train}^* was smaller than 100, the performances started to degrade sharply. These results suggest that the total available labeled samples (400) are sufficient for the present classification task.

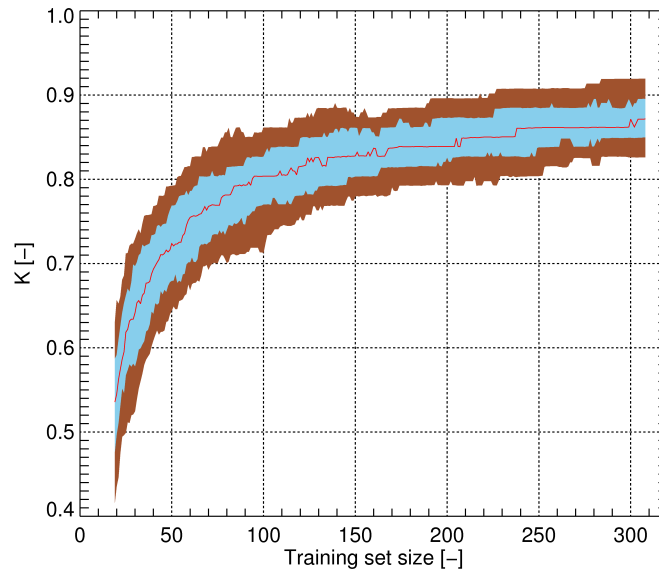


Figure 3.6: Evolution of \mathcal{K} [-], as a function of the training set size. The solid red line indicates the median, while the blue and brown areas represent Q75-25 and Q90-10, respectively. The size of the training set was varied with a step of 1, between 300 and 20. Statistics are based on 200 realizations.

3.5.3 Evaluation of the classification performances

For validation purposes, let us now focus on 200 realizations of the case $N_{\text{train}}^* = 300$, $N_{\text{val}}^* = 100$. The classification achieved accurate global results, both in terms of OA and \mathcal{K} . As shown in Table 3.3, \mathcal{K} and OA mean values were 0.88 and 89 %, and in 90 % of the cases they took values higher than 0.84 and 86 %, respectively. Additionally, \mathcal{K} tended to be close to OA, indicating that correct classification occurring by chance is very limited.

The classification performance associated with each hydrometeor class is summarized in Fig. 3.7. It can be observed that all the hydrometeor classes were identified with median OA_k always greater than 84 %, POD_k greater than 0.84, and $POFD_k$ lower than 0.16. Overall, rainfall

(R) hydrometeor class achieved the best scores, together with columns (C). R hydrometeors showed a POD_k equal to one, meaning that errors for this class were uniquely false detection. On the contrary, C hydrometeors showed low $POFD_k$ and OA_k very close to one, and the errors for this class were due mainly to missed detections, with POD_k scores around 0.9 in median. Graupel (G) was mostly affected by missed detections, and showed a relatively large interquartile spread for POD_k , around the median value of 0.87. Small particles (SP) had the highest false detection rate, with median $POFD_k$ close to 0.15. Dendritic snow (D) exhibited the largest interquartile spreads, around otherwise satisfactory median values of 87 % (OA_k), 0.87 (POD_k), and 0.13 ($POFD_k$), followed by rimed particles (RIM) that exhibited a similar behavior, achieving higher scores for all the metrics. Aggregates (AG) and melting snow (MS) were both correctly predicted, with lower interquartile spread, median OA_k larger than 88 %, POD_k larger than 0.88 and $POFD_k$ lower than 0.12.

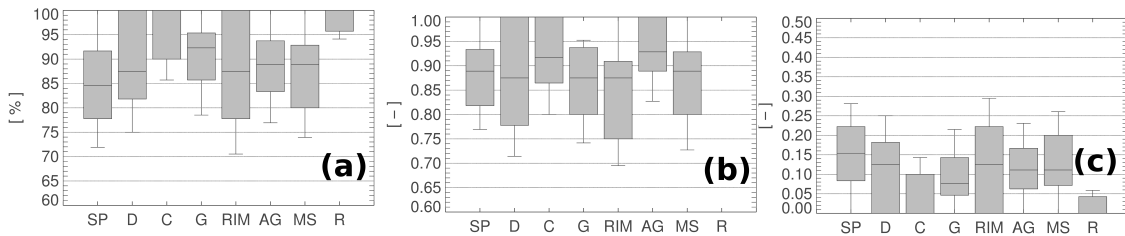


Figure 3.7: Barplots of: (a) OA_k [%], (b) POD_k [-], (c) $POFD_k$ associated with the eight hydrometeor classes undergoing classification. Statistics were calculated over 200 realizations of the SVM validation. Single points (outliers) are represented as circles.

A last consideration concerns the choice of SVM as classifier. Other methods are used to solve similar tasks in various fields of the environmental sciences, for example linear discriminant analysis (LDA) or neural networks (NN) (e.g., *Goosaert and Alam, 2009; Robert et al., 2013*). Comparison with these 2 methods showed that the proposed SVM scheme outperforms LDA by more than 25% and NN by more than 15% in terms of \mathcal{K} .

3.5.4 Ranking of descriptors

The SimpleMKL algorithm was applied to learn the most relevant descriptors in the classification process, as explained in Sect. 3.4.2. Referring to Eq. (3.12), it was observed that five groups of features out of the 13 (one per descriptor, each including the eight or nine statistical features extracted from its distribution in $\Delta t = 60$ s), accounted for about 70% (Fig. 3.8) of the total weights and therefore are considered hereafter as the most important ones. They are, in decreasing order of importance: pixel fraction PF, velocity v , equivolume diameter D_e , form index FORM and thickness T , with associated weights d_m of 0.193, 0.181, 0.13, 0.112 and 0.098, respectively. This does not imply that the remaining eight descriptors were negligible in the classification process, but that one expects to find a more immediate and intuitive physical meaning in these five top-ranked ones.

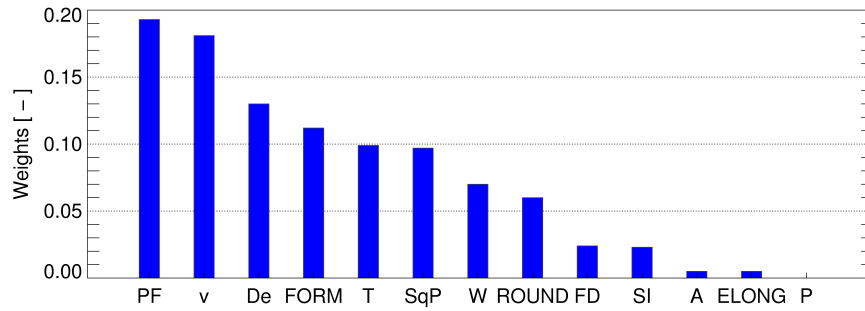


Figure 3.8: Weights d_m of the 13 K_m Kernels, associated with the 13 particle descriptors used in the present study.

3.6 Application on unlabeled data

This section presents some examples of the classification output, on data not included in the training set of the algorithm, and collected during the measurement campaign of Davos (CH).

3.6.1 17 March 2011

A snowfall event occurring on 17 March 2011 is presented in Fig. 3.9. The air temperature recorded in the very close vicinity of the 2DVD was constantly below freezing ($\approx -5^\circ\text{C}$) through the entire event duration, and different ice-phase hydrometeors were identified in the time window shown here. Initially (07:00–09:00 UTC) precipitation was dominated by small particles (SP), followed by a phase of instability (09:00–10:00 UTC) characterized by sharp variations of the identified hydrometeor classes. During the next relatively stable phase (10:00–12:30 UTC), graupel (G) and larger rimed particles (RIM) were identified. Panels (b), (c), and (d) of Fig. 3.9 illustrate the behavior in time of the three top ranked particle descriptors, namely pixel fraction PF, equivolume diameter D_e and fall velocity v . The median PF was around 0.7 during the entire event, indicating relatively high particle compactness. The median D_e was initially below 1 mm (SP phase), and it increased to values between 1 and 2 mm in the latter part of the event characterized mostly by G and RIM classes. v exhibited the same trends as D_e and it increased when rimed particles and graupel were dominant.

3.6.2 12 January 2011

A different situation is depicted in Fig. 3.10, relative to a snowfall event recorded on 12 January 2011. In this case, for the time window shown (19:00–24:00 UTC), precipitation was dominated by aggregates (AG) and dendritic shaped snow (D, at the end of the event). By comparing the present case with the one shown in Fig. 3.9, we observe a wider range of variation of particle sizes, with D_e ranging between 0.5 mm and 8 mm (AG). Particle compactness was lower, with median PF below 0.7 throughout the event, and slightly lower for D than for AG. This is due to the higher geometrical complexity of aggregates and dendrites relative to small particles and graupel. The velocity v did not exhibit peculiar trends, and it remained around

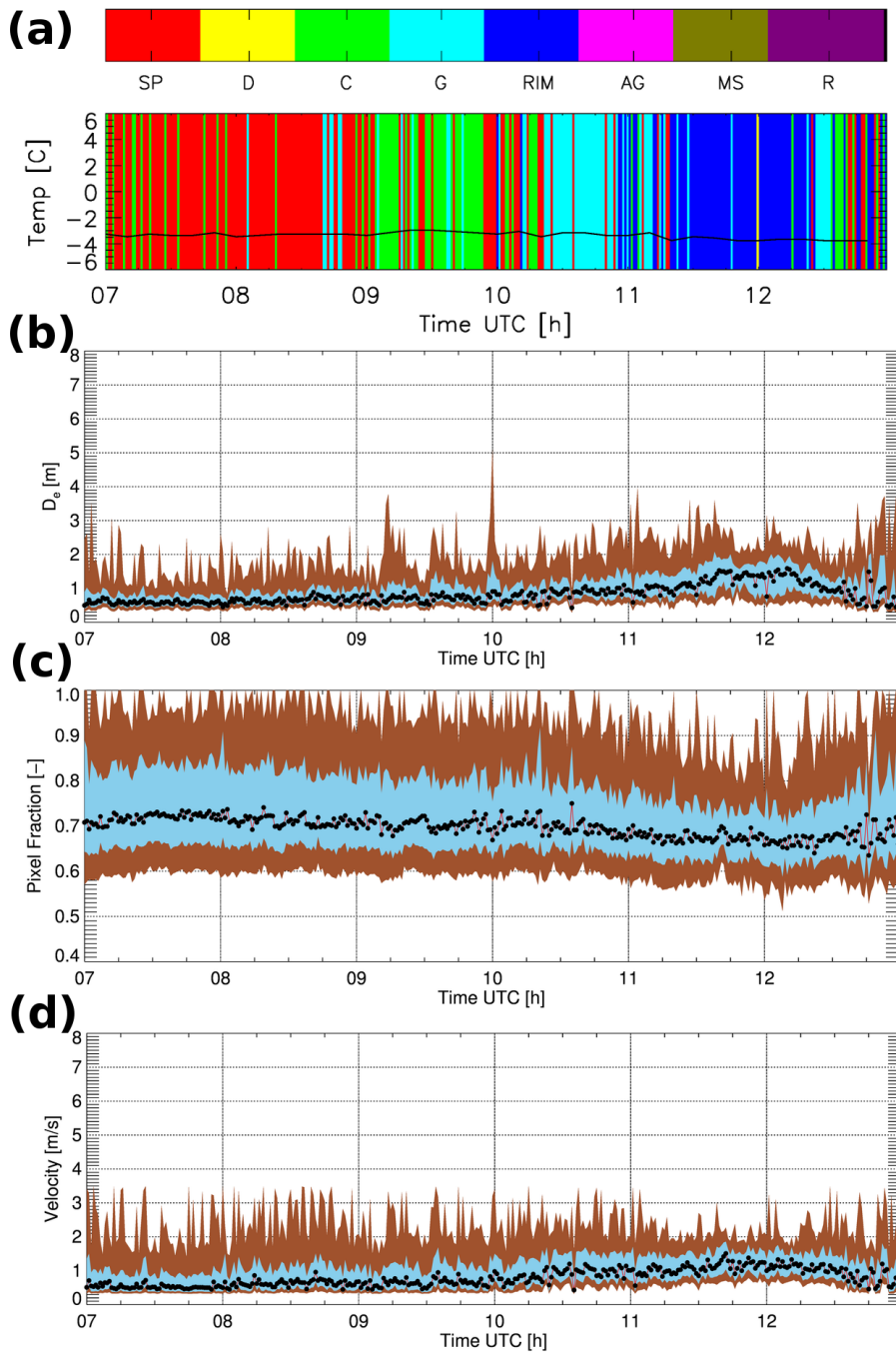
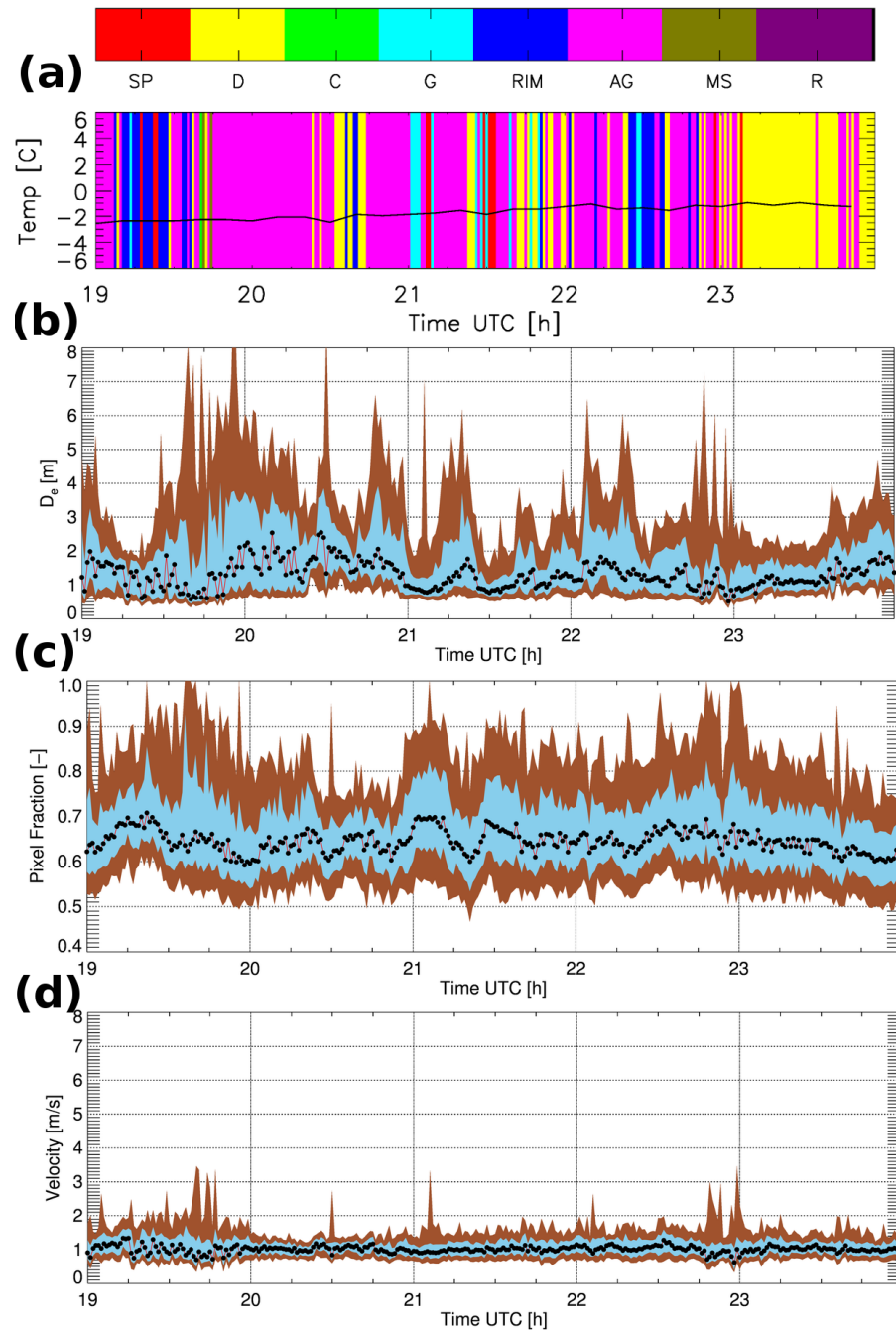


Figure 3.9: Snowfall event recorded on the 17th March 2011. Time series of: (a) dominant hydrometeor type as classified with the SVM and local ambient temperature [°C], as measured by a closely located (distance $\leq 50\text{m}$) weather station, (b) D_e [mm], (c) pixel fraction of camera A PE_A , (d) fall velocity v [m/s]. In panels (b), (c), and (d) black dots connected by the red solid line indicate the median value, while the shaded areas depict Q90-Q10 and Q75-Q25, respectively.

values of 1 ms^{-1} in median.

Figure 3.10: As in Figure 3.9, for the 12th January 2011.

3.6.3 5 August 2010

The precipitation event that occurred on the 5 August 2010 (Fig. 3.11) illustrates well the transition between liquid-phase and ice-phase precipitation. In the first part of the event (05:00–07:45 UTC) the environmental temperature was around 4 °C, and it dropped to 0 °C in the second part of the event (07:45–08:00 UTC). After 08:00 UTC the temperature stabilized again around 0 °C. These trends in temperature are directly reflected in the dominant hydrom-

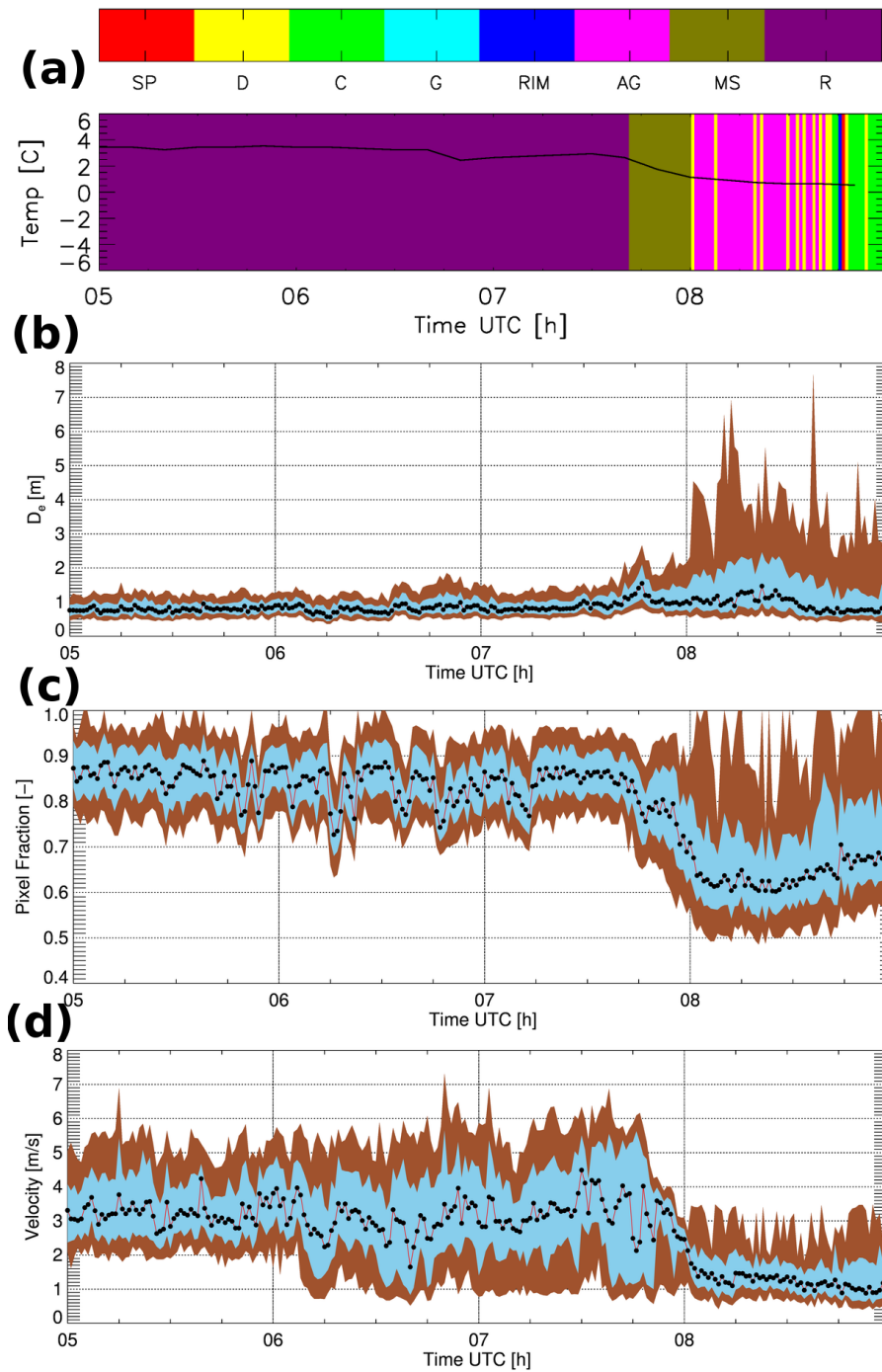


Figure 3.11: As in Figure 3.9, for the 5th August 2010.

eteor types classified: initially rain (R), then melting-snow (MS), and finally aggregates (AG). The rain was characterized by small D_e and $2 \leq v \leq 5 \text{ ms}^{-1}$ (i.e., light rain), which is larger than the typical velocities of ice-phase hydrometeors, and very high compactness with a median PF around 0.9. In the transition from R to MS and AG, a clear and relatively smooth trend was observed for the three descriptors shown: v decreased to median values around 1 ms^{-1} , the

spread of D_e increased, and the median PF dropped to 0.6 in the AG phase at the same time, as the geometrical complexity of falling hydrometeors increased.

Generally, the transition between R, MS and AG was well captured in the large available dataset. Figure 3.12 shows the relative number of classifications for each of these three types of hydrometeors as a function of the temperature. Please note that temperature has not been used as an input in the proposed system (Table 1). R occurred always at positive

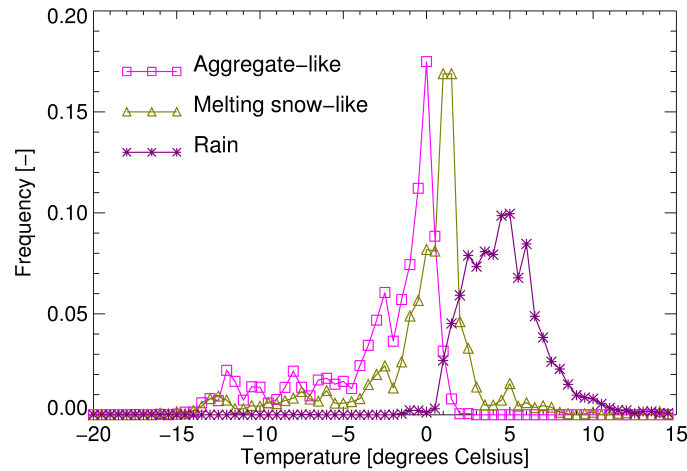


Figure 3.12: Distributions of the occurrence of AG, MS and R as a function of air temperature. The distributions are obtained by aggregation of all the 2DVD measurements collected during the field experiments of Davos 2009-2011 (CH) and Remoray 2012-2013 (FR), and temperature data are given by closely-located weather stations.

temperatures, MS maximum occurrence was between 2 °C and 1 °C, and AG around 0 °C and -1 °C (in agreement with *Hobbs et al., 1974*). These results give us confidence in the ability of the proposed technique to provide a meaningful classification.

3.7 Summary and conclusions

In this Chapter was presented a hydrometeor classification method based on the interpretation of 2DVD data. The classification, conducted with the SVM technique, uses as input the statistical behavior of a set of particle descriptors over time steps with length $\Delta t = 60$ s. The SVM was trained with 400 examples labeled by expert users, and outputs the dominant hydrometeor type within Δt . Additionally, an estimation of the relative descriptive importance of the input features is provided, which is of particular interest when higher-level information on the particle characteristics is required.

Discrimination is performed between eight hydrometeor classes: small particle-like, dendrite-like, column-like, graupel-like, rimed particle-like, aggregate-like, melting snow-like, and rain. Evaluation of the classification performance was conducted both in global and class-specific terms. The classifier achieved accurate results, with median OA and \mathcal{K} of 90 % and 0.88

Chapter 3. Hydrometeor classification from two-dimensional video disdrometer data

respectively. Each of the classes were identified with a median accuracy exceeding 84 %.

Additionally, once trained, the classifier is fast enough to be potentially implemented in real time.

Three classification examples together with the time evolution of the top-ranked particle descriptors were used to illustrate the typical classification products in pure snowfall events and in the transition between snowfall and rainfall. Global hydrometeor type behavior as well as small-scale fluctuations could be observed.

The proposed classification of hydrometeors from the 2DVD measurements provides additional information that can help better understand the microphysical processes characterizing ice-phase precipitation events. This work has the potential to be a starting point for ground-based quantitative evaluation of products derived from polarimetric weather radars. It can also be adapted and implemented to receive inputs from other particle imaging systems (one or two dimensional), both ground-based or airborne, provided that human interpretation can be carried out for the particle in the training set and that geometrical descriptors can be computed from the particle images.

The main limitation is that the current implementation provides bulk information over a given time step of length Δt , which is large enough to be statistically significant, but cannot provide estimation of hydrometeor mixtures over Δt . Future work will focus on the development of a particle-by-particle classification, more challenging in terms of computational requirements, that can lead to explicit quantification of hydrometeor mixtures.

4 A clustering approach to polarimetric hydrometeor classification

This chapter is adapted from the manuscript:

- Grazioli, J., D. Tuia, and A. Berne (2015a), Hydrometeor classification from polarimetric radar measurements: a clustering approach, *Atmos. Meas. Tech.*, 8(1), 149–170, doi: 10.5194/amt-8-149-2015

It presents some innovative ideas to develop data-driven approaches to perform hydrometeor classification from polarimetric radar measurements. An explicit example of implementation for X-band data collected in central Europe is shown. This method will be applied also in Chapter 6 in order to investigate microphysical aspects of snowfall.

4.1 Summary

A data-driven approach to the classification of hydrometeors from measurements collected with polarimetric weather radars is proposed. In a first step, the optimal number of hydrometeor classes (n_{opt}) that can be reliably identified from a large set of polarimetric data is determined. This is done by means of an unsupervised clustering technique guided by criteria related both to data similarity and to spatial smoothness of the classified images. In a second step, the n_{opt} clusters are assigned to the appropriate hydrometeor class by means of human interpretation and comparisons with the output of other classification techniques. The main innovation in the proposed method is the unsupervised part: the hydrometeor classes are not defined a priori, but they are learned from data. The approach is applied to data collected by an X-band polarimetric weather radar during two field campaigns (from which about 50 precipitation events are used in the present study). Seven hydrometeor classes ($n_{\text{opt}=7}$) have been found in the data set, and they have been identified as light rain (LR), rain (RN), heavy rain (HR), melting snow (MS), ice crystals/small aggregates (CR), aggregates (AG), and rimed-ice particles (RI).

4.2 Introduction

Hydrometeor classification (HC) from weather radar data refers to a family of techniques and algorithms that retrieve qualitative information about precipitation: the dominant hydrometeor type within a given sampling volume, where the term “dominant” is used to underline that the actual hydrometeor content is usually a mixture. These methods use as input a set of quantitative measurements provided by the radar itself and some additional information from external sources, such as vertical profiles of temperature or estimates of the 0 °C isotherm height. The classification is conducted on the spatial scale of the radar resolution volume (radar range gate), and its inputs are usually a set of polarimetric variables, such as the radar reflectivity factor at horizontal polarization Z_H , differential reflectivity Z_{DR} , the copolar correlation coefficient ρ_{hv} , and the specific differential phase K_{dp} (definitions in *Bringi and Chandrasekar, 2001; Berne and Krajewski, 2013*).

The most recent HC techniques require polarimetric capabilities. This allows a single instrument, the radar, to acquire multiple simultaneous measurements that are sensitive to distinct characteristics of precipitation. This facilitates the understanding of many microphysical processes (e.g. *Seliga and Bringi, 1976; Jameson, 1983; Vivekanandan et al., 1994; Ryzhkov et al., 2005a; Bechini et al., 2013; Schneebeli et al., 2013*).

Different HC algorithms are used at different frequencies, as in *Straka et al. (2000); Liu and Chandrasekar (2000)* for S-band, *Marzano et al. (2007); Dolan et al. (2013)* for C-band, and *Dolan and Rutledge (2009); Snyder et al. (2010); Marzano et al. (2010b)* for X-band. This is necessary because the scattering properties of hydrometeors vary with respect to the incident wavelength. Recently, after many years of improvements, HC has become a common product,

provided operationally by national meteorological services (e.g. *Gourley et al.*, 2007; *Al-Sakka et al.*, 2013; *Chandrasekar et al.*, 2013).

Most HC methods are based on similar principles: they start by selecting the number and type of hydrometeor classes undergoing classification. Then, through scattering simulations, the theoretical radar observations associated with these hydrometeor classes are reconstructed. Finally, actual observations are associated (labelled) with the appropriate class according to their degree of similarity with the sets of simulations available. This last step is often conducted by means of a fuzzy-logic input–output association (e.g. *Dolan and Rutledge*, 2009) or by means of Bayesian (*Marzano et al.*, 2010b) or neural network (*Liu and Chandrasekar*, 2000) techniques. In some cases these relations rely entirely on the simulation framework available (*Dolan and Rutledge*, 2009). In other cases, they are instead adapted and modified in order to adequately reproduce actual observations (*Marzano et al.*, 2007) or according to empirical constraints (*Al-Sakka et al.*, 2013).

The typical HC techniques mentioned above have become a state-of-the-art approach, stable and robust enough to be implemented operationally. However, it is important to underline that these approaches have some limitations since they rely on strong assumptions. First, the choice of the hydrometeor classes, meaning their content and their number, is mostly subjective. Secondly, the scattering simulations (e.g. *Mishchenko et al.*, 1996), which are usually very accurate for rainfall, are uncertain for ice-phase hydrometeors because of the complex geometries, dielectric properties, and largely unknown size distributions of ice particles (*Tyynela et al.*, 2011). Finally, it is not easy to take into account the accuracy of actual radar measurements when comparing simulations and observations. In the present Chapter is proposed a different approach to HC, in which the classifier is built on actual measured radar data and is not constrained by the output of numerical simulations.

A clustering technique, i.e. a technique that is used to find patterns (groups) in data sets in an unsupervised way (see *Jain et al.*, 1999; *Xu and Wunsch*, 2005; *Von Luxburg*, 2007, for a complete overview), is applied to a database of precipitation measurements collected by a X-band dual-polarization Doppler radar. An optimal partition of these data into n_{opt} groups is found as a trade-off between data similarity (of polarimetric observations within each group) and spatial smoothness of the partition. The content of these groups is then interpreted a posteriori, and a hydrometeor class is assigned to each of them.

The Chapter is structured as follows. Section 4.3 provides some background on clustering algorithms, and Sect. 4.4 presents the polarimetric data employed in the study. Section 4.5 describes the unsupervised part of the classification method, and Sect. 4.6 is devoted to the identification of the optimal number of clusters in the data set. Section 4.7 deals with the labelling of the n_{opt} clusters identified, and Sect. 4.8 presents the summary, discussion, and conclusions.

4.3 Background on clustering techniques

The proposed approach to HC is data-driven. The first two necessary steps are therefore to identify groups (clusters) in the available data set and then to select the optimal number of these groups. In this section we provide some background on the clustering methods that will be employed in the following sections.

4.3.1 Hierarchical data clustering

All techniques that aim at organizing a given set of objects (observations) in a certain number of groups (clusters) are referred to as unsupervised data clustering techniques. The shape (or functional form) of these groups, as well as their number, is unknown a priori (*Jain et al.*, 2000). A particular type of clustering technique is considered here: agglomerative hierarchical clustering (*Ward*, 1963, AHC hereafter). AHC is a stepwise approach that is used to group a set of N_D objects into n_c clusters ($n_c \leq N_D$) in such a way that objects belonging to the same cluster are more similar to each other than to those belonging to others. The technique is called agglomerative because at a step i

$$n_c^i = N_D - i. \quad (4.1)$$

This means that, at the initial step ($i = 0$), individual objects populate the clusters, while at each step two objects (the most similar) are merged, thus reducing the total number of clusters by one. The method is nested, in the sense that, once two samples are grouped in the same cluster, they remain clustered in all the following levels of the hierarchy.

In order to define which objects are the most similar, two criteria need to be defined (*Xu and Wunsch*, 2005): (i) a metric, i.e. a measure of distance between objects, and (ii) a merging rule. At each step i the pair of objects that are situated at the closest distance (according to a certain merging rule) are merged together.

4.3.2 Distance metric

Let \mathbf{x} and \mathbf{y} be two objects, or vectors, defined in a d -dimensional space. As vectors, \mathbf{x} and \mathbf{y} have d components:

$$\begin{aligned} \mathbf{x} &= \{\mathbf{x}[1], \dots, \mathbf{x}[d]\} \\ \mathbf{y} &= \{\mathbf{y}[1], \dots, \mathbf{y}[d]\}. \end{aligned}$$

A list of common distance metrics used to measure the distance $D(\mathbf{x}, \mathbf{y})$ between \mathbf{x} and \mathbf{y} is provided in Table 4.1. Each of these metrics is designed to capture a particular type of similarity between pairs of objects. For instance, the Euclidean distance¹ is defined in a d -dimensional

¹ A particular case of “Minkowski distance”, when $p = 2$, according to the notation of Table 4.1.

4.3. Background on clustering techniques

Table 4.1: Example of commonly used distance metrics $D(\mathbf{x}, \mathbf{y})$. The notation $\|\mathbf{x}\|_p$ refers to the p -norm of \mathbf{x} : $\|\mathbf{x}\|_p = \left(\sum_{i=1}^d |\mathbf{x}[i]|^p \right)^{1/p}$.

$D(\mathbf{x}, \mathbf{y})$	Expression	Definitions
Minkowski	$\ \mathbf{x} - \mathbf{y}\ _p$	p : free parameter
Cosine	$\frac{\mathbf{x}^T \mathbf{y}}{\ \mathbf{x}\ _2 \ \mathbf{y}\ _2}$	T : transpose
Correlative	$\sqrt{\frac{1-r(\mathbf{x}, \mathbf{y})}{2}}$	r : Pearson correlation coefficient

space as

$$D(\mathbf{x}, \mathbf{y}) = \sqrt{\sum_{i=1}^d |\mathbf{x}[i] - \mathbf{y}[i]|^2}, \quad (4.2)$$

and it is a good metric to evaluate the similarity between \mathbf{x} and \mathbf{y} when all the d components have the same order of magnitude. Conversely, the ‘‘correlative distance’’ (see Table 4.1) is less affected by unbalanced components but might be ill-defined when d is small.

4.3.3 Merging rule

The second concept to be introduced is the merging rule. A merging rule defines the criteria that an object \mathbf{x} , or a cluster of objects C_I (a group of objects $\mathbf{x} \in C_I$), has to satisfy in order to be merged with another cluster C_J . In other words, it generalizes the concept of distance between single objects of Table 4.1 to distances between two clusters, or between a cluster and a single object. Even though many merging rules exist, in this Chapter we present the weighted pairwise average (WPA) and weighted centroid (WC) rules (*Jain and Dubes, 1988*):

- WPA defines the distance between C_I and C_J as the average distance between couples of objects belonging to the two clusters, weighted by the number of objects in each subcluster. In this case the definition of distance between clusters, employed as merging rule, is recursive. As an example, given $C_I = C_K \cup C_L$

$$\begin{aligned} D(C_I, C_J) &= D(C_{K \cup L}, C_J) \\ &= \frac{n_K D(C_K, C_J) + n_L D(C_L, C_J)}{n_K + n_L}, \end{aligned} \quad (4.3)$$

where n_K and n_L are the number of objects contained in the clusters C_K and C_L , respectively.

- WC defines the distance between clusters as the distance between the (weighted) centroids of each cluster. The centroid is the centre of mass of a cluster C_I . It is computed as the average position of all the subclusters $C_K \subset C_I$, weighted by the number of objects

Chapter 4. A clustering approach to polarimetric hydrometeor classification

Table 4.2: Main characteristic of the X-band dual-polarization radar MXPoL. Additional information on the instrument can be found in *Scipion et al. (2013)*.

Parameter	Value
Radar Type	Pulsed
Frequency	9.41 [GHz]
Polarization	H-V orthogonal
Transmission/reception	Simultaneous
3 dB beamwidth	1.45 [°]
Max. range	30–35 [km]
Range resolution	75 [m]

in each C_K . Thus,

$$D(C_I, C_J) = D(\bar{\mathbf{x}}_{C_I}, \bar{\mathbf{x}}_{C_J}), \quad (4.4)$$

where $\bar{\mathbf{x}}_{C_I}$ is the weighted centroid of cluster C_I , defined as

$$\bar{\mathbf{x}}_{C_I} = \frac{\sum_{C_K \subset C_I} n_K \sum_{\mathbf{x} \in C_K} \mathbf{x}}{n_I}. \quad (4.5)$$

All hierarchical cluster methods start with N objects distributed into N clusters, and they end with N objects in one single cluster. The key point of any clustering method is therefore the selection of the optimal intermediate partition, named n_{opt} , between the starting and the ending point. A universally applicable criterion to guide this choice does not exist. This selection is usually performed by taking into account the compactness of the clusters, their relative separability (*Halkidi et al., 2002*), and any available prior (physical) knowledge about the data undergoing clustering (*Wilks, 2011*).

4.4 Data and processing

The present section provides a description of the data employed in the following analysis, and some details about data processing.

4.4.1 Data source

The polarimetric radar data considered here were collected with an X-band dual-polarization Doppler weather radar (MXPoL), whose characteristics are summarized in Table 4.2.

In the present work radar data collected during two field deployments are used. The first one took place in Davos (CH), in the Swiss Alps, from September 2009 to July 2011. The radar was deployed at 2133 m a.s.l. on a ski slope dominating the valley of Davos, as shown in Fig. 4.1a. The altitude of the deployment site made it possible, during cold seasons, to collect many observations of ice-phase precipitation when the radar itself was located above the

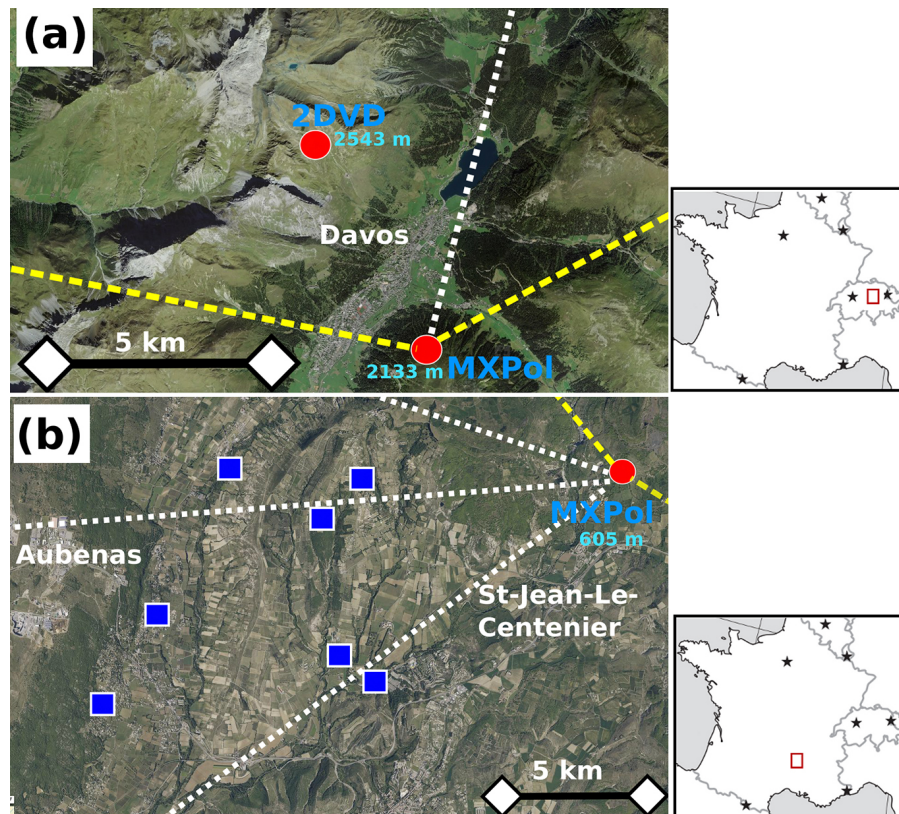


Figure 4.1: Maps of the two field deployments of MXPoL considered in this study. **(a)** Deployment in Davos (CH); **(b)** deployment in Ardèche (FR). The yellow lines indicate the extent of the PPI sector scans, while the white lines indicate the directions of the RHI scans. Red circles are used to mark the locations of instruments directly employed in the study (MXPoL and a 2DVD two-dimensional video disdrometer), while blue squares are used for laser disdrometers (Parsivel) employed only to parametrize the attenuation correction of Z_H and Z_{DR} . The source of the aerial view of **(a)** is <http://www.geo.admin.ch>, and that of **(b)** is <http://www.geoportail.gouv.fr/>.

melting layer and therefore did not suffer from liquid-water signal attenuation. Such radar observations represent the main peculiarity of this field campaign (e.g. *Schneebeli et al.*, 2013; *Scipion et al.*, 2013). However, during warm seasons, the melting layer was often higher than the radar site and relevant observations of liquid phase precipitation, both in stratiform and convective cases, were collected as well. The climate of the Davos region is characterized by approximately 130 days of precipitation per year and total yearly accumulations of about 1100 mm. The most intense snowfall events in winter are associated with north-westerly fluxes (*Mott et al.*, 2014). The scanning sequence of the radar, repeated approximately every 5 min, included plan position indicator (PPI) sector scans over the valley of Davos (at elevation angles of 0, 2, 5, 9, 14, 18, 20, and 27°), a range height indicator (RHI), and a vertically pointing PPI used for the zeroing of Z_{DR} .

The second field deployment, shown in Fig 4.1b, took place in the Ardèche region (FR) from September to November 2012, at an altitude of 605 m a.s.l.. This deployment was part of the

Hydrological cycle in the Mediterranean EXperiment (HyMeX, www.hymex.org; *Ducrocq et al.*, 2014; *Bousquet et al.*, 2014). Stratiform and convective Mediterranean precipitation events were sampled during this campaign, with the radar always located below the melting layer. Convective precipitation included vigorous thunderstorms with intense electric activity. In Ardèche, precipitation (in the fall season) is mainly associated with eastward-moving troughs from the Atlantic region that are at first slowed by the anticyclonic system over Russia and interact with the complex topography of the coastal region in the south of France (*Miniscloux et al.*, 2001; *Boudevillain et al.*, 2011). The scanning sequence of the radar included, in this case, wider (200° in azimuth) sector scans at elevation angles of 3.5 , 4 , 6 , 9 , and 10° . Additionally, two or three RHIs towards different directions and a vertically pointing PPI were collected during each cycle of 5 min.

The novel hydrometeor classification method proposed in this work is entirely based on radar data. However, in the following sections, data collected by a two-dimensional video disdrometer (2DVD; see *Kruger and Krajewski*, 2002) will be used as well for validation purposes. One 2DVD (second-generation, “low”-profile version) was deployed during the Davos field campaign at an altitude of 2543 m and at a horizontal distance of 5.2 km from MXPoL, as shown in Fig. 4.1a.

4.4.2 Polarimetric data

The polarimetric variables calculated from the measurements of MXPoL and employed in the following analysis are Z_H [dBZ], Z_{DR} [dB], K_{dp} [$^\circ \text{ km}^{-1}$], and ρ_{hv} [-]. Z_H and Z_{DR} are corrected for attenuation (in rain only) using the relations linking K_{dp} , Z_H , specific horizontal attenuation α_H [dB km^{-1}], and differential attenuation α_{DR} [dB km^{-1}] according to the method of *Testud et al.* (2000). The power laws between these variables are parametrized using disdrometer measurements for the data collected in France (locations shown in Fig. 4.1b) and using simulated realistic drop size distribution fields (*Schleiss et al.*, 2012) for the data collected in Switzerland. The set of observations corresponding to events during which the radar was located above the melting layer were not corrected for attenuation, assuming the attenuation in dry snow to be negligible (*Matrosov*, 1992).

K_{dp} is estimated from the total differential phase shift Ψ_{dp} [$^\circ$] using a method based on Kalman filtering (*Schneebeli et al.*, 2014). The algorithm is designed to ensure the independence between K_{dp} estimates and other polarimetric variables and to capture the fine-scale variations of K_{dp} . All the polarimetric variables are censored with a mask of signal-to-noise ratio $\text{SNR} > 8$ dB, and all the radar range gates potentially contaminated by ground clutter are censored as well, by means of a threshold of 0.7 on ρ_{hv} .

4.5 Clustering of polarimetric radar data

Hierarchical clustering is applied to radar observations (objects) \mathbf{x} , defined in the multidimensional space of the polarimetric variables. Here the clustering approach is presented and it is applied to the database of Sect. 4.4.

4.5.1 Data preparation

The data object \mathbf{x} is a five-dimensional vector defined for each valid radar resolution volume. The components of \mathbf{x} are

$$\mathbf{x} = \{Z_H, Z_{DR}, K_{dp}, \rho_{hv}, \Delta z\}. \quad (4.6)$$

The last component ($\mathbf{x}[5] = \Delta z$) is not a polarimetric variable, and it is defined as

$$\Delta z_i = z_i - z_{0^\circ},$$

where z_i [m] is the altitude above sea level of the i th resolution volume and z_{0° is the estimated altitude of the 0°C isotherm, taken as a reference. A positive Δz refers to a measurement collected at temperature ranges where ice-phase hydrometeors are expected, while a negative one refers to a measurement likely taken in liquid-phase precipitation. This variable is used as prior information for the clustering algorithm in order to take into account the approximate environmental conditions associated with each measurement. The altitude of the 0°C isotherm z_{0° is approximated by means of the linear interpolation of ground-based temperature measurements collected at a distance ≤ 40 km from the radar location and by assuming a constant lapse rate with altitude. It could also be estimated directly from other sources, such as soundings, numerical models, or radar data directly, when a melting layer is sampled.

The vector \mathbf{x} is not yet suitable to undergo cluster analysis. Two issues need to be tackled.

1. The skewed distribution of K_{dp} values. At X-band, K_{dp} ranges approximately from -1 to 15°km^{-1} (e.g. *Otto and Russchenberg, 2011; Schneebeli and Berne, 2012*), but its distribution of values, calculated over a large set of observations, is positively skewed, with typical modal values below 0.5°km^{-1} . This issue is tackled by log-transforming K_{dp} values. Before log-transforming 1°km^{-1} is added to K_{dp} in order to consider K_{dp} values in the range $[-1, 15]^2$.
2. Due to the differences in their units, the radar variable fields contained in \mathbf{x} have a typical range of values that differs by several orders of magnitude. For instance, Z_H can vary over tens of dBZ, while Z_{DR} and K_{dp} are smaller by one order of magnitude and ρ_{hv}

² $K_{dp} < -1^\circ\text{km}^{-1}$ occurs in less than 0.01 % of the cases in our database.

even by two orders of magnitude. This issue is tackled by means of data standardization (stretching). Even though a classical approach would be to use a z -score transformation, based on mean and standard deviation of a sample of data (e.g. *Wilks, 2011*), a method based on minimum and maximum boundaries is selected. This allows one to preselect physically relevant bounds. The components $\mathbf{x}[i]^*$ of the standardized data are obtained as

$$\mathbf{x}[i]^* = \frac{\mathbf{x}[i] - \mathbf{x}_{\min}[i]}{\mathbf{x}_{\max}[i] - \mathbf{x}_{\min}[i]} \quad i \in \{1, 2, 3, 4\}, \quad (4.7)$$

where $\mathbf{x}_{\min}[i]$ ($\mathbf{x}_{\max}[i]$) is the minimum (maximum) bound allowed for each polarimetric variable. The boundaries employed in the present study are -10 to 60 dBZ for Z_H , -1.5 to 5 dB for Z_{DR} , -3 to 3 for the logarithmically transformed K_{dp} , and 0.7 to 1 for ρ_{hv} (Δz is considered in the next paragraph). Variations of the order of $\pm 20\%$ around the proposed boundaries have a negligible impact on the results presented in the following sections, and the most sensitive boundaries are associated with Z_H .

Δz is stretched within a smaller range of variation in the following way:

$$\mathbf{x}[5]^* = \begin{cases} 0 & \text{if } \Delta z \leq -400 \text{ m;} \\ \kappa & \text{if } \Delta z > 400 \text{ m;} \\ f(\Delta z) \times \kappa & \text{if } -400 \text{ m} < \Delta z \leq 400 \text{ m} \end{cases} \quad (4.8)$$

$0 < \kappa \leq 1$.

κ is a scaling factor and $f(\Delta z)$ denotes any monotonically increasing functional form that gives continuity to Eq. (4.8). Gaussian, sigmoid, and logistic functions have been tested and appeared to be equally adequate. The threshold of ± 400 m is the (rounded) standard deviation of z_{0° estimates. The reason for a different standardization of Δz is to reduce the weight of this non-polarimetric input in the clustering process: this parameter is intended only to flag positive and negative temperatures in a quasi-binary way and not to substitute the information provided by the polarimetric variables (therefore, κ is kept strictly ≤ 1). κ factors ranging between 0.3 and 0.9 lead to similar outputs, and an intermediate value of 0.5 was used.

With the standardization detailed in Eqs. (4.7) and (4.8), the radar observations collected at each radar range gate are summarized by the observation vector \mathbf{x}^* , whose entries are now expressed with a similar order of magnitude.

4.5.2 Subset undergoing clustering analysis

Agglomerative clustering algorithms are generally computationally expensive, because the distances between all samples (and then groups) to be clustered are computed at each step of the hierarchical aggregation chain. Therefore it was decided to define the clusters using a subset of the data and then assign the whole data set to these clusters using a nearest-cluster

rule (e.g. *Volpi et al.*, 2012). About 50 precipitation events belonging to the data set of Sect. 4.4 were manually selected. These events cover the range of precipitation types observed by MXPoL during the field campaigns of Davos (CH) and Ardèche (FR), and they are assumed to be a representative sample of midlatitude temperate precipitation.

A subset of data is taken randomly from these 50 precipitation events from PPI scans conducted at elevation angles between 3.5° and 10° (free of ground clutter contamination). This amount, consisting of 20 000 observations \mathbf{x}^* (defined in Eqs. 4.6, 4.7, and 4.8), is used as input to the subsequent cluster analysis. Different seeds of the initial random selection led to the same results, suggesting that the random sampling does not affect the outcome of the clustering technique presented in the next section.

4.5.3 Clustering algorithm: data similarity and spatial smoothness

An AHC is applied to the polarimetric data set of \mathbf{x}^* objects in order to obtain an optimal partition of the data into a set of clusters. This technique is a trade-off between purely data-driven clustering, as it was described in Sect. 4.3 (that only looks for similarity in the five-dimensional feature space of \mathbf{x}^*), and spatial smoothness of the partition in the physical space. In other words, hydrometeor classes should contain both objects that are similar to each other (data-wise) and that also exhibit spatial consistency, since we assume spatial smoothness of the geographic distribution of precipitation types. Here and in the following an Euclidean distance metric and WPA merging rule will be used. Of the other possible combinations of the distance metrics and merging rules presented in Sect. 4.3, similar results were obtained with the correlative distance and WC rule. The method developed in the present Chapter is sketched in the flow chart of Fig. 4.2. Panel (a) of the figure is explained step by step in the following sections.

Step1: Fig. 4.2a1

Initially the 20 000 selected objects populate $n_c = 20\,000$ clusters. A first hierarchical aggregation is conducted on the data, until reaching a number of 1 000 clusters in the data set³. This step aims at merging the most similar objects before proceeding with more computationally expensive calculations.

Step2: Fig. 4.2a2

Given the remaining $n_c = 1000$ clusters, referred to as C_L ($L = 1, \dots, n_c$), we proceed to the classification of the entire PPI images from which the original 20 000 objects were extracted. Let $\mathbf{x}_p^* \notin C_L$ ($L = 1, \dots, n_c$) be an object taken from one of the PPI images and not belonging to any cluster C_L . This object is now classified into one of the n_c clusters available, specifically

³ By doing this it is assumed that the optimal partitions of the data set are found when $n_c \leq 1000$.

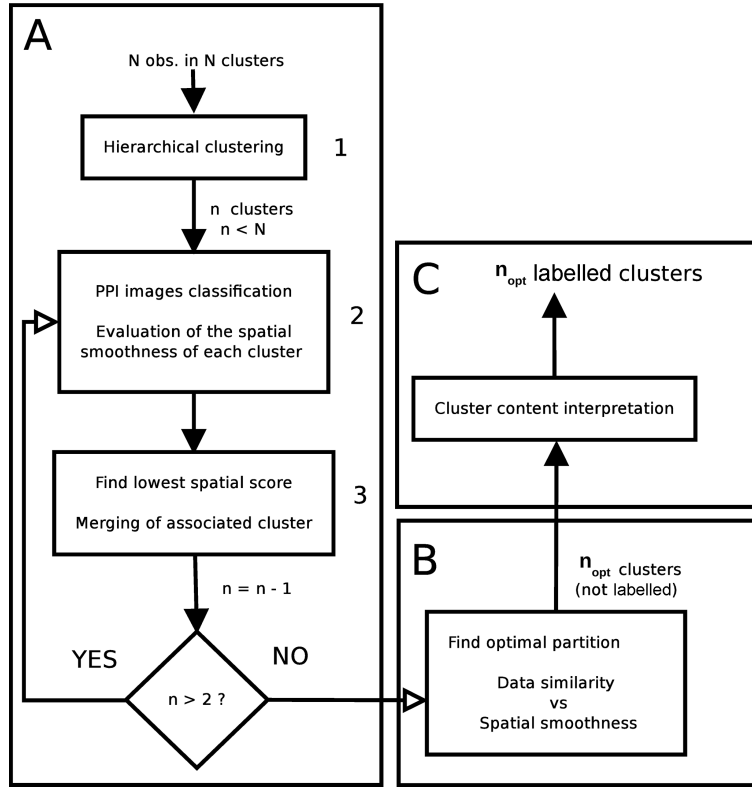


Figure 4.2: Flow chart of the clustering algorithm presented in Sect. 4.5.

the one related to the minimal distance to the object (according to the given merging rule). We proceed until all the objects of the PPI images are classified into one of the n_c clusters available. At this point the spatial smoothness of the partition into n_c clusters is evaluated. Each object \mathbf{x}_p^* has been assigned to a cluster C_M ($1 < M \leq n_c$). At first a spatial smoothness index (SSI) associated with \mathbf{x}_p^* is defined. This index evaluates the spatial consistency of the classification of an object with respect to the classification of its neighbouring objects:

$$SSI(\mathbf{x}_p^*, C_M) = \frac{1}{n_{NN}} \sum_{i(p)=1}^{n_{NN}} \delta_{i(p)}, \quad (4.9)$$

where

$$\delta_{i(p)} = \begin{cases} 0 & \text{if } \mathbf{x}_{i(p)}^* \notin C_M \\ 1 & \text{if } \mathbf{x}_{i(p)}^* \in C_M, \end{cases}$$

where n_{NN} (number of nearest neighbours) is the number of nearest objects considered in the construction of SSI and $\mathbf{x}_{i(p)}^*$ indicates the i th nearest object of \mathbf{x}_p^* . In the present work $n_{NN} = 4$, and very similar results are obtained for $n_{NN} = 2, 4, 8$. The identification of the nearest neighbours is performed in polar coordinates, and the distance between objects is the distance between their respective radar resolution volumes. SSI ranges between 0 and 1. If all the n_{NN} objects belong to the cluster C_M , then SSI is equal to 1. SSI indices are calculated for

each \mathbf{x}_p^* , and they are summarized in a $n_c \times n_c$ matrix \mathbf{M} , hereafter called spatial smoothness matrix. The elements $M_{I,J}$ of \mathbf{M} are defined as

$$M_{I,J} = \sum_{p=1}^{N_I} \text{SSI}(\mathbf{x}_p^*, C_J), \quad (4.10)$$

where N_I is the total number of objects \mathbf{x}_p^* satisfying the condition $\mathbf{x}_p^* \in C_I$. The matrix \mathbf{M} is conceptually similar to a confusion matrix, commonly used to evaluate the goodness of categorical classifications (e.g. *Wilks*, 2011). Diagonal entries $M_{I,I}$ quantify the spatial smoothness of the cluster C_I , while the off-diagonal terms $M_{I,J}$ ($I \neq J$) quantify the probability of objects belonging to a cluster C_I to be surrounded by objects of the cluster C_J .

Analogously to a confusion matrix, the information contained in \mathbf{M} can be further summarized by means of quality indices. As an example, Cohen's kappa can be used to evaluate the global spatial smoothness of a partition of the data set into n_c clusters. Cohen's kappa is defined as

$$\mathcal{K} = \frac{\text{SSO} - S_{\text{est}}}{1 - S_{\text{est}}}, \quad (4.11)$$

where

$$\text{SSO} = \frac{\sum_{I=1}^{n_c} M_{I,I}}{N} \quad (4.12)$$

and

$$S_{\text{est}} = \frac{\sum_{I=1}^{n_c} \left[\left(\sum_{J=1}^{n_c} M_{J,I} \right) \left(\sum_{J=1}^{n_c} M_{I,J} \right) \right]}{N^2}. \quad (4.13)$$

N is the total sum (over rows and columns) of all the elements of \mathbf{M} . \mathcal{K} increases as the level of spatial smoothness increases and takes into account the globally observed spatial smoothness (SSO) as well as the contribution occurring by chance, namely S_{est} . \mathcal{K} evaluates the global spatial smoothness of a partition, but the smoothness of each cluster C_M can be evaluated individually. For this purpose the spatial smoothness per cluster (SS_M) index is defined:

$$\text{SS}_M = \frac{M_{M,M}}{\sum_{I=1}^{n_c} M_{M,I}}. \quad (4.14)$$

Step 3: Fig. 4.2a3

At this stage, the set of observations is divided into n_c clusters, and the spatial smoothness of this partition has been evaluated. A classical hierarchical approach would now proceed by merging the two most similar clusters data-wise, reducing the total number of clusters to

$n_c - 1$ at each iteration. In this case, additional use is made of the information provided by Eq. (4.14). Let the cluster C_W with the lowest spatial smoothness score be defined as

$$C_W \text{ s.t. } SS_W = \min_{L=1, \dots, n_c} \{SS_L\}. \quad (4.15)$$

The cluster C_W is forced to disappear, and it is merged with the most similar (data-wise) one according to the linkage method and the distance metric selected.

In this way, at each step of the AHC, spatial smoothness is used to identify the cluster that exhibits the highest spatial discontinuity (lowest spatial smoothness), while data similarity is used to merge it with one of the other $n_c - 1$ available clusters. The reader should be aware that different constraints on spatial smoothness could be implemented at this stage, and the constraint used in this work is only a simple example. The aggregative algorithm detailed in steps 1–3 recursively repeats step 2 and step 3 until $n_c = 2$.

4.6 Selection of the optimal cluster partition

An important step of hierarchical clustering is the selection of the optimal partition (n_{opt}) of the data set. In the present section some indices are introduced in order to evaluate the quality of data partitions and to guide the final selection of n_{opt} .

4.6.1 Cluster quality metrics

The spatial quality of each partition of the data set is quantified by means of two indices:

1. \mathcal{K} , defined in Eq. (4.11); \mathcal{K} quantifies the global degree of spatial smoothness of a given partition.
2. The accuracy spread index (AS), derived from Eq. (4.14) as follows:

$$AS = \max_{L \in \{1, \dots, n_c\}} \{SS_L\} - \min_{L \in \{1, \dots, n_c\}} \{SS_L\}. \quad (4.16)$$

This index evaluates the inhomogeneity of the spatial characteristics of a partition into n_c clusters. The lower it is, the more homogeneously the n_c clusters perform in terms of spatial smoothness. Lower values are therefore associated with better partitions.

Other indices can be employed to evaluate each partition from the point of view of data similarity only. Most of these indices evaluate the scattering inside each cluster with respect to the distance between clusters, and they assign relatively better scores to partitions with compact and well-separated clusters. In the present work one index of this kind is employed: the SD index (e.g. *Halkidi et al.*, 2002). SD takes into account the average scattering of the

4.6. Selection of the optimal cluster partition

Table 4.3: Rainfall rate R [mm h⁻¹] associated with the three clusters appearing at positive temperatures. Some relevant quantiles ($Q5\%$, $Q25\%$, $Q50\%$, $Q75\%$, $Q95\%$) of the full distribution are given here. The data used to build this table were collected during the HyMeX campaign.

Cluster	Interpretation	Q5 %	Q25 %	Q50 %	Q75 %	Q95 %
Green	Light rain (LR)	0.015	0.05	0.15	0.3	2.8
Dark blue	Rain (RN)	0.42	2.11	4.1	7.6	16.3
Red	Heavy rain (HR)	17.2	25.4	31.3	41.3	68.5

clusters (Scat) and the total separation between clusters (Dist). For a partition of the data set into n_c clusters, Scat is defined as

$$\text{Scat}(n_c) = \frac{1}{n_c} \sum_{L=1}^{n_c} \frac{\|\sigma(C_L)\|_2}{\|\sigma_{\text{Data}}\|_2}, \quad (4.17)$$

where the vector $\sigma(C_L)$ is the total variance of the L th cluster C_L , the vector σ_{Data} is the total variance of the data set, and the $\|\bullet\|_2$ operator is the 2-norm, defined in Table 4.1. Note that, in a d -dimensional space, these quantities are vectors and not scalar. The separation between clusters (Dist) is defined as

$$\text{Dist}(n_c) = \frac{D_{\min}}{D_{\max}} \sum_{L=1}^{n_c} \left(\sum_{M=1 \neq L}^{n_c} \|\bar{\mathbf{x}}_{C_M} - \bar{\mathbf{x}}_{C_L}\|_2 \right)^{-1}, \quad (4.18)$$

where $\bar{\mathbf{x}}_{C_M}$ and $\bar{\mathbf{x}}_{C_L}$ are the centres of mass of the M th and L th clusters, respectively (see Eq. 4.5). D_{\min} (D_{\max}) is the minimum (maximum) distance between all the couples of mass centres. Finally, the SD index is defined as

$$\text{SD}(n_c) = a \text{Scat}(n_c) + \text{Dist}(n_c), \quad (4.19)$$

where a is a normalization factor, equal to $\text{Dist}(n_{\max})$, that forces Scat and Dist to be of the same order of magnitude. SD takes lower values for compact (low Scat) and well-separated (low Dist) partitions; therefore, the optimal number of clusters n_{opt} in a database should exhibit a minimum SD.

4.6.2 Selection of n_{opt} : Fig. 4.2b

Figure 4.3 illustrates the behaviour of the quality indices defined in Sect. 4.6.1 as a function of the number of clusters in the data set for the interval $1 \leq n_c \leq 30$. The curves shown in the figure are obtained as an average of 100 runs of the clustering algorithm.

An optimal solution is selected here when $n_c = n_{\text{opt}} = 7$ clusters. In fact, it can be observed that $n_c = 7$ corresponds to a local minimum for both the SD index and the AS index. When $n_c = 7$ the spatial behaviour of the seven clusters is the most homogeneous (low AS) and the trade-off between compactness and separability of the clusters is optimal (lowest SD).

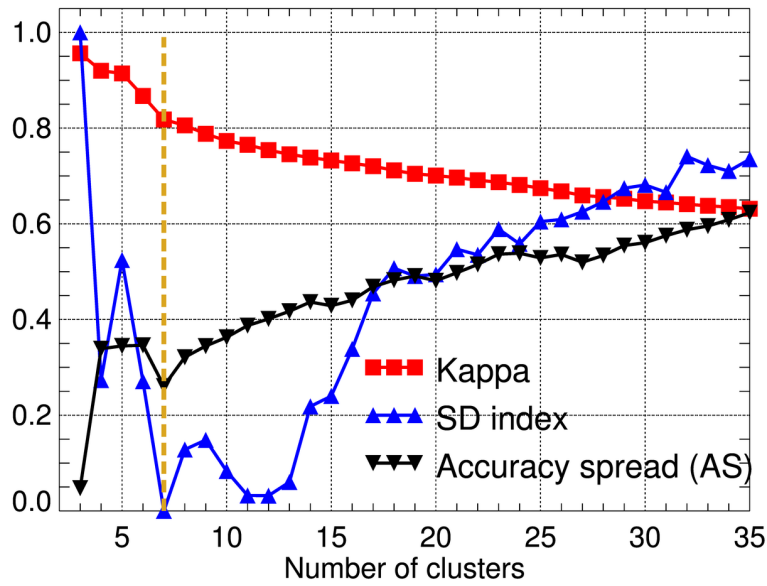


Figure 4.3: Evolution of kappa, accuracy spread (AS) index, and SD index as a function of the number of clusters in the data set. The SD index is stretched between 0 and 1 for illustration purposes. The yellow vertical line at $n_c = 7$ shows the selected final number of clusters, corresponding to a minimum AS and SD. Each curve shows the mean behaviour over 100 runs of the clustering algorithm.

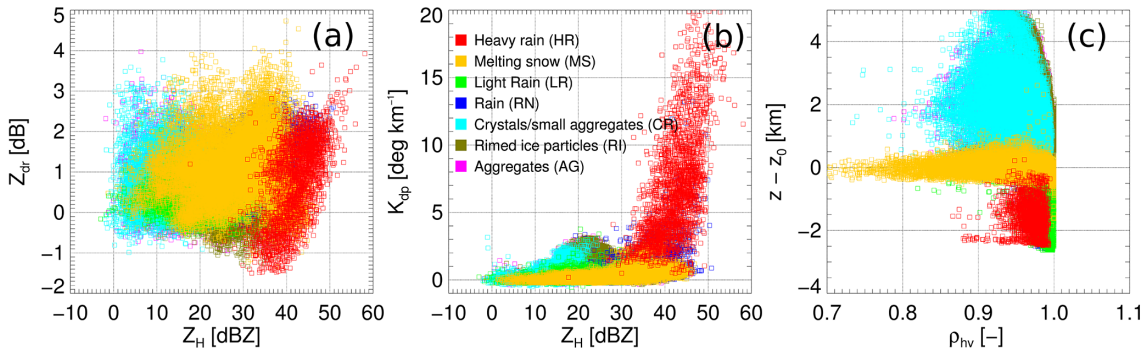


Figure 4.4: Three examples of two-dimensional projection of the seven clusters found in the data set. The clusters include observations collected in Davos (CH) and Ardèche (FR). (a): Z_{DR} vs. ρ_{hv} ; (b): Z_H vs. K_{dp} ; (c): Δz vs. ρ_{hv} . Note that some of the clusters are not fully visible in this two-dimensional projection because they are defined in a five-dimensional space.

4.7 From unlabelled clusters to hydrometeor classes: Fig. 4.2c

This section is devoted to the interpretation of the output of the clustering algorithm (Fig. 4.2c) that is still unknown at this step of the method.

4.7.1 Global characteristics of the clusters

The seven clusters corresponding to the optimal partition of our database contain a set of observations (or objects) that have been grouped according to spatial smoothness and data similarity. These clusters exist in the five-dimensional space given by the dimensions of \mathbf{x}^* , and

it is therefore not trivial to illustrate their content. A way to reproduce a partial visualization of the clusters is to display pairs of two-dimensional projections of the objects \mathbf{x} while keeping in mind that their original nature is five-dimensional. Some of these projections are displayed in Fig. 4.4, in which the seven clusters are colour-coded and labelled with a hydrometeor type. Additionally, Table C.1 in the Appendix C (numerically) and Figs. 4.5 and 4.6 (graphically) provide the one-dimensional distribution of polarimetric variables within each cluster. By looking at Fig. 4.4c, it can be observed that three clusters contain data collected only where the relative altitude with respect to the local 0°C , i.e. Δz , is positive (negative temperatures), three clusters contain data collected always where Δz is negative (positive temperatures) and one cluster contains mostly data collected where $\Delta z \approx 0$. In the following sections, we will proceed by interpreting the clustering results separately for clusters appearing on average at $\Delta z \leq 0$ and $\Delta z > 0$, and we will assign a hydrometeor class to each of the seven clusters.

4.7.2 Clusters at positive temperatures

Three clusters (red, green, and dark blue) in Fig. 4.4 are identified at positive temperatures. It is therefore assumed in a first approximation that they are related to liquid-phase precipitation. In order to properly associate each of them to a more specific category, further analysis is performed. At first, the data classified into one of these three categories are extracted from the observations collected in Ardèche (HyMex campaign, Sect. 4.4) from PPIs taken at elevation angles ranging between 3.5 and 10° . Then, the rainfall rate R [mm h^{-1}] associated with each measurement is computed by means of the following relations (*Otto and Russchenberg, 2012*):

$$R = \begin{cases} 13K_{\text{dp}}^{0.75} & \text{if } Z_H > 30 \text{ dBZ} \\ \left(\frac{Z_h}{243}\right)^{1/1.24} & \text{if } Z_H \leq 30 \text{ dBZ}, \end{cases} \quad (4.20)$$

where $Z_h = 10^{0.1Z_H}$ [$\text{mm}^6 \text{m}^{-3}$] (i.e. the horizontal reflectivity expressed in linear units). The distribution of R stratified for each class is summarized in Table 4.3. The green cluster is characterized by extremely low rainfall intensity, and therefore it is associated hereafter with a hydrometeor class named light rain (LR). This cluster contains mainly precipitation characterized by small spherical drops. It is worth noting (Fig. 4.5b and c) that LR contains Z_{DR} values lower than 1 dB, with a mode around 0.25 dB, and K_{dp} values always close to 0°km^{-1} . LR therefore contains drizzle and the lightest rainfall intensities. The dark blue cluster is characterized by low to intermediate rainfall intensity, and therefore it is associated with a category named rain (RN). Finally, the red cluster contains by far the highest rainfall intensities, and it is hereafter called heavy rain (HR). It is also hypothesized that, when hail occurs, it is classified as HR. This assumption is based on the fact that HR includes observations with a low-correlation coefficient ρ_{hv} (Fig. 4.5d) as well as near-zero or negative Z_{DR} (Fig. 4.5b). These signatures have been documented in cases where hail was measured by polarimetric weather radars (*Al-Sakka et al., 2013*).

Chapter 4. A clustering approach to polarimetric hydrometeor classification

Table 4.4: Confusion matrix comparing the classification of liquid phase hydrometeor classes ($\Delta z < 0$) obtained with the clustering method described in the Chapter and the output of the fuzzy-logic method DR2009, described in Appendix C.2. The classes of the novel method are light rain (LR), rain (RN), and heavy rain (HR). The elements $M_{i,j}$ of the matrix contain the percentage of liquid phase observations classified in the i th class of the first method and simultaneously in the j th class of the second method. The data are obtained from 100 runs of the clustering algorithm.

		Novel method		
DR2009		LR	RN	HR
		Drizzle	59 %	1 %
	Rain	7 %	29 %	6 %

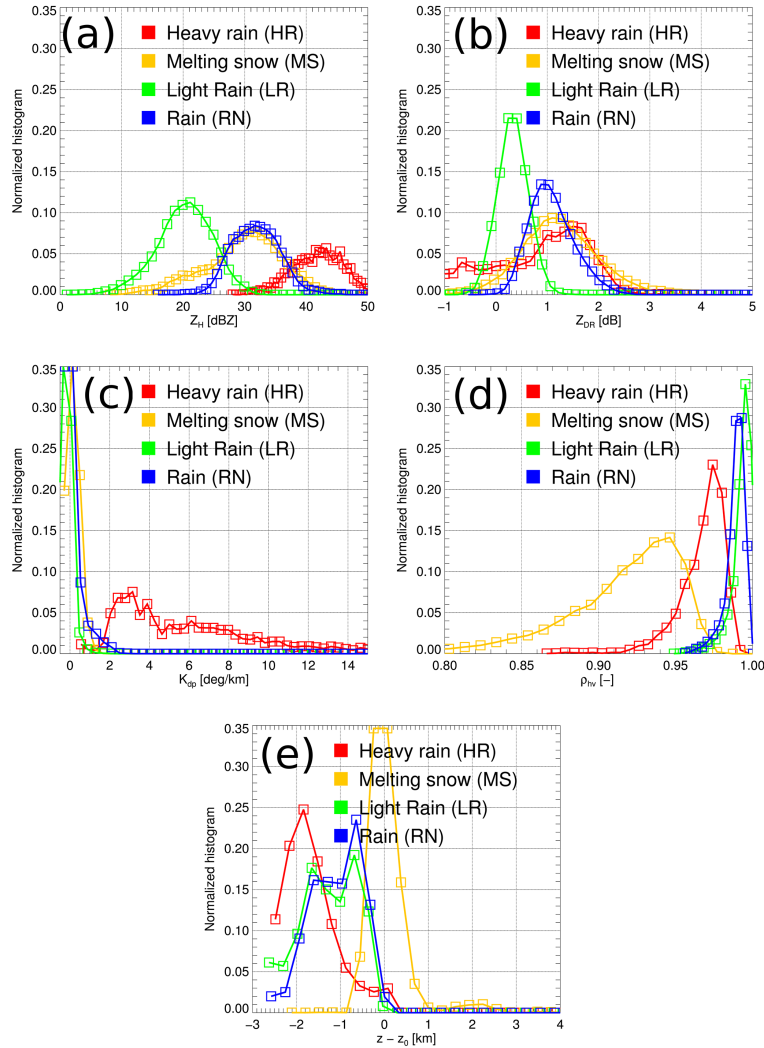


Figure 4.5: Distribution within the four clusters found at positive temperatures ($\Delta z \leq 0$) of (a) Z_H [dBZ], (b) Z_{DR} [dB], (c) K_{dp} [$^{\circ} \text{km}^{-1}$], (d) ρ_{hv} [-], and (e) Δz [km]. The curves are obtained considering the content of 100 runs of the clustering algorithm.

As an additional test, the classification output of our method is compared with a fuzzy-logic classification scheme based on the parametrization of *Dolan and Rutledge (2009)*, hereafter

4.7. From unlabelled clusters to hydrometeor classes: Fig. 4.2c

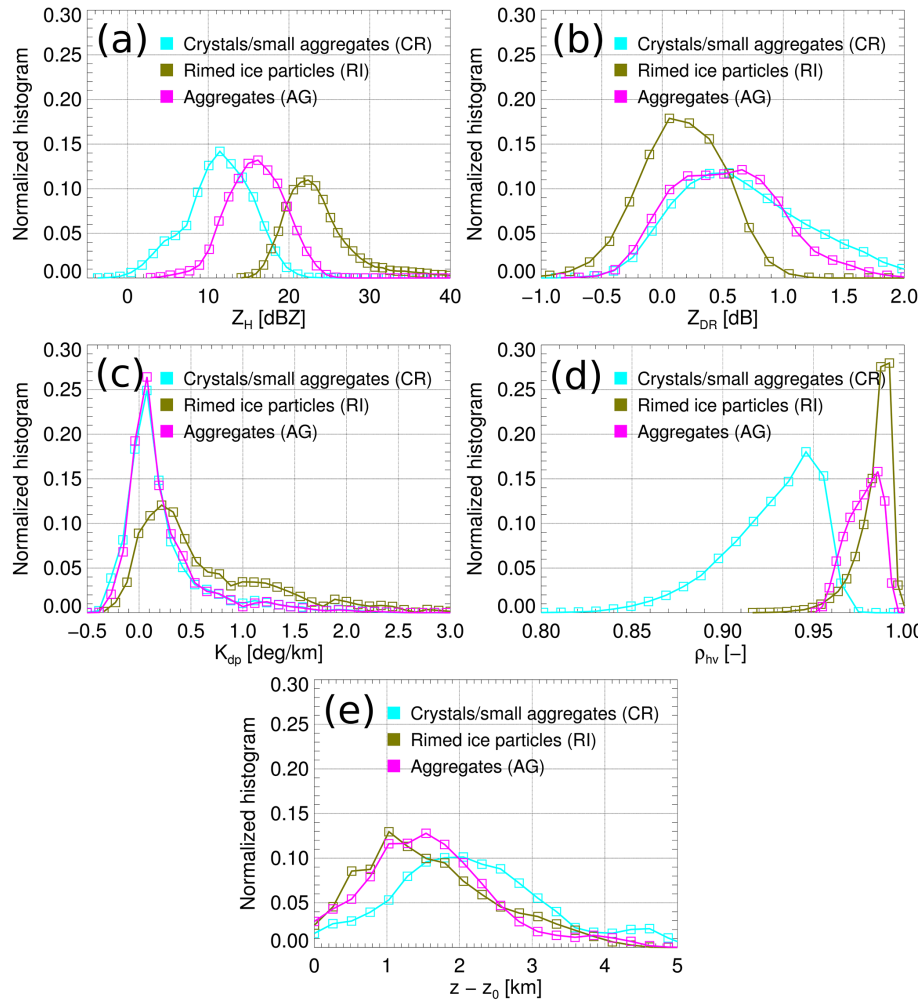


Figure 4.6: Distribution within the three clusters found at negative temperatures ($\Delta z > 0$) of (a) Z_H [dBZ], (b) Z_{DR} [dB], (c) K_{dp} [$^{\circ}$ km $^{-1}$], (d) ρ_{hv} [-], and (e) Δz [km]. The curves are obtained considering the content of 100 runs of the clustering algorithm.

DR2009 (see Appendix C for the details). DR2009 does not provide three “liquid-phase” hydrometeor classes but only rain and drizzle. The contingency table of Table 4.4 shows that the HR class of our method is entirely classified as rain by DR2009. The RN class is mainly classified as rain, and LR is almost entirely associated with drizzle. It is concluded that results from the proposed method agree well with DR2009 for liquid phase hydrometeor classes.

Figure 4.7 illustrates a case where LR, RN, and HR are classified on the same PPI radar image. This case was collected on 24 September 2012 during the HyMeX campaign, when a high-intensity convective front was approaching the radar location from the west side of the domain (more details about the storm in *Bousquet et al., 2014*). This resulted in a layer of high values of Z_H , Z_{DR} , and K_{dp} . The transition from LR to HR within few kilometres appears qualitatively to be a satisfactory illustration of the incoming front. Figure 4.7 also shows a map of classification accuracy: this parameter is defined for each observation (valid range gate) as the difference between the distance of the observation with respect to the two closest

Chapter 4. A clustering approach to polarimetric hydrometeor classification

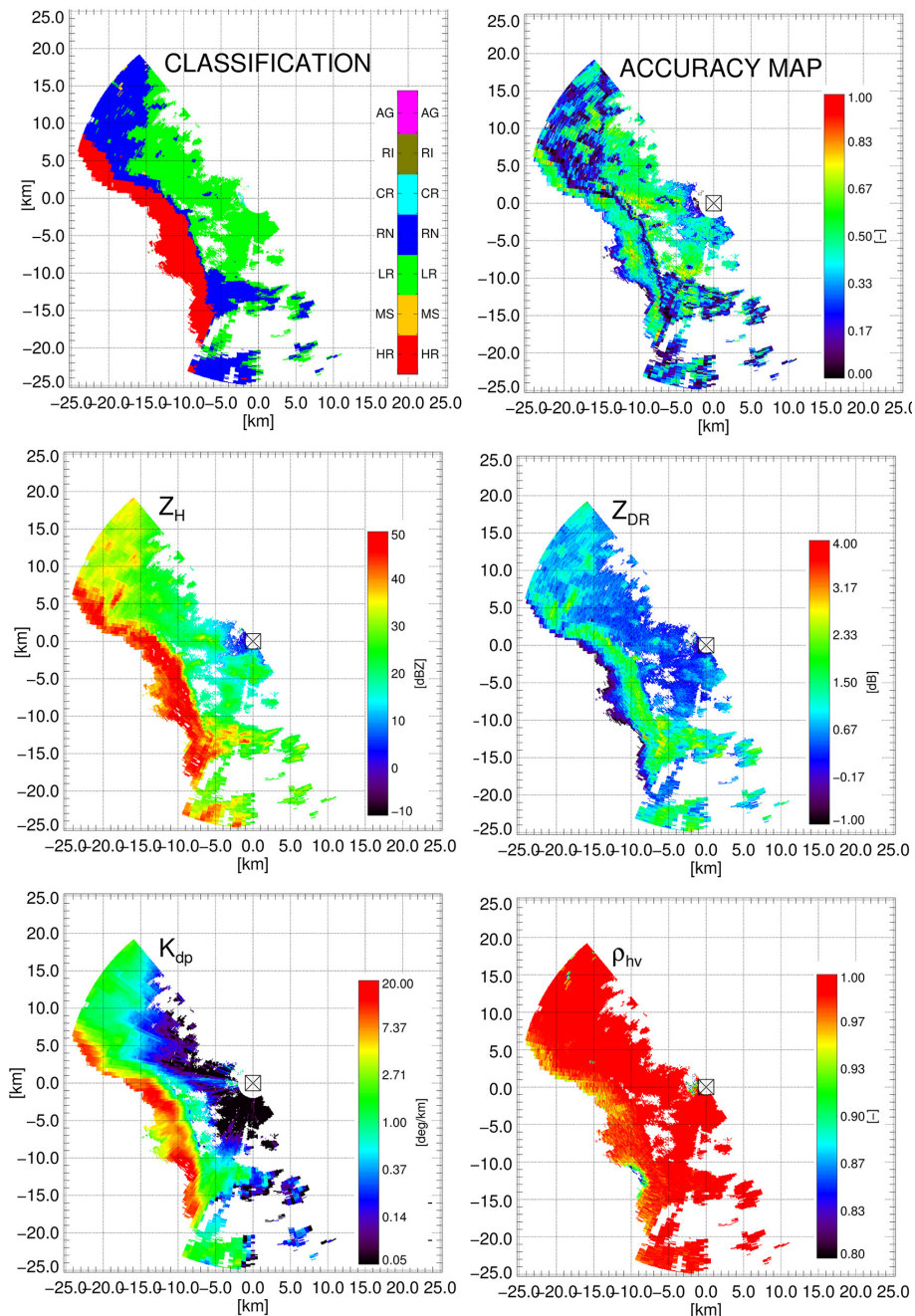


Figure 4.7: Hydrometeor classification and polarimetric observation from a PPI sector scan collected on the 24 September during HyMeX Special Observation Period (SOP) 2012 at 02:12 UTC with an elevation angle of 3.5° . The different panels show the following variables: hydrometeor classification with the clustering approach, classification accuracy, Z_H [dBZ], Z_{DR} [dB], K_{dp} [$^\circ \text{ km}^{-1}$], and ρ_{hv} [-]. The spatial coordinates x and y originate at the radar location.

clusters, and it is normalized by the smaller distance. The classification accuracy is therefore lower in the areas of transition between different hydrometeor types, where the polarimetric signatures change as the dominant hydrometeor type changes.

4.7. From unlabelled clusters to hydrometeor classes: Fig. 4.2c

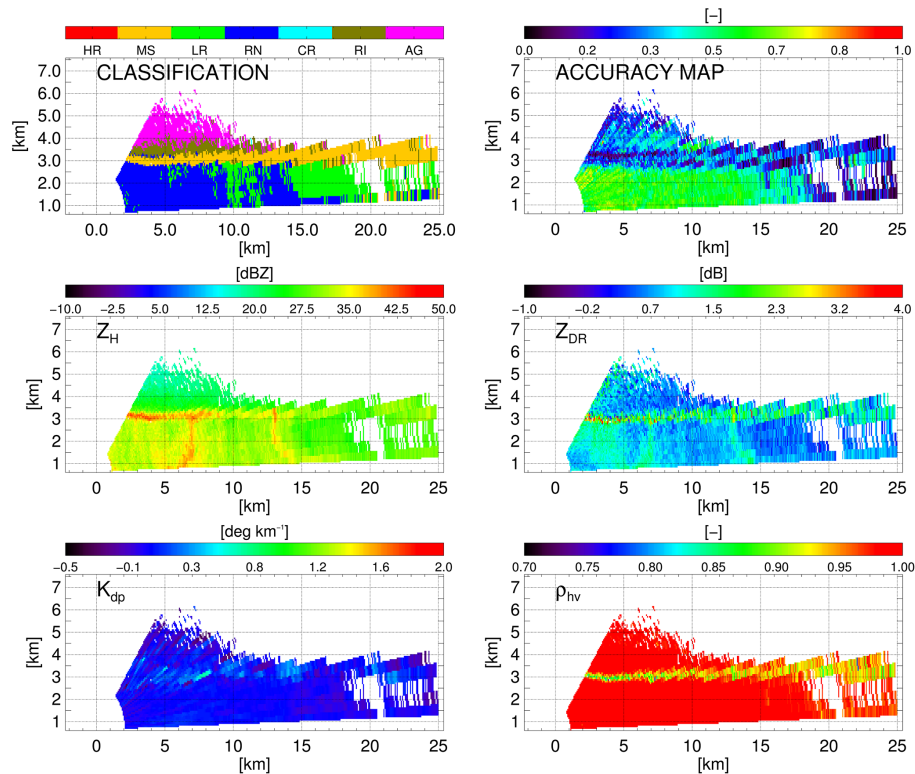


Figure 4.8: Hydrometeor classification and polarimetric observation from an RHI collected on 29 September during HyMeX SOP 2012 at 14:29 UTC. The different panels show the following variables: hydrometeor classification with the clustering approach, classification accuracy, Z_H [dBZ], Z_{DR} [dB], K_{dp} [$^{\circ} \text{km}^{-1}$], and ρ_{hv} [-]. The altitude of the radar is 605 m.

4.7.3 Cluster around 0 °C

The yellow cluster of Figs. 4.4 and 4.5 appears on average around the 0 °C isotherm, and it is interpreted as melting snow (MS). Figure 4.8 shows an example of classification output, where a melting layer is clearly visible in the polarimetric observations. The MS category can be seen to delimit the transition between ice-phase and liquid-phase hydrometeors. The signatures of this transition can also be seen in Z_H , Z_{DR} , and ρ_{hv} . K_{dp} does not exhibit any obvious signature in the regions classified as MS (in agreement with observations documented by *Thompson et al., 2014*).

4.7.4 Clusters at negative temperatures

The clusters identified at negative temperatures (dark green, pink, and cyan clusters in Fig. 4.4) should be attributed to ice-phase hydrometeors. To classify these clusters, one proceeds as follows: first the behaviour of the polarimetric variables within these three clusters is examined, then the classification is compared with the output of DR2009. Subsequently we compare the classification with qualitative (hydrometeor classification) and quantitative (snowfall intensity) observations provided by a two-dimensional video disdrometer (2DVD) and with the output of a numerical weather prediction model (Consortium for Small-scale

Modeling, COSMO).

Polarimetric signatures

Figure 4.6 presents the distribution of the polarimetric variables Z_H , Z_{DR} , K_{dp} , and ρ_{hv} , as well as the relative altitude Δz for the three “ice-phase” clusters.

By looking at panel (a), it can be observed a clear Z_H signature. Z_H is the lowest in the cyan cluster (mode ≈ 12 dBZ), it is slightly higher in the pink cluster (mode ≈ 15 dBZ), and it is the highest in the dark-green cluster (mode > 20 dBZ). Higher Z_H indicates higher hydrometeor concentration, size, and/or ice density.

Z_{DR} , shown in panel (b), exhibits a different pattern. The cyan cluster and the pink cluster show some variability in Z_{DR} . Z_{DR} ranges from -0.3 to 2.5 dB (mode 0.8 dB) in the cyan cluster and from -0.3 to 1.6 dB (mode 0.5 dB) in the pink cluster. This behaviour is interpreted as the signature of particle shape and orientation variability in the cyan and pink clusters, with the pink cluster containing on average hydrometeors that are more geometrically isotropic. The dark-green cluster behaves differently: Z_{DR} has a clear mode around 0.3 dB, the distribution of Z_{DR} values is narrow (ranging between -0.6 and 1 dB), and it includes many negative values, i.e. prolate particles.

ρ_{hv} has a clear signature for the cyan cluster only, characterized by low values that often depart from 1. We interpret this behaviour as an additional effect of the variability of particle shapes within the radar resolution volume.

K_{dp} , shown in panel (c), is lower than 1° km^{-1} for the pink cluster and the cyan cluster. The dark-green cluster exhibits instead relatively large values up to $2.5^\circ \text{ km}^{-1}$. K_{dp} depends on size, concentration, shape, and density of the particles in the radar resolution volume and therefore the dark green cluster contains, on average, more oblate hydrometeors and/or oblate hydrometeors of a larger size and density.

Finally, by looking at panel (e), we observe that the dark-green cluster is found over a broad range of altitudes (temperatures) and that the cyan cluster generally appears at lower temperatures than the other two.

From this analysis, it is shown that the three clusters exhibit distinct polarimetric signatures, which led to hypothesize the following associations. The cyan cluster corresponds to individual crystals and small aggregates (denoted CR): it appears in the coldest areas of precipitation, it shows significant variability of shapes, and low-intensity Z_H returns due to the low concentration and small size of the hydrometeors. The pink cluster corresponds to aggregates (AG). Aggregates generate larger Z_H returns due to their larger sizes, and they tumble as they fall, thus lowering Z_{DR} . The dark green cluster corresponds to heavily rimed-ice particles (RI). The larger density of rimed particles lead to significant Z_H signatures, and the dielectric properties of dense ice (very different with respect to dry crystals and aggregates; *Vivekanandan et al.*,

4.7. From unlabelled clusters to hydrometeor classes: Fig. 4.2c

Table 4.5: As in Table 4.4 but comparing the classification of ice phase hydrometeor classes ($\Delta z > 0$). The classes of the novel method are crystal (CR), aggregates (AG), and rimed-ice particles (RI). The elements $M_{i,j}$ of the matrix contain the percentage of ice phase observations classified in the i th class of the first method and simultaneously in the j th class of the second method. The data are obtained from 100 runs of the clustering algorithm.

		Novel method		
		CR	AG	RI
DR2009	Crystals	6 %	2 %	0 %
	Aggregates	17 %	24 %	6 %
	High-dens. graupel	5 %	7 %	5 %
	Low-dens. graupel	0 %	1 %	15 %
	Vertical Ice	6 %	5 %	1 %

1994) lead to a response also in K_{dp} . Z_{DR} is low because riming tends to smooth particle shapes, and it shows negative values when conically shaped rimed particles are formed (Evaristo *et al.*, 2013). These hypotheses are discussed in the next sections.

Comparison with DR2009

In Sect. 4.7.2 the liquid-phase clusters of the novel method were compared with the output of DR2009. We now perform a similar evaluation, focussing on the ice-phase clusters. As a reminder, our method provides three ice-phase classes: crystal and small aggregates (CR), aggregates (AG), and rimed-ice particles (RI). DR2009 instead provides five ice-phase classes: crystals (CR), aggregates (AG), high-density graupel (HDG), low-density graupel (LDG), and vertically aligned ice (VI, which denotes oblate ice crystals aligned vertically because of an electric field). The contingency table between these categories is shown in Table 4.5. The methods are in overall good agreement. The CR class is associated mostly with the DR2009 classes of aggregates, crystals, and vertical ice. AG is associated with aggregates, and RI is associated with the two graupel categories of DR2009. The only notable discrepancy between the methods happens for the high-density graupel category of DR2009: this class is evenly distributed among CR, AG, and RI, indicating that there is not a clear match for this hydrometeor type.

Comparison with 2DVD classification output

An additional comparison is conducted with the output of the HC scheme developed for two-dimensional video disdrometers. This method, hereafter called HC2DVD is described in detail in *Grazioli et al.* (2014b) and in Chapter 3 of this thesis. As a reminder, HC2DVD takes as input a set of two-dimensional particles images, collected by a 2DVD, and it provides as output an estimate of the dominant hydrometeor type within time intervals of 60 s. The method does not classify individual particles but populations of hydrometeors. HC2DVD discriminates between eight hydrometeor classes: small particle-like (SP), dendrite-like (D), column-like (C), graupel-like (G), rimed-particle-like (RIM), aggregate-like (AG), melting-snow-like (MS),

Chapter 4. A clustering approach to polarimetric hydrometeor classification

Table 4.6: Confusion matrix comparing the classification of ice phase hydrometeor classes during the measurement campaign of Davos as estimated from the clustering method and from the 2DVD (HC2DVD; *Grazioli et al. (2014b)*), taken as ground reference. The comparison is conducted on three hydrometeor classes: crystal (CR), aggregates (AG), and rimed-ice particles (RI). In this case, the matrix is 3×3 , with similar classes in rows and columns, and it can be used to evaluate quantitatively the agreement among methods. The overall accuracy of the comparison is 49 %, and Cohen's kappa is 0.23.

		Novel method		
		CR	AG	RI
HC2DVD	HC2DVD-CR	27.9 %	13.9 %	0.5 %
	HC2DVD-AG	4.5 %	18.2 %	1.0 %
	HC2DVD-RI	15.7 %	16.5 %	1.8 %

and rain (R).

Here HC2DVD is compared with the output of the clustering algorithm for snowfall events collected during the campaign of Davos 2009–2011 (Sect. 4.4). The PPI of the lowest elevation not contaminated by clutter was taken at 9° elevation with a repetition interval of 5 min. This PPI is used for a comparison with HC2DVD. Before discussing the comparison, it must be kept in mind that (i) the closest radar resolution volume centre was about 400 m above the 2DVD and crystal habits can change over this altitude range, and (ii) the sampling times and volumes of the two instruments are different, even though the sampling times overlap. The comparison is conducted on a subset of about 30 manually selected snowfall events. Any precipitation event with a visible melting layer or positive temperatures at the radar location as well as any event characterized by evident spatial and temporal variabilities on the small scale were excluded. Radar resolution volumes within 150 m in horizontal distance from the 2DVD location are compared with the HC2DVD output. A buffer of +2 min is applied in order to match multiple 2DVD observations with a single radar scan. In order to simplify the comparison, some of the categories from HC2DVD are aggregated as follows. Small particles (SP), dendrites (D), and columns (C) are merged together into a single class called “crystals” (HC2DVD-CR). Aggregates (AG) are kept in a single class, named HC2DVD-AG. Finally, graupel (G) and rimed particles (RIM) are merged into a “rimed-ice” class (HC2DVD-RI).

Table 4.6 presents the confusion matrix of the comparison between the novel clustering algorithm and HC2DVD. The agreement between CR and HC2DVD-CR is very good, as is the agreement between AG and HC2DVD-AG. Rimed-ice particles, in contrast, exhibit a good accuracy of detection (when they are detected, their presence is confirmed by HC2DVD), but they are subject to a large number of missed detections. If HC2DVD is taken as ground truth, the overall accuracy of the comparison is 49 % and Cohen's kappa is 0.23.

Similarly, HC2DVD is now compared with the classes of DR2009. Crystals (CR) and vertical ice (VI) are merged in a single class called “crystals” (DR2009-CR), aggregates (AG) are kept in a single class (DR2009-AG), and low-density graupel (LDG) and high-density graupel (HDG) are merged into a “rimed-ice class” (DR2009-RI). Table 4.7 shows the confusion matrix of

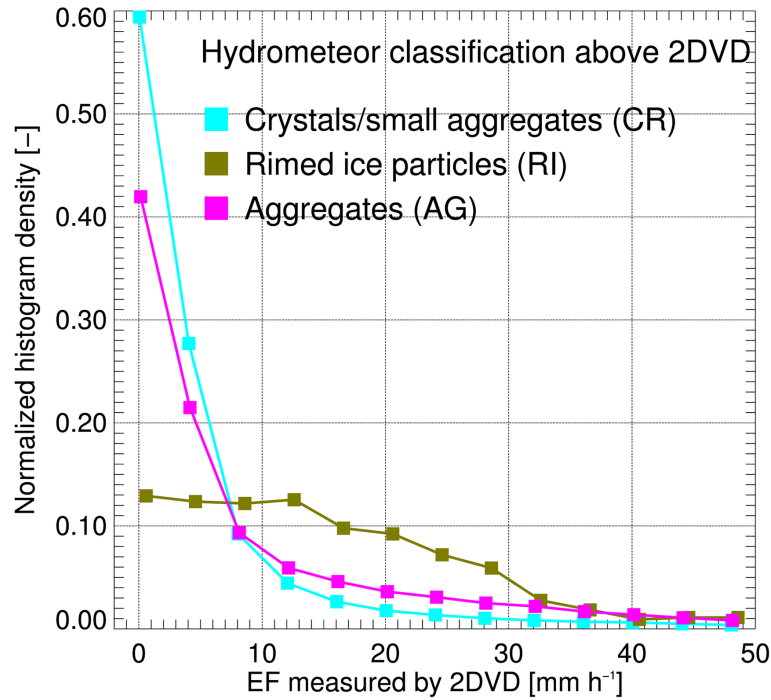


Figure 4.9: Sampled probability density function of snowfall intensity, as quantified by the equivalent flux EF [mm h⁻¹], measured by the 2DVD and associated with the radar hydrometeor classification output above the location of the 2DVD. The data used in this figure were collected during the field deployment of Davos (CH).

the comparison between DR2009 and HC2DVD. In this case, the overall accuracy is 38 % and Cohen's kappa is 0.08. One may conclude that, with HC2DVD as a reference, the newly proposed approach outperforms DR2009. A complete evaluation of the uncertainties related to such comparisons is beyond the scope of the thesis, and it is suggested that the reader consider these results as largely qualitative.

Comparison with 2DVD in terms of snowfall intensity

Additionally to the qualitative information provided by HC2DVD, the 2DVD observations can be used in a quantitative way to investigate the relation between the content of the three clusters and the intensity of snowfall. Here the snowfall intensity is quantified by means of an equivalent flux (EF), defined as

$$EF = \frac{\pi \sum_{i=1}^{N(\Delta t)} De_i^3}{6\Delta t A}, \quad (4.21)$$

where Δt is the temporal resolution at which EF is calculated (1/60 h here), A is the measurement area of the instrument [mm²], $N(\Delta t)$ is the number of particles recorded in Δt , and De_i the equivalent diameter of each snowflake or particle [mm], as defined in *Huang et al.* (2010). Given the assumptions in the estimation of De , EF can be erroneous in absolute terms,

Chapter 4. A clustering approach to polarimetric hydrometeor classification

Table 4.7: As in Table 4.6 but showing the comparison between HC2DVD and DR2009. The comparison is conducted on three hydrometeor classes: crystal (CR), aggregates (AG), and rimed-ice particles (RI). The overall accuracy of the comparison is 38 %, and Cohen's kappa is 0.08.

		DR2009		
		DR2009-CR	DR2009-AG	DR2009-RI
HC2DVD	HC2DVD-CR	20.6 %	21 %	3.6 %
	HC2DVD-AG	5.7 %	16.5 %	3.6 %
	HC2DVD-RI	9.1 %	18.6 %	1.3 %

and therefore it is used here to compare the content of the three clusters in relative terms only. Figure 4.9 shows the distribution of EF as measured by the 2DVD and related to the occurrence of CR, AG, and RI. It can be seen that the snowfall intensity differs among these three. CR exhibits the lowest intensities, AG intermediate ones, and RI the highest intensities. This is the expected behaviour of rimed particles. As riming progresses, the original shape of ice particles becomes imperceptible, the drag decreases, and the particles become more dense (*Pruppacher and Klett, 1997*). Hence, their fall behaviour is smoother and therefore faster, leading to larger EF. The results presented in this section are not a rigorous validation, but they are in agreement with our initial assumptions.

CR, AG, RI: classification example

Figure 4.10 presents an example of ice-phase precipitation, recorded on 26 March 2010 in Davos. This event was associated with the passage of a cold front over Europe that led to a significant temperature drop (more than 10 °C in a few hours in Davos).

The temperature at the location of MXPoI was about -5°C at the time when the data of Fig. 4.10 were collected. By looking at the figure, a stratification of the precipitation into three layers can be observed. At higher altitudes ($y > 5$ km), there is a thin layer classified mostly as crystals (CR). The crystals turn into aggregates (AG) that dominate the precipitation in a second layer ($4 \leq y \leq 5$ km), and, finally ($y \leq 4$ km), RI dominates the precipitation. RI is characterized by larger values of K_{dp} (up to 2°km^{-1}) and Z_H (up to 28 dBZ). CR is instead characterized by low values of Z_H and ρ_{hv} (as low as 0.9) and very low values of K_{dp} , between -0.1 and $0.1^{\circ}\text{km}^{-1}$. In this example, AG exhibits polarimetric signatures that are somewhat intermediate between CR and RI.

For illustrative purpose, the situation corresponding to Fig. 4.10 was simulated using the numerical weather model COSMO (see <http://www.cosmo-model.org>), operationally used by MeteoSwiss. The model was run at 2 km resolution with forcing from MeteoSwiss reanalysis. As shown in Fig. 4.11, COSMO predicts the presence of supercooled liquid water (QC) at altitudes between 2.5 and 3 km. Additionally, at altitudes between 2 and 6 km, large quantities of graupel (QG) mixed with snow (QS) are observed. Both the presence of supercooled liquid water in the clouds and the explicit presence of graupel are in agreement with the layer of

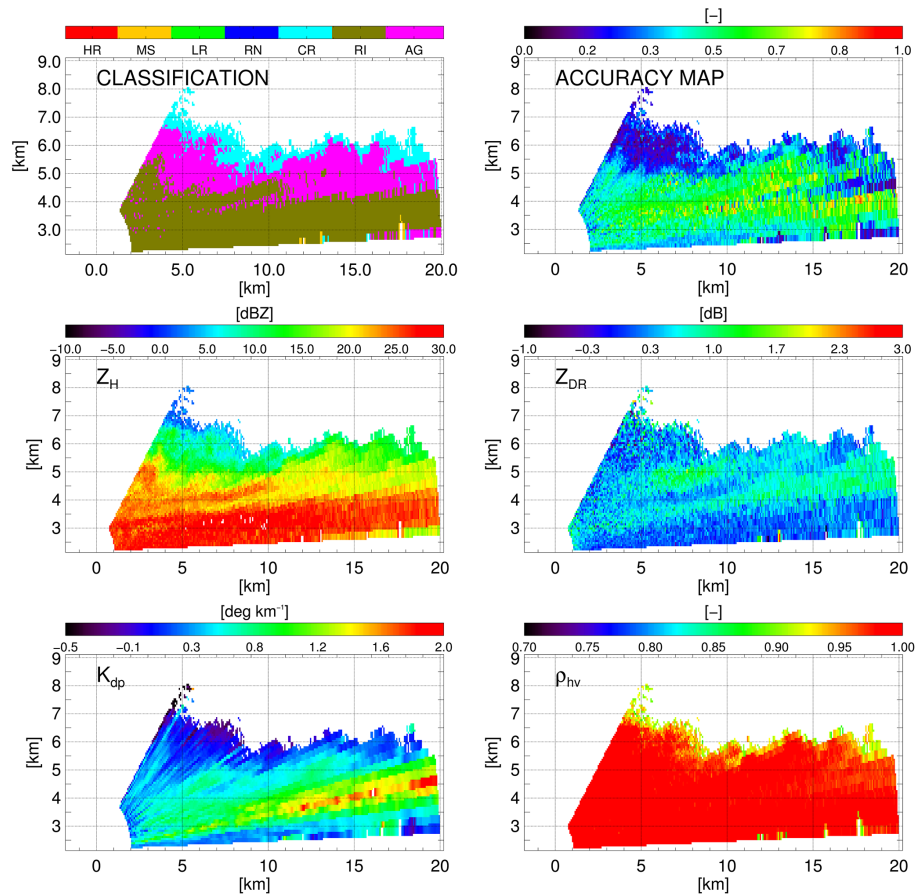


Figure 4.10: As in Fig. 4.8 but for the snowfall event of the 26 March 2010, at 15:31 UTC in Davos (CH). The altitude of the radar is 2133 m.

rimed particles RI identified in Fig. 4.10.

4.8 Summary and conclusions

A novel approach to hydrometeor classification from a polarimetric weather radar was presented in this Chapter. The method was applied to polarimetric data collected by an X-band radar in the Swiss Alps and in the French Prealps. The novel approach was not based on numerical-scattering simulations. The number of hydrometeor classes was not defined a priori, but it was learned from the data, and the content of each hydrometeor class was manually interpreted.

A subset of 20 000 polarimetric observations was randomly extracted from the available data set. A hierarchical clustering algorithm with spatial constraints was applied to the subset in order to merge observations according to both the similarity of polarimetric data and the spatial smoothness of each partition. This means that we made the assumption of smooth spatial transitions between hydrometeor types. Following this strategy, an optimal number of seven clusters was found. Three clusters were found at positive temperatures, and they were

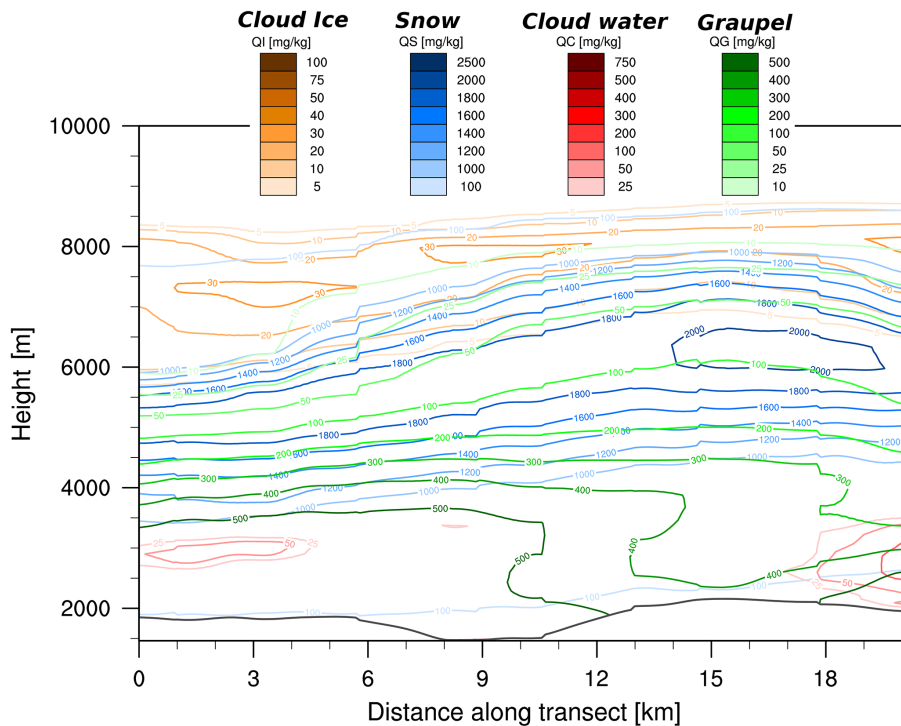


Figure 4.11: Mixing ratios of hydrometeor contents obtained with the COSMO2 numerical weather model along the RHI transect of MXPoI (same as Fig. 4.10) at 15:15 UTC on the 26 March 2010 in Davos (CH). Mixing ratios are given for cloud ice (QI), snow (QS), cloud water (QC), and graupel (QG).

interpreted as light rain (LR), rain (RN), and heavy rain (HR). One cluster appeared systematically around 0 °C, and it was associated with melting snow (MS). Finally, three clusters were found at negative temperatures and their polarimetric signatures were interpreted as being of crystals/small aggregates (CR), aggregates (AG), and rimed-ice particles (RI). The content of the clusters agrees well with the outcome of a fuzzy-logic algorithm, denoted as DR2009 (*Dolan and Rutledge, 2009*). Additionally, the novel approach obtained scores better than DR2009 when compared to a ground-based (video-disdrometer-based) hydrometeor classification scheme, hence suggesting that the new method was better tailored to the observations of the X-band radar employed in this study.

The proposed approach is the first attempt, using unsupervised classification, to move the starting point of a classification algorithm away from scattering simulations conducted over an arbitrarily defined number of hydrometeor classes to the identification of relevant clusters in the data themselves. The initial identification of the clusters is computationally expensive, but this operation is performed only once and the classification of newly collected radar images can be conducted in real time.

Some of the advantages of this approach are that it is immune to possible radar miscalibration and that the data-driven approach ensures that the identified clusters take into account the accuracy of the instrument. Finally, the method is adaptable to other radar systems and can be tuned to include other constraints regarding the spatial smoothness of the partition

or temporal consistency. The main limitations of the method are related to the manual interpretation of the content of the clusters. This may not be trivial, especially in the absence of surface precipitation type reports for comparison. Additionally, the method is as representative as the available database is, and the clusters identified are a priori valid only for the instrument employed to collect the data. The number and type of clusters can be reasonably considered to be very similar for other X-band dual-polarization radars of similar sensitivity.

It is interesting to note that the method exploits a simple hypothesis about the spatial smoothness of the hydrometeor types and that this rule is applied only in the initial steps (when the n_{opt} clusters are identified). Future work will be devoted to also extending the constraints involving spatial smoothness to newly classified images or to including physically justified contiguity rules for specific hydrometeor types. In addition, this clustering approach (or some steps of the approach) could be employed as a support to fuzzy-logic-based classification methods to improve or adapt the membership functions according to the clustering outputs in specific data sets.

5 Riming in winter alpine snowfall during CLACE 2014

This chapter is adapted from the manuscript:

- Grazioli, J., G. Lloyd, L. Panziera, P. Connolly, J. Henneberger, and A. Berne (2015b), Riming in winter alpine snowfall during clace 2014: polarimetric radar and in-situ observations, *Atmos. Chem. Phys.*, in submission

It presents retrievals of snowfall microphysics conducted by means of a polarimetric radar and in-situ instruments, with a special focus on riming. The relation between riming and snowfall accumulation is investigated as well.

5.1 Summary

This Chapter presents observations and analyses of winter alpine snowfall occurring in mixed-phase clouds in a central Alpine valley during January and February 2014. The observations include high resolution polarimetric radar measurements and in-situ measurements of the ice-phase and liquid-phase components of clouds and precipitation. Radar-based hydrometeor classification suggests that riming is a dominant factor leading to efficient snow accumulation. The time steps during which rimed precipitation is dominant are analysed in terms of temporal evolution and vertical structure. In most cases, riming is the result of a turbulent phase during which supercooled liquid water (SLW) is available. In a second phase turbulence and SLW are dissipated, when and where precipitation shows the peak intensity. When instead a turbulent layer is stable in time and provides continuous availability of SLW, riming can be sustained for many hours without SLW depletion, thus generating large accumulations of snow. The microphysical interpretation as well as the synoptic situation associated with one event with those characteristics are detailed in the Chapter. The vertical structure of polarimetric radar observations during intense rimed precipitation shows a peculiar maximum of specific differential phase shift K_{dp} , interpreted (thanks to in-situ measurements) as secondary ice production and/or heavy riming of anisotropic crystals. Below this K_{dp} peak usually an enhancement of Z_H , somehow proportional to the K_{dp} enhancement and interpreted as aggregation of ice crystals.

5.2 Introduction

Precipitation of ice-phase hydrometeors is the result of the interactions between cloud ice crystals, supercooled liquid water (SLW) droplets and water vapour. After nucleation, the processes of vapour deposition, aggregation, and riming contribute to the growth of the crystals up to the point where they begin to fall and further interact with the lower layers of the atmosphere (e.g., *Pruppacher and Klett, 1997; Cantrell and Heymsfield, 2005; Straka and Mansell, 2005*). The characteristics of the ice-phase hydrometeors at the ground level eventually depend on the full falling history and on all the microphysical interactions happening “from the cloud to the ground”.

The shape, density, and growth rate of individual crystals is mostly a function of temperature and relative humidity of the environment in which they form (*Magono and Lee, 1966; Chen and Lamb, 1994; Fukuta and Takahashi, 1999; Bailey and Hallett, 2009; Takahashi, 2014*). Individual crystals can branch together (aggregation) and/or collect supercooled liquid water droplets that freeze upon impact on the surface of the crystals (riming) that are in this way accreted. In contrast to aggregation, riming leads a net increase of the mass of precipitation. This happens because the rimed crystals or snowflakes have much larger fall velocities than individual water droplets in supercooled liquid water clouds, that would otherwise not be able to reach the ground at a significant rate. Aggregation indirectly contributes to the mass transfer by generating larger and faster targets for riming (*Houze and Medina, 2005, hereafter*

HM2005).

Riming is more efficient on large crystals (*Ono, 1969*), even though it was recently shown that the process can also occur on very small crystals, with characteristic dimensions as small as $60\ \mu\text{m}$ (*Avila et al., 2009*). Turbulence and vertical air motion (updraft) contribute significantly to riming. Turbulence influences the motion of ice crystal leading to a larger droplet collection volumes and therefore to large collection efficiencies (*Pinsky and Khain, 1998*). Updraft, in turns, is necessary to sustain the production of SLW (*Rauber and Tokay, 1991*).

The impact of riming on the bulk properties of snowfall is critical. Measurements of freshly fallen snow, both in the Sierra Nevada (US) and in the proximity of Sapporo (Japan), showed that 30% to 60% of the total mass of snowfall is constituted by rimed accretion (*Harimaya and Sato, 1989; Mitchell et al., 1990*). Additionally, the accumulation of rimed snowflakes on the ground is more prone to generate instabilities and to initiate avalanches (*Abe, 2004*). A last aspect to consider is that, during precipitation, riming can be associated with ice splintering and thus to (secondary) ice generation. The most known example of secondary ice production is the Hallett-Mossop ice multiplication mechanism (*Hallett and Mossop, 1974*) occurring at temperatures higher than -8°C on heavily rimed hydrometeors. However, other mechanisms exist to explain secondary ice generation at colder temperatures. One example is constituted by ice-to-ice and ice-to-water collisional mechanisms (*Vardiman, 1978; Yano and Phillips, 2011*), that are in any case favoured by the degree of riming of the colliding crystals. Non-collisional mechanisms, for instance the fragmentation of freezing supercooled droplets in mixed-phase clouds have been hypothesized as well (*Rangno, 2008*).

Dual-polarization (polarimetric) Doppler weather radars operating at microwave frequencies are becoming state-of-the-art instruments to document the microphysics of ice-phase precipitation. These systems are able to provide indirect information about size, intensity, geometry, density, velocity and turbulence of falling hydrometeors (e.g. *Bringi and Chandrasekar, 2001; Doviak and Zrnić, 2006*). Polarimetric data have been used to identify areas of intense growth of dendritic and planar crystals (*Kennedy and Rutledge, 2011; Bechini et al., 2013*) and to formulate hypotheses on the dominant microphysical processes occurring over vertical columns of snowfall (*Schneebeil et al., 2013; Andric et al., 2013; Kumjian et al., 2014*). The combination of numerical modelling, radar observations and in-situ data led to the development of classification methods able to estimate the type of hydrometeors that populate individual radar resolution volumes (e.g. *Straka et al., 2000; Dolan and Rutledge, 2009; Bechini and Chandrasekar, 2015; Grazioli et al., 2015a*). However, the complex microphysics of ice-phase precipitation cannot be fully captured by polarimetric radars alone. Combinations of remote sensing with in-situ instruments have shown to be useful and often necessary to characterize at the same time precipitation, clouds, and environmental conditions (*Hogan et al., 2002, 2003; Bechini et al., 2013*, hereafter BBC2013).

This Chapter presents polarimetric radar and in-situ observations collected during winter alpine snowfall. It investigates the relation between riming and snowfall intensity, the temporal

Chapter 5. Riming in winter alpine snowfall during CLACE 2014

Table 5.1: List of the 13 precipitation events identified by means of radar data during CLACE 2014. The net duration of the events includes only time intervals during which precipitation was observed at the lowest available radar while the net snow accumulation is obtained from the MeteoSwiss MAE station (see Fig. 5.1). The red color is used to highlight one event during which the radar was significantly affected by technical issues.

Event number	Start (UTC) MM-DD HH	End (UTC) MM-DD HH UTC	Net duration [h]	Net snow accumulation [cm]
1	01-30 14	01-30 23	10	1
2	01-31 04	01-31 17	10	2
3	02-01 08	02-02 16	28.5	29
4	02-03 16	02-04 12	18	6
5	02-05 06	02-05 22	8	6
6	02-07 07	02-07 19	10	14
7	02-08 09	02-09 01	8	5
8	02-09 22	02-10 04	2	0
9	02-14 09	02-14 19	3	0
10	02-15 22	02-17 05	28	21
11	02-19 02	02-19 20	13	2
12	02-20 21	02-21 21	14	14
13	02-22 15	02-23 21	8	7

evolution, and the vertical structure of intense winter precipitation events originating in mixed-phase clouds. The Chapter is structured as follows. Section 5.3 provides information about the main instrumental set up. Section 5.4 presents the analyses that relate rimed precipitation with snow accumulation as well as a microphysical description of the vertical structure of precipitation. Section 5.5 is devoted to the detailed description of a particularly intense snowfall event characterized by a persistent turbulent layer driven by wind shear and Sec. 5.6 summarizes the main results and provides conclusions and perspectives.

5.3 Measurement campaign and instruments

The major part of the measurements shown in this Chapter were collected during the Cloud and Aerosol Characterization Experiment (CLACE), occurring in January and February 2014. CLACE takes place yearly in the central Alps of Switzerland, in various measurements sites located above 2000 m (e.g. *Zieger et al.*, 2012).

5.3.1 Instruments

Figure 5.1 shows the location of the three main measurement sites considered in the present work: Kleine Scheidegg (KS, 2061 m), Männlichen (MAE, 2230 m), and Jungfrauoch (JFJ, 3580 m). The topography of the measurement area is very complex, with mountain peaks above 4000 m and steep elevation gradients.

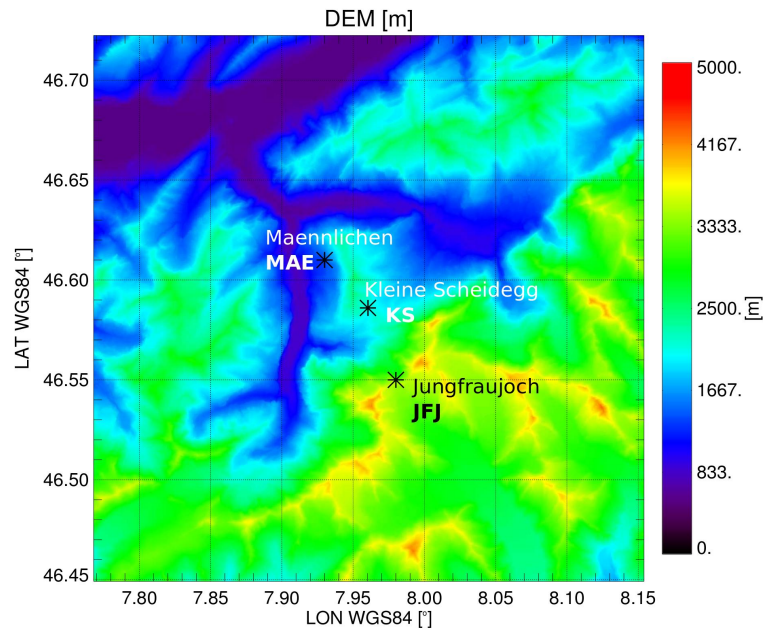


Figure 5.1: Location of the main measurement sites of CLACE 2014 that are considered here. The locations are highlighted on a digital elevation model of the area.

Kleine Scheidegg (KS)

A polarimetric Doppler weather radar was deployed at the KS location. The system, named MXPoL, is an X-band (3.2 cm wavelength) radar with angular resolution of about 1.5° and range resolution of 75 m (complete specifications are given in *Schneebeli et al., 2013; Scipioni et al., 2013*). MXPoL provides as main products the horizontal reflectivity factor Z_H [dBZ], differential reflectivity Z_{DR} [dB], copolar cross correlation coefficient ρ_{hv} , specific differential phase shift upon propagation K_{dp} [$^\circ \text{ km}^{-1}$], mean Doppler velocity v [m s^{-1}] and Doppler spectrum width (*Doviak and Zrnić, 2006*). A hydrometeor classification method (*Grazioli et al., 2015a*, hereafter, GTB2015) was applied to the polarimetric data. GTB2015 classifies dry snowfall into three broad categories: aggregates (AG), individual crystals (CR), rimed ice particles (RI).

During CLACE 2014 MXPoL was operating with a scanning sequence of about 4.5 minutes, repeated indefinitely. During this time interval it performed a Plan Position Indicator (PPI) scan with an elevation of 10° over the Grindelwald valley ($\approx 45^\circ$ North-East of KS in Fig. 5.1), two Range Height Indicator (RHI) scans, one over the Grindelwald valley and one in the direction of JFJ. Vertical profiles of 25 s (with full Doppler power spectrum spectrum, e.g. *Luke et al., 2010*) were collected three times during each sequence. The maximum range distance sampled by MXPoL during CLACE was about 20 km.

Männlichen (MAE)

At the MAE site, snow height was measured by an automatic station whose data are made available by MeteoSwiss. Time series of snow height measurements in time are used to quantify snow accumulations and accumulation rates of the precipitation events. Among other gauging stations in this area, MAE is chosen because: (i) it provides relatively high resolution data (30 minutes), (ii) it is among the closest to KS, (iii) it is located approximately at the altitude of the first radar resolution volume not affected by ground clutter and radar blind range.

Jungfraujoch (JFJ)

The JFJ observatory is a known site for atmospheric studies of aerosols and clouds (e.g. *Baltensperger et al.*, 1997) and during CLACE 2014 it accommodated several sensors. The ones that are of direct interest for the present work are listed here. At first a weather station managed by MeteoSwiss provided general environmental information (temperature, humidity, pressure and so on) and a sonic anemometer provided high resolution wind information. A Cloud Droplet Probe (CDP-100, *Lance et al.*, 2010) yielded quantification of SLW content. CDP measures the light scattered by droplets and determines the optical equivalent diameter over the size range 2 to 50 μm at a 1Hz acquisition frequency. A 3-View Cloud Particle Imager (3V-CPI) provided images and habits of liquid and ice-phase hydrometeors in the 10 to 1280 μm size range. This instrument is the combination of a Two-Dimensional Stereoscopic (2D-S, *Lawson et al.*, 2006) laser shadow imaging probe and of a high frame rate Cloud Particle Imager (CPI Model 2) probe. The 2D-S component of the 3V-CPI instrument, was used to analyse particle imagery in order to produce information on the concentration, size and phase of cloud particles.

The in-situ sensor at the JFJ site and the polarimetric radar (at the KS site, Fig. 5.1), both continuously acquiring data, allow to contextualize radar observations with respect to the cloud conditions over long time intervals. This is a definite added value of CLACE 2014. Similar comparisons between radars and cloud probes have in fact otherwise been performed only on limited time intervals, being the cloud probes usually aircraft-borne (e.g. *Hogan et al.*, 2002, 2003; *Houze and Medina*, 2005).

5.3.2 Precipitation events

The months of January and February 2014 were relatively rich in terms of precipitation. By means of visual inspection of all the observations collected by MXPoI, 13 precipitation events occurring in the measurement domain have been identified. These events have been summarized in Table 5.1. One event (event 9 in the table) is listed for the sake of completeness but it will not be included in the following analysis. In this specific case radar data were missing for technical reasons for more than 40% of the duration of the event.

5.4 Analysis of rimed precipitation

This section analyses the relation between riming and snowfall accumulation as well as the vertical and temporal evolution of precipitation cases showing the signature of riming. The classification of the dominant type of precipitation is based on GTB2015 (see Sec. 5.3.1).

5.4.1 Riming and snowfall accumulation

Riming is among the most efficient turbulent mechanisms to increase the mass flux of precipitation (*Houze and Medina, 2005*). At first it entangles water droplets than will otherwise precipitate with much lower speed. Secondly, it increases the density and lead to smoother shapes of ice-phase hydrometeors thus leading to higher fall velocities and mass fluxes.

Even though the link between rimed precipitation and snowfall amount is understandable, very few studies tried to address it explicitly. Noteworthy exceptions are the studies of (e.g. *Harimaya and Sato, 1989; Mitchell et al., 1990*) that analysed snowfall already deposited on the ground. In a recent study, *Colle et al. (2014)* measured the degree of riming (as defined in *Mosimann et al., 1994*) of falling snow during 12 precipitation events (in the North-East of US). Even though the focus of their work was not on the relation between riming and snowfall intensity, their measurements confirm the expected behaviour. This can be observed in Fig. 5.2, derived from their results. The lowest accumulations of snow are associated with lightly rimed or unrimed (zero average and maximum riming degree) precipitation while larger accumulations are associated with moderately to heavily rimed precipitation cases.

Let us now focus on the database of CLACE 2014. In this case the radar-based classification scheme GTB2015 is employed to quantify the amount of rimed precipitation. Let us define the percentage of rimed precipitation (PRP) as:

$$\text{PRP}(h_1, h_2, \Delta t) = 100 \frac{\#RI}{\#RI + \#AG + \#CR}(h_1, h_2, \Delta t). \quad (5.1)$$

PRP [%] defines the percentage of valid radar observations where riming is identified, between altitudes of h_1 and h_2 [m] and within a given time interval Δt . #RI, #AG, and #CR are the number of radar pixels classified as rimed ice, aggregates, and crystals respectively (*Grazioli et al., 2015a*).

Figure 5.3 shows the comparison between PRP, calculated at the temporal scale of entire precipitation events, and the accumulation of snow measured at the MAE site for the events of CLACE 2014. PRP is calculated considering $h_1 = 2200$ m (i.e., the altitude of the MAE station) and varying h_2 between 2250 and 4000 m, from which the errorbars shown in the figure originate. It is worth noting that on average accumulation scales well with PRP. In particular, the events characterized by near-zero PRP are also associated with near-zero accumulation (e.g. events 1, 2, 11, 8), and all the events showing non negligible accumulation have also proportionally higher PRP. The goal here is not to provide final quantitative relations

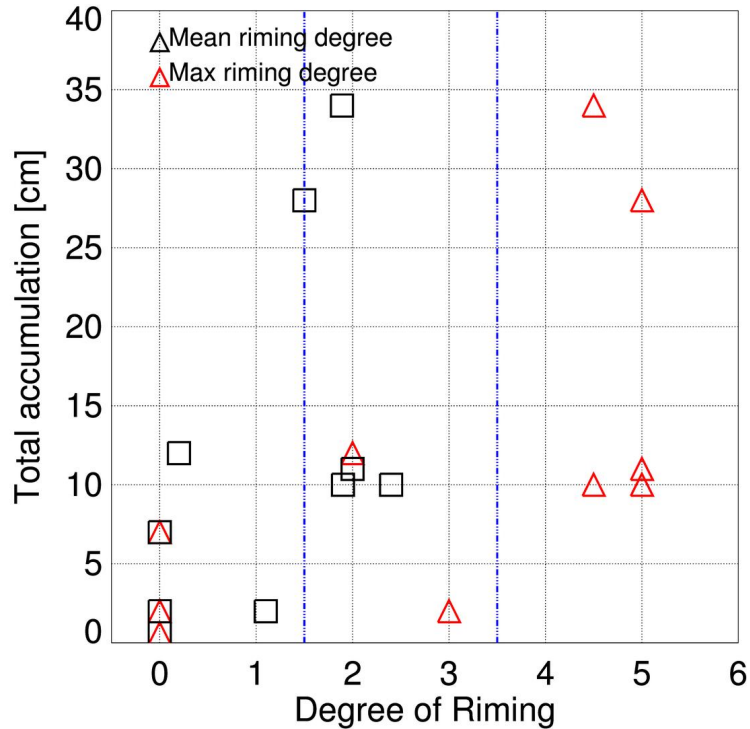


Figure 5.2: Relation between average (or maximum) degree of riming and snowfall accumulation measured during 12 precipitation events occurring at Stony Brook, New York (USA). The values displayed here correspond to tabulated values available in *Colle et al. (2014)*. The blue vertical lines separate lightly, moderately, and heavily rimed particles according to *Mitchell et al. (1990)*.

between these variables, however Fig. 5.3 shows also a regression line, corresponding to a correlation coefficient of almost 0.7 between PRP and snowfall amount. This result confirms the speculated role of riming for the global mass budget of snowfall. The existence of this relation in an Alpine environment was qualitatively hypothesized by *Schneebeli et al. (2013)* who used a different hydrometeor classification algorithm (*Dolan and Rutledge, 2009*) in a different location of the Swiss Alps.

5.4.2 Evolution of rimed precipitation events

In the previous section the important role of riming for the global dynamics of snowfall was highlighted. Rimed precipitation however mostly occurs during limited time intervals and not during the entire precipitation event. In this section the most representative time steps identified by GTB2015 as rimed precipitation will be analysed and the measurements of MXPOL will be compared with the in-situ information of the instruments deployed at JFJ.

The most representative time steps in this sense are identified by means of the following constraints: (i) duration of at least half a hour, (ii) average PRP above 50% (calculated over the whole vertical column), (iii) peaks of at least 15 minutes characterized by PRP greater than

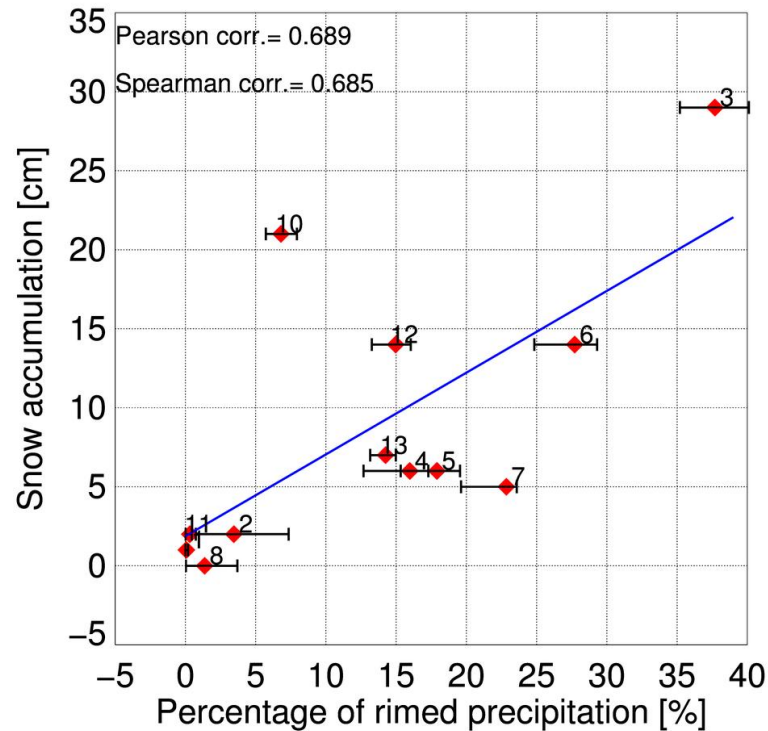


Figure 5.3: Relation between the percentage of rimed precipitation (PRP, retrieved by means of radar data) and snowfall accumulation, for the events listed in Tab.- 5.1. The error bars represent the 5% and 95% quantiles of PRP values calculated for maximum altitudes z_2 (in Eq. 5.1) varying between 2250 m and 4000 m. A linear regression line (in blue) is used to illustrate the average trend.

75% for all the altitudes below the JFJ. The first constraint is justified by the need of collecting a statistically significant number of radar observations at the JFJ height (over a domain of approximately 20 km) to be compared with the in-situ measurements of much higher temporal resolution but collected at a single location. The second constraint ensures that riming is the actual dominant process, as classified by GTB2015, while the third one ensures that a large amount of rimed precipitation is also reaching the ground level.

Figure 5.4 summarizes the global characteristics of the 6 representative time steps isolated in this way.

The events are named after the time interval of Table 5.1 they belong to and they are listed in Table 5.2. Panel (a) puts these cases into a context of snow accumulation. All the time steps in the figure, with the exception of EV4, exhibit above-average snowfall intensities. One of them in particular, EV3, is standing out because only 2.5% of the snowfall time intervals of the same duration occurring during the winter seasons (October-April) from 2000 to 2014 had higher intensities. Panel (b) is used to quantify the percentage of rimed precipitation of each time step and to highlight the relative position of the JFJ (indicated by a dashed black line) within each snow storm. During EV3, EV4, EV6 and EV7, JFJ is situated in the upper edge of the vertical column of rimed precipitation and in the present section they will be referred to

Chapter 5. Riming in winter alpine snowfall during CLACE 2014

Table 5.2: List of the 6 cases, subset of the events of 5.1, during which rimed precipitation was dominant according to the radar-based GTB2015 classifier.

Event label	Start (UTC) MM-DD HH:mm	Duration [h]
EV3	02-01 17:00	9
EV4	02-04 00:00	3
EV5	02-05 18:00	2
EV6	02-07 08:30	2
EV7	02-08 20:00	1.5
EV13	02-22 19:30	2.5

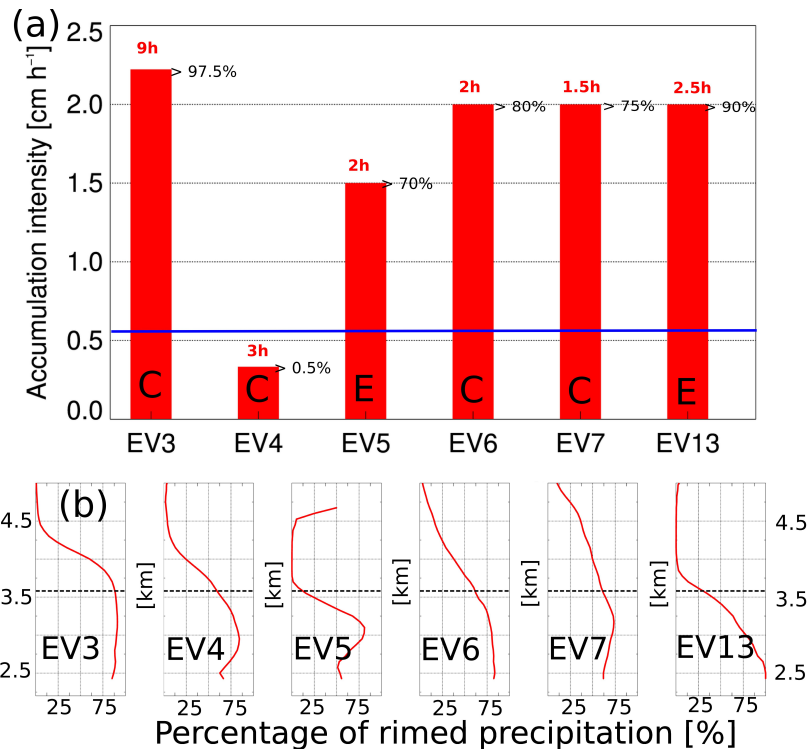


Figure 5.4: Summary characteristics of the 6 cases where riming is identified as dominant mechanism (as listed in Table 5.2). (a): mean snowfall accumulation rate measured at MAE. The red number on top of each bar indicates the duration of the rimed time step. The number on the right side of the bars are the closest quantiles of the distribution of all snowfall events of the same duration in the same location (data from 2000 to 2014). The letters C and E refer to cases indicated in the text as “Core” and “Edge”, respectively. The blue line indicates the mean value (during precipitation only) of CLACE 2014. (b): Average vertical structure of the percentage of rimed precipitation PRP [%] during the selected timesteps.

them as “core events”. On the contrary, during EV5 and EV13, JFJ is located above the “rimed core” and they will be referred to as “edge events”.

Now that the selected cases have been put into context we shall proceed to analyse their characteristics by means of radar observations and in-situ measurements. Each period of interest, that will be called “rimed” phase, is compared with a reference time interval of 3 previous hours, named “preceding” phase. Such comparison is shown in Figs. 5.5 and 5.6.

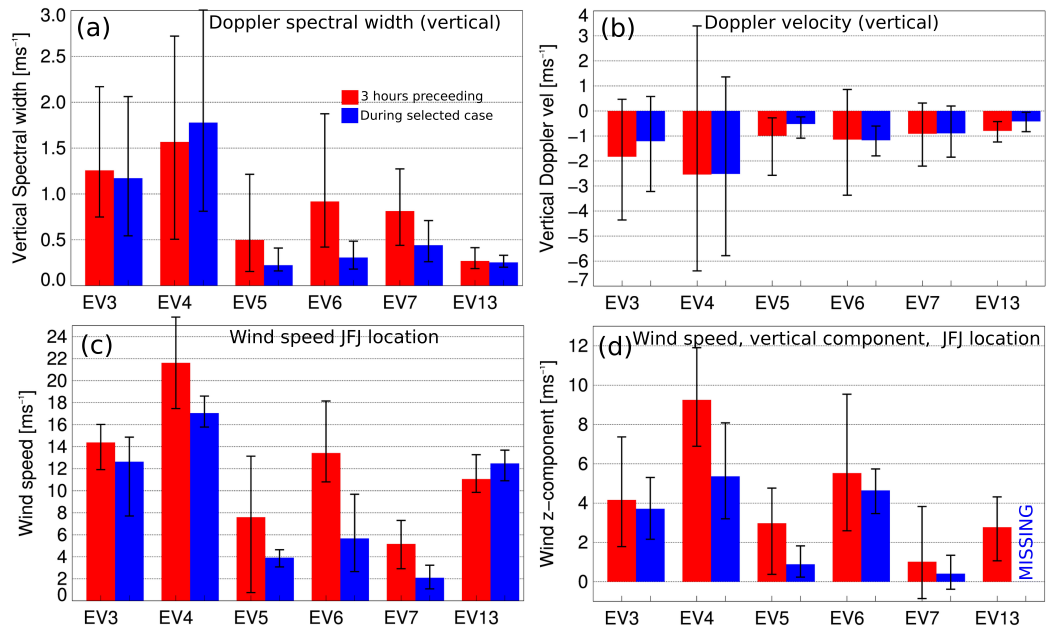


Figure 5.5: Measurements of wind, turbulence, and fall velocities before (red histograms) and during (blue histograms) the 6 cases shown in Fig. 5.4. Panels (a) and (b) show radar data (only for altitude around the JFJ location: 3580 ± 100 m), while panels (c) and (d) show data collected at the JFJ location. (a) Doppler spectral width [m s^{-1}] from radar vertical profiles (i.e. at vertical incidence). (b) Doppler velocity [m s^{-1}] from radar vertical profiles. (c) Wind speed (data from MeteoSwiss station) [m s^{-1}]. (d) Vertical component of the wind (sonic anemometer data) [m s^{-1}]

Fig. 5.5 illustrates the behaviour of variables related to wind and turbulence. In most of the cases the preceding phase is more turbulent than the rimed phase. Turbulence, and in particular updraft are important factors leading to riming by providing SLW droplets and conditions that favour collision (*Rauber and Tokay, 1991; Pinsky and Khain, 1998; Houze and Medina, 2005*). Figure 5.6 on the other hand illustrates the evolution of radar horizontal reflectivity Z_H and in-situ LWC during the selected cases.

Edge events (EV5, EV13)

EV5 and EV13 have been sampled, from the JFJ perspective, above the actual “rimed core” of precipitation (see Fig. 5.4 (b)). It can be observed in Fig. 5.6 (b) that they show the lowest Z_H values at the JFJ height during the rimed phase of the event. As Z_H in our observations increases with decreasing altitude, these two events are sampled closer to the apparent cloud top. Therefore the in-situ measurements provide in this case information about the processes occurring at the highest levels of rimed precipitation. Liquid water is available during both events (Fig. 5.6 b), in much higher concentration during EV13 and it is not depleted as the event evolves.

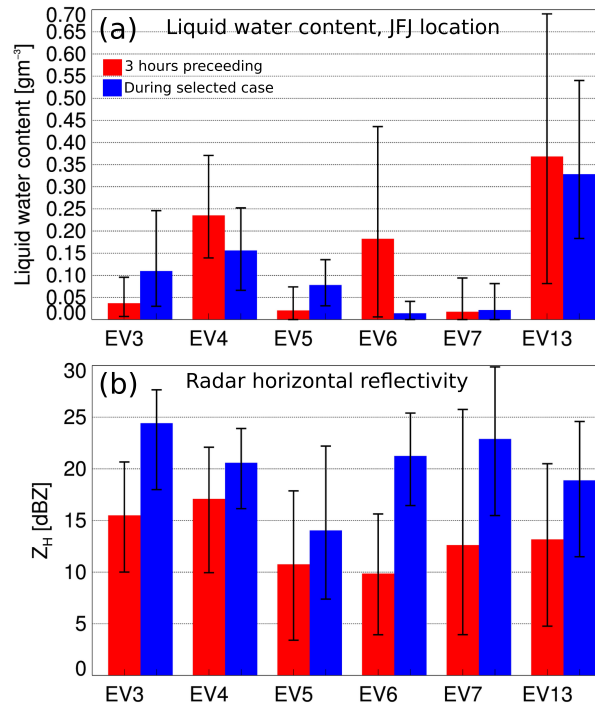


Figure 5.6: As in Fig. 5.5 for Z_H and LWC. (a) Liquid water content LWC [g m^{-3}] measured at the JFJ location. (b) Radar horizontal reflectivity factor Z_H [dBZ] from altitudes around the JFJ location: 3580 ± 100 m.

Core events (EV3, EV4, EV6, EV7)

The “core” events are of major interest for the microphysical descriptions presented here. EV6 and EV7 behave similarly in terms of evolution of wind and turbulence (Fig. 5.5). In both cases the preceding phase (red histograms) is observed to be more turbulent than the rimed phase (blue histograms). All the variables shown in this figure are decreasing during the transition between the two phases. Doppler spectral width, shown in panel (a), reduces of about 50%, as well as the wind speed (panel c). The Doppler velocity (panel b), influenced by particle fall velocity and air motion, shows positive values (particles updraft) and in general a larger variability during the preceding phase. It can be hypothesize that the turbulent part of the events creates the appropriate conditions to generate rimed precipitation, that falls out efficiently during the following calmer part.

As observed in Fig. 5.6, during EV7 the liquid water content is always low, before and during the rimed phase, leading us to believe that in this case riming occurred at much higher altitudes. In favour of this hypothesis there is the significant vertical extension of this snowfall event, as shown in Fig. 5.4 (b), with respect to the other ones. EV6 exhibits a very interesting LWC trend. LWC is practically entirely depleted before the rimed phase, with a transition of maximum values from around 0.45 g m^{-3} to around 0.05 g m^{-3} . We believe that this is the actual signature of the efficient mass transfer due to riming, from the liquid mass suspended in the clouds to the ice mass that precipitates. In the rimed phase of the event, the LWC is collected in the form of rimed accretion, especially on the largest precipitating hydrometeors and therefore it

is not available any more in the form of water droplets.

The trends of EV4 are similar to EV6, even though the magnitude of the variables is very different. Also in this case it can be observed a decrease of turbulence (except for the spectral width) and wind intensity (Fig. 5.5), as well as a decrease of LWC (Fig. 5.6,a) in the transition between the preceding phase and rimed phase. Wind intensities remain extremely high, with the 5% quantile never below 16 m s^{-1} . Such wind intensities affect the snowfall flux towards the ground and introduce significant uncertainty on snow accumulation measurements. This probably contributes to explain why this case did not generate any significant response in terms of snowfall accumulation (Fig. 5.4, a).

EV3 is probably the most interesting one because it shows opposite trends with respect to EV6 and EV7. Notably, LWC is this time higher in the rimed part of the event (Fig. 5.6, a) while turbulence and wind intensity remain almost constant. This case, occurring during the event number 3 of Table 5.1, was lasting about 9 hours (it is about three times longer than the second longest “rimed” case) and it had an average snowfall intensity of more than 2.1 cm h^{-1} . It represents a very high quantile of snowfall intensity in comparison with events of analogous duration (Fig. 5.4) and for this reason it will be further discussed in the next sections.

5.4.3 Vertical structure

One of the distinct advantages of high resolution and easily transportable polarimetric radars is the potential to sample the vertical structure of precipitation even, like in the present case, in complex terrains. Here we interpret the microphysical processes occurring during the most intense cases according to the vertical structure of polarimetric variables (Z_H , Z_{DR} , K_{dp} and ρ_{hv}) extracted from radar RHI scans. The evolution of this measurements varies among the different cases, but many common features, listed in the following, exist.

Upper level of precipitation

Figure 5.7 shows statistics of the vertical evolution of polarimetric variables for a selected RHI of EV3, EV6, and EV7.

In the upper levels of precipitation (above 4.5 km for EV3 and EV6 and above 5 km for EV7) Z_H is low, as well as Z_{DR} and K_{dp} , indicating the presence of small ice crystals that, at the X-band radar wavelength, do not exhibit significant anisotropy (e.g. *Andric et al.*, 2013, hereafter A2013). The copolar cross correlation coefficient ρ_{hv} is relatively low (≤ 0.99) in this region. This probably is a combined effect of low signal-to-noise ratio, that affects the accuracy of ρ_{hv} (*Torlaschi and Gingras*, 2003) and actual physical variability and heterogeneity of crystal shapes and habits within the radar sampling volumes (*Andric et al.*, 2013).

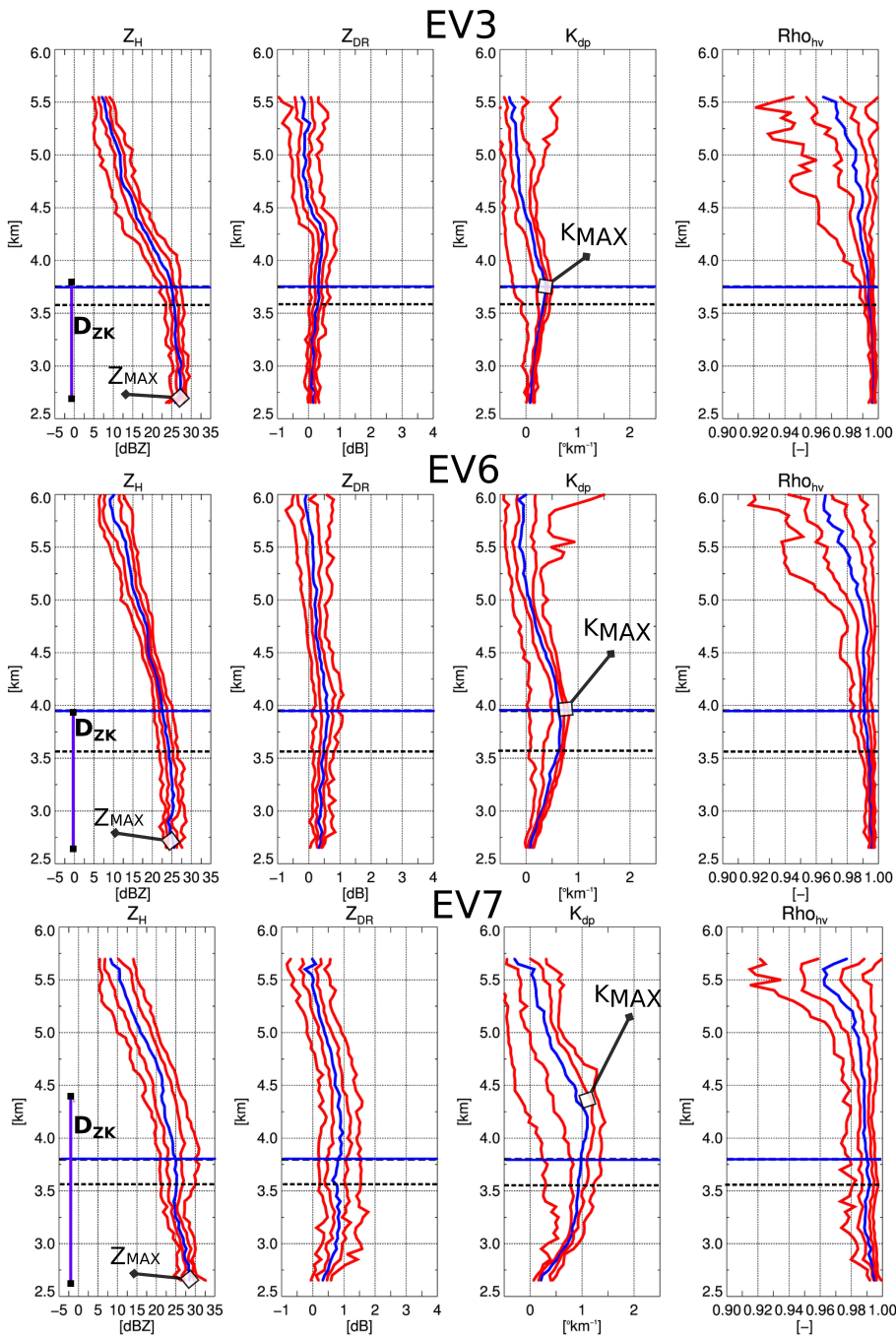


Figure 5.7: Vertical structure of polarimetric radar observations extracted from one RHI scan during three selected cases. The blue horizontal line indicates the estimated altitude of the -15°C temperature level while the dashed black line indicates the altitude of JFJ. The polarimetric variables are extracted considering maximum elevation angles below 45° (the effect of incidence is corrected with the method of Ryzhkov *et al.* (2005b)). The red curves indicate quantiles at 5%, 25%, 75% and 95% while the blue curve indicates the median. EV3 shows RHI data collected on Feb. 01, 2014, 2230 UTC. EV6 shows data collected on Feb. 07, 2014, 1005 UTC. EV7 shows data collected on Feb. 08, 2014, 2100 UTC.

Intermediate level of precipitation

Proceeding towards lower altitudes (from approximately 4.5/5 km down to 3.5 km in all the cases shown in Fig. 5.7) Z_H increases until approaching almost its peak values. It is hypothesized that riming is more intense within this region.

In the top part of this zone the highest values of Z_{DR} in the column are observed, followed below by the highest values of K_{dp} . The enhancement of Z_{DR} is often explained by the presence of ice crystals grown by vapour deposition, that promotes anisotropic shape enhancement (Takahashi, 2014; Andric et al., 2013). The enhancement is in this case moderate, with peak values mostly below 1 dB suggesting that depositional growth is not the only process taking place. In fact, Z_{DR} is largely influenced by the geometry of the particle that contribute the most to the Z_H signal (i.e. the biggest ones, Hubbert et al., 2014) such that the presence of even a few large isotropic aggregates significantly decreases Z_{DR} .

The peak of K_{dp} , below altitudes of higher Z_{DR} and above altitudes of higher Z_H , is a well known but still not completely understood signature observed during snowfall (Kennedy and Rutledge, 2011; Bechini et al., 2013; Andric et al., 2013; Hubbert et al., 2014). The proximity of this signature with respect to the -15°C level (blue line in Fig. 5.7) has lead in the past to associate it to dendritic crystal growth (Kennedy and Rutledge, 2011). However, it was recognized that the concentration of dendrites needed to generate enhancements of this magnitude would lead to unreasonably high values of Z_H when these crystals eventually aggregate (Andric et al., 2013). It has been demonstrated that the particles responsible of this signatures must be small compared to the radar wavelength as they were shown to behave as Rayleigh scatterers by (Bechini et al., 2013; Hubbert et al., 2014). BBC2013 and A2013 proposed two interesting and not mutually exclusive explanations. BBC2013 hypothesized that rimed dendrites would be able to generate such significant K_{dp} enhancement. K_{dp} is in fact, with other conditions fixed, increasing with the density of the ice particles. A2013 suggested instead that secondary ice production of very small oblate crystals would need to take place, either as a result of splintering (Hallett and Mossop, 1974, or other multiplication mechanisms) or as a result of direct nucleation from the liquid phase with a similar process as described in Westbrook and Illingworth (2011).

In the end, both hypotheses are by-products of the riming process and our interpretation is that the enhancement of K_{dp} in this region is the radar signature of riming. From one side, riming of already existing anisotropic crystals would enhance their contribution to K_{dp} by increasing the particle density and thus the dielectric response. From the other side, the formation of secondary ice can follow as well the mechanisms of Vardiman (1978) or Yano and Phillips (2011), less efficient, not constrained by temperature, but always favoured by riming. In the latter case the increase of K_{dp} is driven mostly by the number concentration of ice crystals. During EV3, EV6, and EV7, the measurements of LWC and the turbulent conditions, as well as the radar-based classification (see Sec. 5.4.2) led us to a confident identification of riming at this altitude levels. Figure 5.8 displays the type of particles in the size range 10

to $1280 \mu\text{m}$ recorded at the level of the JFJ by the 2D-S instrument, for EV3, EV6, and EV7 respectively (at the same time-steps shown in Fig. 5.7).

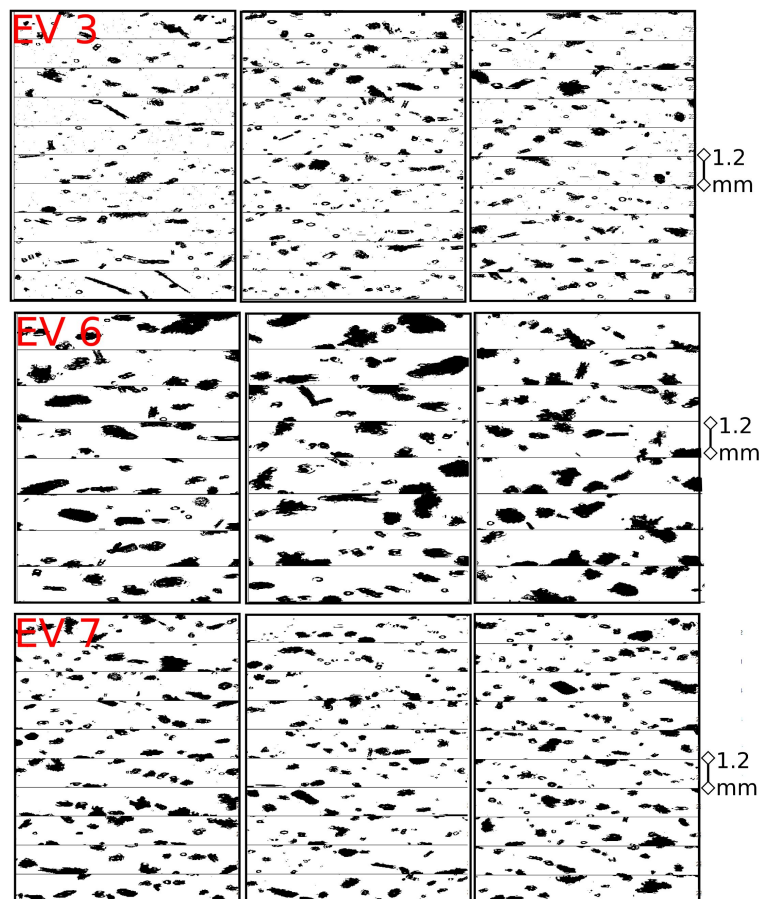


Figure 5.8: Particle images collected at the JFJ location by the 2D-S particle imager. Three cases are shown, corresponding to the polarimetric observations of Fig. 5.7. Top panel: EV3, on Feb. 01, 2014, around 2230 UTC. Mid panel: EV6 on Feb. 06, 2014, around 1000 UTC. Bottom panel: EV7 on Feb. 08, 2014, around 2100 UTC.

During EV6 and EV7 can be observed the presence of heavily rimed particles with non recognizable original shape as well as of rimed particles probably originating from planar crystals. The ice number concentrations measured around these time steps ranged from 5 to 20l^{-1} with modal values around 10l^{-1} for EV6 and from 5 to 23l^{-1} with modal values around 10l^{-1} for EV7¹. The mean mass of the crystals in the size range sampled (obtained by dividing the total 2D-S ice mass content by the ice number concentration) during these time intervals was about $10 \mu\text{g}$ and $6 \mu\text{g}$ during EV6 and EV7, respectively. On the contrary, during EV3 rimed crystals are observed together with a large amount of small particles (some of them highly oblate), of various shapes. The ice number concentration around this time step ranged from 25 to 100l^{-1} with modal values around 50l^{-1} (larger than the case of EV6 and EV7) and the

¹These are reference values calculated within a 10 min time window. The given range of variation is based on 5% and 95% quantile.

5.5. Case study (EV3): turbulence, wind shear, and snowfall enhancement

mean mass of the ice crystals was about $3.5\mu\text{g}$. It can be hypothesized that during EV7 the K_{dp} signal is generated mostly by heavier riming of larger anisotropic crystals (but still in the Rayleigh regime) while during EV6 it results from the higher concentration of smaller oblate particles. This also is confirmed by the higher values of Z_{DR} during EV6 and EV7 especially, at this altitude, if one recalls that Z_{DR} is mostly influenced by the oblateness of larger particles. It is also worth noting, by looking at the particle images of Fig. 5.8 (and many other not shown here) that the K_{dp} enhancement seems not to be associated with pristine ice crystals habits. This would tend to rule out pristine dry dendrification as the dominant K_{dp} enhancement mechanism.

Lower level of precipitation

Returning to Fig. 5.7, below the K_{dp} peak Z_H continues to increase while both K_{dp} and Z_{DR} decrease steadily. Below altitude values of approximately 3.5 km (for all three cases) Z_{DR} and K_{dp} further decrease towards near-zero values and Z_H further increase even though at a lower rate. Further riming, in combination with aggregation of the crystals, are both processes that explain this trend (e.g. Kumjian *et al.*, 2014) and that may be acting together, in a positive feedback (Houze and Medina, 2005).

Z_H maxima and K_{dp} maxima

As observed and documented in the present section, typical vertical profiles of polarimetric radar variables in snowfall in which riming has been identified show a maximum in K_{dp} at a certain altitude, and a maximum of Z_H usually at the lowest level of precipitation sampled by the radar (suggesting therefore further increase at lower, non sampled, levels). The maximum of the median K_{dp} values per height level is labelled as K_{MAX} in Fig. 5.7 while its counterpart for Z_H is named Z_{MAX} . The two quantities are situated at a vertical distance D_{ZK} (positive if K_{MAX} is above Z_{MAX}). Fig. 5.9 (a) is showing the distribution of D_{ZK} for all the RHI collected during the six cases listed in Table 5.2. It can be observed that K_{MAX} is indeed systematically above Z_{MAX} with a mean distance of about 680 m. It is worth also noting in Fig. 5.9 (b), that larger K_{MAX} are associated also to larger Z_{MAX} even though the correlation between the quantities is weak ($r^2 \approx 0.25$). The peak of K_{dp} might therefore be considered as an indication of high Z_H values at lower levels.

5.5 Case study (EV3): turbulence, wind shear, and snowfall enhancement

5.5.1 Detailed description of EV3

Let us now come back to the peculiar case of EV3. EV3 occurred during the precipitation event leading to the largest snow accumulation (Fig. 5.3). There was an average precipitation

Chapter 5. Riming in winter alpine snowfall during CLACE 2014

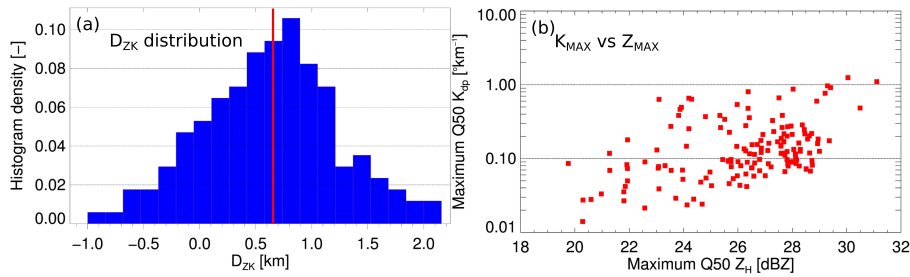


Figure 5.9: (a) Frequency distribution (i.e. sample histogram) of $D_z k$ [km] values. (b) Scatter-plot of K_{MAX} [$^{\circ} \text{km}^{-1}$] vs Z_{MAX} [dBZ]. The graphs are calculated for all the time intervals listed in Tab. 5.2, and the quantities displayed are shown in Fig. 5.7

intensity of 2.1 cm h^{-1} for a 9 h duration. Over the past 14 years, less than 2.5% of snowfall cases of this duration (in the same location) led to higher intensities. As documented in Fig. 5.6, SLW droplets were available during the whole event and they were not rapidly depleted as it happened in other cases. It is therefore instructive to investigate which mechanisms sustained the production of snowfall.

The synoptic situation occurring on the 1st February at 12 UTC, just a few hours before the beginning of EV3, is represented in Fig. 5.10.

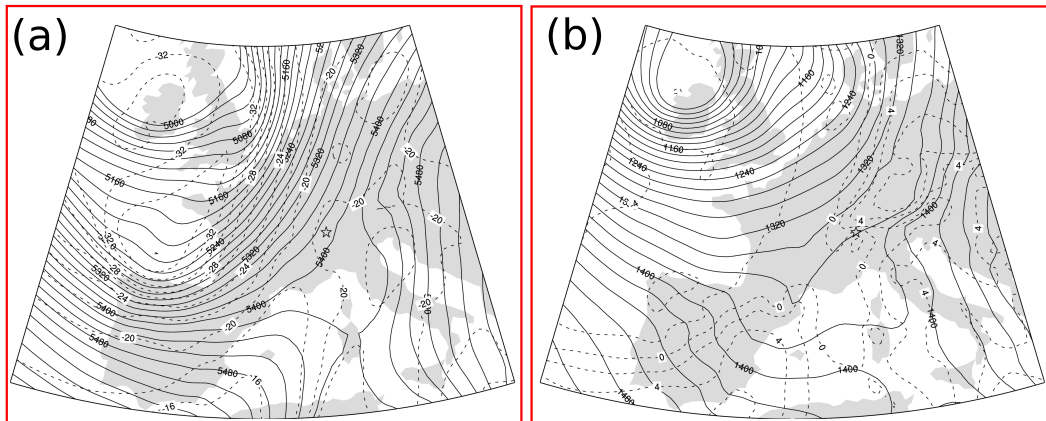


Figure 5.10: (a) 500 hPa and (b) 850 hPa geopotential height [m] (continuous lines) and temperature [$^{\circ} \text{C}$] (dashed lines) over Central Europe at 12 UTC on the 2nd February 2014. The geographical location of the CLACE campaign is indicated by a star. The atmospheric fields are derived by ERA-Interim reanalysis grids at $0.5^{\circ} \times 0.5^{\circ}$ horizontal resolution.

The 500 hPa geopotential height (panel a) shows the presence of a deep trough extending from the British Isles to Western Europe, approaching the Alpine slopes from the West. A cold front was associated with the trough, as clearly visible from the 850 hPa temperature shown in panel (b). The atmospheric sounding of Payerne (Lat. 46.82, Lon. 6.94) at 12 UTC, not shown here, indicates the presence of a strong south-westerly flow above 2 km. A low-level jet was also observed between 1 and 1.3 km. The sounding of the 2nd of February at 00 UTC (not

5.5. Case study (EV3): turbulence, wind shear, and snowfall enhancement

shown) reveals that after the passage of the cold front the temperature decreased of more than 10°C at an altitude of about 2 km over Payerne, consistent with the constant temperature drop which was also observed at the JFJ station in the afternoon. The passage of the cold front occurred between 21 and 00 UTC, as clearly shown by the measurements of atmospheric pressure collected at the JFJ (see Fig. 5.11, b), and by the sharp change in wind direction observed in Gütsch (Lat. 46.65, Lon. 8.61, alt. 2283 m), a nearby meteorological station not influenced by wind channelling as the JFJ. The cold front produces a significant and steady accumulation of snowfall at the ground level in MAE, as shown in Fig. 5.11, (a).

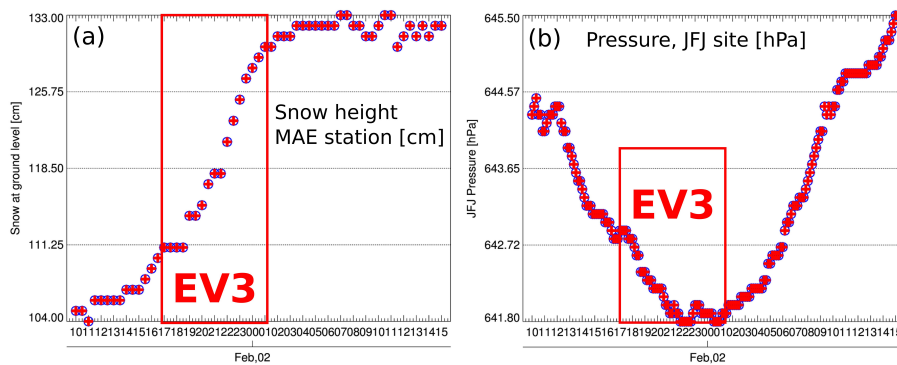


Figure 5.11: Evolution of: (a) in-situ environmental pressure [hPa] measured at the JFJ location, (b) snow accumulation at the ground level [cm], measured at the MAE site during EV3.

From the observations of Fig. 5.7, the vertical structure of EV3 appeared similar to the other “rimed” cases in terms of polarimetric variables. However, by looking at the average vertical structure of two Doppler-related radar variables (Doppler velocity and Doppler spectral width at vertical incidence) for the six cases of Table 5.2, an obvious difference emerges (Fig. 5.12). EV6, EV7, EV8 and EV13 do not exhibit particular signatures: the distribution of Doppler velocities is globally narrow and the occurrence of updrafts (positive values of Doppler velocity at vertical incidence) is very limited. Doppler spectral width values are lower than 1 m s^{-1} , with median values always lower than 0.5 m s^{-1} . EV4 on the contrary is extremely turbulent over the whole range of heights: even at the lowest heights updrafts are frequent and over all the heights values of spectral width up to 3 m s^{-1} are observed. EV3 finally, shows a peculiarity: the turbulence in this case appeared to be confined between approximately 3000 m and 4000 m. In this layer the spectral width reaches values up to 2.5 m s^{-1} and updrafts are observed, while at altitudes below 3000 m the range of velocities and spectral width do not show any signature of turbulence.

Figure 5.12 revealed the presence of a turbulent layer between 3000 m and 4000 m of altitude at the temporal scale of the entire duration of EV3. Figures 5.13 and 5.14 illustrate the dynamics of EV3 in a more complete and dynamic way.

Figure 5.13 (a) depicts the vertical structure of Doppler spectral width: the turbulent layer is clearly visible at the expected altitudes and it is relatively stable in time. In Fig. 5.13 (b), showing the Doppler velocity at vertical incidence, frequent updrafts are observed within the

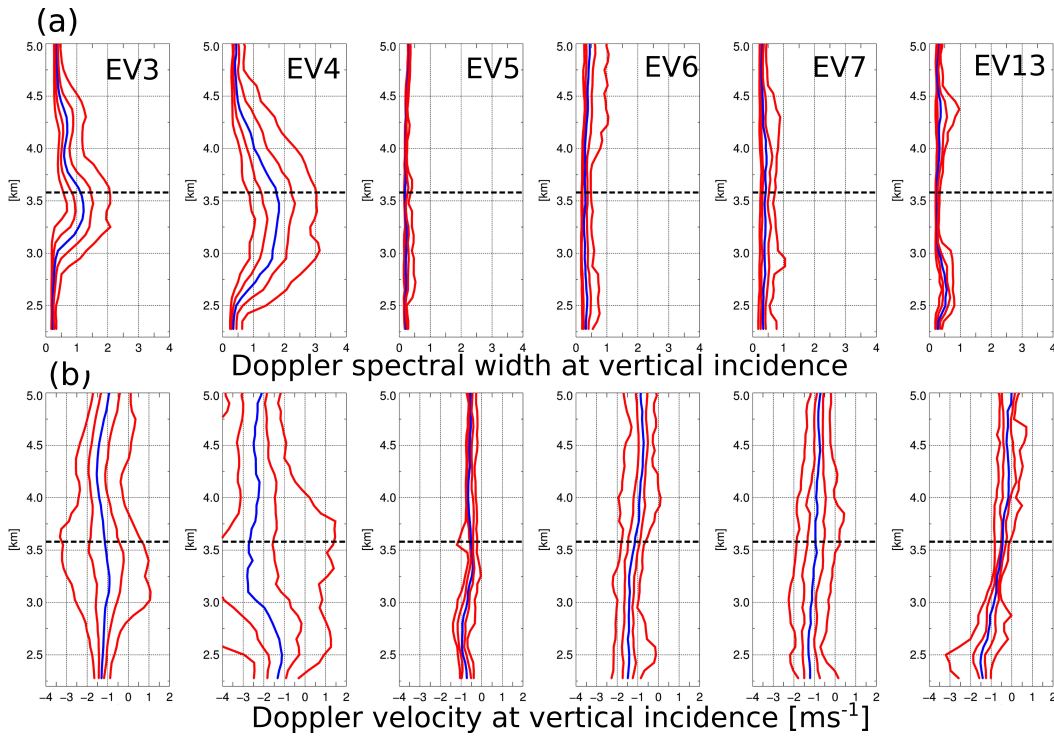


Figure 5.12: Vertical structure of: (a) Doppler velocity, and (b) Doppler spectral width over the whole duration of EV3, EV4, EV5, EV6, EV7, EV13. Both variables are measured at vertical incidence angles.

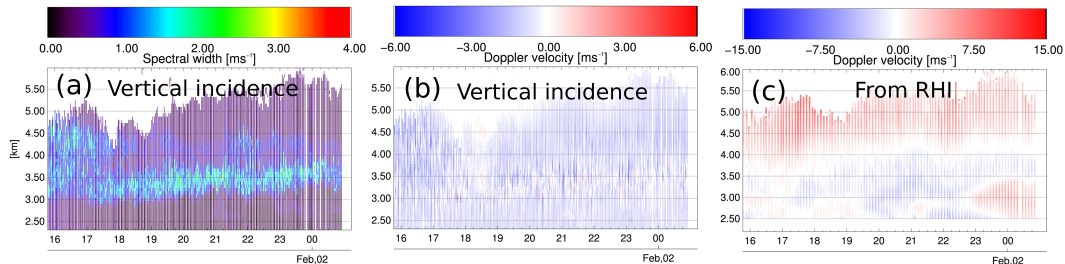


Figure 5.13: Time evolution of the vertical structure of Doppler-related variables during EV3. (a): Doppler spectral width at vertical incidence [m s^{-1}]. (b): Doppler velocity at vertical incidence [m s^{-1}]. (c) Doppler velocity from RHI scans [m s^{-1}]. Each observation of panel (c) is the mean over the same height of all the observations collected during an RHI scan. Only one RHI direction ($\approx 45^\circ$ North to East) is used to generate such plot.

turbulent layer. Figure 5.13 (c) shows for each height and time the mean value of Doppler velocity measured within a radar RHI scan².

In this case it is observed that the turbulent layer is caused by wind shear: two air masses with different relative motion with respect to the radar location are in contact. The change of sign of the Doppler velocities from negative to positive happens at the top of the turbulent layer, where the two air masses are mixing. Because the JFJ is situated at the altitudes where the turbulent layer is observed, it is now easier to explain the availability of SLW at this level

²Each vertical cut of this kind of plots is the summary of an entire RHI scan. Such plots do not consider RHI elevations angle higher than 45° in order to preserve polarimetric signals or horizontal wind components

5.5. Case study (EV3): turbulence, wind shear, and snowfall enhancement

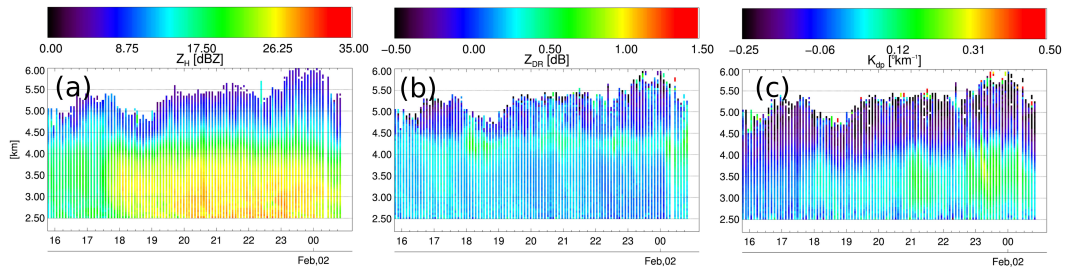


Figure 5.14: As in panel (c) of Fig. 5.13 but showing: (a) Z_H [dBZ], (b) Z_{DR} [dB], (c) K_{dp} [$^{\circ} \text{km}^{-1}$]

during EV3, documented in Fig. 5.6. This is in fact the result of the steady turbulent mixing and updrafts that lead to a constant generation of SLW. The rate of SLW input was probably higher than the collection efficiency of the ice particles within the layer itself and therefore, despite the continuous collection, SLW remained in excess.

Below the wind shear we observe (Fig. 5.14) throughout the event the peak of K_{dp} and the steady increase of Z_H already discussed in relation to Fig. 5.6. Z_{DR} exhibits the same trends as in Fig. 5.6 and forms a hat of slightly enhanced values at the top of the turbulent layer.

5.5.2 The role of turbulence and wind shear

The role of turbulence in the generation and enhancement of snowfall has been documented by HM2005. HM2005 observed shear layers (with turbulent mixing within) associated with the interaction between baroclinic storms and mountain ranges (both in the USA and in central Europe). An enhancement of precipitation was observed on the windward side of the mountain ranges during these cases. The enhancement was likely associated with intense aggregation and riming within the turbulent layer, that lead to rapid fallout of water masses that would otherwise not be able to precipitate. The case depicted in the present Chapter is located in an inner Alpine valley and not on the first slopes, as in HM2005. While the consequences in terms of snow accumulation and the global microphysical interpretation of HM2005 is well applicable to our case, the reasons of the formation of the wind shear are different. In the present case, it is probably the result of the interaction between large scale south-westerly flow with the main mountain peaks situated south of the KS location (see Fig. 5.1). It is worth noting that the height of those peaks (about 4000 m) corresponds roughly with the upper edge of the turbulent layer.

The effect of wind shear and turbulent recirculation on the microphysics of snowfall has been observed by Hogan *et al.* (2002) (H2002). Also in this case, the large scale conditions and geographical locations described in H2002 are very different with respect to CLACE 2014. However, the microphysical processes described may as well occur in alpine regions. In particular H2002 explained that wind shear and updrafts allow together to continuously feed the regions above the shear layer with SLW and ice fragments (deriving from secondary ice production mechanisms) and favour the growth of anisotropic ice crystals at this level. This phenomenon create an enhancement of Z_{DR} , very similar to what has been observed in the

present case in Fig. 5.14 (c). Additionally, H2002 recognized that secondary ice, by-product of the riming process, can be recirculated in the layer of shear and grow into oblate small ice particles as the ones that can be no noticed in Fig. 5.8. This mechanism, resulting in increased concentration of particles can explain the enhancement of K_{dp} observed within the turbulent layer. It is worth noting that K_{dp} was unfortunately not available in the study of H2002. This parameter has the definite advantage over Z_{DR} of being unbiased by the presence of large isotropic particles (like aggregates) that unavoidably are formed in areas of turbulent mixing. About the generation of secondary ice, H2002 was presenting evidences for a Hallett-Mossop mechanism (Hallett and Mossop, 1974), that occurs at temperatures warmer than -8°C . The enhancement of K_{dp} happens in our case at lower temperatures and this lead us to assume that other multiplication mechanisms (e.g. Vardiman, 1978; Yano and Phillips, 2011) may be taking place. These collisional mechanisms require only earlier stages of riming, presence of supercooled liquid water, ice crystals, and turbulence (all conditions that are met during EV3).

Figure 5.15 summarize schematically the possible role that the turbulent layer was playing during EV3. Above the layer (enhanced Z_{DR}) favourable conditions exist for anisotropic crystal growth thanks to the recirculation of SLW and ice fragments from the lower levels. Within the turbulent layer, aggregation and riming are initiated. Both riming itself and the availability of large quantities of small crystals, likely deriving from collisional ice multiplication contribute to the peak of K_{dp} . Aggregation and size sorting (e.g. Dawson et al., 2015) results in an increase of Z_H in the bottom part of the turbulent layer. Aggregation and further riming will then continue to raise Z_H until precipitation reaches the ground. In this global view, precipitation will be enhanced as long as turbulence persists.

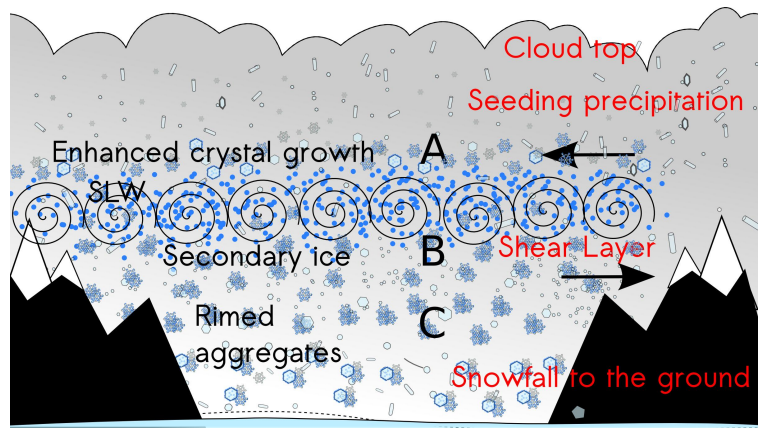


Figure 5.15: Schematic representation of the role of turbulence observed during EV3. The label “A” indicates area of enhanced Z_{DR} , label “B” enhanced K_{dp} , and label “C” enhanced Z_H .

5.6 Summary and Conclusions

This Chapter presented polarimetric radar and in-situ measurements of precipitation in a mixed-phase cloud environment during CLACE 2014, in the central Alps of Switzerland. It was shown, thanks to the comparison between radar-based hydrometeor classification and

measurements of snow accumulation, that riming is a leading factor to explain enhancements of snow accumulation. The phases of the precipitation events that exhibited significant riming have been further analysed. In most of the cases, radar observations of rimed precipitation were following time periods of enhanced turbulence and availability of SLW. During the observations, instead, the turbulence was usually lower (favouring thus the precipitation) and SLW was depleted in the cores of rimed precipitation, being probably collected in the form of rimed accretion on the precipitating ice crystals. One noteworthy exception was constituted by a snowfall event named EV3 (statistically, the most intense one). In this case, a stable layer of wind-shear driven turbulence, associated with the passage of a cold front, was creating favourable conditions for the sustained production of SLW, ice-to-ice interaction, and efficient fallout of water masses by means of a mechanism similar to what presented in *Houze and Medina* (2005). A microphysical interpretation of this mechanism has been proposed.

The vertical structure of the events during which riming was significant has been examined by means of the radar polarimetric variables and in-situ ice particle probes. A common feature of these cases was shown to be a peak of K_{dp} , associated either with relatively large concentrations of small ice crystals (probably associated with secondary ice generation) or with the riming of ice crystals with anisotropic shapes. The enhancement of K_{dp} has been shown to be related to the maximum Z_H measured in the vertical column of precipitation. Even though previous studies hypothesized the K_{dp} signature to be associated with dendritic growth, particle images (limited however to 1.28 mm of maximum sampling size) collected within this area of the storm did not show any evident or dominant pristine and unrimed crystal habit in these cases.

The present study provided insight about the relation between riming and accumulation, the microphysics of riming, and the potential role of sustained turbulence on snowfall generation. It also illustrated the complementarity of in-situ and remote sensing instruments for the description of snowfall microphysics in complex terrain. Future studies should include also radar measurements at higher frequencies, to better capture the transition between clouds and precipitation, and in-situ particle imagers of larger maximum sampling size in order to visualize the hydrometeors that contribute mostly to the total Z_H signal and that are larger targets for riming. The potential role of turbulence in the microphysics and accumulation of snow should be further investigated, in order to understand if the patterns described for EV3 are recurring.

6 Conclusions and outlook

6.1 Summary

This thesis work was mainly devoted to the interpretation of polarimetric radar data, in terms of precipitation microphysics.

Microphysical retrievals are conducted at the scale of the radar range gate but one polarimetric variable, K_{dp} , is usually calculated by smoothing the radar data over large spatial scales. A novel K_{dp} estimation method was presented in chapter 2, designed to follow finer scale variations over individual range gates. The method performed better than other algorithms of the same family, but an accurate evaluation revealed that K_{dp} values at the small scale can be largely biased.

The first kind of microphysical retrieval that can come to mind is hydrometeor type. Hydrometeor classification was investigated at first (Chapter 3) by developing a supervised identification algorithm for two-dimensional video disdrometers. This method provides, over time intervals of 60 seconds, the dominant hydrometeor class observed within the small sampling volume of the instrument. The method, in the context of the present thesis, is seen also as a comparison tool to link radar data and in-situ measurements. Hydrometeor classification from polarimetric radar data has also been tackled in Chapter 4. A novel classification approach, based on observations (data) rather than on scattering simulations as initial step, is proposed. The data-driven approach leads in the end to similar classification capabilities than simulation-driven approaches with the advantage of being better tailored on the characteristics of the instrument collecting the measurements and on the available datasets.

A measurement campaign, conducted in the central Alps of Switzerland during January and February 2014, was the perfect occasion to test the capabilities of an X-band high resolution radar in terms of microphysical interpretations and retrievals (Chapter 5). It was observed, thanks to hydrometeor classification and in-situ measurements, that the process of riming appears to be the driving microphysical aspect leading to high accumulation of snow. The

vertical structure of snowfall events with enhanced riming has been interpreted thanks to high resolution profiles of K_{dp} , Z_H , and Z_{DR} that allowed to discriminate areas of crystal growth, riming, aggregation, and secondary ice production. In addition, the combination of Doppler-variables, polarimetry, and in-situ measurements allowed to observe that the turbulence generated by wind shear creates favourable conditions for a sustained production of rimed precipitation, leading in turns to significant accumulations of snow.

6.2 Contribution of this thesis

The main contributions of this thesis can be summarized in the following way:

- A novel K_{dp} estimation algorithm has been proposed, that is able to follow small-scale variations better than classical methods.
- The estimation accuracy of K_{dp} has been evaluated at the scale of the radar range gate. It was shown, for the first time quantitatively, that at the small scale K_{dp} can be affected by large errors and negative biases.
- A hydrometeor classification algorithm for 2-DVD data was presented. It was shown that video disdrometers have a lot of potential in terms of automatic microphysical retrievals and they can constitute precious ground-truth for polarimetric weather radars.
- Hydrometeor classification from polarimetric weather radars can be based on observations instead than on numerical simulations. In this way the hydrometeor classes better reflect the actual capabilities of each radar system and better represent of the climatology of the available data sets.
- Riming has been experimentally shown to be a dominant factor affecting snowfall accumulation. The vertical structure of rimed precipitation has been described and interpreted thanks to multi-sensor observations.
- It is only through a combination of remote sensing and in-situ instruments that precipitation can be accurately described.

6.3 Perspectives

The research presented here has shown some aspects that deserve further attention and development. At first, it must be noted that the hydrometeor classification technique developed for the 2DVD (Chapter 3) was applied only to populations of hydrometeors observed during 60 s time intervals. The next natural step would be to apply similar methods to classify individual particles, such that explicit mixtures could be quantified as well. The framework for this future implementation exists even though geometrical descriptors of higher complexity and a large

amount of human supervision will be necessary. It is also worth to underline that the method is a-priori easily adaptable to other particle imagers.

Other important aspects to further develop are related to the unsupervised hydrometeor classification approach presented in Chapter 4. It was shown that unsupervised clustering can lead to microphysically significant partitions of datasets of polarimetric data. In our case this was done using short range (≤ 30 km) X-band radar data. The next step would be to adapt the approach to lower radar frequencies and longer ranges, where beam broadening effect will be significant. Additionally, the spatial constraints employed in the work presented in the thesis were objectively oversimplified and more refined spatial descriptors would be beneficial to the approach. Finally, once demonstrated that unsupervised data-driven methods can lead to similar results than model-driven approaches, the natural follow up is to use both strategies in a semi-supervised manner by taking advantage of the merits of each approach.

The end of Chapter 5 was devoted to the interpretation of the effect of wind shear on the possible enhancement of snowfall production in an Alpine valley. Even though one case was shown here, it was not the only example when this kind of enhancement was observed in the central Alps. It is not unreasonable to believe that such effects may have a major role in the production of snowfall in similar locations and therefore it would be worth to investigate this relation over a larger and more statistically significant sample of snowfall events. Because LTE has available such data for different locations of the Swiss Alps, it would be interesting to access similar databases collected in other locations and in other climatic regions to better understand the process.

A Appendix of Chapter 2

A.1 Adaptations for S- and C-band frequencies of the KFE algorithm

The relation between K_{dp} and δ_{hv} depends on the frequency of the radar wave and consequently needs to be adapted for radars that operate at S- or at C-band frequencies. We therefore provide linear fits, similar to those given in Eq.(2.18), such that the constant b in the measurement vector (see Eq.2.23) and the constant c contained in the F-matrix (see Eq.2.24) can be adapted accordingly.

At S-band, the following relations were found:

$$\delta_{hv}^{\text{fit}} = \begin{cases} 0.19K_{dp} + 0.024 & ; K_{dp} \leq 1.1^\circ \text{ km}^{-1} \\ 0.019K_{dp} + 0.15 & ; K_{dp} > 1.1^\circ \text{ km}^{-1} \end{cases} \quad (\text{A.1})$$

At C-band, the relation is as follows:

$$\delta_{hv}^{\text{fit}} = \begin{cases} 0.53K_{dp} + 0.036 & ; K_{dp} \leq 2.5^\circ \text{ km}^{-1} \\ 0.15K_{dp} + 1.03 & ; K_{dp} > 2.5^\circ \text{ km}^{-1} \end{cases} \quad (\text{A.2})$$

A.2 Parametrization of covariance matrices

The determination of the necessary covariance matrices is usually not a straightforward task, since the true spatial behaviour of the differential phase needs to be known in a variety of precipitation situations and for different radar range resolutions. This information is generally not available, hence an easy way to get the parametrization of the covariance matrices is provided here. This parametrization allows to accurately compute the covariance matrices as a function of the radar range resolution (affecting $C(\epsilon_{s(i)})$) and the standard deviation of the noise in Ψ_{dp} , denoted as $\sigma_{\Psi_{dp}}$ (affecting $C(\epsilon_{z(i)})$). For the parametrization of $C(\epsilon_{s(i)})$, the covariance matrix was calculated for a range resolution Δr of 50, 100, 150, 200 and 250 m. Every element in the resulting matrices was then polynomially fitted as a function of the range resolution. It was found that a linear fit on the square root of the matrix elements was an appropriate approximation, which also ensures that negative values in the parametrized

covariance matrix are suppressed. The result of this procedure is depicted in the following matrix:

$$C(\epsilon_{s(i)}) = \begin{pmatrix} (0.11, 1.56)^2 & (0.11, 1.85)^2 & 0 & (0.01, 1.10)^2 \\ (0.11, 1.85)^2 & (0.18, 3.03)^2 & 0 & (0.01, 1.23)^2 \\ 0 & 0 & 0 & 0 \\ (0.01, 1.10)^2 & (0.01, 1.23)^2 & 0 & (-0.04, 1.27)^2 \end{pmatrix} \quad (\text{A.3})$$

Every matrix element consists of two parameters, which are the polynomial coefficients. For example, the (1,1) matrix element that reads 0.11, 1.56 stands for the value ${}^{1,1}C(\epsilon_{s(i)}) = (0.11 + 1.56\Delta r)^2$, where Δr is in km).

With the same procedure, a parametrization of the $C(\epsilon_{z(i)})$ is obtained as a function of $\sigma_{\Psi_{dp}}$ (which needs to be expressed in degrees):

$$C(\epsilon_{z(i)}) = \begin{pmatrix} \sigma_{\Psi_{dp}}^2 & 0 & 0 \\ 0 & \sigma_{\Psi_{dp}}^2 & 0 \\ 0 & 0 & 1.57 \end{pmatrix} \quad (\text{A.4})$$

In our case, $\sigma_{\Psi_{dp}}$ is 2° . The above measurement covariance matrix is dominated by the noise in Ψ_{dp} , although there is also a slight dependence on the range resolution. It was however found that neglecting this dependence does not remarkably influence the algorithm's performance. In addition, the off-diagonal elements of $C(\epsilon_{z(i)})$ were set to zero, since no clear dependence with $\sigma_{\Psi_{dp}}$ was observed and since the exact calculations showed that these values are anyway very small.

The matrix $C(\epsilon_{s(i)})$ also slightly scales with the frequency of the radar, since the K_{dp} values are usually lower at lower frequencies. However, due to the fact that $C(\epsilon_{s(i)})$ is multiplied with different scaling factors in order to generate the ensemble of K_{dp} estimates, this effect is only of marginal importance and can therefore be ignored.

A.3 Simulated rainfall events

The rainfall events employed in the numerical evaluation of K_{dp} , and generated with the method of *Schleiss et al.* (2012), cover a range of rainfall typologies associated with a temperate mid-latitude climatology. The summary characteristics of each event are reported in Table A.1. The classification of the rain events in the three classes of Transitional, Convective and Stratiform is rather qualitative and based on the observation of their spatial structure and intensity. The description of these classes can be found in *Jaffrain and Berne* (2012). An example of the rainfall fields associated with one time step of each event can be found in Figure A.1.

A.4. Realistic profiles of phase related variables

Table A.1: Summary of the general characteristics of the 6 simulated rain events employed.

Event	Type	Intermittency [%]	Advection [m s^{-1}]	Max R [mm h^{-1}]	Mean R [mm h^{-1}]
1	Transitional	20	10 NE	12	4.5
2	Convective	55	10 NE	52	5
3	Stratiform	0	10 NW	8	2
4	Transitional	20	10 NW	19	3
5	Convective	50	7.5 NW	51	8.5
6	Convective	70	7.5 NW	125	15

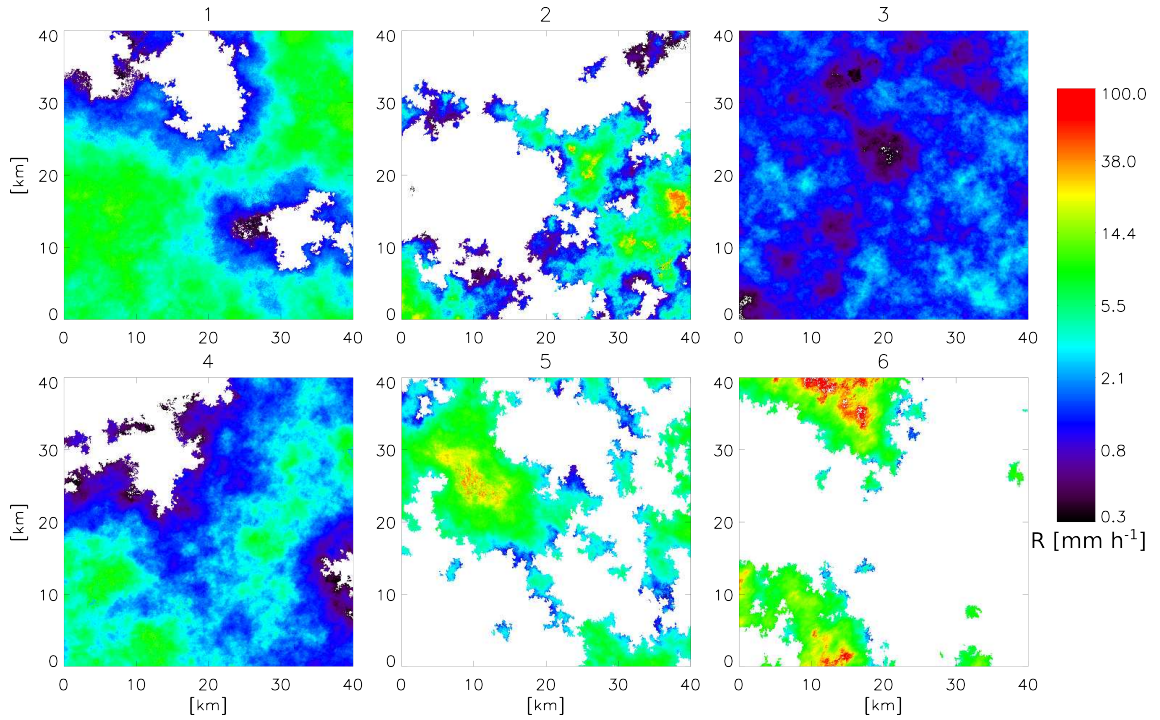


Figure A.1: Example of 6 simulated rain fields with a domain size of 40 km and a resolution of 0.1 km, corresponding to different events types. The variable plotted is the rain rate R [mm h^{-1}].

A.4 Realistic profiles of phase related variables

The present section aims to provide more details about the simulation of phase related radar variables. In the main body of the thesis, the two dimensional DSD fields and the scattering simulations have been described while here the focus is on the transition between these two aspect i.e., how the extraction of the profiles has been implemented.

The simulated DSD fields are grids of pixels with a spatial resolution of 0.1 km, and for each pixel the three parameters of a Gamma DSD are available. In order to obtain a statistically significant amount of profiles, they are assumed to cross the observed domain in the horizontal (East to West) or vertical (South to North) direction, as schematically shown in Figure A.2. In this way the simulated radar is virtually displaced horizontally and vertically along the edges of the domain, to record different profiles. It is important to note that this approach allows to obtain a large (statistically significant) dataset. The displacement of the radar furthermore

does not influence negatively the likelihood of each profile extracted.

Once each profile is localized within the DSD domain, the scattering simulations allow to assign to each range gate a value of K_{dp} and δ , according to the procedure described in the main body of the thesis. The most important step, at this point, is to assign the proper DSD to each range gate. Where the beam of the radar is fully included in a single pixel of the DSD fields, the Gamma DSD of that pixel is employed in the integrations, by discretization of the diameters with a step ΔD of 0.01 mm. On the contrary, where the beam of the radar covers more than a single pixel, the number of particles $N(D)$ assigned to each ΔD comes from a weighted average of the contribution of all the pixels involved. The weights are given by a Gaussian weighting function, describing the radar beam *Doviak and Zrnić (1993)*.

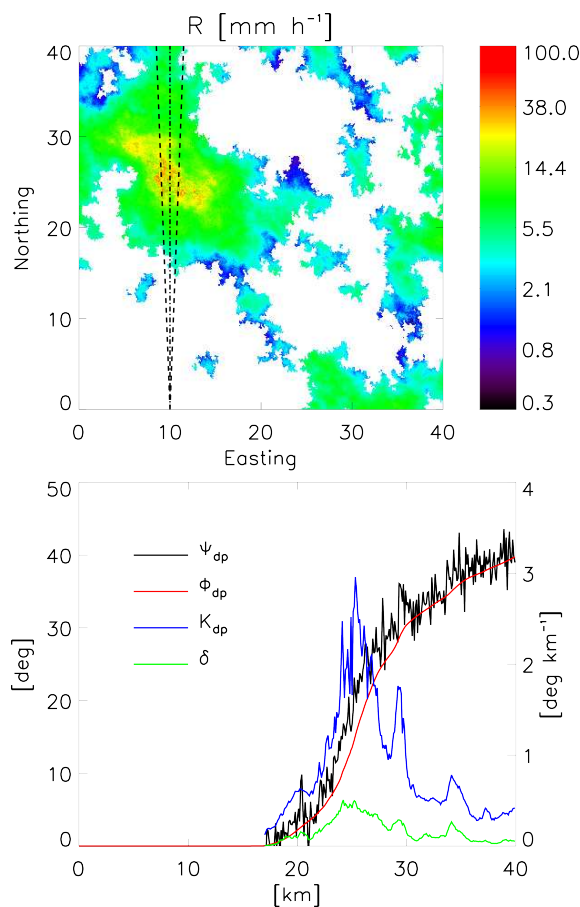


Figure A.2: Example of a simulated profile of the radar observable Ψ_{dp} and of the intrinsic K_{dp} and Φ_{dp} , extracted from a DSD field of a convective event. The upper panel shows the direction and broadening of the simulated radar beam while the bottom panel shows the extracted profiles.

A.5 Statistical Descriptors

In order to avoid any confusion related to the meaning of the statistical descriptor employed in Chapter 2, their explicit formulation is provided here. As global statistics, we introduced:

A.6. Accuracy evaluation at C-band and S-band using simulated fields

Normalized Absolute Error MNAE [%], Mean Normalized Bias (MNB) [%], Nash-Sutcliffe Efficiency (NSE) [-], Root Mean Squared Error (RMSE) [$^{\circ}$ km $^{-1}$] and Pearson correlation coefficient (ρ) [-]. Furthermore, in the analysis of the accuracy as a function of the K_{dp} value we mentioned the Normalized Relative Error (NRE) [%]. They are defined as:

$$MNAE = \frac{1}{n} \sum_{i=1}^n \frac{|K_{dp}^{e,i} - K_{dp}^{t,i}|}{K_{dp}^{t,i}} \times 100; \quad (A.5)$$

$$MNB = \frac{1}{n} \sum_{i=1}^n \frac{(K_{dp}^{e,i} - K_{dp}^{t,i})}{K_{dp}^{t,i}} \times 100; \quad (A.6)$$

$$NSE = 1 - \left[\frac{\sum_{i=1}^n (K_{dp}^{e,i} - K_{dp}^{t,i})^2}{\sum_{i=1}^N (\bar{K}_{dp}^t - K_{dp}^{t,i})^2} \right]; \quad (A.7)$$

$$RMSE = \sqrt{\frac{\sum_{i=1}^n (K_{dp}^{e,i} - K_{dp}^{t,i})^2}{n}}; \quad (A.8)$$

$$\rho = \frac{\text{Cov}(K_{dp}^t, K_{dp}^e)}{\sigma(K_{dp}^t)\sigma(K_{dp}^e)}; \quad (A.9)$$

$$NRE(i) = \frac{(K_{dp}^{e,i} - K_{dp}^{t,i})}{K_{dp}^{t,i}} \times 100; \quad (A.10)$$

where n is the total number of observations, $K_{dp}^{e,i}$ and $K_{dp}^{t,i}$ are the i -th estimated and true K_{dp} value and \bar{K}_{dp}^t indicates the mean of the true values. The Cov operator denotes covariance while σ is the standard deviation.

A.6 Accuracy evaluation at C-band and S-band using simulated fields

In the main body of the thesis, calculations were performed at the X band. It is useful to summarize the results of the same type of analysis, when conducted at C and S band. It is possible to generate an equal amount of profiles of Ψ_{dp} , and other phase related variables K_{dp} and δ at any radar frequency of interest. As the frequency decreases (wavelength increases), the effect of δ becomes less accentuated, and K_{dp} itself scales almost linearly with the frequency *Bringi and Chandrasekar (2001)*. The analysis of the estimation accuracy for the ALL, MWD

and KFE methods follows the same steps as described in the end of Chapter 2.

At first, at C and S band the optimal estimation length L for the MWD method is found to be of 2 km, as for X band. Shorter estimation lengths are unstable, while longer ones lead to an abrupt decrease in NSE and correlation coefficient ρ (not shown here). The MNAE for the three methods (always in the order ALI, MWD2, KFE), takes the value of 27, 22.8, 25.7% while the MNB is 6.4, 4.4 and 3.4%.

When other estimators, like NSE, ρ , and RMSE are taken into account, the KFE and MWD2 methods perform better. RMSEs for the three methods are 0.44, 0.37 and 0.33 [$^{\circ} \text{km}^{-1}$], NSEs are 0.66, 0.78 and 0.83, ρ are 0.82, 0.88 and 0.91. By looking at the evolution of the Normalized Relative Error as a function of K_{dp} , as shown in Figure A.3, we can extend the conclusions that we drew from the calculations at X-band. As K_{dp} increases, it tends to be underestimated with increasingly negatively bias (up to -50% for ALI, and -30% for MWD2), while the KFE algorithm is able to keep the bias to values higher than -25% (except for the highest K_{dp} values)

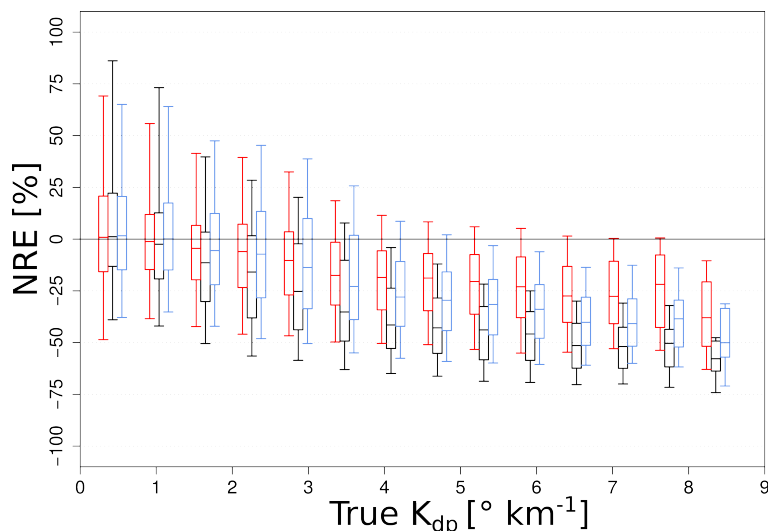


Figure A.3: Evolution of NRE [%] as a function of the true K_{dp} value for the ALI (black), MWD2 (blue) and KFE (red) methods. Calculation at C-band frequency.

A similar behaviour of the algorithms is observed at S-band even if the relative performances at this frequency tends to be closer to each other (Figure A.4). MNAEs for the three methods are 29.5, 24 and 26 [%], MNBs are 7.4, 5.5 and 4.5 [%], NSEs are 0.72, 0.78 and 0.82, ρ are 0.85, 0.89 and 0.91, RMSEs are 0.18, 0.17 and 0.15 [$^{\circ} \text{km}^{-1}$].

We can state that KFE outperforms the other algorithms at X, C and S bands but the major benefits of this algorithm are observed at X and C bands, where K_{dp} has a larger range of variation and more sensitivity with respect to the precipitation intensity (*Anagnostou et al., 2006*).

A.6. Accuracy evaluation at C-band and S-band using simulated fields

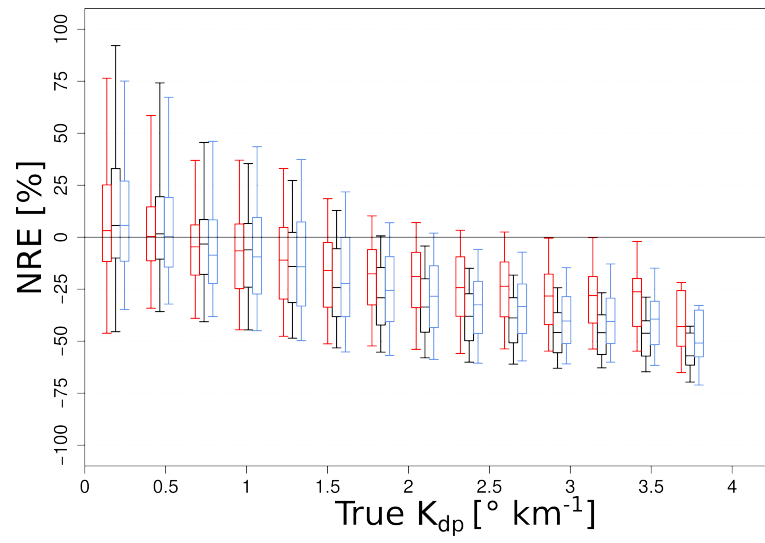


Figure A.4: As in Figure A.3, at S-band frequency.

B Appendix of Chapter 3

B.1 Minimum number of particles for a reliable classification

The classification method described in Chapter 3 employs as input a set of statistical features calculated over N particles, within a time step of length Δt . Thus, when N is small, sampling problems can affect the estimation of such statistics. We want to set a minimum N_{\min} , such that if $N > N_{\min}$ the classification output is reliable.

Figure B.1a shows the contribution that time steps of length Δt with small N had with respect to the total amount of data available, both in terms of total number of particles and in terms of total number of time steps.

We can observe that time steps with low N contribute negligibly to the total particle count, but significantly to the total count of available time steps. In other words, time steps with a low number of particles carry only a small part of the total precipitation, but they are observed frequently.

Figure B.1b illustrates the classification performance achieved when $N < 60$. This was obtained by taking random subsets of the available training set (with known labels), and using them as validation of the SVM algorithm trained previously. We can observe that for $N < 20$ the performance degraded sharply, and become more than 20 % lower than cases with $N > 60$. A threshold $N_{\min} = 20$ was therefore selected.

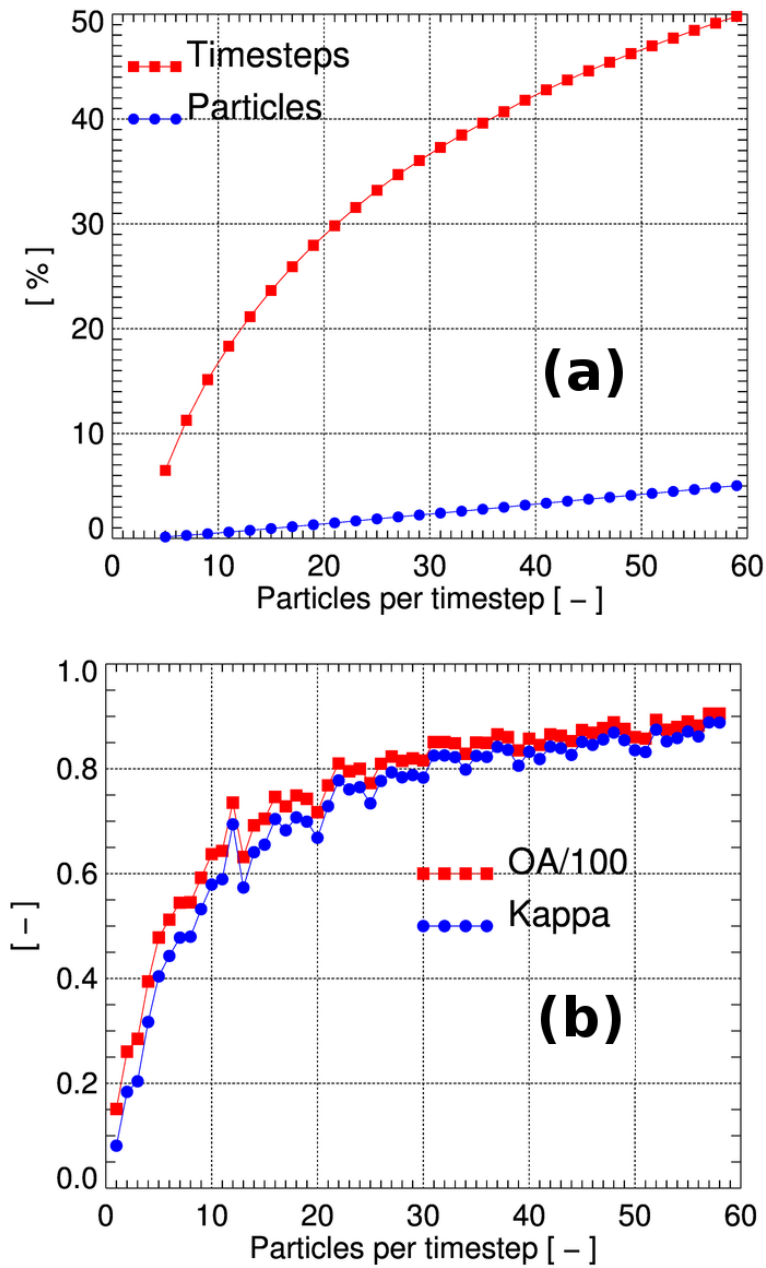


Figure B.1: (a) Contributions [%] of time steps of length Δt with less than 60 particles to the total database of observations. (b) Classification performance as a function of the number of particles recorded per time step. Time steps with less than 3 particles did not contribute to these statistics.

C Appendix of Chapter 4

C.1 Polarimetric characteristics of the seven clusters

Table C.1 provides the relevant statistics of each of the seven clusters identified in this work from a database of X-band radar data.

C.2 DR2009 algorithm

The algorithm denoted as DR2009 in Chapter 4 of the thesis is based on the work of *Dolan and Rutledge (2009)*, with some adaptations that we will highlight as they appear in this section. In this Appendix, we provide the exact parametrization of the membership functions for the fuzzy-logic scheme, as well as the weights assigned to each polarimetric variable. The input variables of the algorithm are Z_H [dBZ], Z_{DR} [dB], K_{dp} [$^{\circ}$ km $^{-1}$], ρ_{hv} [-], and Δz [m], and their weights in the fuzzy-logic scheme are 0.25, 0.25, 0.25, 0.08, and 0.17, respectively. Δz is the relative altitude with respect to the 0 $^{\circ}$ C isotherm, as defined in Sec 4.5.1, and this input is not used in *Dolan and Rutledge (2009)*.

The hydrometeor classes available are aggregates (AG), crystals (CR), drizzle (DZ), high-density graupel (HDG), low-density graupel (LDG), rain (R), vertical ice (VI), and wet snow (WS; not present in *Dolan and Rutledge, 2009*). The membership function employed for all the polarimetric inputs is a membership beta function β , while for Δz a trapezoidal one is used. β is defined as

$$\beta = \frac{1}{1 + \left(\frac{x-m}{a}\right)^{2b}}, \quad (\text{C.1})$$

where x is the considered polarimetric variable, m is the midpoint, a is the width, and b the slope. Table C.2 summarizes the values of the parameters for each polarimetric variable and each hydrometeor class.

Appendix C. Appendix of Chapter 4

Table C.1: Statistics describing the content of the seven clusters identified in Sects. 5 and 6. For each polarimetric variable and for each cluster, we provide the mean value, standard deviation σ , and a set of quantiles (Q1 %, Q5 %, 10 %, Q25 %, Q50 %, Q75 %, Q90 %, Q95 %, Q99 %).

Var.	Class	Colour	Mean	σ	Q1 %	Q5 %	Q10 %	Q25 %	Q50 %	Q75 %	Q90 %	Q95 %	Q99 %
Z_H	Melting snow (MS)	Yellow	30.2	6.2	14.1	18.8	21.5	26.6	30.9	34.5	37.6	39.5	42.3
Z_{DR}	Melting snow (MS)	Yellow	1.4	0.74	-0.2	0.2	0.4	0.8	1.3	1.7	2.3	2.6	3.2
K_{dp}	Melting snow (MS)	Yellow	0.3	0.29	-0.2	-0.1	0.0	0.2	0.3	0.5	0.7	0.9	1.2
ρ_{hv}	Melting snow (MS)	Yellow	0.92	0.041	0.78	0.83	0.86	0.9	0.93	0.95	0.96	0.97	0.97
Z_H	Heavy rain (HR)	Red	42.3	4.2	32.7	35.3	36.8	39.3	42.4	45.3	47.4	50.6	53.1
Z_{DR}	Heavy rain (HR)	Red	0.9	0.97	-1.2	-0.8	-0.6	0.2	1.1	1.6	2.0	2.4	2.9
K_{dp}	Heavy rain (HR)	Red	6.1	3.87	0.91	2.2	2.5	3.3	5.3	8.2	11.8	14.2	18.5
ρ_{hv}	Heavy rain (HR)	Red	0.97	0.015	0.92	0.94	0.95	0.96	0.97	0.98	0.99	0.99	0.99
Z_H	Light rain (LR)	Green	20.1	4.5	9.2	12.8	14.8	18	21	24	26.4	27.8	30.4
Z_{DR}	Light rain (LR)	Green	0.4	0.3	-0.2	-0.1	-0.1	0.1	0.2	0.4	0.6	0.8	1.1
K_{dp}	Light rain (LR)	Green	0.05	0.18	-0.2	-0.1	0	0	0	0.1	0.2	0.4	0.8
ρ_{hv}	Light rain (LR)	Green	0.99	0.009	0.97	0.98	0.99	0.99	0.99	1	1	1	1
Z_H	Rain (RN)	Blue	32.2	3.9	24.1	26.3	27.4	29.4	32.1	34.9	37.1	38.5	41.8
Z_{DR}	Rain (RN)	Blue	1.2	0.44	0.3	0.5	0.6	0.8	1.1	1.4	1.8	1.9	2.3
K_{dp}	Rain (RN)	Blue	0.3	0.42	-0.1	-0.05	0	0.1	0.2	0.4	0.8	1.3	2.1
ρ_{hv}	Rain (RN)	Blue	0.99	0.007	0.97	0.98	0.98	0.99	0.99	0.99	1	1	1
Z_H	Crystals/small aggregates (CR)	Cyan	11.2	4.1	-1.1	2.2	6.2	9.5	12.2	14.9	17	18	20.3
Z_{DR}	Crystals/small aggregates (CR)	Cyan	0.8	0.57	-0.3	0	0.1	0.4	0.8	1.2	1.7	2.1	2.5
K_{dp}	Crystals/small aggregates (CR)	Cyan	0.25	0.42	-0.2	-0.15	-0.1	0	0.2	0.4	0.8	1.3	1.9
ρ_{hv}	Crystals/small aggregates (CR)	Cyan	0.93	0.03	0.85	0.88	0.89	0.92	0.94	0.95	0.96	0.97	0.97
Z_H	Rimed-ice particles (RI)	Olive	24	4.4	16.5	18.2	19.6	21.2	23.3	25.9	29.6	33.2	38.2
Z_{DR}	Rimed-ice particles (RI)	Olive	0.24	0.35	-0.6	-0.3	-0.2	0	0.3	0.5	0.7	0.8	1
K_{dp}	Rimed-ice particles (RI)	Olive	0.7	0.64	-0.1	0	0.1	0.2	0.5	1	1.6	2	2.6
ρ_{hv}	Rimed-ice particles (RI)	Olive	0.99	0.01	0.95	0.97	0.97	0.98	0.99	0.99	0.99	0.99	0.99
Z_H	Aggregates (AG)	Magenta	16.5	7.7	10.9	12	14	16.5	19	21	22.1	24	28
Z_{DR}	Aggregates (AG)	Magenta	0.6	0.45	-0.3	-0.1	0	0.2	0.5	0.8	1.2	1.4	1.6
K_{dp}	Aggregates (AG)	Magenta	0.25	0.4	-0.2	-0.1	0	0.1	0.2	0.4	0.8	1.2	1.9
ρ_{hv}	Aggregates (AG)	Magenta	0.98	0.009	0.96	0.96	0.97	0.97	0.98	0.99	0.99	0.99	0.99

The trapezoidal membership function T employed for Δz instead takes the form of

$$T = \begin{cases} 0 & \text{if } x < l_1; \\ \frac{x-l_1}{l_2-l_1} & \text{if } l_1 < x \leq l_2; \\ 1 & \text{if } l_2 < x \leq r_1; \\ \frac{r_2-x}{r_2-r_1} & \text{if } r_1 < x \leq r_2; \\ 0 & \text{if } x > r_2, \end{cases} \quad (\text{C.2})$$

where l_1 , l_2 , r_1 , and r_2 define the four vertices of the trapezoid. The values for these parameters are reported in Table C.3.

C.2. DR2009 algorithm

Table C.2: Parameters of the membership beta functions β employed in the DR2009 algorithm: midpoint m , width a , and slope b for the available hydrometeor classes.

Variable Class		a	m	b
Z_H	Aggregates (AG)	17.0	16.0	3.0
Z_{DR}	Aggregates (AG)	0.7	0.7	3.0
K_{dp}	Aggregates (AG)	0.2	0.2	2.0
ρ_{hv}	Aggregates (AG)	0.011	0.989	1.0
Z_H	Crystals (CR)	22.0	-3.0	3.0
Z_{DR}	Crystals (CR)	2.6	3.2	3.0
K_{dp}	Crystals (CR)	0.15	0.15	2.0
ρ_{hv}	Crystals (CR)	0.015	0.985	1.0
Z_H	Drizzle (DZ)	29.0	2.0	3.0
Z_{DR}	Drizzle (DZ)	0.5	0.5	3.0
K_{dp}	Drizzle (DZ)	0.18	0.18	2.0
ρ_{hv}	Drizzle (DZ)	0.007	0.992	1.0
Z_H	High-density graupel (HDG)	11.0	43.0	3.0
Z_{DR}	High-density graupel (HDG)	2.5	1.2	3.0
K_{dp}	High-density graupel (HDG)	5.1	2.5	2.0
ρ_{hv}	High-density graupel (HDG)	0.018	0.983	1.0
Z_H	Low-density graupel (LDG)	10.0	34.0	3.0
Z_{DR}	Low-density graupel (LDG)	1.0	0.3	3.0
K_{dp}	Low-density graupel (LDG)	2.1	0.7	2.0
ρ_{hv}	Low-density graupel (LDG)	0.007	0.993	1.0
Z_H	Rain (R)	17.0	42.0	3.0
Z_{DR}	Rain (R)	2.8	2.7	3.0
K_{dp}	Rain (R)	12.9	12.6	2.0
ρ_{hv}	Rain (R)	0.01	0.99	1.0
Z_H	Vertical ice (VI)	28.5	3.5	3.0
Z_{DR}	Vertical ice (VI)	1.3	-0.8	3.0
K_{dp}	Vertical ice (VI)	0.08	-0.1	2.0
ρ_{hv}	Vertical ice (VI)	0.035	0.965	1.0
Z_H	Wet snow (WS)	20.0	30.0	3.0
Z_{DR}	Wet snow (WS)	1.4	2.2	3.0
K_{dp}	Wet snow (WS)	1.0	1.0	2.0
ρ_{hv}	Wet snow (WS)	0.135	0.835	1.0

Table C.3: Parameters of the trapezoidal membership function T applied to the relative altitude with respect to the 0 °C isotherm (Δz [m]). l_1 , l_2 , l_3 , and l_4 are the four vertices of the trapezoid T .

Variable Class		l_1	l_2	r_1	r_2
Δz	Aggregates (AG)	0	500	20 000	25 000
Δz	Crystals (CR)	0	500	20 000	25 000
Δz	Drizzle (DZ)	-25 000	-20 000	-100	0
Δz	High-density graupel (HDG)	-600	100	20 000	25 000
Δz	Low-density graupel (LDG)	-600	100	20 000	25 000
Δz	Rain (R)	-25 000	-20 000	-100	0
Δz	Vertical ice (VI)	-50	0	20 000	25 000
Δz	Wet snow (WS)	-1000	-700	700	1000

Bibliography

- Abe, O. (2004), Shear strength and angle of repose of snow layers including graupel, in *Annals of Glaciology*, vol. 38, pp. 305–308, Int Glaciol Soc; Swiss Fed Inst Snow & Avalanches, Davos, Switzerland, doi: 10.3189/172756404781815149.
- Al-Sakka, H., A.-A. Boumahmoud, B. Fradon, S. J. Frasier, and P. Tabary (2013), A new fuzzy logic hydrometeor classification scheme applied to the french X-, C-, and S-band polarimetric radars, *J. Appl. Meteor. Clim.*, 52(10), 2328–2344, doi: 10.1175/JAMC-D-12-0236.1.
- Anagnostou, M. N., E. N. Anagnostou, and J. Vivekanandan (2006), Correction for rain path specific and differential attenuation of X-band dual-polarization observations, *IEEE T. Geosci. Remote Sens.*, 44(9), 2470–2480, doi: 10.119/TGRS.2006.873204.
- Andric, J., M. R. Kumjian, D. S. Zrnica, J. M. Straka, and V. M. Melnikov (2013), Polarimetric signatures above the melting layer in winter storms: An observational and modeling study, *J. Appl. Meteor. Clim.*, 52(3), 682–700, doi: 10.1175/JAMC-D-12-028.1.
- Andsager, K., K. V. Beard, and N. F. Laird (1999), Laboratory measurements of axis ratios for large rain drops, *J. Atmos. Sci.*, 56(15), 2673–2683.
- Avila, E. E., N. E. Castellano, C. P. R. Saunders, R. E. Buergesser, and G. G. Aguirre Varela (2009), Initial stages of the riming process on ice crystals, *Geophys. Res. Lett.*, 36, doi: 10.1029/2009GL037723.
- Bailey, M. P., and J. Hallett (2009), A comprehensive habit diagram for atmospheric ice crystals: conformation from the laboratory, AIRS II, and other field studies, *J. Atmos. Sci.*, 66(9), 2888–2899, doi: 10.1175/2009JAS2883.1.
- Baltensperger, U., H. W. Gaggeler, D. T. Jost, M. Lugauer, M. Schwikowski, E. Weingartner, and P. Seibert (1997), Aerosol climatology at the high-alpine site jungfrau-joch, Switzerland, *J. Geophys. Res. Atmos.*, 102(D16), 19,707–19,715, doi: 10.1029/97JD00928.
- Battaglia, A., E. Rustemeier, A. Tokay, U. Blahak, , and C. Simmer (2010), PARSIVEL snow observations: a critical assessment, *J. Atmos. Oceanic Technol.*, 27(2), 333–344, doi: 10.1175/2009JTECHA1332.1.

Bibliography

- Beard, K., and R. Kubesh (1991), Laboratory measurements of small raindrop distortion. Part 2: Oscillation frequencies and modes, *J. Atmos. Sci.*, 48(20), 2245–2264.
- Beard, K. V. (1976), Terminal velocity and shape of cloud and precipitation drops aloft, *J. Atmos. Sci.*, 33(5), 851–864.
- Beard, K. V., and C. Chuang (1987), A new model for the equilibrium shape of raindrops, *J. Atmos. Sci.*, 44(3), 1509–1524.
- Beard, K. V., V. N. Bringi, and M. Thurai (2010), A new understanding of raindrop shape, *Atmos. Res.*, 97(4), 396–415, doi: 10.1016/j.atmosres.2010.02.001.
- Bechini, R., and V. Chandrasekar (2015), A semisupervised robust hydrometeor classification method for dual-polarization radar applications, *J. Atmos. Oceanic Technol.*, 32(1), 22–47, doi: 10.1175/JTECH-D-14-00097.1.
- Bechini, R., L. Baldini, V. Chandrasekar, R. Cremonini, and E. Gorgucci (2011), Observations of KDP in the ice region of precipitating clouds at X- and C-band radar frequencies, in *Proc. 35th AMS Conf. Radar Meteorol.*, p. P7A.4, Pittsburgh, USA.
- Bechini, R., L. Baldini, and V. Chandrasekar (2013), Polarimetric radar observations in the ice region of precipitating clouds at c-band and x-band radar frequencies, *J. Appl. Meteor. Clim.*, 52, 1147–1169, doi: 10.1175/JAMC-D-12-055.1.
- Berne, A., and W. F. Krajewski (2013), Radar for hydrology: Unfulfilled promise or unrecognized potential?, *Adv. Water Resour.*, 51(1), 357–366, doi: 10.1016/j.advwatres.2012.05.005.
- Bluestein, H. B., and J. C. Snyder (2015), An observational study of the effects of dry air produced in dissipating convective storms on the predictability of severe weather, *Weather Forecast.*, 30(1), 79–114, doi: 10.1175/WAF-D-14-00065.1.
- Boser, B., I. Guyon, and V. Vapnik (1992), A training algorithm for optimal margin classifiers, in *5th ACM Workshop on Computational Learning Theory*, pp. 144–152, Pittsburgh, USA.
- Boudevillain, B., G. Delrieu, B. Galabertier, L. Bonnifait, L. Bouilloud, P.-E. Kirstetter, and M.-L. Mosini (2011), The Cévennes-Vivarais Mediterranean Hydrometeorological Observatory database, *Water Resour. Res.*, 47, W07701, doi: 10.1029/2010WR010353.
- Bousquet, O., et al. (2014), Multiple-frequency radar observations collected in southern France during the field phase of the hydrometeorological cycle in the Mediterranean experiment (hymex), *Bull. Amer. Meteor. Soc.*, accepted.
- Brandes, E., A. Ryzhkov, and D. Zrnica (2001), An evaluation of radar rainfall estimates from specific differential phase, *J. Atmos. Oceanic Technol.*, 18(3), 363–375.
- Brandes, E. A., K. Ikeda, G. Zhang, M. Schonhuber, and R. R. M. (2007), A statistical and physical description of hydrometeor distributions in Colorado snowstorms using a video disdrometer, *J. Appl. Meteor. Clim.*, 46(5), 634–650, doi: 10.1175/JAM2489.1.

- Bringi, V. N., and V. Chandrasekar (2001), *Polarimetric doppler weather radar*, 662 pp., Cambridge University Press.
- Brocard, E., M. Schneebeli, and C. Mätzler (2011), Detection of cirrus clouds using infrared radiometry, *IEEE T. Geosci. Remote Sens.*, 49(2), 595–602, doi: 10.1109/TGRS.2010.2063033.
- Brooks, H. E., J. W. Lee, and J. P. Craven (2003), The spatial distribution of severe thunderstorm and tornado environments from global reanalysis data, *Atmos. Res.*, 67-8(SI), 73–94, doi: 10.1016/S0169-8095(03)00045-0.
- Camps-Valls, G., and L. Bruzzone (2005), Kernel-based methods for hyperspectral image classification, *IEEE T. Geosci. Remote Sens.*, 43(6), 1351–1362, doi: 10.1109/TGRS.2005.846154.
- Camps-Valls, G., and L. Bruzzone (Eds.) (2009), *Kernel Methods for Remote Sensing Data Analysis*, 434 pp., Wiley.
- Cantrell, W., and A. Heymsfield (2005), Production of ice in tropospheric clouds, *Bull. Amer. Meteor. Soc.*, 86(6), 795–897, doi: 10.1175/BAMS-86-6-795.
- Cao, Q., G. F. Zhang, E. Brandes, T. Schuur, A. Ryzhkov, and K. Ikeda (2008), Analysis of video disdrometer and polarimetric radar data to characterize rain microphysics in Oklahoma, *J. Appl. Meteor. Clim.*, 47(8), 2238–2255, doi: 10.1175/2008JAMC1732.1.
- Chandrasekar, V., R. Keranen, S. Lim, and D. Moisseev (2013), Recent advances in classification of observations from dual polarization weather radars, *Atmos. Res.*, 119, 97–111, doi: 10.1016/j.atmosres.2011.08.014.
- Chen, J. P., and D. Lamb (1994), The theoretical basis for the parametrization of ice crystal habits - growth by vapor-deposition, *J. Atmos. Sci.*, 51(9), 1206–1221, doi: 10.1175/1520-0469(1994)051<1206:TTBFTP>2.0.CO;2.
- Ciais, P., et al. (2005), Europe-wide reduction in primary productivity caused by the heat and drought in 2003, *Nature*, 437(7058), 529–533, doi: 10.1038/nature03972.
- Colle, B. A., D. Stark, and S. E. Yuter (2014), Surface microphysical observations within east coast winter storms on long island, new york, *Mon. Weather Rev.*, 142(9), 3126–3146, doi: 10.1175/MWR-D-14-00035.1.
- Cover, T. M. (1965), Geometrical and statistical properties of systems of linear inequalities with applications in pattern recognition, *IEEE Transactions on Electronics and Computers*, EC-14(3), 326–334.
- Dawson, D. T., I. I., E. R. Mansell, and M. R. Kumjian (2015), Does wind shear cause hydrometeor size sorting?, *J. Atmos. Sci.*, 72(1), 340–348, doi: 10.1175/JAS-D-14-0084.1.

Bibliography

- Delanoe, J., A. Protat, O. Jourdan, J. Pelon, M. Papazzoni, R. Dupuy, J. F. Gayet, and C. Jouan (2013), Comparison of airborne in situ, airborne radar-lidar, and spaceborne radar-lidar retrievals of polar ice cloud properties sampled during the polarcat campaign, *J. Atmos. Oceanic Technol.*, 30(1), 57–73, doi: 10.1175/JTECH-D-11-00200.1.
- Dolan, B., and S. A. Rutledge (2009), A theory-based hydrometeor identification algorithm for X-band polarimetric radars, *J. Atmos. Oceanic Technol.*, 26(10), 2071–2088, doi: 10.1175/2009JTECHA1208.1.
- Dolan, B., S. A. Rutledge, S. Lim, V. Chandrasekar, and M. Thurai (2013), A robust C-band hydrometeor identification algorithm and application to a long-term polarimetric radar dataset, *J. Appl. Meteor. Clim.*, 52(9), 2162–2186, doi: 10.1175/JAMC-D-12-0275.1.
- Doviak, R., and D. Zrnić (1993), *Doppler radar and weather observations, second edition*, 562 pp., Academic Press, San Diego.
- Doviak, R., and D. Zrnić (2006), *Doppler radar and weather observations, second edition*, 592 pp., Dover Publications.
- Drufuca, G., and I. Zawadzki (1975), Statistics of rain gauge data, *J. Appl. Meteor.*, 14, 1419–1429.
- Ducrocq, V., et al. (2014), Hymex-sopi the field campaign dedicated to heavy precipitation and flash flooding in the northwestern mediterranean, *Bull. Amer. Meteor. Soc.*, 95(7), 1083+, doi: 10.1175/BAMS-D-12-00244.1.
- Elmore, K. L. (2010), The nssl hydrometeor classification algorithm in winter surface precipitation: evaluation and future development, *Weather Forecast.*, 26(5), 756–765, doi: 10.1175/WAF-D-10-05011.1.
- Evaristo, R., T. Bals-Elsholz, E. Williams, A. J. Fenn, M. Donovan, and D. Smalley (2013), Relationship of graupel shape to differential reflectivity: theory and observations, in *29th Conference on Environmental Information Processing Technologies*, Austin, USA.
- Evensen, G. (1994), Sequential data assimilation with a non-linear quasi-geostrophic model using Monte-Carlo methods to forecast error statistics, *J. Geophys. Res.*, 99(C5), 10,143–10,162.
- Fabry, F. (1996), On the determination of scale ranges for precipitation fields, *J. Geophys. Res.*, 101(D8), 12,819–12,826.
- Feind, R. E. (2008), Comparison of three classification methodologies for 2d probe hydrometeor images obtained from the armored t-28 aircraft, *Tech. Rep. SDSMT/IAS/R08-01*, Institute of Atmospheric Sciences, South Dakota School of Mines and Technology, Rapid City, SD, USA.
- Foresti, L., D. Tuia, M. Kanevski, and A. Pozdnoukhov (2011), Learning wind fields with multiple kernels, *Stoch. Env. Res. Risk A.*, 25(1), 51–66, doi: {10.1007/s00477-010-0405-0}.

- Frei, C., R. Scholl, S. Fukutome, R. Schmidli, and P. L. Vidale (2006), Future change of precipitation extremes in Europe: Intercomparison of scenarios from regional climate models, *J. Geophys. Res.*, *111*(D6), doi: 10.1029/2005JD005965.
- Fukuta, N., and T. Takahashi (1999), The growth of atmospheric ice crystals: A summary of findings in vertical supercooled cloud tunnel studies, *J. Atmos. Sci.*, *56*(12), 1963–1979, doi: 10.1175/1520-0469(1999)056<1963:TGOAIC>2.0.CO;2.
- Garrett, T. J., C. Fallgatter, K. Shkurko, and D. Howlett (2012), Fall speed measurement and high-resolution multi-angle photography of hydrometeors in free fall, *Atmos. Meas. Tech.*, *5*(11), 2625–2633, doi: 10.5194/amt-5-2625-2012.
- Gelb, A. (1988), *Applied optimal estimation*, 374 pp., The MIT press.
- Germann, U., and J. Joss (2001), Variograms of radar reflectivity to describe the spatial continuity of Alpine precipitation, *J. Appl. Meteor.*, *40*(6), 1042–1059.
- Goosaert, E., and R. Alam (2009), Ensemble classifier for winter storm precipitation in polarimetric radar data, in *Seventh conference on artificial intelligence and its applications to the environmental sciences*, Phoenix, USA.
- Gorgucci, E., G. Scarchilli, and V. Chandrasekar (1999), Specific differential phase estimation in the presence of nonuniform rainfall medium along the path, *J. Atmos. Oceanic Technol.*, *16*(11, Part 2), 1690–1697.
- Gorgucci, E., V. Chandrasekar, and L. Baldini (2009), Can a unique model describe the raindrop shape–size relation? A clue from polarimetric radar measurements, *J. Atmos. Oceanic Technol.*, *26*(9), 1829–1842, doi: 10.1175/2009JTECHA1183.1.
- Gourley, J. J., P. Tabary, and J. Parent-du Chatelet (2007), A fuzzy logic algorithm for the separation of precipitating from nonprecipitating echoes using polarimetric radar observations, *J. Atmos. Oceanic Technol.*, *24*(8), 1439–1451, doi: 10.1175/JTECH2035.1.
- Grazioli, J., M. Schneebeli, and A. Berne (2014a), Accuracy of phase-based algorithms for the estimation of the specific differential phase shift using simulated polarimetric weather radar data, *IEEE Geosci. Remote Sens. Lett.*, *11*(4), 763–767, doi: 10.1109/LGRS.2013.2278620.
- Grazioli, J., D. Tuia, S. Monhart, M. Schneebeli, T. Raupach, and A. Berne (2014b), Hydrometeor classification from two-dimensional video disdrometer data, *Atmos. Meas. Tech.*, *7*(9), 2869–2882, doi: 10.5194/amt-7-2869-2014.
- Grazioli, J., D. Tuia, and A. Berne (2015a), Hydrometeor classification from polarimetric radar measurements: a clustering approach, *Atmos. Meas. Tech.*, *8*(1), 149–170, doi: 10.5194/amt-8-149-2015.
- Grazioli, J., G. Lloyd, L. Panziera, P. Connolly, J. Henneberger, and A. Berne (2015b), Riming in winter alpine snowfall during clace 2014: polarimetric radar and in-situ observations, *Atmos. Chem. Phys.*, in submission.

Bibliography

- Gregory, D., J. J. Morcrette, C. Jakob, A. C. M. Beljaars, and T. Stockdale (2000), Revision of convection, radiation and cloud schemes in the ecmwf integrated forecasting system, *Q. J. Roy. Meteor. Soc.*, 126(566, A), 1685–1710, doi: 10.1256/smsqj.56607.
- Halkidi, M., Y. Batistakis, and M. Vazirgiannis (2002), Clustering validity checking methods: Part ii, *SIGMOD Rec.*, 31(3), 19–27.
- Hallett, J., and S. C. Mossop (1974), Production of secondary ice particles during the riming process, *Nature*, 249(5452), 26–28, doi: 10.1038/249026a0.
- Hanesch, M. (1999), Fall velocity and shape of snowflakes, Ph.D. thesis, Swiss Federal Institute of Technology Zurich.
- Harimaya, T., and Y. Sato (1989), Measurement of the riming amount on snowflakes, *J. Fac. Sci. Hokkaido University*, 8, 355–366.
- Hastie, T., and R. Tibshirani (1998), Classification by pairwise coupling, *Ann. Stat.*, 26(2), 451–471.
- Heymsfield, A. (1972), Ice crystal terminal velocities, *J. Atmos. Sci.*, 29(7), 1348–1357.
- Heymsfield, A. (1977), Precipitation development in stratiform ice clouds - microphysical and dynamical study, *J. Atmos. Sci.*, 34(2), 367–381.
- Hobbs, P. V., S. Chang, and J. D. Locatelli (1974), The dimensions and aggregation of ice crystals in natural clouds, *J. Geophys. Res.*, 79(15), 2199–2206, doi: 10.1029/JC079i015p02199.
- Hogan, R. J., P. R. Field, A. J. Illingworth, R. J. Cotton, and T. W. Choullarton (2002), Properties of embedded convection in warm-frontal mixed-phase cloud from aircraft and polarimetric radar, *Q. J. Roy. Meteor. Soc.*, 128(580, B), 451–476, doi: 10.1256/003590002321042054.
- Hogan, R. J., P. N. Francis, H. Flentje, A. J. Illingworth, M. Quante, and J. Pelon (2003), Characteristics of mixed-phase clouds. i: Lidar, radar and aircraft observations from clare'98, *Q. J. Roy. Meteor. Soc.*, 129(592, A), 2089–2116, doi: 10.1256/qj.01.208.
- Houze, R. A., and S. Medina (2005), Turbulence as a mechanism for orographic precipitation enhancement, *J. Atmos. Sci.*, 62(10), 3599–3623.
- Houze, R. A. J. (1993), *Cloud dynamics*, 573 pp., Academic Press, San Diego.
- Huang, G., V. N. Bringi, R. Cifelli, D. Hudak, and W. A. Petersen (2010), A methodology to derive radar reflectivity liquid equivalent snow rate relations using c-band radar and a 2d video disdrometer, *J. Atmos. Oceanic Technol.*, 27, 637–651.
- Hubbert, J., and V. N. Bringi (1995), An iterative technique filtering technique for the analysis of copolar differential phase and dual-frequency polarimetric variables, *J. Atmos. Oceanic Technol.*, 12(3), 643–648.

- Hubbert, J., V. Chandrasekar, V. N. Bringi, and P. F. Meischner (1993), Processing and interpretation of coherent dual-polarized radar measurements, *J. Atmos. Oceanic Technol.*, 10(2), 155–164.
- Hubbert, J. C., S. M. Ellis, W. Y. Chang, S. Rutledge, and M. Dixon (2014), Modeling and interpretation of s-band ice crystal depolarization signatures from data obtained by simultaneously transmitting horizontally and vertically polarized fields, *J. Appl. Meteor. Clim.*, 53(6), 1659–1677, doi: 10.1175/JAMC-D-13-0158.1.
- Hurrell, J. W. (1995), Decadal trends in the north-atlantic oscillation - regional temperatures and precipitation, *Science*, 269(5224), 676–679, doi: 10.1126/science.269.5224.676.
- Ignaccolo, M., and C. De Michele (2014), Phase space parameterization of rain: The inadequacy of gamma distribution, *J. Appl. Meteor. Clim.*, 53(2), 548–562, doi: 10.1175/JAMC-D-13-050.1.
- Illingworth, A. J. (2004), Improved precipitation rates and data quality by using polarimetric measurements, in *Weather radar: principles and advanced applications*, edited by P. Meischner, pp. 130–166, Springer.
- Ivanova, K., E. E. Clothiaux, H. N. Shirer, T. P. Ackerman, J. C. Liljegren, and M. Ausloos (2002), Evaluating the quality of ground-based microwave radiometer measurements and retrievals using detrended fluctuation and spectral analysis methods, *J. Appl. Meteor.*, 41(1), 56–68.
- Jaffrain, J., and A. Berne (2011), Experimental quantification of the sampling uncertainty associated with measurements from Parsivel disdrometers, *J. Hydrometeor.*, 12(3), doi: 10.1175/2010JHM1244.1.
- Jaffrain, J., and A. Berne (2012), Quantification of the small-scale spatial structure of the raindrop size distribution from a network of disdrometers, *J. Appl. Meteor. Clim.*, 51(5), 941–953, doi: 10.1175/JAMC-D-11-0136.1.
- Jain, A. K., and R. C. Dubes (1988), *Algorithms for Clustering Data*, 320 pp., Prentice-Hall, Inc., Upper Saddle River, NJ, USA.
- Jain, A. K., M. N. Murty, and P. J. Flynn (1999), Data clustering: a review, *ACM Computing Survey*, 31(3), 264–323.
- Jain, A. K., R. P. W. Duin, and J. C. Mao (2000), Statistical pattern recognition: A review, *IEEE Transactions on Pattern Analysis and Machine Intelligence*, 22(1), 4–37, doi: 10.1109/34.824819.
- Jameson, A. R. (1983), Microphysical interpretation of multi-parameter radar measurements in rain: Part II: estimation of raindrop distribution parameters by combined dual-wavelength and polarization measurements, *J. Atmos. Sci.*, 40(7), 1803–1813.

Bibliography

- Jameson, A. R., and A. B. Kostinski (1997), Fluctuation properties of precipitation. Part I: on deviations of single-size drop counts from the Poissonian distribution, *J. Atmos. Sci.*, *54*, 2174–2186.
- Jiao, L., and Y. Liu (2012), Analyzing the shape characteristics of land use classes in remote sensing imagery, *ISPRS Annals of Photogrammetry, Remote Sensing and Spatial Information Sciences*, *I-7*, 135–140, doi: 10.5194/isprsannals-I-7-135-2012.
- Joss, J., and E. Gori (1978), Shapes of raindrop size distributions, *J. Appl. Meteor.*, *17*, 1054–1061.
- Kalman, R. E. (1960), A new approach to linear filtering and prediction theory, *Trans. ASME J. Basic Eng.*, *82*, Series D.
- Kennedy, P. C., and S. A. Rutledge (2011), S-band dual polarization radar observations of winter storms, *J. Appl. Meteor. Clim.*, *50*(4), doi: 10.1175/2010JAMC2558.1.
- Kruger, A., and W. F. Krajewski (2002), Two-dimensional video disdrometer: a description, *J. Atmos. Oceanic Technol.*, *19*(5), 602–617.
- Kumjian, M. R., S. A. Rutledge, R. M. Rasmussen, P. C. Kennedy, and M. Dixon (2014), High-resolution polarimetric radar observations of snow-generating cells, *J. Appl. Meteor. Clim.*, *53*(6), 1636–1658, doi: 10.1175/JAMC-D-13-0312.1.
- Lance, S., C. A. Brock, D. Rogers, and J. A. Gordon (2010), Water droplet calibration of the cloud droplet probe (cdp) and in-flight performance in liquid, ice and mixed-phase clouds during arcpac, *Atmos. Meas. Tech.*, *3*(6), 1683–1706, doi: 10.5194/amt-3-1683-2010.
- Lawson, R. P., D. O'Connor, P. Zmarzly, K. Weaver, B. Baker, Q. Mo, and H. Jonsson (2006), The 2d-s (stereo) probe: Design and preliminary tests of a new airborne, high-speed, high-resolution particle imaging probe, *J. Atmos. Oceanic Technol.*, *23*(11), 1462–1477, doi: 10.1175/JTECH1927.1.
- Liebe, H., G. Hufford, and T. Manabe (1991), A model for the complex permittivity of water at frequencies below 1 THz, *Int. J. Infrared Milli.*, *12*(7), 659–675.
- List, R., and R. Schemena (1971), Free-fall behavior of planar snow crystals, conical graupel and small hail, *J. Atmos. Sci.*, *28*(1), 110–&, doi: 10.1175/1520-0469(1971)028<0110:FFBOPS>2.0.CO;2.
- Liu, G. (2008), A database of microwave single-scattering properties for nonspherical ice particles, *Bull. Amer. Meteor. Soc.*, *89*(10), 1563–1570, doi: 10.1175/2008BAMS2486.1.
- Liu, H. P., and V. Chandrasekar (2000), Classification of hydrometeors based on polarimetric radar measurements: Development of fuzzy logic and neuro-fuzzy systems, and in situ verification, *J. Atmos. Oceanic Technol.*, *17*(2), 140–164.

- Löffler-Mang, M., and J. Joss (2000), An optical disdrometer for measuring size and velocity of hydrometeors, *J. Atmos. Oceanic Technol.*, 17(2), 130–139, doi: 10.1175/1520-0426(2000)017<0130:AODFMS>2.0.CO;2.
- Löffler-Mang, M., and J. Joss (2000), An optical disdrometer for measuring size and velocity of hydrometeors, *J. Atmos. Oceanic Technol.*, 17(2), 130–139.
- Lovejoy, S., D. Schertzer, and V. C. Allaire (2008), The remarkable wide range spatial scaling of TRMM precipitation, *Atmos. Res.*, 90(1), 10–32, doi: 10.1016/j.atmosres.2008.02.016.
- Luke, E. P., P. Kollias, and M. D. Shupe (2010), Detection of supercooled liquid in mixed-phase clouds using radar Doppler spectra, *J. Geophys. Res.*, 115, D19201, doi: 10.1029/2009JD012884.
- Magono, C., and C. W. Lee (1966), Meteorological classification of natural snow crystals, *J. Fac. Sci., Hokkaido Univ., Series VII*, 2(4), 321–335.
- Mandelbrot, B. B., and J. R. Wallis (1968), Noah, Joseph, and operational hydrology, *Water Resour. Res.*, 4(5), 909–918, doi: 10.1029/WR004i005p00909.
- Marshall, J. S., R. C. Langille, and W. M. Palmer (1947), Measurement of rainfall by radar, *J. Meteor.*, 4, 186–192.
- Marzano, F., D. Scaranari, and G. Vulpiani (2007), Supervised fuzzy-logic classification of hydrometeors using C-band weather radars, *IEEE T. Geosci. Remote Sens.*, 45(11), 3784–3799, doi: 10.1109/TGRS.2007.903399.
- Marzano, F. S., D. Cimini, and M. Montopoli (2010a), Investigating precipitation microphysics using ground-based microwave remote sensors and disdrometer data, *Atmos. Res.*, 97(4, SI), 583–600, doi: 10.1016/j.atmosres.2010.03.019.
- Marzano, F. S., G. Botta, and M. Montopoli (2010b), Iterative bayesian retrieval of hydrometeor content from X-band polarimetric weather radar, *IEEE T. Geosci. Remote Sens.*, 48(8), 3059–3074.
- Matrosov, S. Y. (1992), Radar reflectivity in snowfall, *IEEE T. Geosci. Remote Sens.*, 30(3), 454–461.
- Matrosov, S. Y. (2010), Evaluating polarimetric X-band radar rainfall estimators during HMT, *J. Atmos. Oceanic Technol.*, 27(1), 122–134, doi: 10.1175/2009JTECHA1318.1.
- Matrosov, S. Y., R. A. Kropfli, R. F. Reinking, and B. E. Martners (1999), Prospects for measuring rainfall using propagation differential phase in X- and K_a -radar bands, *J. Appl. Meteor.*, 38(6), 766–776.
- Matrosov, S. Y., K. A. Clark, B. E. Martner, and A. Tokay (2002), X-band polarimetric radar measurements of rainfall, *J. Appl. Meteor.*, 41(9), 941–952.

Bibliography

- Matrosov, S. Y., K. A. Clark, and D. E. Kingsmill (2007), A polarimetric radar approach to identify rain, melting-layer, and snow regions for applying corrections to vertical profiles of reflectivity, *J. Appl. Meteor. Clim.*, *46*(2), 154–166.
- Maynard, R. H. (1946), Radar and weather, *J. Meteor.*, *2*(4), 214–226.
- Mercer, J. (1905), Functions of positive and negative type and their connection with the theory of integral equations, *Philos. Tr. R. Soc.*, *CCIX*(A456), 215–228.
- Miniscloux, F., J.-D. Creutin, and S. Anquetin (2001), Geostatistical analysis of orographic rain bands, *J. Appl. Meteor.*, *40*(11), 1835–1854, doi: 10.1175/1520-0450(2001)040<1835:GAOOR>2.0.CO;2.
- Mishchenko, M., L. Travis, and A. Lacis (2002), *Scattering, Absorption, and Emission of Light by Small Particles*, 445 pp., Cambridge University Press.
- Mishchenko, M. I., and L. D. Travis (1998), Capabilities and limitations of a current FORTRAN implementation of the T-matrix method for randomly oriented, rotationally symmetric scatterers, *J. Quant. Spectrosc. Radiat. Transfer*, *60*(3), 309–324.
- Mishchenko, M. I., L. D. Travis, and D. W. Mackowski (1996), T-matrix computations of light scattering by nonspherical particles: A review, *J. Quant. Spectrosc. Radiat. Transfer*, *55*(5), 535–575.
- Mitchell, D. L., R. Zhang, and R. L. Pitter (1990), Mass-dimensional relationships for ice particles and the influence of riming on snowfall rates, *J. Appl. Meteor.*, *29*(2), 153–163, doi: 10.1175/1520-0450(1990)029<0153:MDRFIP>2.0.CO;2.
- Mosimann, L., E. Weingartner, and A. Waldvogel (1994), An analysis of accreted drop sizes and mass on rimed snow crystals, *J. Atmos. Sci.*, *51*(11), 1548–1558, doi: 10.1175/1520-0469(1994)051<1548:AAOADS>2.0.CO;2.
- Mott, R., D. Scipion, M. Schneebeli, N. Dawes, A. Berne, and M. Lehning (2014), Orographic effects on snow deposition patterns in mountainous terrain, *J. Geophys. Res. Atmos.*, *119*(3), 1419–1439, doi: 10.1002/2013JD019880.
- Nesbitt, S. W., and A. M. Anders (2009), Very high resolution precipitation climatologies from the tropical rainfall measuring mission precipitation radar, *Geophys. Res. Lett.*, *36*, doi: 10.1029/2009GL038026.
- Nespor, V., W. F. Krajewski, and A. Kruger (2000), Wind-induced error of raindrop distribution measurement using a two-dimensional video disdrometer, *J. Atmos. Oceanic Technol.*, *17*(11), 1483–1492.
- Ono, A. (1969), The shape and riming properties of ice crystals in natural clouds, *J. Atmos. Sci.*, *26*, 138–147, doi: 10.1175/1520-0469(1969)026<0138:TSARPO>2.0.CO;2.

- Oraltay, R. G., and J. Hallett (1989), Evaporation and melting of ice crystals: A laboratory study, *Atmos. Res.*, 24(1-4), 169–189.
- Otto, T., and H. W. J. Russchenberg (2011), Estimation of specific differential phase and differential backscatter phase from polarimetric weather radar measurements of rain, *IEEE Geosci. Remote Sens. Lett.*, 8(5), 988–992, doi: 10.1109/LGRS.2011.2145354.
- Otto, T., and H. W. J. Russchenberg (2012), Rainfall rate retrieval with IDRA, the polarimetric X-band radar at Cabauw, netherlands., in *Proc. ERAD 2012 - The seventh European conference on radar in meteorology and hydrology*, Toulouse, FR.
- Park, S.-G., V. N. Bringi, V. Chandrasekar, M. Maki, and K. Iwanami (2005), Correction of radar reflectivity and differential reflectivity for rain attenuation at X band. Part I: theoretical and empirical basis, *J. Atmos. Oceanic Technol.*, 22(11), 1621–1632, doi: 10.1175/JTECH1803.1.
- Peng, C.-K., S. V. Buldyrev, S. Havlin, M. Simons, H. E. Stanley, and A. L. Goldberger (1994), Mosaic organization of DNA nucleotides, *Phys. Rev. E*, 49(2), 1685–1689, doi: 10.1103/PhysRevE.49.1685.
- Pinsky, M. B., and A. P. Khain (1998), Some effects of cloud turbulence on water-ice and ice-ice collisions, *Atmos. Res.*, 48(SI), 69–86.
- Platt, C. M. R. (1997), A parameterization of the visible extinction coefficient of ice clouds in terms of the ice/water content, *J. Atmos. Sci.*, 54(16), 2083–2098, doi: 10.1175/1520-0469(1997)054<2083:APOTVE>2.0.CO;2.
- Pruppacher, H. R., and R. L. Klett (1997), *Microphysics of clouds and precipitation*, no. 18 in Atmospheric and Oceanographic Sciences Library, 2nd ed., 954 pp., Kluwer Academic Press.
- Rakotomamonjy, A., F. Bach, S. Canu, and Y. Grandvalet (2008), SimpleMKL, *J. Mach. Learn. Res.*, 9, 2491–2521.
- Rangno, A. L. (2008), Fragmentation of freezing drops in shallow maritime frontal clouds, *J. Atmos. Sci.*, 65(4), 1455–1466, doi: 10.1175/2007JAS2295.1.
- Rauber, R. M., and A. Tokay (1991), An explanation for the existence of supercooled water at the top of cold clouds, *J. Atmos. Sci.*, 48(8), 1005–1023, doi: {10.1175/1520-0469(1991)048<1005:AEFTEO>2.0.CO;2}.
- Raupach, T. H., and A. Berne (2015), Correction of raindrop size distributions measured by parsivel disdrometers, using a two-dimensional video disdrometer as a reference, *Atmos. Meas. Tech.*, 8(1), 343–365, doi: 10.5194/amt-8-343-2015.
- Rico-Ramirez, M. A., and I. Cluckie (2008), Classification of ground clutter and anomalous propagation using dual-polarization weather radar, *IEEE T. Geosci. Remote Sens.*, 46(7), 1892–1904, doi: 10.1109/TGRS.2008.916979.

Bibliography

- Robert, S., L. Foresti, and M. Kanevski (2013), Spatial prediction of monthly wind speeds in complex terrain with adaptive general regression neural networks, *Int. J. Climatol.*, 33(7), 1793–1804, doi: 10.1002/joc.3550.
- Ryan, B. F. (2000), A bulk parameterization of the ice particle size distribution and the optical properties in ice clouds, *J. Atmos. Sci.*, 57(9), 1436–1451, doi: 10.1175/1520-0469(2000)057<1436:ABPOTI>2.0.CO;2.
- Ryzhkov, A., and D. S. Zrnica (1996), Assessment of rainfall measurement that uses specific differential phase, *J. Appl. Meteor.*, 35(11), 2080–2090.
- Ryzhkov, A. V., T. J. Schuur, D. W. Burgess, P. L. Heinselman, S. E. Giangrande, and D. S. Zrnica (2005a), The joint polarization experiment, polarimetric rainfall measurements and hydrometeor classification, *Bull. Amer. Meteor. Soc.*, 86(6), 809–824, doi: 10.1175/BAMS-86-6-809.
- Ryzhkov, A. V., S. E. Giangrande, V. M. Melnikov, and T. J. Schuur (2005b), Calibration issues of dual-polarization radar measurements, *J. Atmos. Oceanic Technol.*, 22(8), 1138–1155, doi: 10.1175/JTECH1772.1.
- Sachidananda, M., and D. S. Zrnica (1986), Differential propagation phase-shift and rainfall rate estimation, *Radio Sci.*, 21(2), 235–247.
- Sachidananda, M., and D. S. Zrnica (1987), Rain rate estimates from differential polarisation measurements, *J. Atmos. Oceanic Technol.*, 4(4), 588–598.
- Schleiss, M., J. Jaffrain, and A. Berne (2012), Stochastic simulation of intermittent DSD fields in time, *J. Hydrometeorol.*, 13(2), 621–637, doi: 10.1175/JHM-D-11-018.1.
- Schneebeli, M., and A. Berne (2012), An extended Kalman filter framework for polarimetric X-band weather radar data processing, *J. Atmos. Oceanic Technol.*, 29(5), 711–730, doi: 10.1175/JTECH-D-10-05053.1.
- Schneebeli, M., and C. Mätzler (2009), A calibration scheme for microwave radiometers using tipping curves and Kalman filtering, *IEEE T. Geosci. Remote Sens.*, 47(12), 4201–4209, doi: 10.1109/TGRS.2009.2023784.
- Schneebeli, M., J. Sakuragi, T. Biscaro, C. F. Angelis, I. Carvalho da Costa, C. Morales, L. Baldini, and L. A. T. Machado (2012), Polarimetric x-band weather radar measurements in the tropics: radome and rain attenuation correction, *Atmos. Meas. Tech.*, 5(9), 2183–2199, doi: 10.5194/amt-5-2183-2012.
- Schneebeli, M., N. Dawes, M. Lehning, and A. Berne (2013), High-resolution vertical profiles of polarimetric X-band weather radar observables during snowfall in the Swiss Alps, *J. Appl. Meteor. Clim.*, 52(2), 378–394, doi: 10.1175/JAMC-D-12-015.1.
- Schneebeli, M., J. Grazioli, and A. Berne (2014), Improved estimation of the specific differential phase shift using a compilation of kalman filter ensembles, *IEEE T. Geosci. Remote Sens.*, 52(8), 5137–5149, doi: 10.1109/TGRS.2013.2287017.

- Scholkopf, B., and A. J. Smola (2001), *Learning with Kernels: Support Vector Machines, Regularization, Optimization, and Beyond*, MIT Press, Cambridge, MA, USA.
- Schönhuber, M., G. Lammer, and W. L. Randeu (2008), *The 2D video disdrometer. Chapter 1 in 'Precipitation: Advances in Measurement, Estimation and Prediction'*, S. Michaelides, Ed.
- Schuur, T. J., A. V. Ryzhkov, D. S. Zrnica, and M. Schonhuber (2001), Drop size distributions measured by a 2D video disdrometer: Comparison with dual-polarization radar data, *J. Appl. Meteor.*, 40(6), 1019–1034, doi: 10.1175/1520-0450(2001)040<1019:DSDMBA>2.0.CO;2.
- Scipion, D., R. Mott, M. Lehning, M. Schneebeli, and A. Berne (2013), Seasonal small-scale spatial variability in alpine snowfall and snow accumulation, *Water Resour. Res.*, 49(3), 1446–1457, doi: 10.1002/wrcr.20135.
- Seliga, T. A., and V. N. Bringi (1976), Potential use of differential reflectivity measurements at orthogonal polarizations for measuring precipitation, *J. Appl. Meteor.*, 15(1), 69–76.
- Shupe, M. D. (2007), A ground-based multisensor cloud phase classifier, *Geophys. Res. Lett.*, 34(22), doi: 10.1029/2007GL031008.
- Smith, P. L. (1984), Equivalent radar reflectivity factors for snow and ice particles, *J. Climate Appl. Meteor.*, 23(8), 1258–1260.
- Snyder, J. C., H. B. Bluestein, G. Zhang, and S. J. Frasier (2010), Attenuation correction and hydrometeor classification of high-resolution, X-band, dual-polarized mobile measurements in severe convective storms, *J. Atmos. Oceanic Technol.*, 27(12), 1979–2001, doi: 10.1175/2010JTECHA1356.1.
- Straka, J. M., and E. R. Mansell (2005), A bulk microphysics parameterization with multiple ice precipitation categories, *J. Appl. Meteor.*, 44(4), 445–466, doi: 10.1175/JAM2211.1.
- Straka, J. M., D. S. Zrnica, and A. V. Ryzhkov (2000), Bulk hydrometeor classification and quantification using polarimetric radar data: synthesis of relations, *J. Appl. Meteor.*, 39(8), 1341–1372.
- Sullivan, S. (2009), Evaluation of support vector machines and minimax probability machines for weather prediction, in *Seventh conference on artificial intelligence and its applications to the environmental sciences*, Phoenix, USA.
- Takahashi, T. (2014), Influence of liquid water content and temperature on the form and growth of branched planar snow crystals in a cloud, *J. Atmos. Sci.*, 71(11), 4127–4142, doi: 10.1175/JAS-D-14-0043.1.
- Testud, J., E. Le Bouar, E. Obligis, and M. Ali-Mehenni (2000), The rain profiling algorithm applied to polarimetric weather radar, *J. Atmos. Oceanic Technol.*, 17(3), 332–356.
- Thompson, E. J., S. A. Rutledge, B. Dolan, V. Chandrasekar, and B. L. Cheong (2014), A dual-polarization radar hydrometeor classification algorithm for winter precipitation, *J. Atmos. Oceanic Technol.*, 31(7), 1457–1481, doi: 10.1175/JTECH-D-13-00119.1.

Bibliography

- Thurai, M., and V. N. Bringi (2005), Drop axis ratios from a 2D video disdrometer, *J. Atmos. Oceanic Technol.*, 22(7), 966–978, doi: 10.1175/JTECH1767.1.
- Thurai, M., D. Hudak, and V. N. Bringi (2008), On the possible use of copolar correlation coefficient for improving the drop size distribution estimates at c band, *J. Atmos. Oceanic Technol.*, 25(10), 1873–1880, doi: 10.1175/2008JTECHA1077.1.
- Thurai, M., M. Szakall, V. N. Bringi, K. V. Beard, S. K. Mitra, and S. Borrmann (2009), Drop shapes and axis ratio distributions: comparison between 2d video disdrometer and wind-tunnel measurements, *J. Atmos. Oceanic Technol.*, 26(7), 1427–1432, doi: 10.1175/2009JTECHA1244.1.
- Torlaschi, E., and Y. Gingras (2003), Standard deviation of the copolar correlation coefficient for simultaneous transmission and reception of vertical and horizontal polarized weather radar signals, *J. Atmos. Oceanic Technol.*, 20(5), 760–766, doi: 10.1175/1520-0426(2003)20<760:SDOTCC>2.0.CO;2.
- Trenberth, K. E., A. Dai, R. M. Rasmussen, and D. B. Parsons (2003), The changing character of precipitation, *Bull. Amer. Meteor. Soc.*, 84(9), 1205–1217, doi: 10.1175/BAMS-84-9-1205.
- Tuia, D., G. Camps-Valls, G. Matasci, and M. Kanevski (2010), Learning relevant image features with multiple-kernel classification, *IEEE T. Geosci. Remote Sens.*, 48(10), 3780–3791, doi: 10.1109/TGRS.2010.2049496.
- Tyynela, J., J. Leinonen, D. Moisseev, and T. Nousiainen (2011), Radar backscattering from snowflakes: comparison of fractal, aggregate, and soft spheroid models, *J. Atmos. Oceanic Technol.*, 28(11), 1365–1372, doi: 10.1175/JTECH-D-11-00004.1.
- Ulbrich, C. W. (1983), Natural variations in the analytical form of the raindrop-size distribution, *J. Climate Appl. Meteor.*, 22(10), 1764–1775.
- Ulbrich, C. W., and D. Atlas (2007), Microphysics of raindrop size spectra: tropical continental and maritime storms, *J. Appl. Meteor. Clim.*, 46, 1777–1791.
- Vardiman, L. (1978), The generation of secondary ice particles in clouds by crystal-crystal collision, *J. Atmos. Sci.*, 35(11), 2168–2180.
- Vivekanandan, J., V. N. Bringi, M. Hagen, and P. Meischner (1994), Polarimetric radar studies of atmospheric ice particles, *IEEE T. Geosci. Remote Sens.*, 32, 1–10.
- Vivekanandan, J., D. S. Zrnic, S. M. Ellis, R. Oye, A. V. Ryzhkov, and J. Straka (1999), Cloud microphysics retrieval using S-band dual-polarization radar measurements, *Bull. Amer. Meteor. Soc.*, 80(3), 381–388, doi: 10.1175/1520-0477(1999)080<0381:CMRUSB>2.0.CO;2.
- Volpi, M., D. Tuia, and M. Kanevski (2012), Memory-based cluster sampling for remote sensing image classification, *IEEE Trans. Geosci. Remote Sens.*, 50(8), 3096–3106.

- Volpi, M., D. Tuia, F. Bovolo, M. Kanevski, and L. Bruzzone (2013), Supervised change detection in vhr images using contextual information and support vector machines, *Int. J. Appl. Earth Obs. Geoinf.*, 20(SI), 77–85, doi: 10.1016/j.jag.2011.10.013.
- Von Luxburg, U. (2007), A tutorial on spectral clustering, *Statistics and Computing*, 17(4), 395–416.
- Vulpiani, G., M. Montopoli, L. Delli Passeri, A. G. Gioia, P. Giordano, and F. S. Marzano (2012), On the use of dual-polarized C-band radar for operational rainfall retrieval in mountainous areas, *J. Appl. Meteor. Clim.*, 51, 405–425, doi: 10.1175/JAMC-D-10-05024.1.
- Wang, Y. T., and V. Chandrasekar (2009), Algorithm for estimation of the specific differential phase, *J. Atmos. Oceanic Technol.*, 26(12), 2565–2578, doi: 10.1175/2009JTECHA1358.1.
- Wang, Y. T., and V. Chandrasekar (2010), Quantitative precipitation estimation in the CASA X-band dual-polarization radar network, *J. Atmos. Oceanic Technol.*, 27(10), 1665–1676, doi: 10.1175/2010JTECHA1419.1.
- Ward, J. (1963), Hierarchical grouping to optimize an objective function, *Journal of the American statistical association*, 58(301), 236–244.
- Westbrook, C. D., and A. J. Illingworth (2011), Evidence that ice forms primarily in supercooled liquid clouds at temperatures >-27 degrees c, *Geophys. Res. Lett.*, 38, doi: 10.1029/2011GL048021.
- Westbrook, C. D., and A. J. Illingworth (2013), The formation of ice in a long-lived supercooled layer cloud, *Q. J. Roy. Meteor. Soc.*, 139(677), 2209–2221, doi: 10.1002/qj.2096.
- Whiteman, D. N., and S. H. Melfi (1999), Cloud liquid water, mean droplet radius, and number density measurements using a raman lidar, *J. Geophys. Res. Atmos.*
- Wilks, D. S. (Ed.) (2011), *Statistical Methods in the Atmospheric Sciences, International Geophysics*, vol. 100, Academic Press.
- Xu, R., and D. Wunsch (2005), Survey of clustering algorithms, *IEEE T. Neural Netw.*, 16(3), 645–678, doi: 10.1109/TNN.2005.845141.
- Xue, M., K. K. Droegemeier, and V. Wong (2000), The Advanced Regional Prediction System (ARPS); A multi-scale nonhydrostatic atmospheric simulation and prediction model. Part I: model dynamics and verification, *Meteorol. Atmos. Phys.*, 75(3-4), 161–193, doi: 10.1007/s007030070003.
- Yano, J.-I., and V. T. J. Phillips (2011), Ice-ice collisions: An ice multiplication process in atmospheric clouds, *J. Atmos. Sci.*, 68(2), 322–333, doi: 10.1175/2010JAS3607.1.
- Yuter, S. E., D. E. Kingsmill, L. B. Nance, and M. Loeffler-Mang (2006), Observations of precipitation size and fall speed characteristics within coexisting rain and wet snow, *J. Appl. Meteor. Clim.*

Bibliography

- Zeng, J., and W. Qiao (2011), Support vector machine-based short-term wind power forecasting, in *Power Systems Conference and Exposition (PSCE), 2011 IEEE/PES*, pp. 1–8, doi: 10.1109/PSCE.2011.5772573.
- Zhang, G., J. Vivekanandan, and E. Brandes (2001), A method for estimating rain rate and drop size distribution from polarimetric radar measurements, *IEEE T. Geosci. Remote Sens.*, 39(4), 830–841.
- Zhang, G., M. Xue, Q. Cao, and D. Dawson (2008), Diagnosing the intercept parameter for exponential raindrop size distribution based on video disdrometer observations: model development, *J. Appl. Meteor. Clim.*, 47(11), 2983–2992, doi: 10.1175/2008JAMC1876.1.
- Zhang, G., S. Luchs, A. Ryzhkov, M. Xue, L. Ryzhkova, and Q. Cao (2011), Winter precipitation microphysics characterized by polarimetric radar and video disdrometer observations in central oklahoma, *J. Appl. Meteor. Clim.*, 50(7), 1558–1570, doi: 10.1175/2011JAMC2343.1.
- Zieger, P., et al. (2012), Spatial variation of aerosol optical properties around the high-alpine site jungfraujoeh (3580 m a.s.l.), *Atmos. Chem. Phys.*, 12(15), doi: 10.5194/acp-12-7231-2012.
- Zrnic, D. S., and A. V. Ryzhkov (1996), Advantages of rain measurements using specific differential phase, *J. Atmos. Oceanic Technol.*, 13(2), 454–464.



Jacopo Grazioli

Curriculum Vitae

Education

- 2011–2015 **PhD in hydrometeorology**, *École Polytechnique Fédérale de Lausanne*, Switzerland.
- 2008–2010 **M.Sc. in environmental engineering**, *Università degli studi di Padova*, Italy.
- 2005–2008 **Bachelor in environmental engineering**, *Università degli studi di Padova*, Italy.
- 2000–2005 **Maturità scientifica**, *Liceo scientifico Enrico Fermi di Pieve di Cadore*, Italy.

PhD thesis

- Title *Polarimetric weather radar: from signal processing to micro-physical retrievals.*
- Institution *École Polytechnique Fédérale de Lausanne*
- Supervisors Professor Alexis Berne

Other research projects

- Winter 2010 **Master thesis**, Near and intermediate field evolution of a negatively buoyant jet. Laboratory experiments and Mathematical modeling.
- Autumn 2010 **Semester project**, Designing a wastewater treatment plant serving a population of 40000 equivalent inhabitants and a component of industrial discharge.
- Autumn 2009 **Semester project**, Designing an integrated solid waste management plan for the province of Carbonia-Iglesias (Sardinia, Italy).
- Spring 2008 **Bachelor thesis**, Reactivation of anaerobic bacterial sludge.

Experience

- 2011–2015 **Teaching assistant**, *École Polytechnique Fédérale de Lausanne*, Switzerland, Assistant for the M.Sc. course “Spatial statistics and analysis” and for the Bachelor course “Remote sensing” .
- 2008 **Environmental laboratory intern**, *Università degli studi di Padova*, Italy, Intern in a laboratory conducting chemical, mechanical, and biological analysis of liquid and solid waste .

Languages

Italian	Native
English	Fluent
French	Advanced
Polish	Beginner

Computer skills

OS	Microsoft Windows, Linux (Ubuntu)
Office	LaTeX, Open Office, Excel
Programming	IDL, GDL, R, MATLAB

Other skills

Statistics and Mathematics	Applied statistics, geostatistics, application of supervised and unsupervised classification methods, data mining.
Remote sensing	Interpretation and processing of polarimetric radar data. Interpretation of Lidar, rain gauges, and disdrometers data.
Organizational	Management and organization of scientific campaigns. Deployment, maintenance, management of instruments and data acquisition. Writing of technical and scientific reports, transfer of knowledge.

Publications

- 2015 “Riming in winter alpine snowfall during CLACE 2014: polarimetric radar and in-situ observations”: Grazioli, J., G. Lloyd, L. Panziera, P. Connolly, J. Henneberger, A. Berne *Atmos. Chem. Phys.*, **submitted**
- 2015 “Deployment and performance analyses of high-resolution Iowa XPOL radar system during the NASA IFloodS Campaign”: Mishra, K. V., W. F. Krajewski, R. Goska, D. Ceynar, B. Seo, A. Kruger, J. Niemeier, M. B. Galvez, V. N. Bringi, L. Tolstoy, P. Kucera, W. Petersen, J. Grazioli, A. L. Pazmany, *J. Hydrometeorol.*, **in revision**
- 2015 “Hydrometeor classification from polarimetric radar measurements: a clustering approach”: Grazioli, J., D. Tuia, A. Berne, *Atmos. Meas. Tech.*, 8, 149-170
- 2014 “Multiple-frequency radar observations collected in southern France during the Åeld phase of the hydrometeorological cycle in the Mediterranean experiment (HyMeX)”: Bousquet, O., A. Berne, J. Delanoe, Y. Dufournet, J. J. Gourley, J. Van-Baelen, C. Augros, L. Besson, B. Boudevillain, O. Caumont, E. Defer, J. Grazioli, D. J. Jorgensen, P.-E. Kirstetter, J.-F. Ribaud, J. Beck, G. Delrieu, V. Ducrocq, D. Scipion, A. Schwarzenboeck, J. Zwiebel: *Bull. Amer. Meteor. Soc.*, online first, 2014.
- 2014 “Precipitation, soil moisture and runoff variability in a small river catchment (Ardèche, France) during HyMeX Special Observation Period 1”: J. Huza, A. J. Teuling, I. Braud, J. Grazioli, L. A. Melsen, G. Nord, T. H. Raupach, R. Uijlenhoet, *J. Hydrol.*, 516, 330-342
- 2014 “Hydrometeor classification from two-dimensional video disdrometer data”: Grazioli, J., D. Tuia, S. Monhart, M. Schneebeli, T. Raupach, A. Berne, *Atmos. Meas. Tech.*, 7, 2869-2882
- 2014 “Improved estimation of the specific differential phase shift using a compilation of Kalman Filter ensembles”: Schneebeli, M., J. Grazioli, A. Berne, *IEEE T. Geosci. Remote Sens.*, 52, 5137-5149

Chemin du Closalet 24 – Pr everenges, Switzerland (CH) 1028

☎ (+41) 078 95 38 753 • ✉ jacopo.grazioli@epfl.ch

🌐 <http://people.epfl.ch/jacopo.grazioli?lang=en>

- 2014 “Accuracy of phase-based algorithms for the estimation of the specific differential phase shift using simulated polarimetric weather radar data”: Grazioli, J., M. Schneebeli, A. Berne, *Geoscience and Remote Sensing Letters, IEEE*, vol.11, No.4, 763-767

Awards

- 2010 Special mention of the M.Sc. evaluation committee, as a recognition for an outstanding university career.

Other academic activities

- 2013-present **Reviewer** for *Journal of Atmospheric and Oceanic Technology*, *Advances in Water Resources*, *Journal of Selected Topics in Applied Earth Observations and Remote Sensing*, and *Atmospheric Measurement techniques*.